THE CONSTRUCTION AND CHARACTERISTICS OF AN AMMONIA BEAM MASER EMPLOYING A FABRY-PÉROT CAVITY

Thesis submitted to the
University of Keele for
the Degree of Doctor of Philosophy

by

Gerald D.S.Smart

Department of Physics
University of Keele.

September 1973.

CONTENTS

ACKNOWLEDGEMENTS

The Author would like to thank

Professor D.J.E. Ingram for the provision of experimental facilities.

Dr. D.C. Lainé for his unfailing help and encouragement throughout this work.

Dr. W.S. Bardo and Dr. C.A. Scott for many useful discussions.

Mr. H. Wardell and the staff of the University Workshop for the construction of the vacuum chambers and the Fabry-Pérot cavity, and for their painstaking work during the machining of the mirrors.

Mr. G. Dudley and the staff of the Department workshop for the construction of numerous other maser components, and for their continued assistance throughout the experimental work.

The S.R.C., the University of Keele, and the Plessey Co. Ltd. for personal finance.

Mrs. B. Haywood for her care in typing this thesis.

Mr. N. Banks, Mr. M.T. Cheyney and Mr. R. Edge for the preparation of the illustrations.

ABSTRACT

The construction of an ammonia molecular beam maser employing an open resonator is described. The operation of this maser as an amplifier enables the effects of mode degeneracy in the resonator to be examined in a controlled manner. Its operation above oscillation threshold can give rise to biharmonic effects with beat frequencies of a few hundred Hz. A transient behaviour of the maser makes possible the measurement of low field Zeeman splittings within the maser linewidth.

PREFACE

The principle of stimulated emission is often attributed to Einstein, 1917, since it is suggested by his thermodynamic arguments concerning the interactions between electromagnetic waves and a quantum-mechanical system. The principle predicts that the emission of radiation, as a result of atomic or molecular transitions, should be induced by the presence of a signal field and should have phase coherence with that field. This idea did not take practical shape until the successful operation of the molecular beam maser in 1954.

This event marked the beginning of a new field of study in Physics - Quantum Electronics - which has led to the development of a wide range of new devices. All of these devices rely on atomic or molecular processes for amplification or oscillation. Some Quantum Electronic devices, such as the laser, the solid state maser and the molecular or atomic frequency standard, have made considerable impact on modern life. Others have found widespread use as research tools, noteably for molecular spectroscopy and for investigations of the interaction of radiation with matter.

The molecular beam maser itself was first proposed by Townes in 1951. The device was developed principally as a result of the search for improved sensitivity in molecular beam spectrometers, but it was quickly realised that its usefulness was not confined only to spectroscopy. Two papers give the details of its first operation using ammonia as the working substance. Gordon, 1955 describes the observation of the hyperfine structure of the ammonia inversion spectrum using the device,

while Gordon et al, 1955 describes the device itself and its use both as a spectrometer and as an oscillator. In the latter paper it was pointed out that its low-noise properties as an amplifier are excellent, although little use for it in this role has subsequently been found owing to the bandwidth restriction imposed by the narrow spectral line. It was realised by Gordon et al that the bandwidth restriction can be turned to advantage when the device is used as a stable-frequency oscillator, and they measured a frequency stability of better than 1 part in 10^{10} with their early equipment.

During the rest of the decade, considerable research effort was expended in order to examine the properties of the molecular beam maser oscillator and to improve its frequency stability and reproduceability. Many of the instruments built employed ammonia in its various isotopic forms as the working substance. However before the device was developed sufficiently to be used widely as a frequency standard, it was superseded by the caesium beam standard and later the hydrogen maser, which are inherently capable of greater frequency stability. Work on beam maser oscillators, aimed mainly at discovering methods of reproducing the oscillation frequency, was continued into the late 1960's, chiefly at the Russian Lebedev institute from which much of the recent literature on molecular beam masers has emerged.

The use of the beam maser as a spectrometer over a wide range of frequencies has continued to the present time. Recently a revival of interest has been noticed in this area due to the need for accurate spectroscopic data in the field of Astrophysics. As a research tool, it has also been used to make some useful contributions to knowledge of

coherence phenomena associated with the interaction of matter and radiation.

The Keele Maser Group, which includes the Author, has been pursuing a continuing series of investigations of the analogies which exist between various electric and magnetic dipole systems (Bardo, 1969). During these studies some transient phenomena which are observed in laser systems have also been seen in the ammonia beam maser. The work described in this dissertation represents the start of a further systematic study in which spatial effects observed in the laser will be investigated using an analogous beam maser system. These effects are observed as a result of the complicated modes supported by the Fabry-Pérot cavity, and also because of the extra degree of freedom allowed by this cavity compared with more conventional microwave cavities.

Although the Fabry-Pérot cavity has been widely employed in lasers, only a few instances of its use in molecular beam maser systems have been reported. It was clear at the inception of the project that there were some interesting effects to be observed using this type of cavity. Barchukov et al, 1964 reported the observation of a low frequency beat phenomenon which they were unable to explain satisfactorily. Since that time no further work to investigate this phenomenon has been reported. Using a formaldehyde beam maser with a Fabry-Pérot cavity, Krupnov and Skvortsov, 1964 observed a split stimulated emission line characteristic of molecular beam experiments with high order modes. No work has been performed in such modes of the Fabry-Pérot cavity under oscillation conditions, although work by Becker, 1965 suggests that frequency hysteresis may be observed here.

At the beginning of the project, little was understood about the design of microwave Fabry-Pérot cavities. Information which could be

found in literature was either incomplete or misleading. It was therefore necessary to devise techniques to measure the important parameters of the Fabry-Pérot cavity, and to use these techniques for the empirical design of a cavity later to be used in the work. In the design of other components of the maser (e.g. vacuum systems, microwave detection systems, devices to generate molecular beams), sufficient information was readily available to permit rapid construction of the maser. In some of these areas, however (noteably the design of state separators) the experience had to be adapted to the needs of the Fabry-Pérot cavity.

The work described in this dissertation falls naturally into two parts. In chapters 1 - 3 the design and construction of the maser is described, together with the techniques and measurements associated with the evaluation of the maser components. In chapters 4 - 6 the experimental study of the maser is presented, and discussed in the light of theory also presented in these chapters. This does not represent an exhaustive study of the operation of the Fabry-Pérot maser, but is intended to establish guidelines from which further systematic work on the maser may be planned. It also establishes some parallels in behaviour between the Fabry-Pérot maser and some laser systems. It shows that study of the maser can be fruitful in providing some new techniques which may yield useful information related to the field of laser research.

CHAPTER 1

THE MICROWAVE FABRY-PÉROT RESONATOR

1.1 INTRODUCTION

The first proposals to use Fabry-Pérot interferometers as resonators in the infra-red and optical region of the electromagnetic spectrum were by Prokhorov, 1958 in the U.S.S.R. and by Schawlow and Townes, 1958 and Dicke, 1958 in the U.S.A. Subsequently, laser resonators have employed plane and spherical mirrors in a number of different configurations. In the microwave region, particularly at millimetre and sub-millimetre wavelengths, the Fabry-Pérot resonator is also of considerable interest. Plane parallel and semi-confocal mirror arrangements have generally been preferred. In the present work the main interest is in the plane parallel configuration.

Applications for the resonator in the microwave region include high Q wavemeters (Zimmerer, 1962), gas cells for microwave spectroscopy (Schulten, 1966; Murina and Prokhorov, 1963), cavities for molecular beam masers (Krupnov and Skvortsov, 1964; Barchukov et al, 1963) and a precision Stark voltmeter (Hara et al, 1971). As a wavemeter the Fabry-Pérot resonator can be used to make absolute wavelength measurements. In spectroscopic work with Stark fields it is particularly useful because a uniform D.C. electric field is easily produced between the mirrors. In a beam maser application the high Q values which it is possible to obtain with this resonator have been found advantageous when the maser line is too weak to oscillate with a conventional cavity (Marcuse, 1961A; 1961B).

In this chapter some theoretical aspects of the plane parallel Fabry-Pérot resonator are discussed in Sec. 1.2. A brief exposition of some previous studies which bear on the subject matter of this thesis is given in Sec. 1.3. A detailed description of the resonator designed and built for the present work is presented in Sec. 1.4 and followed in Sec. 1.5 by a description of some exploratory measurements carried out on it.

1.2 THEORY OF THE FABRY-PÉROT RESONATOR

A number of attempts to provide a theory which satisfactorily predicts electromagnetic field distributions, diffraction losses and phase shifts for Fabry-Pérot resonators have been made. These include Culshaw, 1962, Ogura and Yoshida, 1964 and Ooms, 1968. Two of particular interest are the iterative calculations of Fox and Li, 1961 and the waveguide diffraction theory of Vainshtein, 1963. These two represent very different approaches to the problem but nevertheless agree closely with one another and with experiment. They are briefly described in Secs. 1.2.2 and 1.2.3 and are compared with the experimental results of other workers in Sec. 1.3 and with the results obtained in the present work in Sec. 1.5. First, however, a semi-quantitative approach which gives some insight into the behaviour of the cavity is presented.

1.2.1 The Simple Cavity Theory

The Fabry-Pérot cavity has been described semi-quantitatively by Schawlow and Townes, 1958 on the basis of the theory of closed resonators. The resonant frequencies of a closed rectangular cavity of dimensions 2ℓ, $2a$ and $2a$ are given by

$$\nu_{rsq} = (c/4)\{(q/\ell)^2 + (r/a)^2 + (s/a)^2\}^{\frac{1}{2}} \qquad 1.1$$

where c is the speed of light and q, r and s are integers. In an open cavity with square mirrors of dimension $2a \times 2a$, separated by a distance 2ℓ as

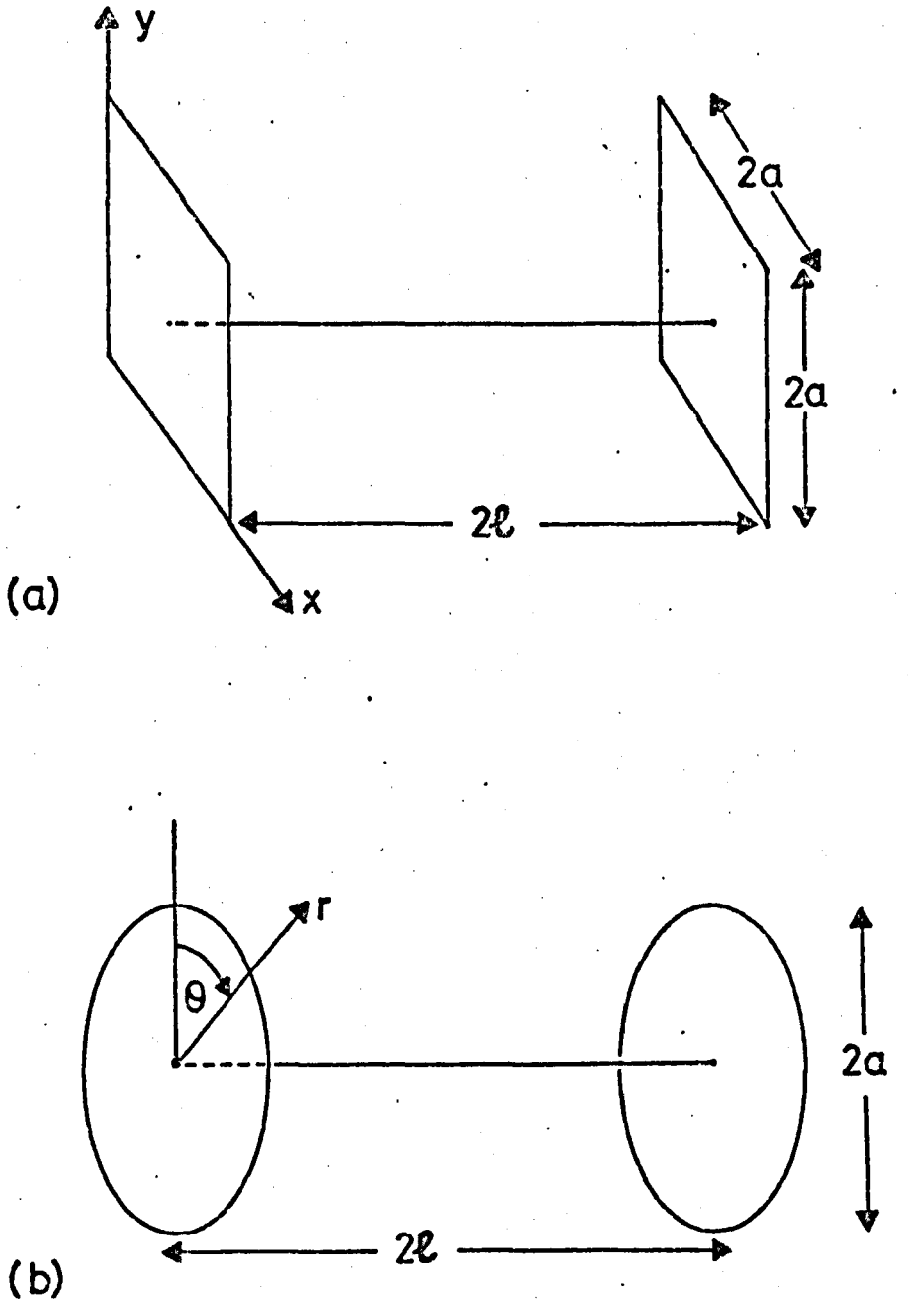

Fig 1.1 Diagrams showing open resonators (a) with square mirrors and (b) with circular mirrors.

depicted in Fig. 1.1(a), it is expected that the same resonant modes will be supported, but that only those modes which have low values of the integers r and s should be evident owing to the large diffraction losses for off-axial modes. The electromagnetic field amplitude distribution over one of the mirrors, taken as the x, y plane as shown in Fig. 1.1(a), is given by

$$A = A_o \sin(\pi r x/a)\sin(\pi s y/a) \qquad 1.2$$

The modes predicted by Schawlow and Townes are usually designated the $TEM_{r-1,s-1,q}$ modes, so that the lowest order mode is the TEM_{ooq}.

It is possible to write functions analogous to those of Eqns. 1.1 and 1.2 for an open cavity with circular mirrors. The frequency determining equation is the same as that for the TM_{mnq} modes of a cylindrical cavity:

$$\nu_{mnq} = (c/2)\{(q/\ell)^2 + (2u_{mn}/\pi a)^2\}^{\frac{1}{2}} \qquad 1.3$$

where u_{mn} is the n-th root of the m-th order Bessel function of the first kind, J_m. The field amplitude distribution over a mirror, with the origin of co-ordinates r, θ at its centre as shown in Fig. 1.1(b), is

$$A = A_o J_m(u_{mn} r/a)\cos(m\theta) \qquad 1.4$$

The scaling factor u_{mn}/a allows the n-th zero of the function to fall at the edge, r = a, of the mirror. This is shown in Fig. 1.2 where A is plotted against r/a for four values of m and n. The modes of the Fabry-Pérot cavity with circular mirrors are usually designated the $TEM_{m,n-1,q}$ modes, and the lowest order mode is again the TEM_{ooq}.

1.2.2 The Method of Iterative Computation

Fox and Li, 1961 based their iterative computations on Huygen's principle. In effect they replaced the successive reflections at the two

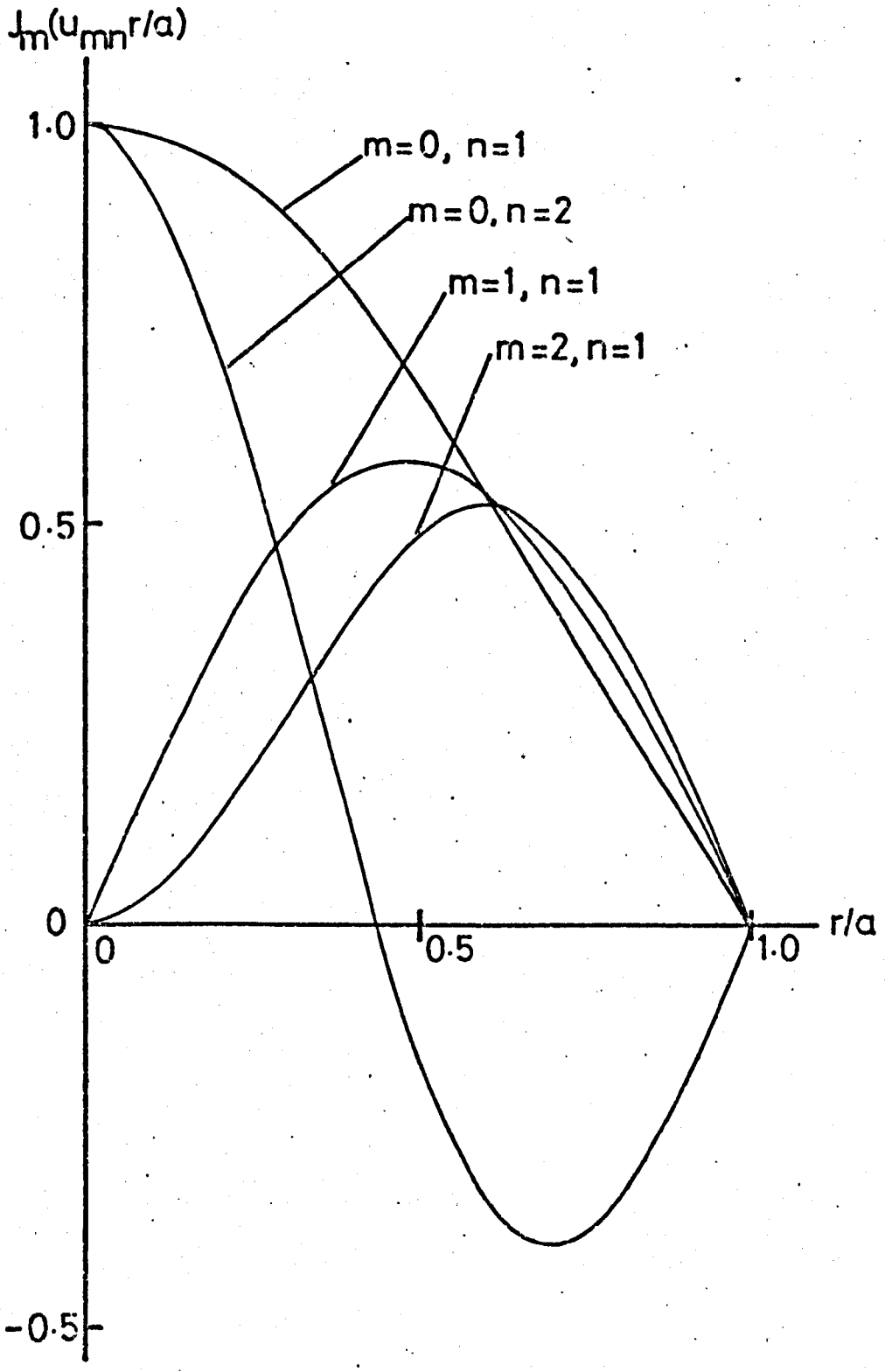

Fig 1.2 The Bessel function $J_m(u_{mn}r/a)$ drawn for four values of m and n, and for values of r in the range $0 \leqslant r \leqslant a$.

mirrors by diffraction at a series of equally spaced apertures. They computed the amplitude and phase at each aperture by applying Huygen's principle to the wavefront at the previous aperture. They discovered that, if they started with a plane wavefront at the first aperture, a steady state field was obtained after about 300 "reflections".

By starting with an even field function (having constant amplitude at the first aperture), Fox and Li obtained a steady distribution with a single maximum of field amplitude which they took to be the lowest order mode of the cavity. By starting with an odd function of field (a plane wavefront with field amplitude reversed over half of the aperture), they obtained the next lowest order mode of the cavity. In general the method is capable of yielding these two modes only, although Checcacci et al,1966A have calculated the next mode using the periodic fluctuations in amplitude and phase, which occur after about 80 "reflections" and appear to be a beat between this mode (before it dies out) and the fundamental.

Fox and Li performed computations for infinite strip mirrors, for rectangular mirrors and for plane circular mirrors, with various values of the Fresnel number

$$N = a^2/2\ell\lambda \qquad 1.6$$

where λ is the wavelength of the radiation. The approximations they used to simplify their algebra limits the validity of their calculations to the region where

$$N \ll (2\ell/a)^2 \qquad 1.7$$

However, in Sec. 1.5.3 their diffraction loss figures, extrapolated outside this range, are seen to show good agreement with the waveguide diffraction theory described in the next section.

1.2.3 The Waveguide Diffraction Theory

Vainshtein, 1963, applies a theory which he has previously developed to describe diffraction at the open end of a waveguide, to the Fabry-Pérot resonator. Since a guided wave close to the cut-off frequency is almost entirely reflected at the end of the waveguide, a wave propagating almost normally to the mirrors of an open resonator is virtually trapped within the resonator.

Vainshtein considers the three cases treated by Fox and Li, infinite strip mirrors, rectangular mirrors and circular mirrors, as well as the open ended cylindrical cavity which is frequently used in molecular beam masers. For each he is able to derive particularly simple expressions for the natural frequencies, electromagnetic field distributions, diffraction losses and phase shifts of the resonator modes. In general these turn out to be in the form of a small correction to the solutions for the equivalent closed cavity.

For a cavity with circular mirrors the complex resonant frequencies derived by Vainshtein are given by

$$\nu_{mnq} = \frac{c}{2}\left[\left(\frac{q}{\ell}\right)^2 + \left(\frac{2u_{mn}}{\pi a\{1 + \varepsilon(1 + i)/M\}}\right)^2\right]^{\frac{1}{2}} \qquad 1.8$$

where $\varepsilon = 0.824$ is a Riemann function, $M = \sqrt{(4\pi a^2/\ell\lambda)}$ is related to the Fresnel number by

$$M = \sqrt{(8\pi N)} \qquad 1.9$$

and u_{mn} has the same meaning as in Eqn. 1.3. The natural frequencies predicted by Eqn. 1.8 are $|\nu_{mnq}|$ and their spectrum is the same as that for the TM modes of the closed cylindrical cavity - see Eqn. 1.3. The

frequency separations of the modes, however, are smaller by a factor of approximately $(1 - 2\varepsilon/M)$.

The diffractive (or radiative) loss from the resonator is a function of $\text{arc}(\nu_{mnq})$. It is conveniently expressed as the fractional energy loss per transit (i.e. the energy lost from the resonator in time $2\ell/c$ expressed as a fraction of the total energy stored in the resonator) which is given by

$$f_d = 8u_{mn}^2 \, \varepsilon \, (M + \varepsilon)/\{(M + \varepsilon)^2 + \varepsilon^2\}^2 \qquad 1.10$$

In Vainshtein's theory the electromagnetic field amplitude and phase shift are expressed as a function of position in the r, θ plane by a complex amplitude

$$A = A_o J_m \left(\frac{u_{mn} \, r/a}{1+\varepsilon(1+i)/M} \right) \cos(m\theta) \qquad 1.11$$

The field amplitude is given by $|A|$ and is the same as that obtained from Eqn. 1.4, except that the n-th zero of the Bessel function no longer falls at the edge of the mirror. This is shown in Fig. 1.3 where the functions computed by Fox and Li, and Eqn. 1.11 are compared for two values of m and n.

The computed results and the Vainshtein theory agree closely except for the amplitude ripples obtained by Fox and Li. According to Vainshtein, these ripples are due to the transformation of some of the energy in the fundamental mode into higher order modes by diffraction at the open edge of the cavity. Thus any mode which is physically propagated by the cavity comprises the equivalent fundamental mode together with small amounts of higher order modes produced

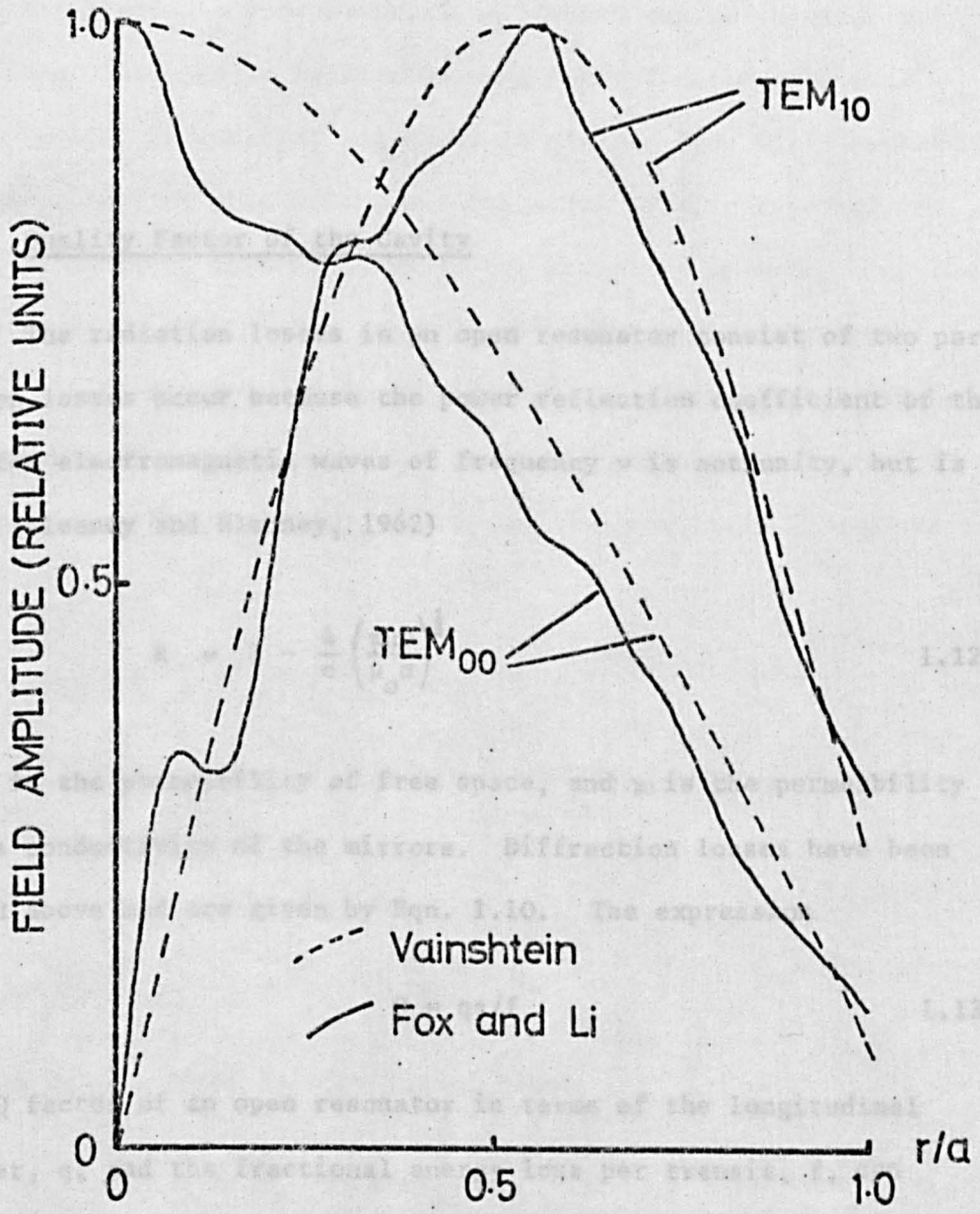

Fig 1.3 A comparison of the electromagnetic field amplitude functions given by the Vainshtein theory and the Fox and Li computations for the TEM_{00} and TEM_{10} modes in a cavity with circular mirrors having a Fresnel number, N=5.

by diffraction. The high order modes have comparatively large fractional energy loss values so that the energy transferred to them is quickly lost from the cavity. Vainshtein's theory treats all diffracted energy as being immediately lost from the resonant structure.

1.2.4 Quality Factor of the Cavity

The radiation losses in an open resonator consist of two parts. Conduction losses occur because the power reflection coefficient of the mirrors for electromagnetic waves of frequency ν is not unity, but is given by (Bleaney and Bleaney, 1962)

$$R = 1 - \frac{4}{c}\left(\frac{\pi\mu\nu}{\mu_o\sigma}\right)^{\frac{1}{2}} \qquad 1.12$$

where μ_o is the permeability of free space, and μ is the permeability and σ the conductivity of the mirrors. Diffraction losses have been described above and are given by Eqn. 1.10. The expression

$$Q = q\pi/f \qquad 1.13$$

for the Q factor of an open resonator in terms of the longitudinal mode order, q, and the fractional energy loss per transit, f, can be derived by considering a wave reflecting back and forth in the resonator. The fractional loss may be divided into its two parts by writing

$$\frac{1}{Q} = \frac{1}{Q_c} + \frac{1}{Q_d} \qquad 1.14$$

where

$$Q_c = q\pi/f_c \qquad \text{(conduction loss)} \qquad 1.15$$

$$Q_d = q\pi/f_d \qquad \text{(diffraction loss)} \qquad 1.16$$

For a given mirror material, f_c (which may be regarded as the fractional loss due to reflection in a theoretical cavity with infinite mirrors) is constant and equal to (1-R). Eqn. 1.15 shows that Q_c is proportional to mode order, and therefore to mirror separation. On the other hand, f_d is a function of the resonator geometry. Eqn. 1.10 gives $f_d \propto N^{1.5}$ for large N, while Fox and Li obtain $f_d \propto N^{1.4}$ approximately (see Ogura and Yoshida, 1964). The diffraction loss mechanism, therefore, dominates at high separations. A graph showing typical contributions Q_c and Q_d and the resultant Q is given in Fig. 1.4.

1.2.5 Coupling to the Cavity

Consider the effect of adding a coupling hole to the cavity. Eqn 1.14 becomes

$$\frac{1}{Q_\ell} = \frac{1}{Q_c} + \frac{1}{Q_d} + \frac{1}{Q_a} \qquad 1.17$$

Here Q_ℓ has been written for the loaded Q and

$$Q_a = q\pi/f_a \qquad 1.18$$

where f_a is the fractional loss per transit due to the coupling hole. The coupling coefficient, β, may be defined as the ratio of the power transmitted through the hole to that lost internally in the cavity:

$$\beta = \frac{f_a}{f_c+f_d} = \frac{f_a Q_u}{q\pi} \qquad 1.19$$

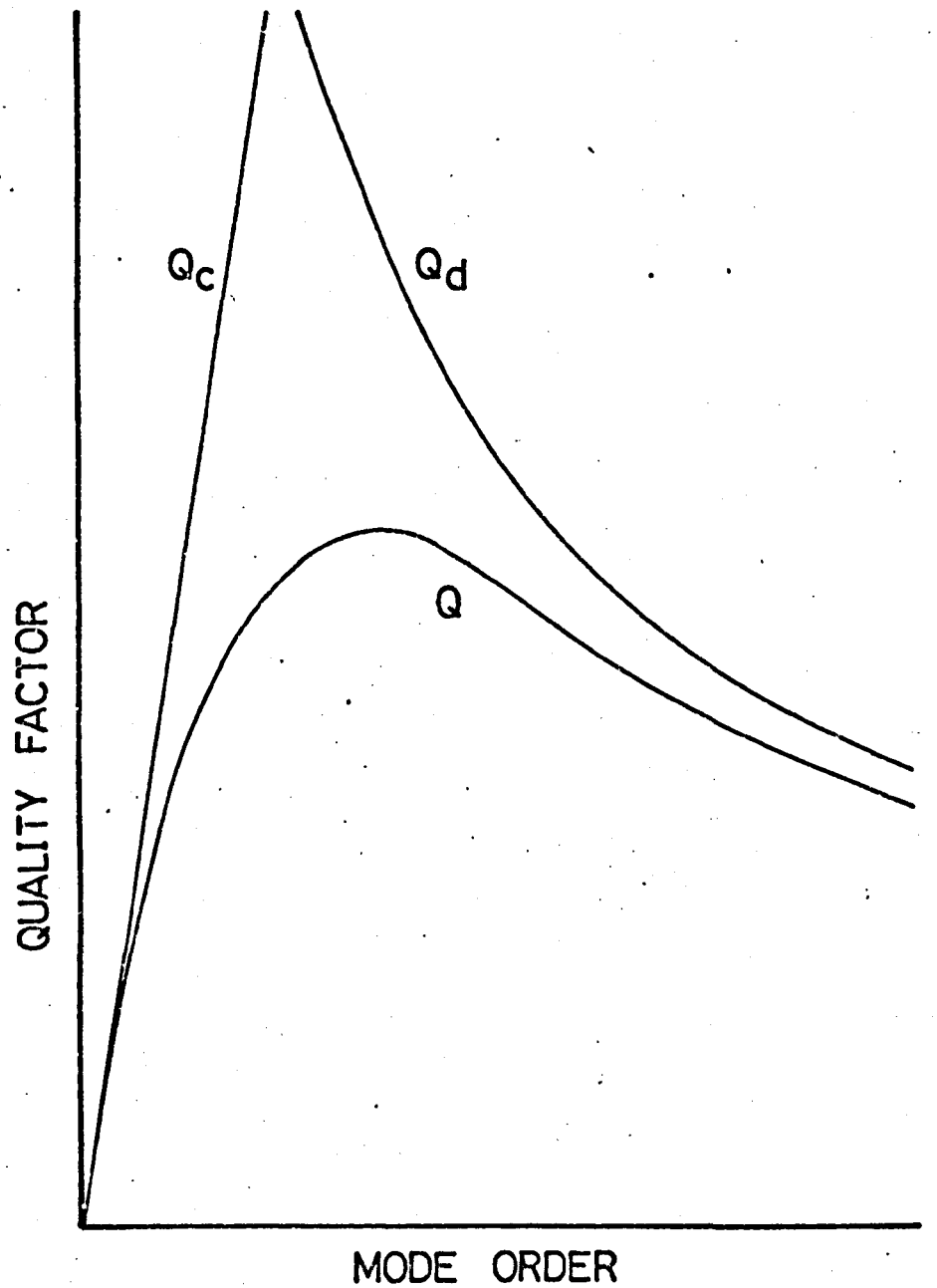

Fig 1.4 Typical behaviour of the contributions Q_c and Q_d to the quality factor, together with their resultant, Q, shown plotted against mode order, q.

where Q_u has been written for the unloaded Q defined by Eqn. 1.14.

Since the fractional loss per transit through the hole, like the conduction loss, is constant with longitudinal order q,

$$\beta \propto Q_u/q \qquad 1.20$$

Thus in a cavity having negligible diffraction loss ($f_d << f_c$) for which $Q_u \propto q$, the coupling coefficient is constant with changes in q. As soon as diffraction loss becomes significant, β becomes smaller with increase in q.

An interesting point which emerges from consideration of Eqn. 1.20 is that if it is required to adjust the cavity mirrors for optimum Q in a given mode (i.e. for minimum diffraction loss), then this condition is obtained where β has a maximum. This knowledge was used whenever the cavity had to be retuned (see Sec. 1.5.1).

1.2.6 Mirror Flatness

The extent to which the mirror surfaces depart from geometrical planes must be an important contributory factor to the diffraction loss from the cavity. However, there is no easy way to calculate accurately the effect of mirror imperfections. It seems likely that not only the average displacement from the mean plane will be important, but also the exact shape and extent of individual areas so displaced. For example, in the extreme case of a large area which departs from the plane in such a way as to form a concavity over part or all of a mirror surface, the diffraction loss will actually be reduced.

Estimates of the maximum surface departures (expressed as a fraction of the radiation wavelength) which may be allowed, in order that

the loss due to this cause may be small compared with the other losses in the cavity, vary; for example, Checcacci and Scheggi, 1965 found $\lambda/100$ sufficient at high longitudinal orders, while Krupnov and Skvortsov, 1964 suggest $\lambda/4000$ is required at small mirror separations. In fact, the required surface accuracy should depend on the expected Q of the cavity, on the wavelength, λ and on the longitudinal mode order, q, as the following semi-quantitative treatment shows.

Consider a wave reflecting back and forth inside a cavity. A mirror surface deviation of height (or depth) δ produces a distortion of the wavefront of size 2δ at each reflection. Each distortion may be added to the previous distortions so that, after n reflections, the total distortion of the wavefront is $2n\delta$. In order that this should not have a deleterious effect on the cavity Q, the distortion must never be so great (i.e. a half-wavelength), that it cancels the undistorted wavefront in phase. This requirement may be expressed

$$2n\delta < \lambda/2 \qquad 1.21$$

Now the wave under consideration falls to 1/e of its original power after $Q/q\pi$ reflections. It may be regarded as insignificant after $kQ/q\pi$ reflections, where $k \sim 1$, and therefore the relationship 1.21 need only be maintained for values of n up to $kQ/q\pi$. Eqn. 1.21 then becomes

$$\delta < \frac{q\pi\lambda}{4kQ} \qquad 1.22$$

or

$$\delta < \frac{Kq\lambda}{Q} \qquad 1.23$$

where

$$K = \frac{\pi}{4k} \sim 1 \qquad 1.24$$

The exact value of K will depend on the severity with which the phrase "loss due to this cause should be small compared with other cavity losses" is interpreted, and also on the nature of the mirror imperfections. The criteria of Checcacci and Scheggi, and Krupnov and Skvortsov quoted above yield K = 3.2 and K = 0.13 respectively. In the present work for q = 1, where Q = 3000 and . could be measured to an accuracy of 5%, no change in Q was detected when the surface was improved from $\lambda/10000$ to $\lambda/20000$, indicating a value of K = 0.30.

A more accurate description of the nature of this loss mechanism, is almost certainly obtained from a picture of perturbations of the cavity wave, which are caused by the mirror imperfections. Such perturbations result in some of the energy in the propagating mode being transferred to higher order modes, where it is soon lost by diffraction. Unfortunately such a treatment is not conducive to any numerical conclusions.

1.3 MEASUREMENT METHODS

1.3.1 Mode Identification by Frequency Measurement

The various resonances present in a cavity can often be identified by a comparison of their resonant frequencies with those predicted by the theory. Fig. 1.5 shows a spectrum of resonances obtained with a Fabry-Perot cavity having rectangular mirrors, which was operated by Checcacci et al, 1964 at X-band as a model of a laser resonator. The cavity dimensions, $a = 25\lambda$ and $\ell = 50\lambda$, may be used,

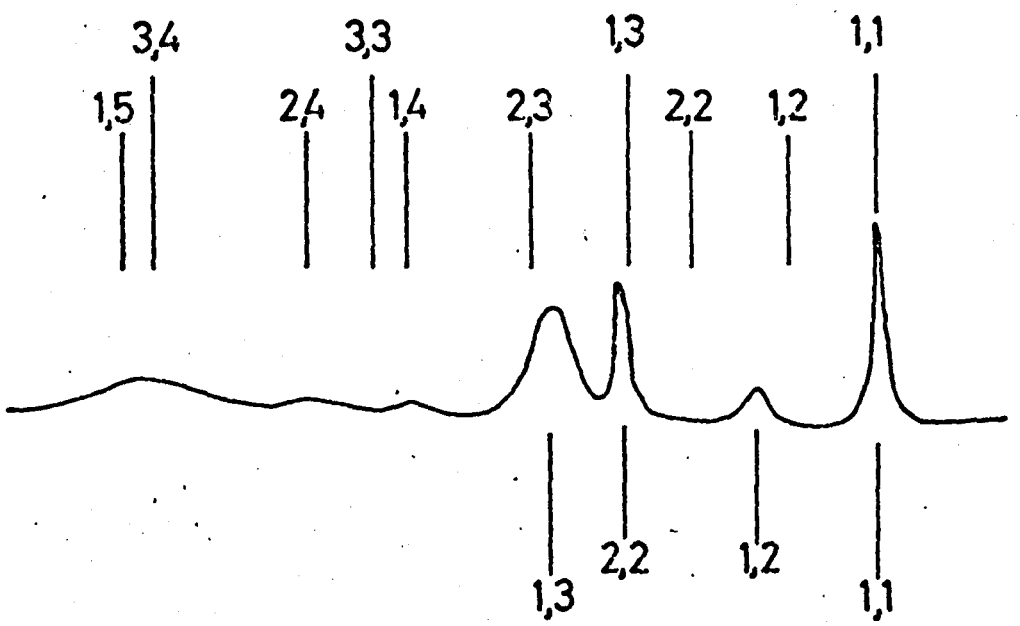

Fig 1.5 Mode spectrum of a microwave Fabry-Pérot cavity (after Checcacci et al, 1964)

together with the inequality $q^2 >> r^2 + s^2$ to simplify Eqn. 1.1:

$$\nu_{rsq} = (cq/2\ell)\{1 + 2(r^2 + s^2)/q^2\}^{\frac{1}{2}} \qquad 1.25$$

The resonant frequencies predicted by Eqn. 1.25 are shown above the spectrum, while four of the resonances are identified below it. The figures used to label each resonance are the appropriate values of the integers r and s, so that the four identified are due to the TEM_{00q} (1,1), TEM_{01q} (1,2), TEM_{11q} (2,2) and TEM_{02q} (1,3) modes of the cavity. Although the frequencies observed do not correspond exactly with those predicted, the frequency separations between neighbouring resonances are in the ratio 3 : 3 : 2 expected from Eqn. 1.25. The discrepancies cannot be attributed to the correction term introduced by the Vainshtein theory because they are opposite in sign and much greater in magnitude than this correction. They are probably due to imperfect machining of the cavity mirrors.

1.3.2 Mode Identification from Electromagnetic Field Distribution

Checcacci and Scheggi, 1965 used a perturbation method to investigate the field distribution inside the cavity. A small perturbing object is placed in the field between the mirrors, and the power it absorbs is measured by the reduction in the power transmitted or reflected by the cavity. Tsipenyuk shows (see Hibben, 1969) that in an open resonator, in contrast to the situation in a closed cavity, the effect of power absorption by the perturbing object dominates over its frequency pulling effect. As the object is moved about inside the resonator, the power it absorbs is proportional to the intensity of the microwave field in its vicinity (Zimmerer, 1963). In order to obtain accurate profiles of the electromagnetic field using this method, the perturbation of the field must always be small.

Bogomolov, 1963 and Krupnov and Skvortsov, 1965A used the perturbation method to identify resonance modes by observing the number and positions of the electromagnetic field maxima. Krupnov and Skvortsov used a 2 mm. long copper dipole at 4 mm. wavelength, while Bogomolov used a 3 mm. diameter brass sphere at a wavelength of 8 mm. Checcacci et al, 1966B used a perturbing absorber in the shape of a thin rod, 2 wavelengths long, held parallel to the cavity axis in order to average the axial periodicity of the electromagnetic field. In an elegant experiment they obtained results for the electromagnetic field distribution in the cavity in extremely close agreement with the computations of Fox and Li, 1961. They were able to confirm the existence of the Fresnel ripples predicted by the computations.

1.3.3 Quality Factor of the Cavity

The dependence of the resonator Q-factor on the axial order q has often been investigated. Zimmerer et al, 1963 and Welling and Andreson, 1964 have both obtained qualitative agreement with the curve of Fig. 1.4, but they did not attempt to make comparisons with theory. The work of Bogomolov, 1963 is of particular interest here, because he used a cavity consisting of waveguide coupled, plane circular metal mirrors similar to the one constructed for the present work. His measurements made with light microwave coupling to the cavity were closely in agreement with Vainshtein's theory over the diffraction limited region. These measurements were made at a wavelength of 8.72 mm. using a mirror diameter to wavelength ratio $D/\lambda = 17.4$, and showed a maximum Q value of 7500 at longitudinal mode order $q = 6$.

Barchukov and Prokorov, 1959 and 1961 also used waveguide coupled circular metal mirrors. In the first of these papers (1959) they

suggest that the optimum value of the ratio D/λ for a resonator with small mirror separation is 13 or 14. These observations are not confirmed by the theory nor by the experimental work described in Sec. 1.5.3. In some later work (1961) they measured maximum Q values of 12000 and 17000 at longitudinal mode orders $q = 5$ and 15 respectively. These measurements show diffraction losses well below those expected for plane mirrors, which suggests that their mirror surfaces were slightly concave. Checcacci and Scheggi, 1965 showed that machining errors which produce mirror concavity considerably decrease the diffraction loss.

1.4 CONSTRUCTION OF THE CAVITY

1.4.1 Design Considerations

Restrictions on the size and shape of the cavity were dictated by the dimensions of the vacuum chamber of the maser. The mirrors were made as large as was practical, and the cavity frame was designed in such a way as to allow operation in as many longitudinal mode orders as the dimensional constraints allowed. The mirror diameter chosen was 150 mm. ($D/\lambda = 12.0$ at $\lambda = 12.5$ mm, the ammonia J = 3, K = 3 line wavelength) which allows approximately 20 mm. clearance between the edges of the mirrors and the nearest metal parts of the vacuum chamber. Even so, the radiation fringe field of the cavity is disturbed by its surroundings, as evidenced by the fact that periodic changes of the cavity Q with the position of the lid of the main vacuum chamber are noticed while the lid is being lowered into position.

The cavity frame, mirrors and mirror mountings were all made rigidly in order to withstand mechanical vibrations and shock. They are described in Sec. 1.4.2. Attention was given to the provision of adequate means for tuning the mirror separation from outside the vacuum chamber. One thermal and two mechanical tuning mechanisms are described in Sec. 1.4.4. Also a means for changing the orientation of the coupling waveguides from outside the vacuum chamber was provided. This facility, which proved invaluable to some of the investigations carried out with cavity, is described in Sec. 1.4.5. Two views of the cavity are shown in Figs. 1.6 and 1.7.

1.4.2 The Cavity Mirrors and Cavity Frame

The circular mirrors are housed in a strong brass frame which

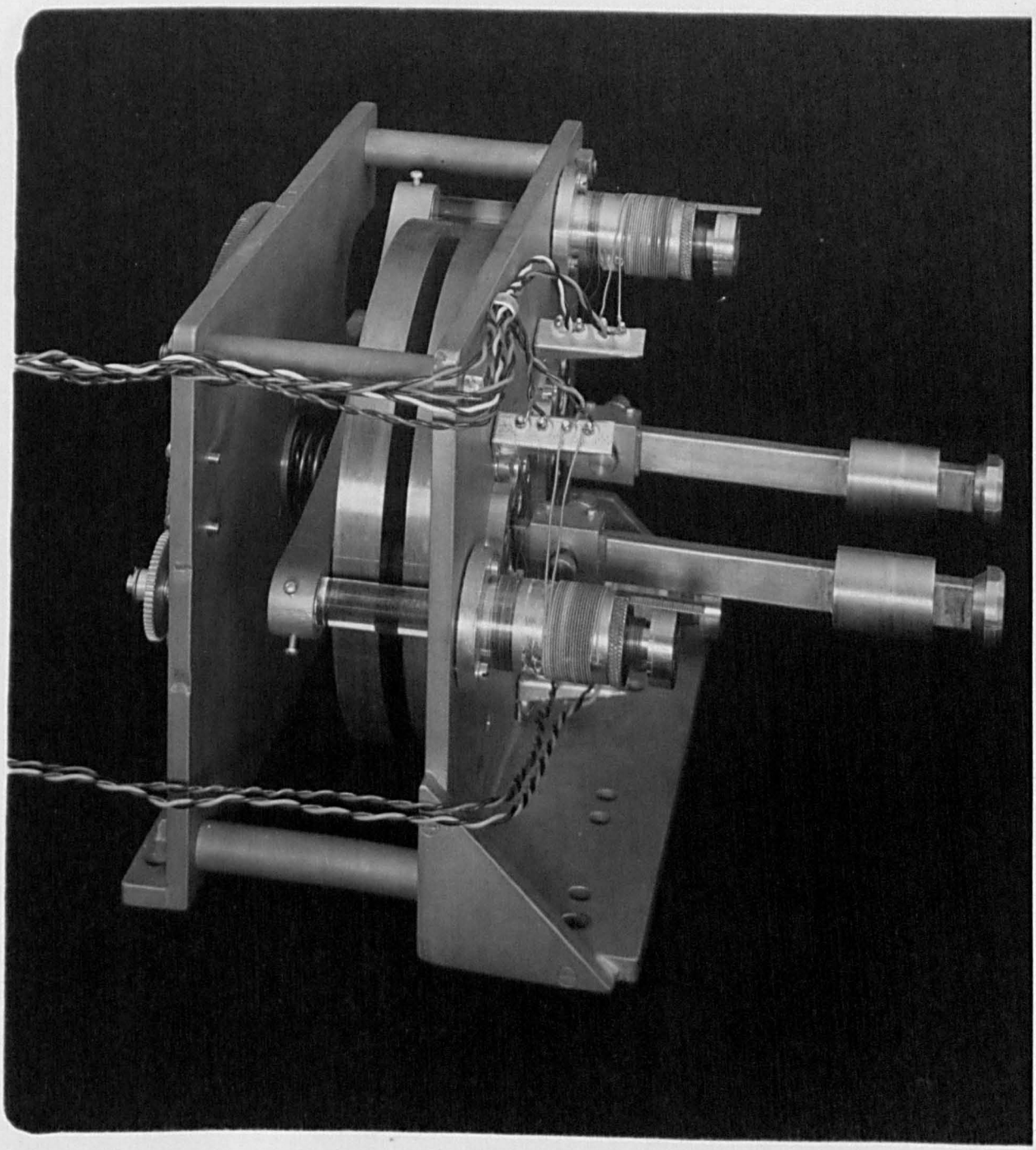

Fig. 1.6 View of the Fabry-Pérot cavity showing the tuning micrometers, thermal tuning barrels and coupling waveguides.

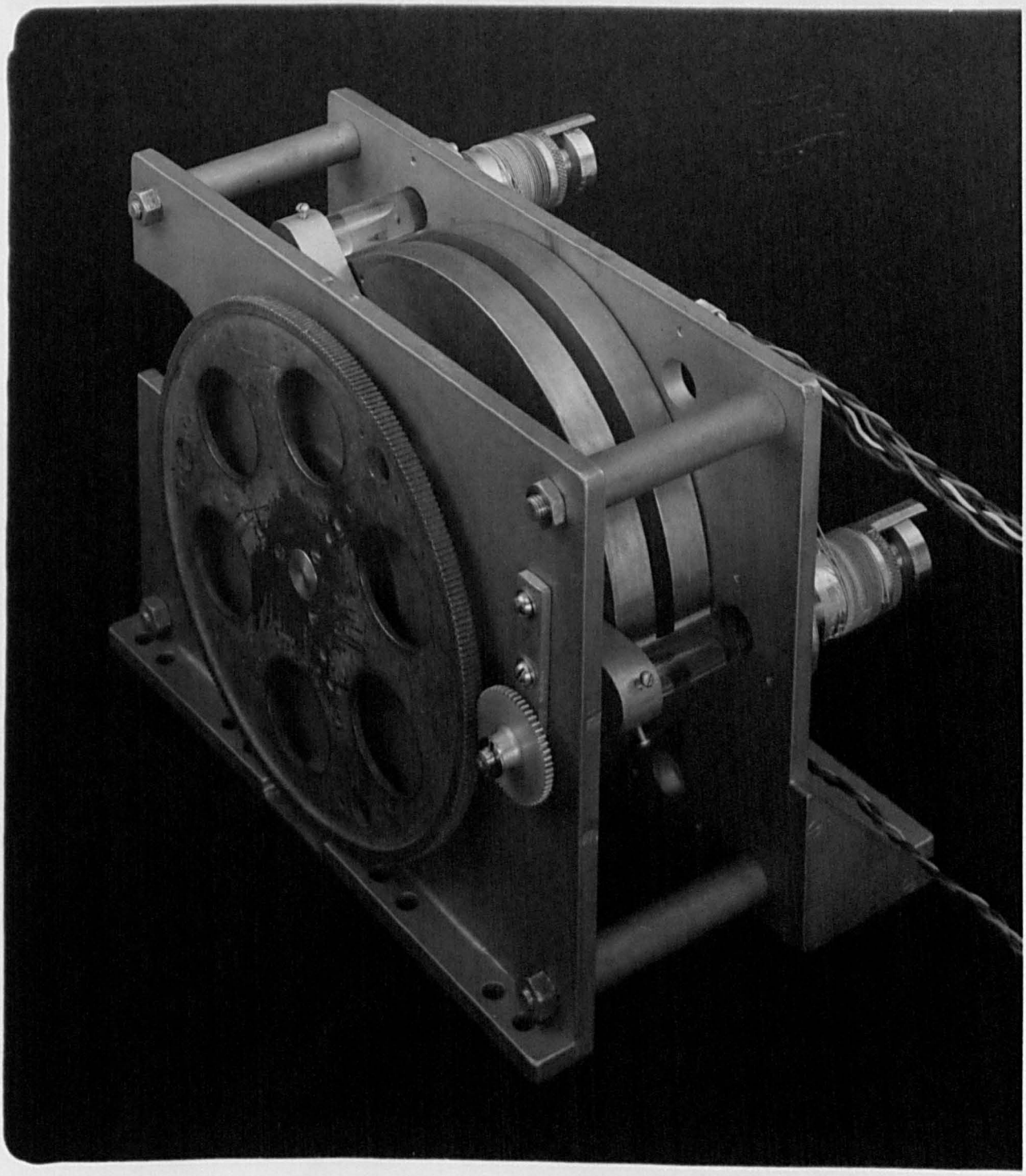

Fig. 1.7 View of the Fabry-Pérot cavity showing the gear train used for fine mechanical tuning.

bolts firmly into the vacuum chamber. The frame consists of two vertical plates separated by four rods. The spacing rods may be exchanged for rods of a different length in order to operate the cavity at different mirror separations. Two sets of four rods were made, and these give sufficient adjustment to operate the cavity in the first five longitudinal mode orders at λ = 12.5 mm. The shorter rods allow operation at mirror separations of $\lambda/2$, λ and $3\lambda/2$. By reversing the rear plate of the frame and using the longer spacing rods, the cavity may be operated at separations of 2λ and $5\lambda/2$ and yet still be fitted into the vacuum chamber.

The circular mirrors are discs of copper 150 mm. in diameter and 13 mm. thick. The machining of their reflecting surfaces is described in Sec. 1.4.3. One of the mirrors is bolted directly to the front plate of the cavity frame. This is the coupling mirror, which carries the two coupling holes and waveguides, 750 mm. apart symmetrically on the horizontal diameter of the mirror. The second mirror, the tuning mirror, is bolted to a three-armed frame. Each arm carries a 13 mm. diameter glass rod which passes forward, through the front plate of the cavity frame, into one of the three micrometer assemblies. The three-armed frame is pressed forward at its centre by a spring. Thus the mirror is supported, via the glass rods and the three-armed frame, by the three micrometer assemblies. In order to operate the cavity in the first five longitudinal mode orders, three sets of glass rods of different lengths are used.

1.4.3 Machining the Mirrors

The first mirrors were constructed of brass and were conventionally surface ground. Their flatness was measured by taking photographs in sodium light of multiple reflection fringes formed between the mirror

surface and a 150 mm. diameter glass optical flat. An example of an area of the fringes obtained is shown in Fig. 1.8(a). It is evident from this photograph that considerable chatter of the grinding wheel has taken place during machining. However the surface imperfections due to this cause were only of the order of 4 fringes in extent, corresponding to a surface deviation from the mean of $\pm$ 6 x 10^{-4} mm. Worse than this was an overall convexity of the surface, probably due to mechanical distortion of the mirror during machining. The height of the centre of the mirror above the edge corresponded to 8 fringes, giving a deviation of $\pm$ 1.2 x 10^{-3} mm. In addition considerable mounding of the surface in the vicinity of the coupling holes was noticed which at worst was 10 fringes or 3.0 x 10^{-3} mm. This is shown in Fig. 1.8(b).

Later two pairs of mirrors were constructed in copper. One pair was surface ground with great care: the grinding machine was allowed to run for about 4 hours before starting the work in order to allow its temperature to stabilize, and the final passes across the mirror surface removed only 1.2 x 10^{-2} mm. of metal so that the tool pressure on the surface was minimal. In this way tool chatter was eliminated and maximum overall deviations from flatness of $\pm$ 3 x 10^{-4} mm. were achieved. Typical fringes obtained with these mirrors are shown in Fig. 1.8(c) and 1.8(d) and demonstrate a marked improvement over those obtained with the brass mirrors. In particular Fig. 1.8(d) shows that distortion of the mirror surface close to the coupling hole has virtually been eliminated. Fig. 1.9 shows multiple reflection fringes across the whole of one of the mirrors, it is from photographs such as this that the figures given here for the overall surface deviations were obtained.

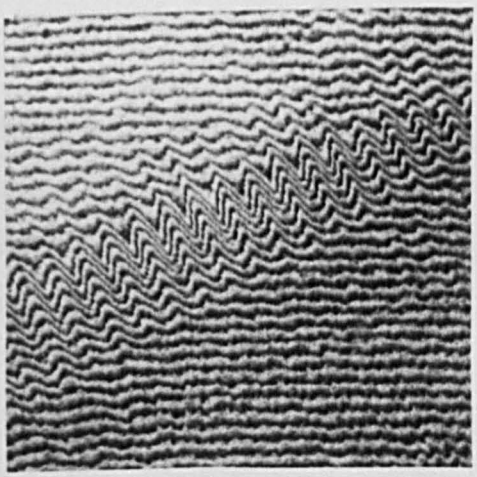

(a)

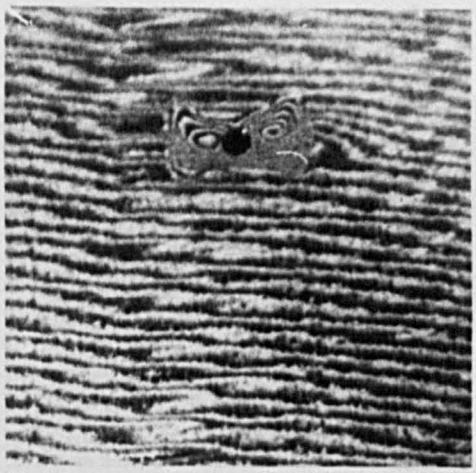

(b)

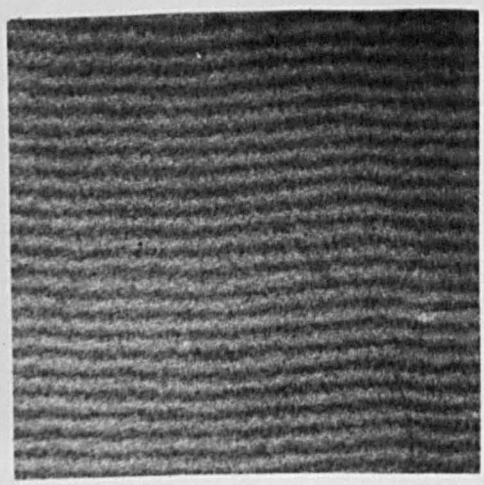

(c)

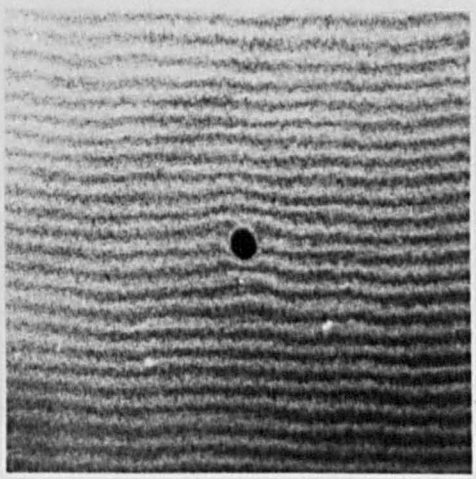

(d)

Fig. 1.8 Multiple reflection fringes formed by selected areas of the mirrors ;
(a) and (b) brass mirrors ;
(c) and (d) copper mirrors.

Fig. 1.9 Multiple reflection fringes formed between a mirror surface and a glass optical flat.

A second pair of copper mirrors was diamond turned to determine whether there was any significant difference in the quality of the surface when machined in this way. Not only the flatness was in question here, but also the surface conductivity because it was suspected that working of the metal surface might decrease its conductivity. No difference in the quality of the two pairs of mirrors, as determined by cavity Q-factor measurements, was noticed. Flatness of the two pairs of plates was not significantly different except in the region of the coupling holes where, on the diamond turned plates a surface mound of 1.2×10^{-3} mm. was obtained together with tool chatter following the hole. The cavity Q-factor measurements made with the brass and copper plates are described and discussed in Sec. 1.5. The surface ground and diamond turned copper plates were used interchangeably in the maser.

1.4.4 Cavity Tuning Mechanisms

In the original design for the cavity there were two tuning mechanisms: mechanical tuning by means of the three micrometer screws, and thermal tuning of the three micrometer barrels. Later a second mechanical mechanism which enabled the pressure of the spring behind the three-armed frame to be changed was fitted. All three of these mechanisms alter the position of the rear or tuning mirror.

Each micrometer assembly consists of an aluminium barrel carrying a stainless steel micrometer screw having 40 threads per inch. The aluminium barrel is partially insulated thermally from the cavity front plate by a mica washer. The barrel is bifilar wound with a heater coil of glass-covered "Eureka" wire and a sensor coil of 40 gauge enamelled copper wire. The three glass rods which support the tuning mirror bear on the stainless steel micrometer screws. Coarse

mechanical adjustment of the position and tilt angle of the mirror, before the vacuum chamber is sealed and pumped out, is afforded by these three screws.

Some idea of the coarseness of this mechanical tuning method, and indeed of the need for a firm mounting structure for the cavity mirrors may be gained from the following. At a mirror separation of $\lambda/2$ (6.25 mm), a 1 MHz change in the cavity frequency is obtained by moving the plates relative to one another through a distance of 2.5×10^{-4} mm. This corresponds to a movement of 1/2500 of a full turn on each of the three micrometer screws, i.e. approximately 1/8 degree of arc.

The need for a method of making fine tuning adjustments when the cavity is under vacuum, was met by heating the aluminium micrometer barrels. This tuning method makes use of the differential thermal expansion between the aluminium of the barrels and the stainless steel of the micrometer screws. The temperature of a barrel was sensed by the change in resistance of its sensor winding, and this signal was used to control the current in its heater winding. The electronic control equipment used is capable of holding the temperature of the barrel stable to $\pm$ .02°C. At a separation of $\lambda/2$, a 1 MHz change in the cavity tuning is produced by a temperature change of 0.45°C at the three micrometers.

It was subsequently found that the thermal tuning was inadequate to deal with long term drift in the frequency of the cavity. This was due to mechanical creep of the structure, possibly aggravated by the temperature of the whole cavity being held above ambient by the thermal tuning. A mechanical method of tuning the cavity from outside the vacuum chamber was devised. A finely-threaded plug, screwed into the rear

plate of the cavity frame, supports the centre pressure spring. The plug is bolted to a large gear wheel which meshes, via an idler gear, with a small pinion turned by a rotatable vacuum feed-through. By turning the gear train from outside the vacuum chamber, the plug can be screwed into the frame and the spring compressed. In this way the pressure on the three-armed frame may be changed, causing it to bend and move the tuning mirror which itself remains absolutely flat. The cavity is tuned through 1 MHz by about 5 turns of the vacuum feed-through. Not only does this mechanism provide fine tuning but it also gives a very wide tuning range and so can be used to compensate for creep in the cavity frame or other components.

1.4.5 Microwave Coupling to the Cavity

Microwaves are coupled to the cavity through two holes placed symmetrically on the horizontal diameter of the coupling mirror at a distance apart equal to the mirror radius. This is similar to the coupling scheme used by Krupnov and Skvortsov, 1964 in a formaldehyde beam maser. The holes are 2.6 mm. in diameter in a 0.63 mm. diaphragm. Their coupling parameters may be varied by means of two small waveguide stub tuners close to the back of the coupling mirror. The maximum coupling parameter is obtained for the fundamental mode at a mirror separation of $\lambda/2$ and is 0.043 at each hole.

Various methods of making the physical connection between the waveguides and the mirror were tried. The problem is chiefly one of making a firm mechanical and good electrical joint at a thin diaphragm without distorting the inner surface of the mirror. The arrangement finally chosen was a form of choke coupling based on the choke frequently used at waveguide flanges (Harvey, 1963A). A

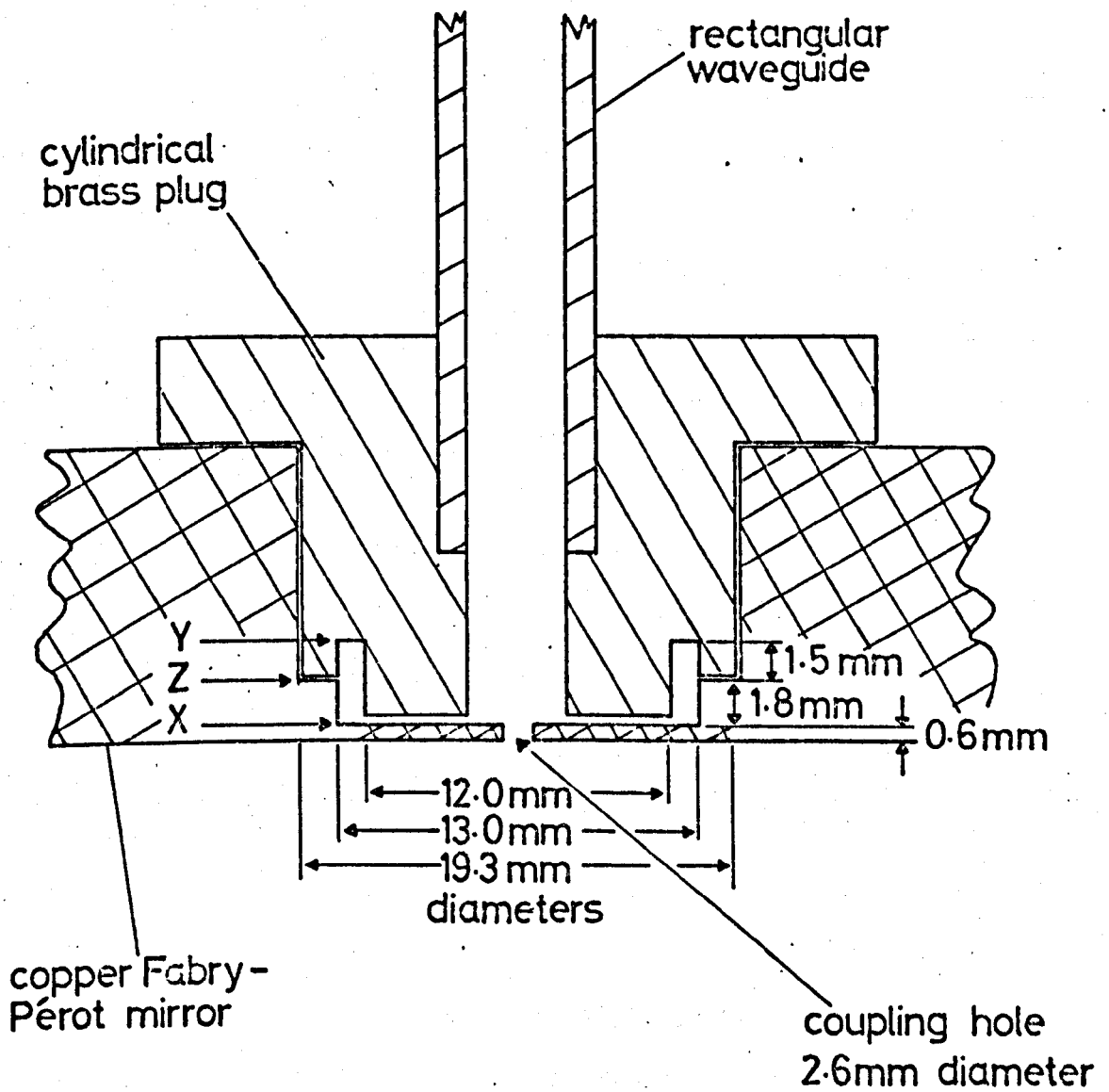

Fig 1.10 Cross-section of the choke coupling between waveguide and Fabry-Pérot mirror.

drawing of the coupling is shown in Fig. 1.10. Ideally the join between the two components should be on the plane X where the current in the wall of the quarter-wave choke is zero. However this would have left only the diaphragm thickness to support the waveguide. The wall current is a maximum at the top of the choke grove, Y, so the join was placed in a compromise position, halfway up the choke wall at Z.

One of the advantages of using the choke coupling is that the joint is cylindrical. This not only makes machining simpler, but also enables the waveguide orientations to be changed. Indeed, if the choke barrels are not bolted to the back of the mirror, the waveguide orientations may be changed by rotating the waveguides from outside the vacuum chamber. This facility was used extensively during the investigations described in Chapters 4 and 5.

1.5 EXPERIMENTAL INVESTIGATION OF THE CAVITY

1.5.1 Tuning the Cavity

A procedure was found whereby the cavity could be adjusted to resonate in a desired mode. Some small brass posts were machined to be slightly smaller in length than a free-space half wavelength at the ammonia J = 3, K = 3 line frequency. By adjusting the three cavity micrometers so that one or more of these distance pieces could just be slipped between the mirrors at three points on the cavity circumference, the mirrors were made parallel with a separation almost equal to an integral number of free-space half wavelengths. Microwave power from a frequency swept klystron was then passed into the cavity via one coupling waveguide, and crystal video detection equipment was

attached to the other waveguide. In this way, a display of power transmitted through the cavity was obtained.

The three micrometers were advanced by equal small increments until a cavity resonance was observed on the display. Maximum sensitivity of the oscilloscope Y-trace amplifier and the full (unattenuated) klystron power output usually had to be used if the cavity matching stubs had not previously been set, in order to detect the resonance. The resonance found was invariably the fundamental TEM_{01} mode in the appropriate longitudinal order. As soon as this mode had been located, the matching stubs were adjusted for maximum transmission so that further tuning of the cavity could be carried out using a strong transmitted microwave signal. If a higher order mode within the same longitudinal order was required, it was located by further advancing the three micrometers by equal increments until the mode was encountered. The matching stubs were then readjusted for maximum transmission in this mode.

The cavity was finally tuned for maximum Q by making further small adjustments to the micrometers. These adjustments were aimed at obtaining maximum transmission through the cavity at the mode centre frequency. This condition coincided with maximum Q, as has been shown in Sec. 1.2.5.

Initial tuning to the desired mode as described above was usually carried out on the bench. In order that the cavity should resonate at the maser frequency after it had been placed in the maser vacuum chamber and the chamber pumped out, it was tuned on the bench to a frequency slightly higher than that of the maser by an experimentally determined amount. This allowed not only for the change in dielectric constant when the chamber was evacuated, but also for the effect of atmospheric pressure on the waveguide vacuum seals, which tended to

strain the cavity and alter its tuning. This need for off-tuning the cavity was eliminated when the mechanical fine tuning mechanism was added to the cavity, and when a spring device to counteract the effect of atmospheric pressure was fitted to the coupling waveguides. The mechanical fine tuning mechanism is described in Sec. 1.4.4 and the spring device in Sec. 3.2.6.

1.5.2 Identification of Cavity Modes

In Sec. 1.3.1 the perturbation method of investigating the electromagnetic field distribution within the cavity was described. In the present work this method was used at 12.5 mm wavelength to identify the mode resonances of the cavity.

A small piece of copper wire about 3 mm long held parallel to the electric field vector in the cavity was used as the perturbing object. This was cemented to a thin nylon thread (which alone did not perturb the electromagnetic field) stretched horizontally across the cavity between the mirrors, parallel to their surfaces. Microwave power transmitted through the cavity was monitored by crystal video detection as a function of the position of the wire in the cavity. The drop in signal on the oscilloscope indicated the amount of power absorbed by the wire which in turn was approximately proportional to the microwave field intensity in the vicinity of the wire.

It was found that very accurate positioning of the thread parallel to the mirror surfaces was needed to map the field intensity accurately. Also the crystal video (or similar) detection scheme needed to be sensitive to very small changes in the microwave power transmitted through the cavity. For these reasons, the perturbation method was only used as a qualitative indicator of the mode or modes resonant in the cavity.

The fundamental TEM_{00} and the TEM_{10} modes were readily identified by this method. At a mirror separation of $\lambda/2$ they had loaded Q factors of 2800 and 1700 respectively. Two further resonances were also observed. The first had a Q of 1000 and was identified as a superimposition of the TEM_{20} and TEM_{01} modes which lie close to one another in frequency. The second had a Q of about 400 and appeared to be a superimposition of the three modes TEM_{30}, TEM_{11} and TEM_{40}.

1.5.3 Quality factor Measurements.

The experimental details of the methods used to make Q-factor measurements on the cavity are described in appendix C. These measurements were made for the TEM_{00} and TEM_{10} modes in the first five longitudinal orders, but were not practicable for larger mirror separations owing to the decrease in the coupling parameter which accompanied increase in the mirror separation (see Sec. 1.2.5). The measurements made on the TEM_{00} mode at a wavelength of 12.5 mm (frequency 24.0 GHz) are discussed here in the light of the predictions of the Vainshtein theory and the Fox and Li computations.

In Fig. 1.11 the experimental points represent the values of unloaded Q-factor which have been obtained from the measured values of the loaded Q by the method described in appendices B and C. The two solid lines have been calculated using the Vainshtein diffraction loss equation (Eqn. 1.10) and the loss values computed by Fox and Li. In order to obtain these curves, the diffraction loss has been combined with the conduction loss in the manner described in Sec. 1.2.4, the conduction loss being calculated for mirrors of pure copper. It is interesting to note that the two calculated curves show very good agreement with one another despite the fact that the Fox and Li values have been extrapolated to cavity geometries for which their computational approximations are invalid.

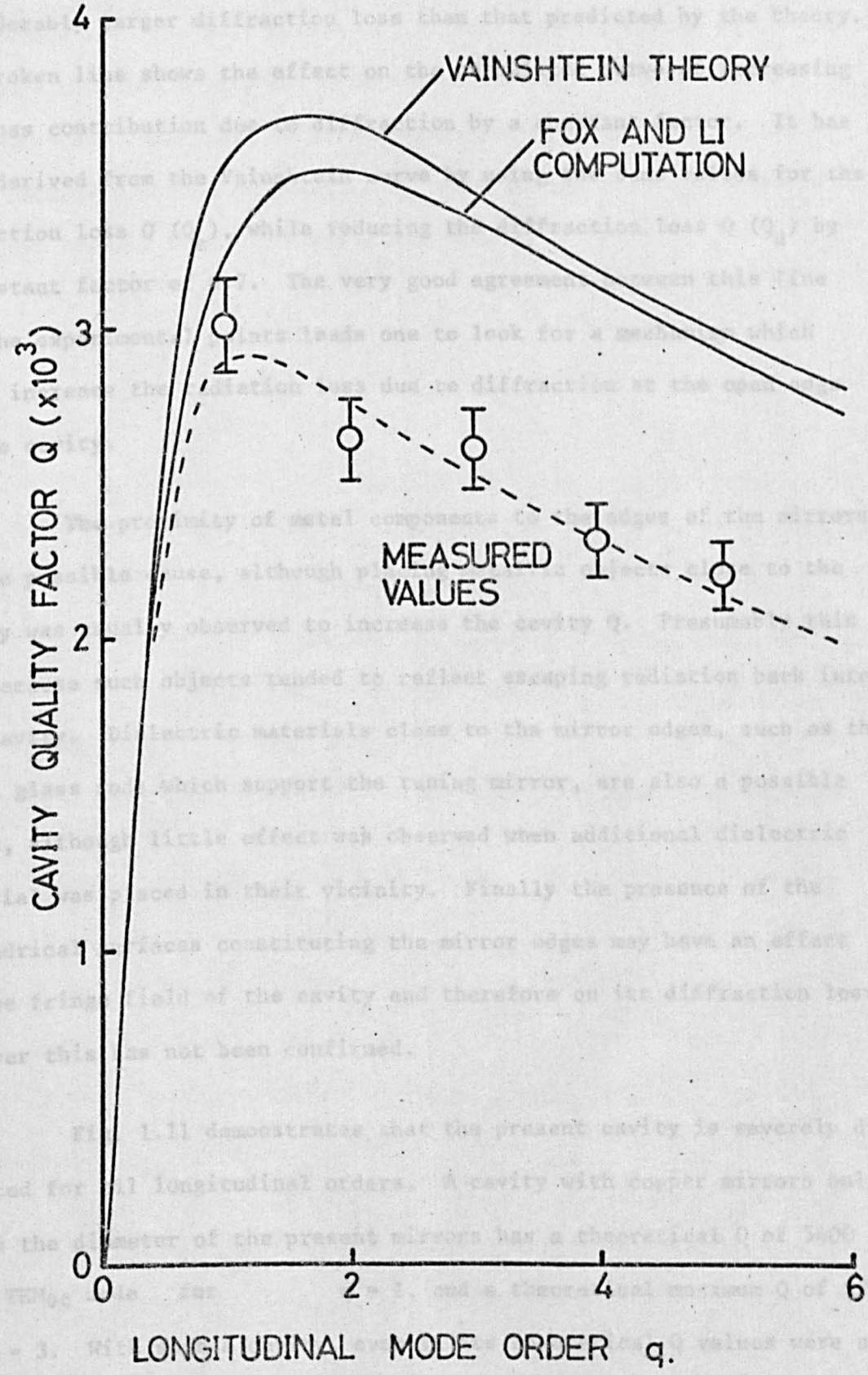

Fig 1.11 Calculated and measured cavity Q at wavelength 12·5mm.

From Fig. 1.11 it is clear that the cavity exhibits a considerably larger diffraction loss than that predicted by the theory. The broken line shows the effect on the calculated curve of increasing the loss contribution due to diffraction by a constant factor. It has been derived from the Vainshtein curve by using the same values for the conduction loss Q (Q_c), while reducing the diffraction loss Q (Q_d) by a constant factor of 0.7. The very good agreement between this line and the experimental points leads one to look for a mechanism which could increase the radiation loss due to diffraction at the open edge of the cavity.

The proximity of metal components to the edges of the mirrors is one possible cause, although placing metallic objects close to the cavity was usually observed to increase the cavity Q. Presumably this was because such objects tended to reflect escaping radiation back into the cavity. Dielectric materials close to the mirror edges, such as the three glass rods which support the tuning mirror, are also a possible cause, although little effect was observed when additional dielectric material was placed in their vicinity. Finally the presence of the cylindrical surfaces constituting the mirror edges may have an effect on the fringe field of the cavity and therefore on its diffraction loss. However this has not been confirmed.

Fig. 1.11 demonstrates that the present cavity is severely diffraction limited for all longitudinal orders. A cavity with copper mirrors only 1.5 times the diameter of the present mirrors has a theoretical Q of 5600 in the TEM_{00} mode for $q = 1$, and a theoretical maximum Q of 8300 at $q = 3$. With such a cavity, even if its theoretical Q values were not obtained, it should have been possible to pursue the Zeeman effects described in Chapter 5 to higher values of magnetic field and also to

obtain oscillation in the TEM_{10} mode as proposed in Chapter 6. It was unfortunate that the only guides to the attainable Q values which were available when the cavity was designed overestimated these values (Barchukov and Prokhorov, 1961; Barchukov and Petrov, 1962), while the Q factors obtained in practice with the present cavity proved to be rather smaller than the theoretical values.

CHAPTER 2

THE MOLECULAR BEAM

2.1 INTRODUCTION

The production and use of molecular beams is of interest in a number of different fields of Physics such as mass spectroscopy, microwave and radio frequency spectroscopy, gas kinetics and surface physics. The beam of molecules used in a molecular beam maser is essentially different from those used for other purposes in one important feature. It must contain an excess number of molecules in the upper of the two energy levels of the maser transition, over the number in the lower level. Not only is a molecular beam required, but it must also be state separated.

The formation of molecular beams by effusion of gas from a nozzle has been the subject of considerable study. Effusers which have been examined range from bundles of fine capillary tubes to single channels. The directivity of the molecular beam formed by these effusers has been the subject of a number of investigations (e.g. Giordmaine and Wang, 1960; Naumov, 1963) since for most purposes the ideal beam has a narrow profile. Generally the beam must be collimated by circular or slit diaphragms, and the wasted molecules often present a severe pumping problem, which is somewhat alleviated if the directivity of the beam before collimation is high. The velocity distribution of the molecules in the beam has also been the subject of a number of fascinating investigations (e.g. Miller and Kusch, 1955; Olander et al, 1970; Siekhaus et al., 1970). Recently the use of supersonic beams has opened up a new field of study (English and Zorn, 1973; Dyke et al, 1972).

The electrostatic state separation of molecular beams has received considerable attention both theoretically (e.g. Shimoda, 1957; Hirono, 1959) and experimentally (e.g. Becker, 1963A; Takeuchi et al, 1966). Usually separators with cylindrical symmetry have been preferred because of the cylindrical symmetry of the generally used E_{010} mode cavity.

This chapter is concerned mainly with state separation of molecular beams, with emphasis on the separation of a beam with planar symmetry consisting of a flat sheet of molecules. Such a beam shape is particularly suitable for a maser using the Fabry-Pérot type of cavity. In Sec. 2.2 the principle of electrostatic state separation, which is used in the majority of molecular beam masers, is described. Some basic equations relating to the separation of a beam of ammonia molecules are presented.

In Sec. 2.3 the behaviour of cylindrical and planar state separators is discussed. The theory of the parallel ladder separator is presented in some detail, and separators used in this work are described in the light of this theory. Finally Sec. 2.4 describes the effects of electric and magnetic fields on a state separated molecular beam.

2 2 ELECTROSTATIC STATE SEPARATION OF AMMONIA

2.2.1 The Ammonia Inversion

The ammonia inversion is an example of a hindered molecular motion, i.e. a motion which is not possible classically but which occurs, because of the wave nature of the molecule, by quantum mechanical tunneling. Classically, the ammonia molecule is a pyramidal structure having the nitrogen atom at the apex of the pyramid and the three hydrogen atoms at

the corners of the base as shown in fig. 2.1(a). If the molecule possesses only a small amount of vibrational energy, the nitrogen atom should be unable to penetrate the plane of the hydrogen atoms; this corresponds to a situation where the nitrogen atom is trapped in one of the two wells of the potential energy diagram Fig. 2.1(b).

A quantum mechanical description of the atom, however, cannot ignore the existence of the second potential energy well. In the two lowest vibrational energy states, the nitrogen atom has insufficient energy to surmount the central potential barrier, but may cross this barrier by the quantum mechanical tunnel effect. The two wave functions Ψ_A and Ψ_B which describe the structures of Fig. 2.4.1(a) interact, and in the absence of applied magnetic or electric fields, there is an equal probability of finding the nitrogen atom on either side of the hydrogen plane. The molecule exists in two forms described by the symmetric and anti-symmetric wave functions

$$\Psi = (1/\sqrt{2})(\Psi_A \pm \Psi_B)$$

with the plus and minus sign respectively. The symmetric wave function has a lower energy associated with it than has the anti-symmetric function, so that a pair of energy levels exist as a result of the inversion.

Each rotational level within the two lowest vibrational states is split by the inversion. Whereas transitions between vibrational levels and between rotational levels typically give rise to transition frequencies in the near and far infra-red respectively, microwave frequencies are associated with inversion transitions. The exact frequency of an inversion transition depends on the vibrational and rotational state in which it occurs.

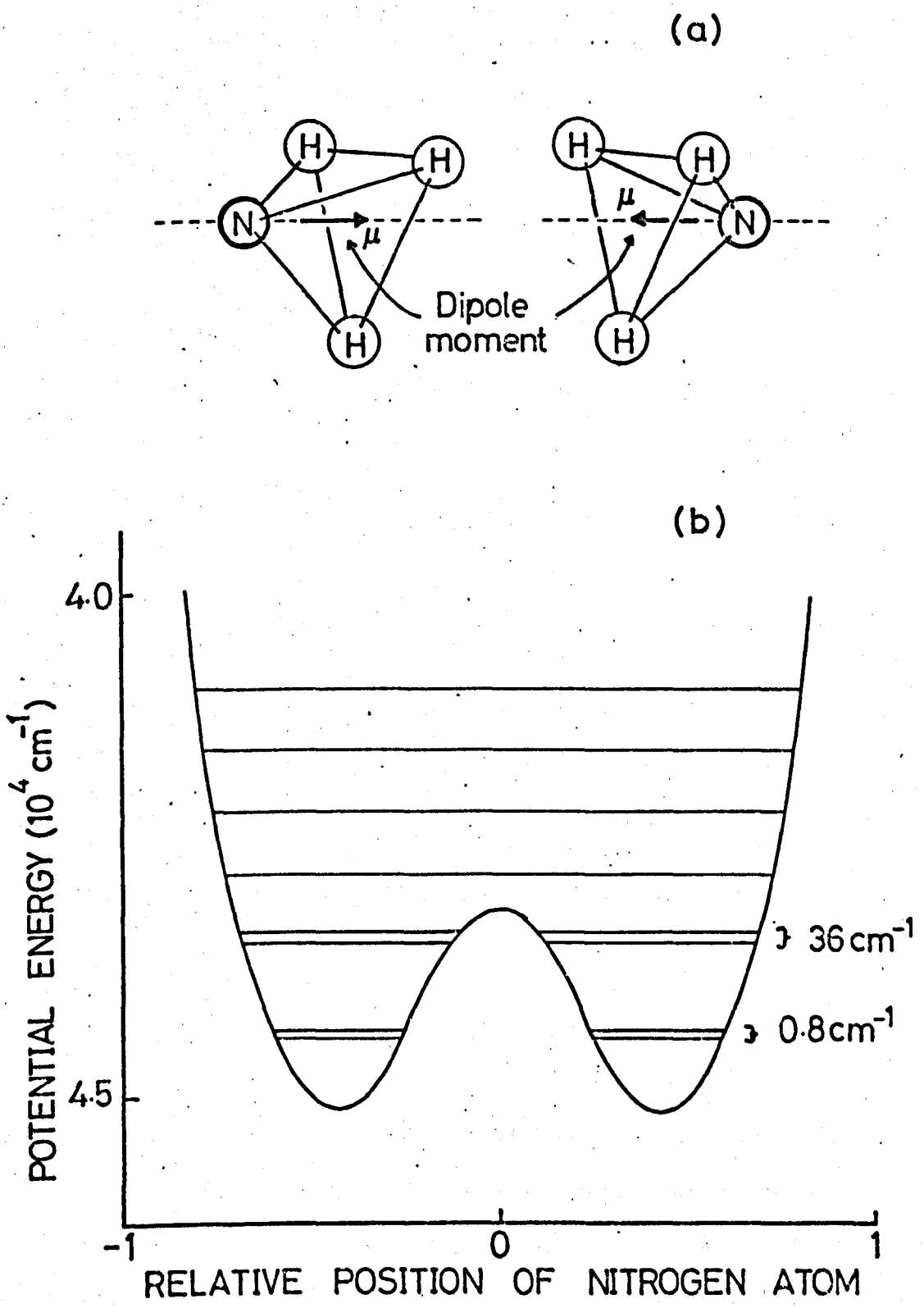

Fig 2.1 (a) Classical models of the ammonia molecule.
(b) Potential energy curve for ammonia showing vibrational energy levels.

2.4.2 The Stark Effect in Ammonia

Although the two models of the ammonia molecule pictured in Fig. 2.1(a) possess an electric dipole moment μ, the molecule described by either of the wave functions Ψ in Eqn. 2.1 possesses no net moment. The inversion averages the effective dipole moment to zero. In the presence of an electric field, however, the inversion is partially quenched, and a dipole moment is induced.

Feynman, 1965 considers the effect of the electric field as a perturbation on the molecule described by Eqn. 2.1. He derives the effect of this perturbation on the energies of the upper and lower inversion levels respectively as

$$W = W_o \pm \sqrt{\{A^2 + (\mu_{12} E)^2\}} \qquad 2.2$$

where the unperturbed energies are given by $W_o + A$ and $W_o - A$, μ_{12} is the dipole moment matrix element connecting the two levels, and E is the magnitude of the electric field.

The dipole moment matrix element, μ_{12}, is given by the expression

$$\mu_{12} = \frac{\mu MK}{J(J+1)} \qquad 2.3$$

where μ is the permanent dipole moment pictured in Fig. 2.1(a) which the molecule would possess in the absence of inversion, J is the total angular momentum quantum number, K is the projection of J on the molecular axis and M is the projection of J on the direction of the applied electric field, E. Thus Eqn. 2.2 may be written

$$W = W_o \pm \left[\left(\frac{h\nu_{12}}{2} \right)^2 + \left(\frac{\mu MKE}{J(J+1)} \right)^2 \right]^{\frac{1}{2}} \qquad 2.4$$

where ν_{12} has been written for the transition frequency between the unperturbed inversion levels, and h is Planck's constant.

This behaviour of the energy levels in an electric field is shown in Fig. 2.2 for J = 3 and K = 3. To a first approximation, the M = 0 level does not change its energy in the applied field. Levels for which M = ±1, ±2 or ±3 change quadratically with field for fields below about 3KV mm^{-1}. At high fields where $\mu_{12} E >> A$ the inversion is completely quenched and the Stark effect is linear.

2.4.3 The Principle of State Separation

The force on a molecule in an electric field may be derived from Eqn. 2.4 using

$$\underline{F} = - \text{grad } \underline{W}$$

The component of $\underline{F}$ in a direction y is given by

$$Fy = \frac{-\partial W}{\partial y} = \mp \frac{\left(\frac{\mu MK}{J(J+1)} \right)^2 E \frac{\partial E}{\partial y}}{\left[\left(\frac{h\nu_{12}}{2} \right)^2 + \left(\frac{\mu MKE}{J(J+1)} \right)^2 \right]^{\frac{1}{2}}} \qquad 2.6$$

In a uniform field, no force acts on the molecule, but in a non-uniform field for which E < 3KV mm^{-1}, a force whose magnitude is proportional to $E\partial E/\partial y$ is exerted. The sign of the force is negative (i.e. towards low

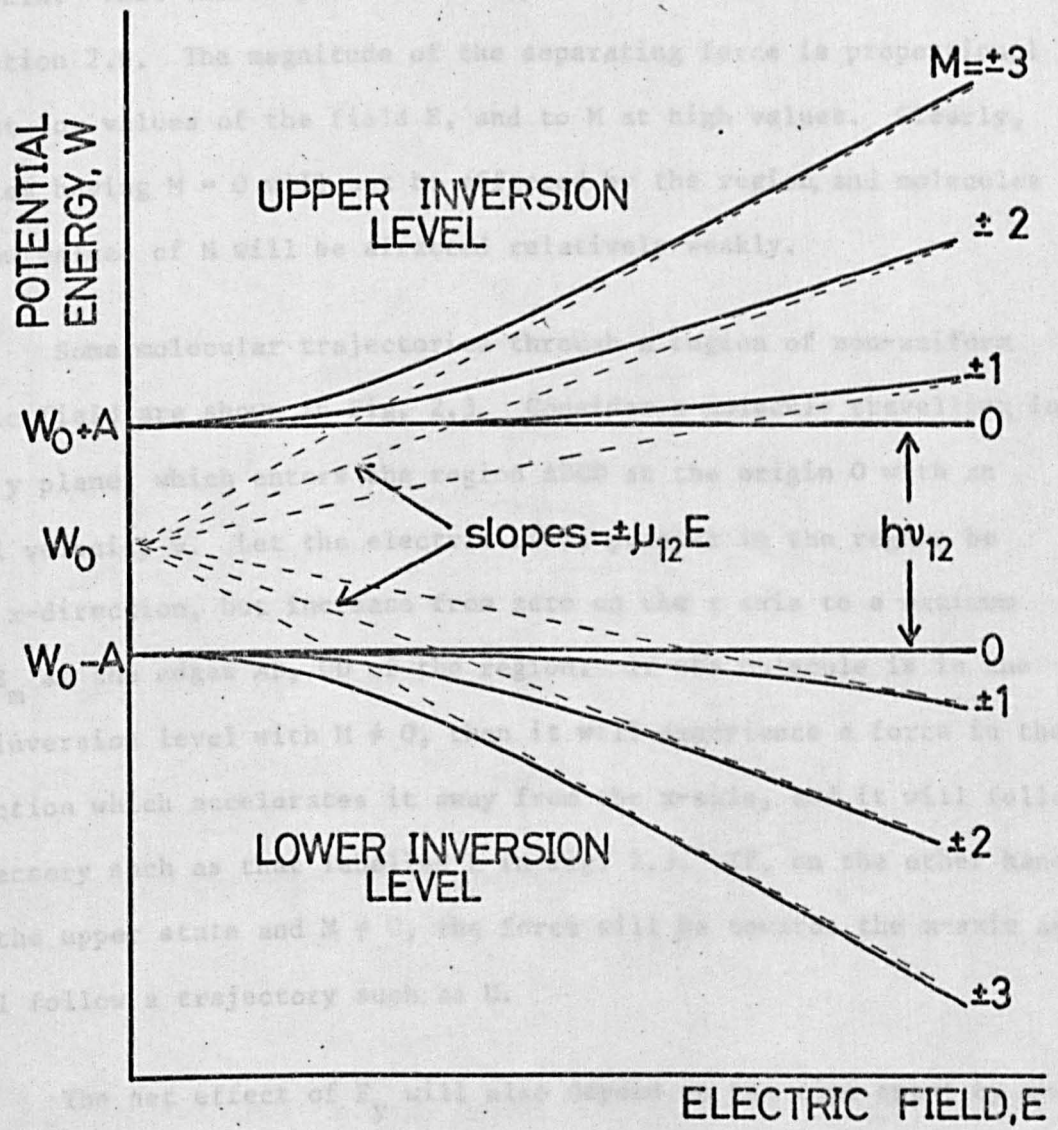

Fig 2.2 Stark effect for the J=3, K=3 inversion transition of ammonia.

electric flux density) for molecules in the upper inversion level, and positive (towards high electric flux density) for those in the lower level.

In principle a region of non-uniform electric field may be used to spatially separate molecules in the upper and lower inversion levels of ammonia. That this separation is imperfect is seen from a consideration of equation 2.6. The magnitude of the separating force is proportional to M^2 at low values of the field E, and to M at high values. Clearly, molecules having $M = 0$ will not be affected by the region, and molecules with low values of M will be affected relatively weakly.

Some molecular trajectories through a region of non-uniform electric field are shown in Fig. 2.3. Consider a molecule travelling in the x, y plane, which enters the region ABCD at the origin O with an initial velocity v. Let the electric field present in the region be in the x-direction, but increase from zero on the x axis to a maximum value E_m at the edges AB, CD of the region. If the molecule is in the lower inversion level with $M \neq 0$, then it will experience a force in the y-direction which accelerates it away from the x-axis, and it will follow a trajectory such as that labelled L in Fig. 2.3. If, on the other hand, it is in the upper state and $M \neq 0$, the force will be towards the x-axis and it will follow a trajectory such as U.

The net effect of F_y will also depend on the time spent by the molecule in the region and hence on its initial x-component of velocity v_x. If v_x is small and/or M is large, the molecule may make several oscillations about the x-axis (trajectory U'). If v_x is large and/or M is small, the molecule may still be diverging from the x-axis when it leaves the region (U''). However if the region of non-uniform field is

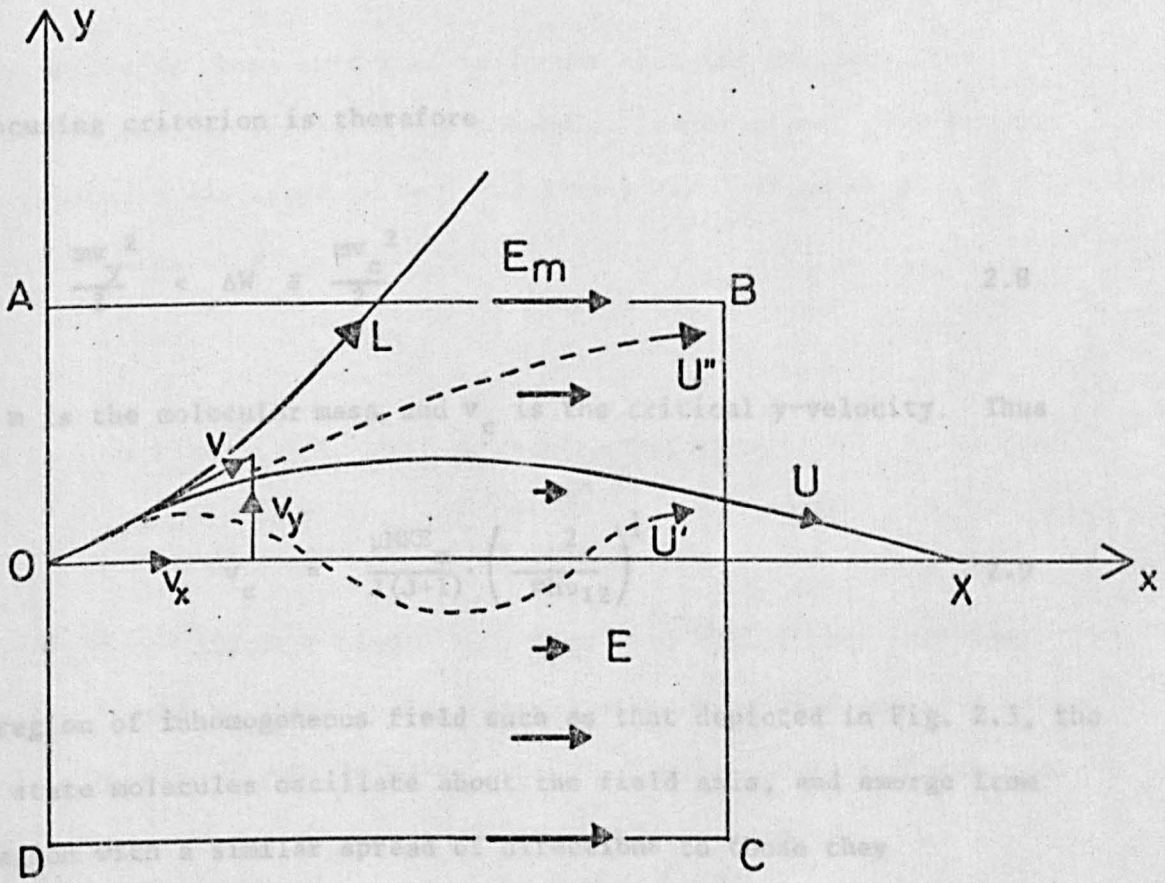

Fig 2.3 Molecular trajectories through a region of non-uniform electric field.

sufficiently long in the x-direction to allow for the highest x-components of velocity, then any upper state molecule whose initial y-component of kinetic energy is smaller than the maximum Stark energy ΔW will be trapped by the state separator. ΔW is given by

$$\Delta W = \left[\left(\frac{h\nu_{12}}{2}\right)^2 + \left(\frac{\mu MK\, E_m}{J(J+1)}\right)^2\right]^{\frac{1}{2}} - \frac{h\nu_{12}}{2} \qquad 2.7$$

The focusing criterion is therefore

$$\frac{mv_y^2}{2} < \Delta W \equiv \frac{mv_c^2}{2} \qquad 2.8$$

where m is the molecular mass and v_c is the critical y-velocity. Thus

$$v_c \simeq \frac{\mu MKE_m}{J(J+1)} \cdot \left(\frac{2}{mh\nu_{12}}\right)^{\frac{1}{2}} \qquad 2.9$$

In a region of inhomogeneous field such as that depicted in Fig. 2.3, the upper state molecules oscillate about the field axis, and emerge from the region with a similar spread of directions to those they possessed on entry. The length of the focusing region is important in determining how many oscillations about the axis are made by the molecules. A state separator is often designed so as to bring molecules having the most probable x-velocity and the average value of M to a focus at a point such as X on the x-axis. This point then determines the optimum position for the cavity. In this sense it is possible to describe the state separator by analogy with a converging lens (Becker, 1963A).

Helmer et al, 1960 have shown that a state separator of non-uniform cross-section is preferable to a uniform one. If A_1 and A_2 are the entrance and exit cross-section areas of the state separator respectively, and Ω_1 and Ω_2 are the solid angles of capture occupied by the molecular trajectories, averaged over A_1 and A_2, then

$$A_1 \Omega_1 = A_2 \Omega_2 \qquad 2.10$$

Thus a separator whose exit area is larger than its entrance area narrows the angular spread of the molecular trajectories. The tapered state separator described in Sec. 2.3.3 is a realisation of such a non-uniform separator.

2.3 STATE SEPARATORS FOR THE FABRY-PEROT MASER

2.3.1 Practical Shapes of State Separator

Most molecular beam masers have used cylindrical cavities, generally in the E_{010} mode. Cylindrical separating or focusing (the two terms are used synonymously here) systems, having electric fields with radial symmetry, have therefore been most widely studied.

A quadrupole separator having longitudinal electrodes with approximately hyperbolic cross-sections was used in the first beam maser to operate - Gordon et al, 1954. This electrode shape enables the radial field in the separator to be calculated accurately, since the field magnitude is proportional to the distance from the axis of the separator. Multipole focusers, with more than four longitudinal electrodes equally spaced around the circumference of the circular cross-section of the focuser, were widely used in early masers (Shimoda, 1957; Vonbun, 1958).

Later the ring and bifilar helix types were proposed by Krupnov, 1959 and investigated by Basov and Zuev, 1961 and Mednikov and Parygin, 1963.

Becker, 1963A has compared the efficiencies of the various types of cylindrical focusers in terms of the input beam flux which just causes maser oscillation for a given electrode voltage. He found that the ring and helix types were most efficient, and that by comparison the six-pole and quadrupole types had efficiencies of about 60% and 40% respectively. The ring focuser is a more rigid structure than the helix and is generally preferred.

A number of separator systems to produce planar beams of molecules have been envisaged, but none have been widely used. Krupnov, 1959 proposed a state separator consisting of two planes of rods, arranged circumferentially around a Fabry-Perot cavity with plane parallel mirrors, and charged alternately to positive and negative potentials - Fig. 2.4(a). The gas nozzles are arranged to shoot radial molecular beams between the two planes of electrodes and towards the centre of the cavity. Upper state molecules are focused into the plane of symmetry of the separator, and lower state molecules are turned away from this plane.

Marcuse, 1962 used two closely spaced planes of radially arranged rods in a hydrogen cyanide maser having a semi-confocal cavity. His arrangement is shown in Fig. 2.4(b). Its action is similar to that of Krupnov's proposed system. The transverse ladder type shown in Fig. 2.4(c) has been used in a 4 mm formaldehyde maser by Krupnov and Skvortsov, 1964, while the longitudinal ladder arrangement of Fig. 2.4(d) has been used in a radio frequency formaldehyde maser by Takami and Shimizu, 1966.

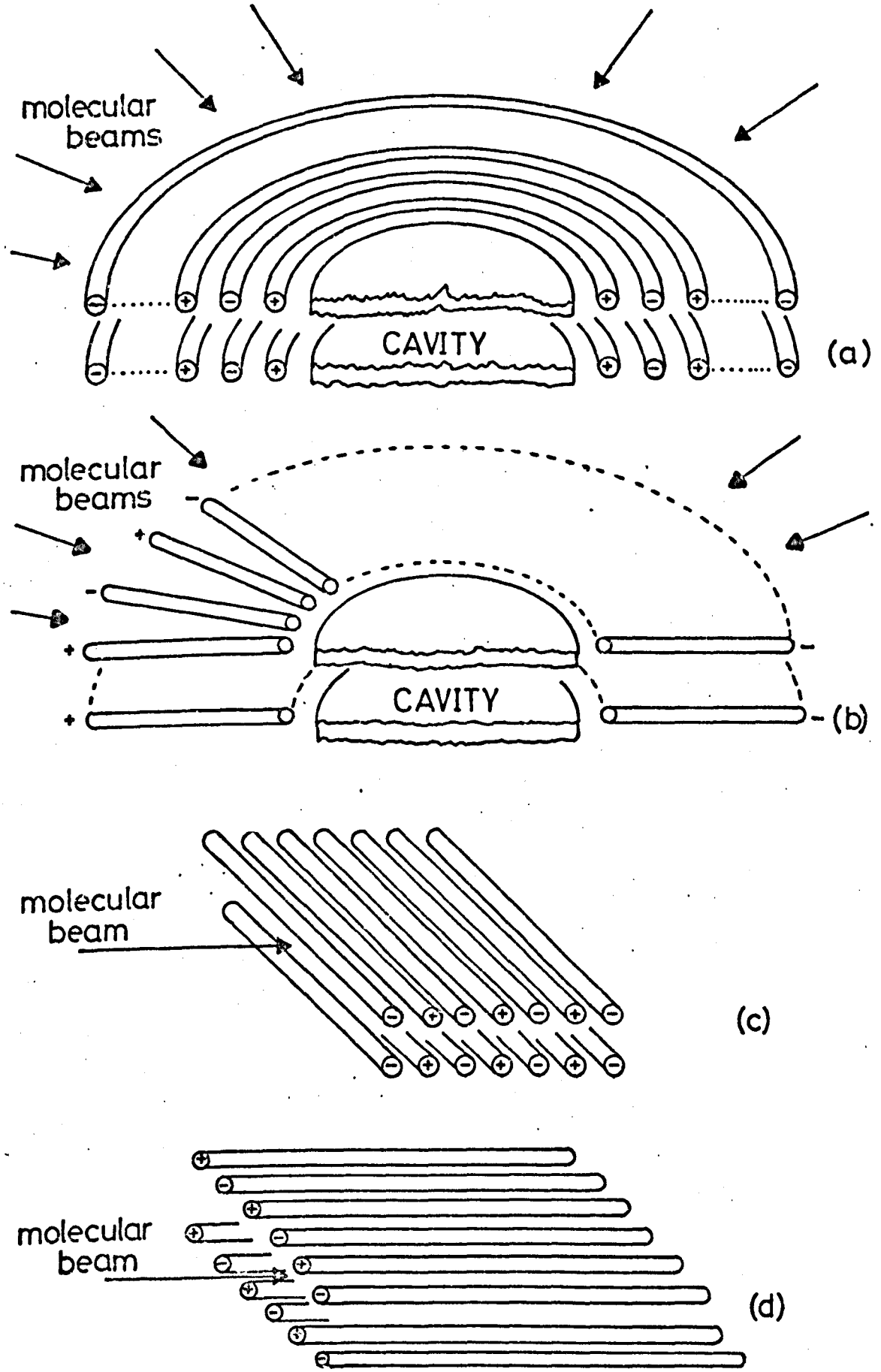

Fig. 2.4 Types of state separator for a flat beam:
(a) circumferential; (b) radial;
(c) transverse ladder; (d) longitudinal ladder.

No detailed comparison of the focusing efficiency of flat beam separators with that of cylindrical focusers is available. Takami and Shimizu, 1966 suggest that the focusing efficiency of their longitudinal ladder type was somewhat lower than that of a cylindrical multipole type but the dimensions of their separator were far from optimum. Becker, 1963B has compared transverse and longitudinal ladder types and found no difference in their focusing effect. The transverse ladder separator is in fact the analogue, in planar shape, of the ring focuser. This indicates that its efficiency should be high.

The transverse ladder separator was chosen for the present work, not only from qualitative considerations of efficiency, but also because its construction is somewhat simpler than the longitudinal arrangement. In addition it can be made physically shorter than the longitudinal separator for a given length of the region of interaction with the molecules. This last point was important because the space available for the separator in the present maser is limited.

2.3.2 Theory of the Transverse Ladder Separator

The theory described in this section is due to Becker, 1963B. It appears to be the only detailed treatment of the ladder focuser available in the literature.

Fig. 2.5(a) represents one half of a transverse ladder separator consisting of electrodes with diameter t, equally spaced by the distance d. Suppose the electric field $\underline{E}$ in the region of positive y has x- and y-components E_x and E_y respectively. Clearly $\underline{E}$ is periodic in x with a period 2d. Becker shows that E_x and E_y may be described by a pair of Fourier series,

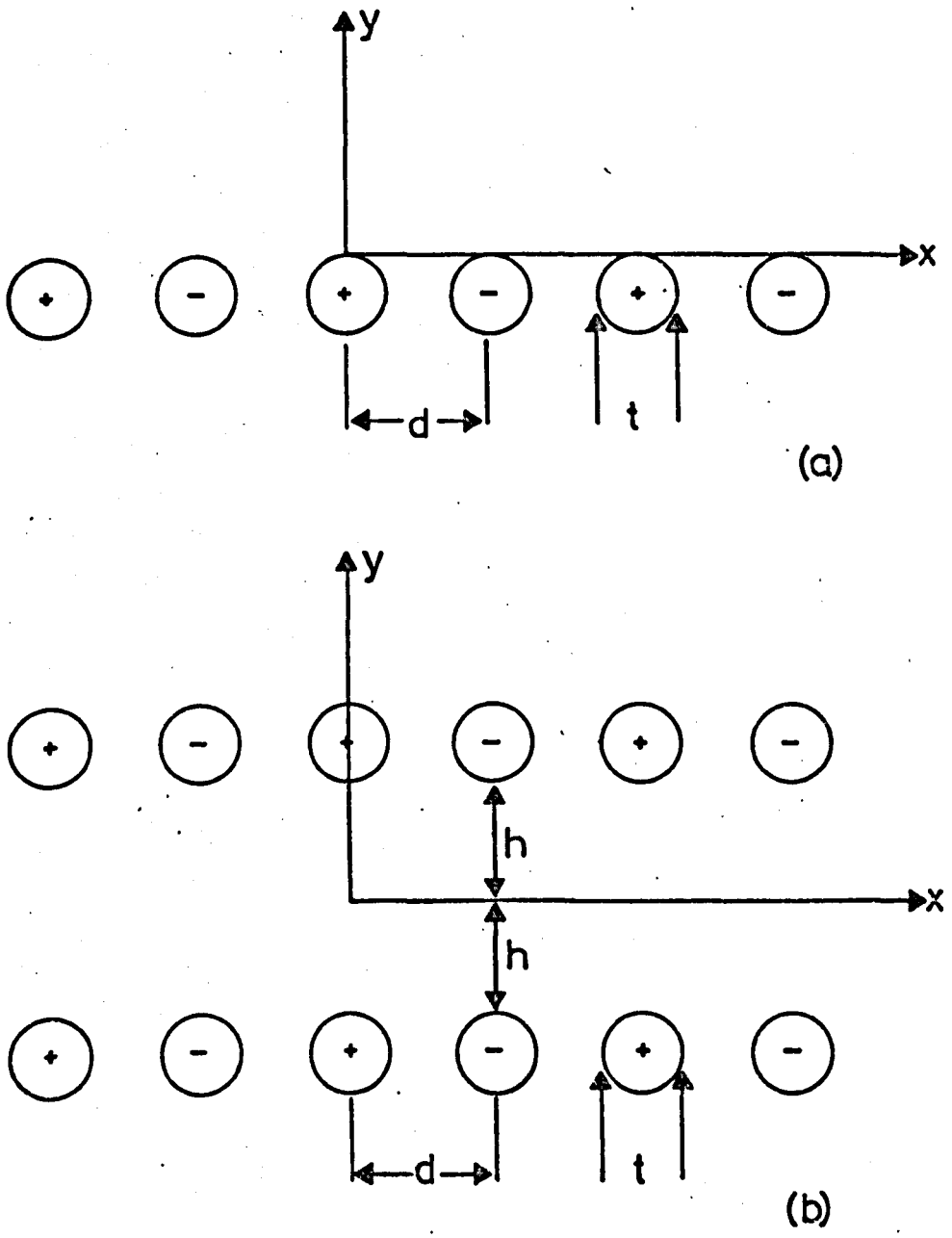

Fig. 2.5 (a) Model for one transverse ladder electrode assembly.
(b) Model for the transverse ladder separator.

$$E_x = E_1 \exp(-\pi y/d)\sin(\pi x/d) + E_3 \exp(-3\pi y/d)\sin(3\pi x/d) + E_5 \exp(-5\pi y/d)\sin(5\pi y/d) + \ldots. \quad 2.12$$

$$E_y = E_1 \exp(-\pi y/d)\cos(\pi x/d) + E_3 \exp(-3\pi y/d)\cos(3\pi x/d) + E_5 \exp(-5\pi y/d)\cos(5\pi y/d) + \ldots. \quad 2.13$$

In Sec. 2.2.3 it was seen that the focusing force on a molecule is proportional to $E\partial E/dy$ (or $\partial E^2/\partial y$) in the region of quadratic Stark effect. A molecule travelling in the x-direction past the electrode assembly of Fig. 2.5(a) would experience an effective force proportional to the average value of $\partial E^2/\partial y$ defined by

$$\overline{\frac{\partial E^2}{\partial y}} = \frac{1}{2d} \int_0^{2d} \frac{\partial E^2(x)}{\partial y}\, dx \quad 2.14$$

Substituting Eqns. 2.12 and 2.13 in 2.14 gives

$$\overline{\frac{\partial E^2}{\partial y}} = -(2\pi/d)E_1^2 \exp(-2\pi y/d) - (6\pi/d)E_3^2 \exp(-6\pi y/d) - \ldots. \quad 2.15$$

Becker found that for a practical electrode arrangement in which the ratio d/t is not large, terms involving E_3 and higher Fourier coefficients can be ignored. In this case it is possible to obtain E_1 by integration of Eqn. 2.12, and Eqn. 2.15 may be written

$$\overline{\frac{\partial E^2}{\partial y}} \simeq -\frac{\pi^3 V^2}{2d^3} \exp(-2\pi y/d) \quad 2.16$$

where V is the voltage applied to the electrodes.

Becker used a model of an electrode assembly in an electrolytic tank, to make measurements of the electric potential due to the assembly.

From these measurements he calculated $\partial E^2/\partial y$ for a large number of points (x, y) in the vicinity of the electrodes, and arrived at values for the average of $\partial E^2/\partial y$ as defined by Eqn. 2.14. These values fitted the function

$$\overline{\frac{\partial E^2}{\partial y}} = AV^2 \exp(-2\pi y/d) \qquad 2.17$$

to better than 1%, and the constant A agreed with the factor $\pi^3/2d^3$ of Eqn. 2.16 to within 4%. Eqn. 2.16, therefore, described the focusing effect of the single electrode assembly very well.

In order to extend this treatment to the double electrode arrangement of Fig. 2.5(b) (where the x-axis has been moved to coincide with the axis of symmetry), Becker assumed that the two contributions to the averaged $\partial E^2/\partial y$ could be added together. This is only true if the presence of the second electrode assembly does not distort the field of the first. The condition for this to be true is

$$h >> d/4\pi \qquad 2.18$$

where h is half the distance separating the electrode assemblies. For example if $h = d/2$ the field at the second electrodes due to the first is approximately 5% of the field close to the first electrodes. In terms of the co-ordinates of Fig. 2.5(b) the sum of the two contributions may be obtained using Eqn. 2.15 as

$$\overline{\frac{\partial E^2}{\partial y}} \cdot \frac{2d^3}{\pi^3 V^2} \simeq \exp(-2\pi h/d)\{\exp(2\pi y/d) - \exp(-2\pi y/d)\} \qquad 2.19$$

In Fig. 2.6 the function of Eqn. 2.19 is shown plotted against y/h for four values of h down to $h = d/4$. These curves are of considerable

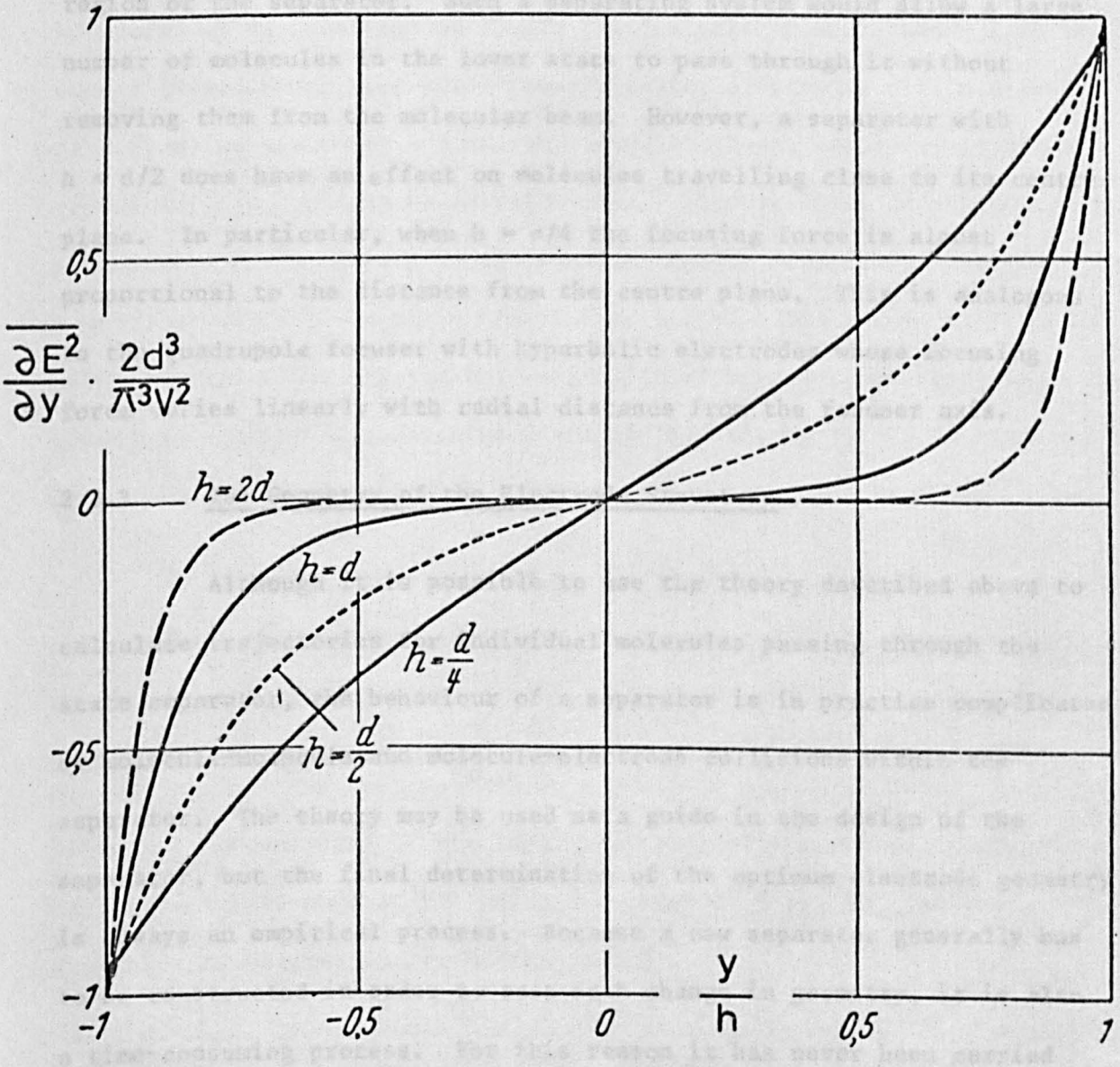

Fig. 2.6 Relative focussing force plotted for four electrode geometries (after Becker, 1963 B).

design interest. At large separations of the electrode planes ($h > d$, say), the focusing effect is concentrated near the electrode planes and little or no force is exerted on a molecule travelling through the central region of the separator. Such a separating system would allow a large number of molecules in the lower state to pass through it without removing them from the molecular beam. However, a separator with $h < d/2$ does have an effect on molecules travelling close to its centre plane. In particular, when $h = d/4$ the focusing force is almost proportional to the distance from the centre plane. This is analogous to the quadrupole focuser with hyperbolic electrodes whose focusing force varies linearly with radial distance from the focuser axis.

2.3.3 The Geometry of the Electrode Structure.

Although it is possible to use the theory described above to calculate trajectories for individual molecules passing through the state separator, the behaviour of a separator is in practice complicated by molecule-molecule and molecule-electrode collisions within the separator. The theory may be used as a guide in the design of the separator, but the final determination of the optimum electrode geometry is always an empirical process. Because a new separator generally has to be constructed in order to test each change in geometry, it is also a time-consuming process. For this reason it has never been carried through to its logical conclusion so as to yield a complete empirical understanding of the behaviour of a particular type of separator. Although the transverse ladder separator is an ideal subject for such a study (because the electrode assemblies can be made as two units whose relative positions can be easily altered) the present work is no exception in this respect. The state separators used in the present work have been modelled on those used by Becker, 1963B, but his

experimental investigations of them were far from exhaustive.

The electrode assemblies used by Becker consisted of wires of diameter t = 1.0 mm separated by a distance d = 2.5 mm. These assemblies were used up to a voltage of 20 KV. In the present work, where a 30 KV supply (Brandenburg type 202B) was available, electrodes with a diameter of 1.6 mm. separated by 4.0 mm. were used (although later a separation of 3.2 mm. was found to be satisfactory). The two banks of electrodes were placed 3.2 mm. apart in the parallel ladder separator, thus giving a value of 0.4 for the ratio h/d of Fig. 2.5(b). The curves of Fig. 2.6 show that h/d = 0.5 is probably a good compromise between obtaining strong focusing action in the centre plane of the separator, and maintaining a large cross-section area with which to capture the molecular beam.

Table 2.1 shows some of Becker's results for state separators with various geometries operated at a voltage of 8 KV. His two parallel ladder separators had values for the ratio h/d of 0.8 and 0.48. The latter had the lower threshold beam flux.

Table 2.1 Comparison of the input molecular flux required, to reach oscillation threshold at a separator voltage of 8 KV, for various separator geometries (after Becker, 1963B).

separator shape	electrode spacing 2h (mm)	average h/d ratio	input flux (mols sec^{-1})
parallel	4.0	0.8	12×10^{17}
parallel	2.4	0.48	6.5×10^{17}
linear taper	2.4 - 4.0	0.64	3.8×10^{17}
linear taper	1.5 - 3.0	0.45	5.5×10^{17}

It was mentioned in Sec. 2.2.3 that a separator with a non-uniform cross-section should give improved performance over one with parallel electrodes. Table 2.1 shows threshold beam fluxes for two separators with cross-sections which taper linearly from a small entrance to a large exit. These had the same electrode structures as the parallel separators of the table but show significantly lower threshold beam fluxes than the latter.

A tapered ladder separator was also constructed for the present work. It had electrode assemblies with t = 1.6 mm and d = 3.2 mm separated by a distance 2h which tapered from 1.6 mm at its entrance to 4.8 mm at its exit. Thus its average value for the ratio h/d was 0.5, which is close to those used by Becker. A rather small value of the ratio (0.25) was chosen for the entrance of the state separator, in order to make use of the powerful focusing effect near the central plane of an electrode assembly with h = d/4 (see Fig. 2.6). Although this state separator gave considerably better performance than the parallel separator, its geometry was probably not very close to the optimum since its narrow entrance appeared to limit the input molecular flux. This point will be returned to in Sec. 3.4.3 where some of the measured characteristics of the maser are discussed.

2.3.4 Maser Components for Molecular Beam Formation

The two state separators described in the previous section are shown in Fig. 2.7. They are constructed of brass rods and P.T.F.E. insulators using jigs to bend the electrodes and to hold the components in their correct relative positions during assembly. The edges of all metal parts and all soldered joints were carefully smoothed to minimise arcing. The shape of the electrode structures also allowed the joints

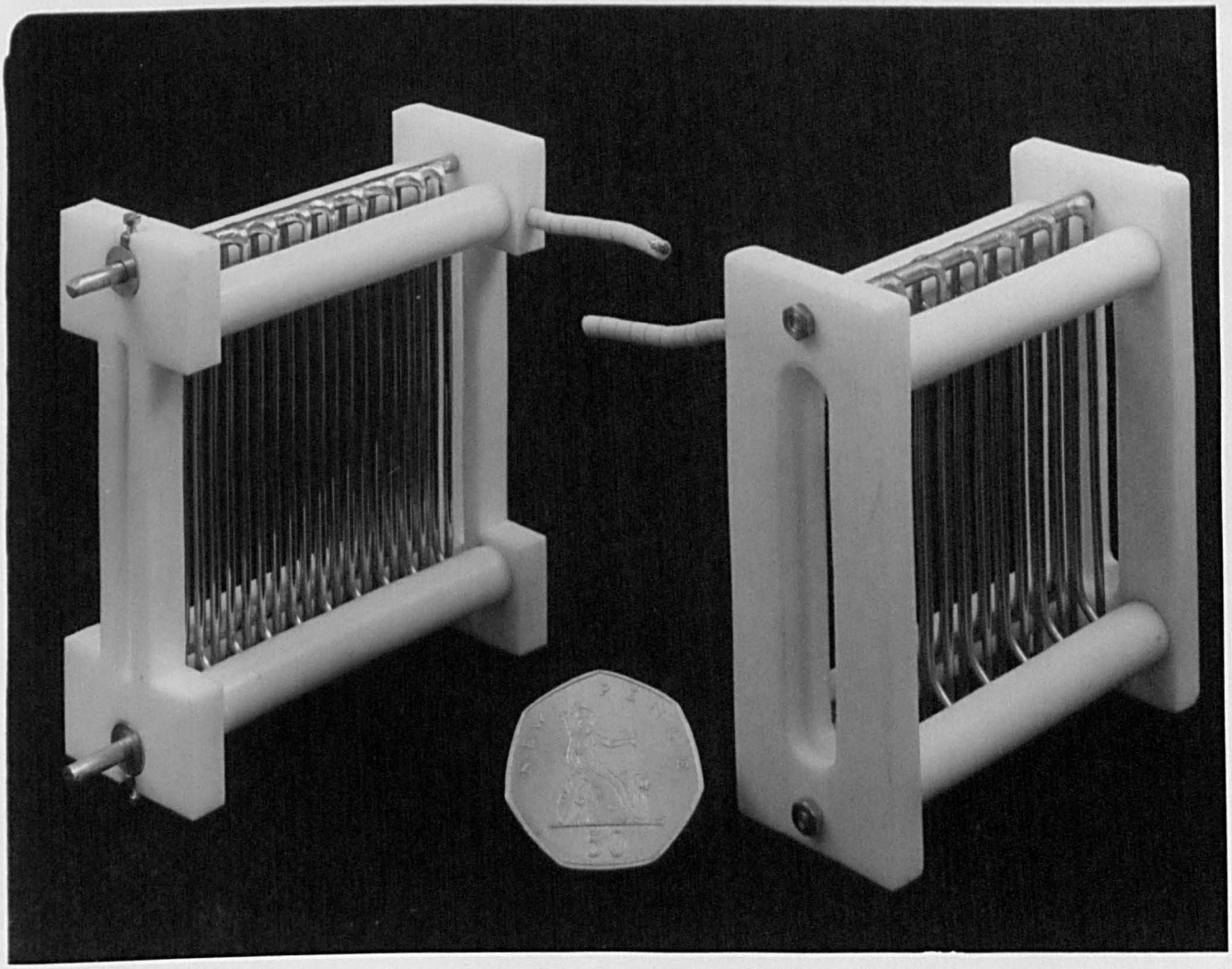

Fig. 2.7 Parallel state separator (right)
and tapered state separator (left).

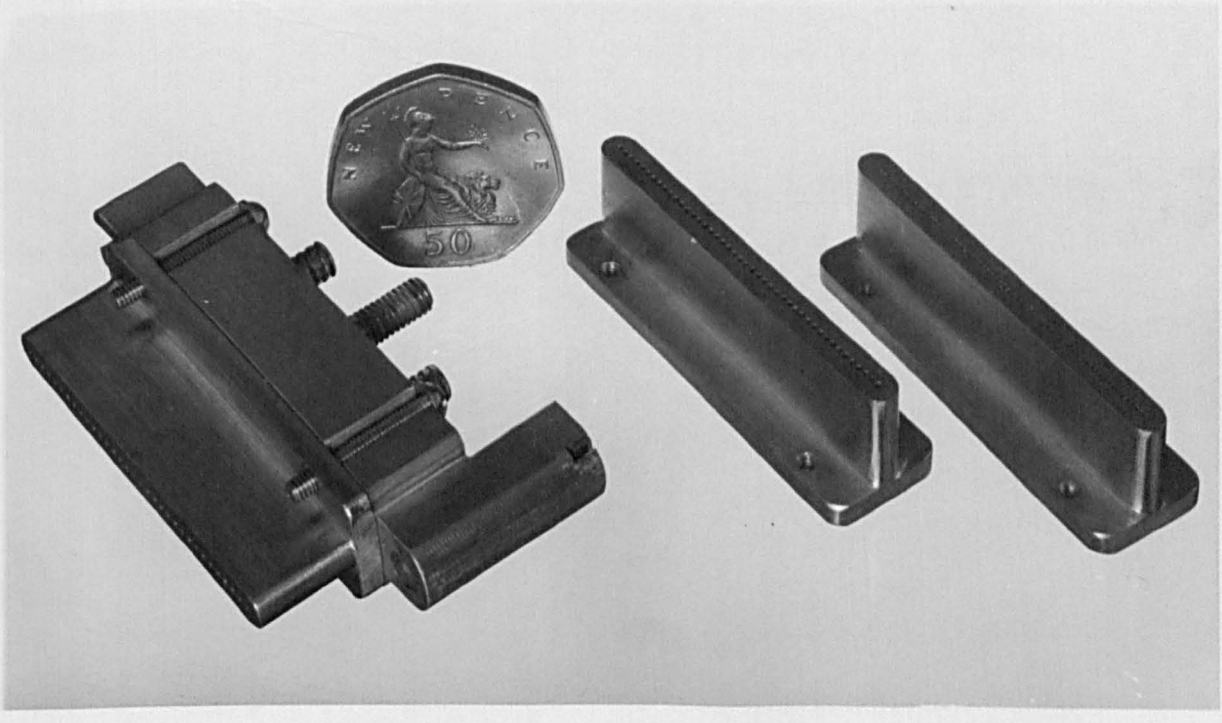

Fig. 2.8 Nozzle chamber and spare nozzle units.

between the high tension electrodes and their support rods to be shrouded in P.T.F.E. cylinders to further reduce the tendency for arcing.

The nozzles used to supply a beam of ammonia molecules consisted of a row of 33 holes, each 1.0 mm in diameter and 10 mm long. Although other nozzle units were also constructed this was the only one used consistently in the maser. The nozzle units bolt interchangeably to a nozzle chamber which is supplied with ammonia gas at the working pressure (about 0.35 torr). This pressure is monitored by a gauge connected directly to the nozzle chamber. The nozzle assembly is shown in Fig. 2.8 together with two of the interchangeable nozzle units.

2.4 SECONDARY EFFECTS OF ELECTRIC AND MAGNETIC FIELDS

2.4.1 Adiabatic Focusing

Molecules which pass through a state separator experience a time-varying electric field as a result of their motion through the spatially non-uniform field of the separator. In a separator which has a transverse electrode assembly, the molecules may experience Fourier components of the electric field with frequencies of several MHz. These will cause transitions to occur between closely spaced energy levels. In a radio frequency molecular beam maser transitions can be induced between the maser levels so that the process of state separation is ineffective in producing a population difference between the levels (Takami and Shimizu, 1966). A state separator with longitudinal electrodes, specially shaped at their ends to reduce the rate of change of electric field experienced by the molecules at the extremities of the separator, must be used in such a maser.

In masers operating in the microwave region however, the adiabatic focusing condition of Shimizu and Shimoda, 1961, which can be written

$$\frac{h}{(W_2-W_1)^2} \cdot \bar{v}\mu_{12} \frac{\partial E}{\partial x} \ll 1 \qquad 2.20$$

is always fulfilled, even for a separator with transverse electrodes. In Eqn.2.20, W_1 and W_2 are the energies of the lower and upper levels respectively, $\bar{v}$ is the mean molecular velocity, μ_{12} is the matrix element between the two maser states and $\partial E/\partial x$ is the rate of change of the electric field in the direction of travel of the molecules in the beam.

2.4.2 Preferential Orientation of the Molecular Beam

Mednikov and Parygin, 1963 suggest that there may in fact be an advantage in using transverse electrodes. A microwave molecular beam maser generally employs a cylindrical cavity operating in the E_{010} mode which has a longitudinal electric field. The molecules which couple most strongly with such a field are those whose effective dipole moment axis, i.e. axis of total angular momentum, is most closely aligned with the molecular beam axis. If no change of orientation of the molecule occurs in the space between the state separator and the cavity, they are those with M = 0 in a separator with a predominantly transverse electric field (longitudinal electrodes) and those with M = 3 in a separator with a predominantly longitudinal field (transverse electrodes). In Secs. 2.2.2 and 2.2.3 it was seen that the effectiveness of electrostatic state separation is zero for molecules with M = 0, and increases with increase in M. It is to be expected, therefore, that

a state separator with transverse electrodes will produce a more effective molecular beam than one with longitudinal electrodes.

Experimental work by Krupnov and Skvortsov, 1965C, however, shows that it is the effect of the fringe field of the state separator which determined the orientation of the molecules. Clearly a molecule passing through a region of electric field E which changes in direction, must either retain its orientation in space and change its quantization with respect to the field (i.e. make transitions between its M levels), or retain its quantization (i.e. its orientation with respect to the field direction) and change its orientation in space. The latter behaviour, which is usually termed spatial reorientation, occurs when the inequality of Eqn. 2.20 holds for transitions between M levels whose energy splittings are caused by the field E itself.

Krupnov and Skvortsov, 1965C calculate that the adiabatic condition of Eqn. 2.20 is respected for Stark split levels of formaldehyde, and Basov et al, 1964 give quantum mechanical arguments to show that spatial reorientation of ammonia molecules takes place if the field strength E is greater than about 10 V mm^{-1}. Thus reorientation of the molecules by the fringe field of the state separator must take place. Since the fringe field of both types of state separator is expected to be longitudinal, molecules with the highest values of M are always oriented near longitudinally on entering the cavity, whatever their orientation within the state separator. The preferential state separation of molecules with high values of M always produces a molecular beam whose upper state molecules have a preferred longitudinal orientation, so that the choice between transverse and longitudinal separator electrodes is not critical.

2.4.3 Spatial Reorientation

Spatial reorientation by the fringe field of the state separator has been discussed above. In the experiments of Basov et al, 1964 and Strakovskii et al, 1966, further reorientation of the molecules was caused by applying a potential difference to two electrodes placed on either side of the beam. Significant effects on the amplitude and frequency of the maser oscillation were noticed for field strengths up to about 60 V mm^{-1}. Basov et al show that the behaviour of a molecule in an inhomogeneous field of this magnitude is not necessarily adiabatic. Transitions between the closely spaced Stark sub-levels can occur; this corresponds in classical terms to the inability of the molecule to follow the rapidly changing field direction, so that some of the interaction energy is absorbed in changing the molecule's internal state.

Basov et al also show that spatial reorientation occurs in homogeneous and inhomogeneous magnetic fields. Their equations are a little difficult to follow because they do not distinguish between the two sets of quantum numbers, which they use, and which describe two different base state representations. A more complete treatment is presented here.

Consider a molecule whose magnetic dipole moment operator is given by $\mu_m \underline{J}/\sqrt{\{J(J+1)\}}$. The Hamiltonian for the molecule in a time-varying magnetic field $\underline{B}(t)$ is

$$\mathcal{H}(t) = C\underline{J}.\underline{B}(t) \qquad 2.21$$

where $C = \mu_m/\sqrt{\{J(J+1)\}}$. If the molecule is described by a wave-function $\psi(0)$ at time $t = 0$, then after time t it will be given by

$$\psi(t) = \exp\left(\frac{i}{\hbar}\int_0^t \mathcal{H}(t')dt'\right)\psi(0) \qquad 2.22$$

Initially the beam of molecules is quantized with respect to the longitudinal fringe field of the state separator, i.e. along the beam axis. Let the base states with respect to this axis be characterised by a quantum number m and let the molecule under consideration have m = p initially. Then $\Psi(t)$ must be written

$$\Psi(t) = \sum_m a_m(t)|m\rangle \qquad 2.23$$

where by Eqn. 2.22 the a_m's develop in time according to

$$a_m(t) = \langle m|\exp\left(-\frac{i}{\hbar}\int_o^t \mathcal{H}(t')dt'\right)|p\rangle \qquad 2.24$$

Suppose the magnetic field is applied at right angles to the molecular beam axis, along the z-axis. It is possible to transform Eqn. 2.24 to a new set of base states, defined with respect to the z-axis and characterised by a quantum number q, by writing the original states as

$$|m\rangle = \sum_q b_{m,q}|q) \qquad 2.25$$

In terms of the base states $|q)$ the a_m's are given by

$$a_m(t) = \sum_q b_{m,q}(q|\exp\left(-\frac{i}{\hbar}\int_o^t \mathcal{H}(t')dt'\right)|\sum_q b_{p,q}|q) \qquad 2.26$$

Since the z-component of $\underline{J}$ is given by q and the field $\underline{B}(t)$ has only a z-component, the Hamiltonian equation 2.21 can be written

$$\mathcal{H}(t) = CqB(t) \qquad 2.27$$

Thus Eqn. 2.26 can be reduced to

$$a_m(t) = \sum_q b^*_{m,q} b_{p,q} \exp\left(-\frac{i}{\hbar}Cq\int_o^t B(t')dt\right)$$

Putting J = 1, m = 0 and p = 0 in this equation the probability

$$|a_o(t)|^2 = \cos^2\left(\frac{c}{\hbar}\int_o^t B(t')dt'\right) \qquad 2.28$$

can be obtained. This is the result given by Basov et al which shows that a molecule with J = 1, having m = 0 initially, returns periodically to the state m = 0 with certainty. If J = 3 terms of the form $\cos^2 j\theta$ together with terms of the form $\cos j\theta \cos k\theta$ are formed, where j,k = 1,2 or 3 and θ is the term in brackets in Eqn. 2.28.

In general the expectation values of the a_m's behave in a complicated fashion. A particularly simple case is that of a molecule in a uniform field for all time. In this case the quantum mechanical solution must be the equivalent of a steady precession of the magnetic moment about the field direction. The changes are not adiabatic because the molecule does not return to its original state if it is passed back along its path. Since the molecule exists initially in a mixed state in the $|q)$ representation, its behaviour in this representation is quite complicated. However, if the molecule were found initially in a single $|q)$ base state it would remain in that state for all time.

The molecule precesses in a constant, uniform field at an angular velocity

$$\omega = \frac{\mu_m B}{\hbar\sqrt{\{J(J+1)\}}} \qquad 2.29$$

For ammonia molecules with J = 3, K = 3, $\mu_m = 0.53 \times \mu_n$ where μ_n is the nuclear magneton, so that $\omega = 7.7 \times 10^2$ rad. sec^{-1} in a magnetic field of 1×10^{-4} T. Clearly changes in the magnetic field seen by the molecule must have Fourier components with smaller angular velocity than this value in order that the molecule's precession shall be able to speed up and slow down, following the changes in field.

CHAPTER 3

THE MASER

3.1 INTRODUCTION

In this chapter the construction and operation of the Fabry-Pérot maser are described. The main features of a molecular beam maser are shown in Fig. 3.1. A molecular beam is formed inside a vacuum chamber by effusion of gas from a nozzle unit. The beam passes through a state separator in which lower state molecules are removed. The beam of predominantly upper state molecules passes into the microwave cavity where the molecules interact with an electromagnetic field. The cavity forms part of a microwave circuit in which the stimulated emission or oscillation signals from the maser can be detected. Spent molecules are removed by a fast pumping system which keeps the pressure in the chamber low enough to permit formation of a molecular beam.

In Sec. 3.2. factors which affect the design of the vacuum, pumping and gas supply systems are discussed, and the construction of the maser used in this work is described. The cavity has been described in Chap. 1, and the nozzle assembly and state separators in Chap. 2. Their mounting in the vacuum chambers and mutual alignment are dealt with here.

Some of the measurements made on the maser have required the development of special detection techniques. Sec. 3.3 is devoted to a brief study of the problems involved in the detection of small microwave signals, together with descriptions of the detection schemes used in this work.

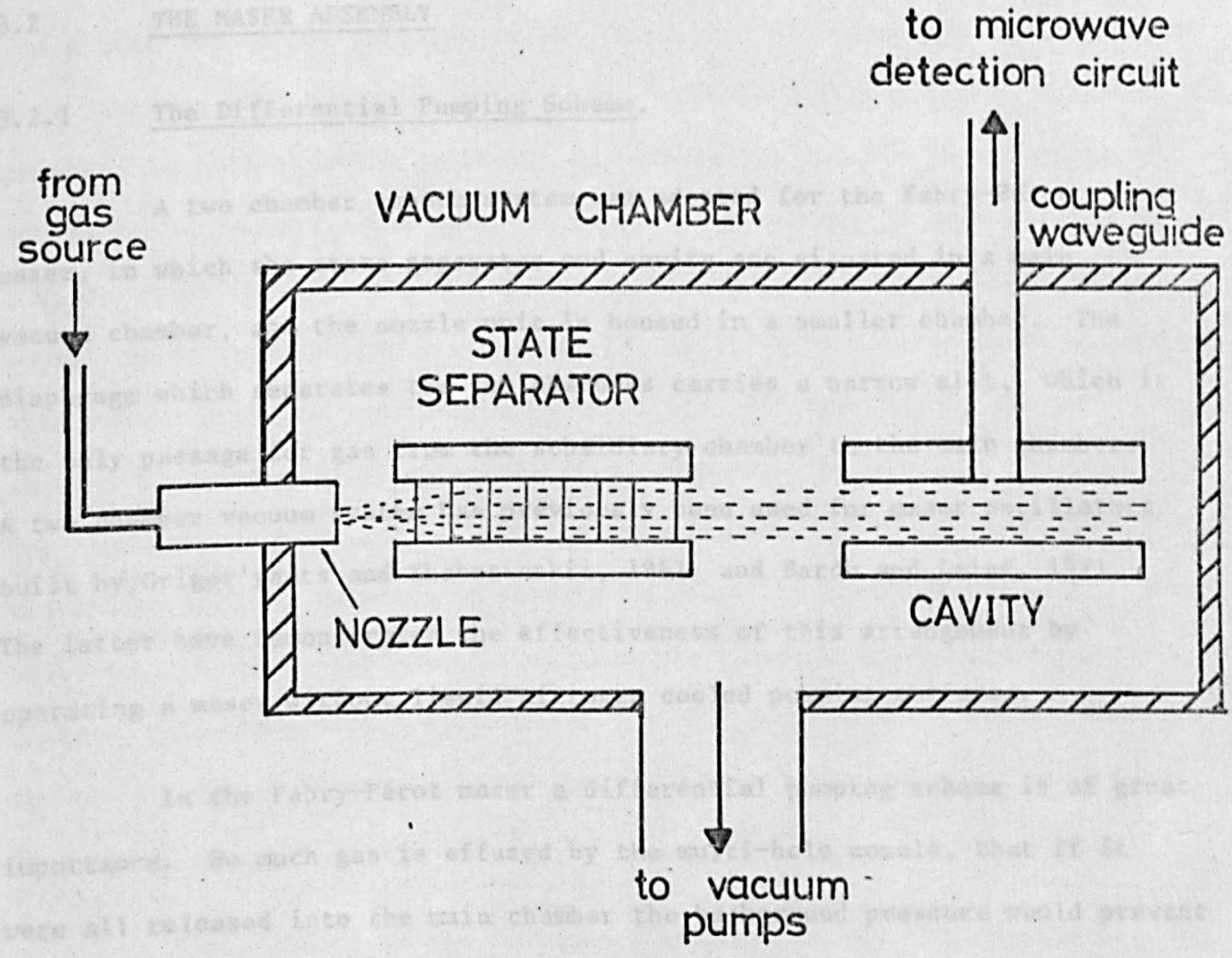

Fig. 3.1 The essential components of a maser

Finally Sec. 3.4 presents some measurements which have been made to determine the general behaviour and to establish the optimum operating conditions of the maser. Conclusions and inferences which may be drawn from these results are discussed.

3.2 THE MASER ASSEMBLY

3.2.1 The Differential Pumping Scheme.

A two chamber vacuum system was adopted for the Fabry-Pérot maser, in which the state separator and cavity are situated in a main vacuum chamber, and the nozzle unit is housed in a smaller chamber. The diaphragm which separates the two chambers carries a narrow slit, which is the only passage for gas from the subsidiary chamber to the main chamber. A two chamber vacuum system has previously been used for maser oscillators built by Grigor'yants and Zhabotinskii, 1961 and Bardo and Lainé, 1971. The latter have demonstrated the effectiveness of this arrangement by operating a maser without liquid nitrogen cooled pumping surfaces.

In the Fabry-Pérot maser a differential pumping scheme is of great importance. So much gas is effused by the multi-hole nozzle, that if it were all released into the main chamber the background pressure would prevent formation of a strong molecular beam. The diaphragm slit, which is 1.6 mm wide and 50 mm long, only allows the central part of the effusion from the nozzle to pass into the main chamber; the remainder is pumped away in the subsidiary chamber. The angular spread of the beam selected by the slit may be altered by moving the nozzle with respect to the diaphragm. Typically it is placed a few mm. from the diaphragm so that the pressure in the subsidiary chamber need only be maintained at a value low enough to prevent

many collisions from taking place in this small distance. A pressure of 5×10^{-3} torr, for which the mean free path of ammonia molecules is 15 mm, is probably sufficient.

The pumping arrangement is shown in Fig. 3.2. Two Edwards type 203 2 inch diameter diffusion pumps are mounted below the main chamber, and one below the subsidiary chamber. These are charged with Silicone 704 oil which has a limiting vapour pressure of 10^{-7} torr, and all three are backed by the same Metrovac GRD1 two stage rotary pump. Liquid nitrogen cooled surfaces are provided in both chambers to assist in pumping the ammonia gas by freezing it out as solid ammonia. The pressure in the main chamber is monitored by an Edwards IG2HB ionization gauge with a N.G.N. Thermion control unit. Under normal operating conditions (in which the maser is maintained under vacuum when not in use) the terminal pressure of 4×10^{-6} torr may be reached after about 6 hours of pumping with the diffusion pumps. However, if the maser and its components have been left open to the atmosphere for some days it may require as much as 48 hours of pumping to reach the terminal pressure. The pressure reduces to 1.5×10^{-6} torr when the liquid nitrogen traps are charged, and rises once more to about 4×10^{-6} torr when a molecular beam of ammonia of normal operating intensity (0.35 torr behind the nozzles) is introduced into the system.

The pressure in the subsidiary chamber has not been monitored. It is unlikely to be in excess of 5×10^{-4} torr, however, since English and Zorn, 1973 suggest that it is only possible to maintain about two orders of magnitude difference in pressure between the two chambers of such a differential pumping system. This is particularly likely to be true in this case because of the large total area (75 mm^2) of the slit connecting the two chambers.

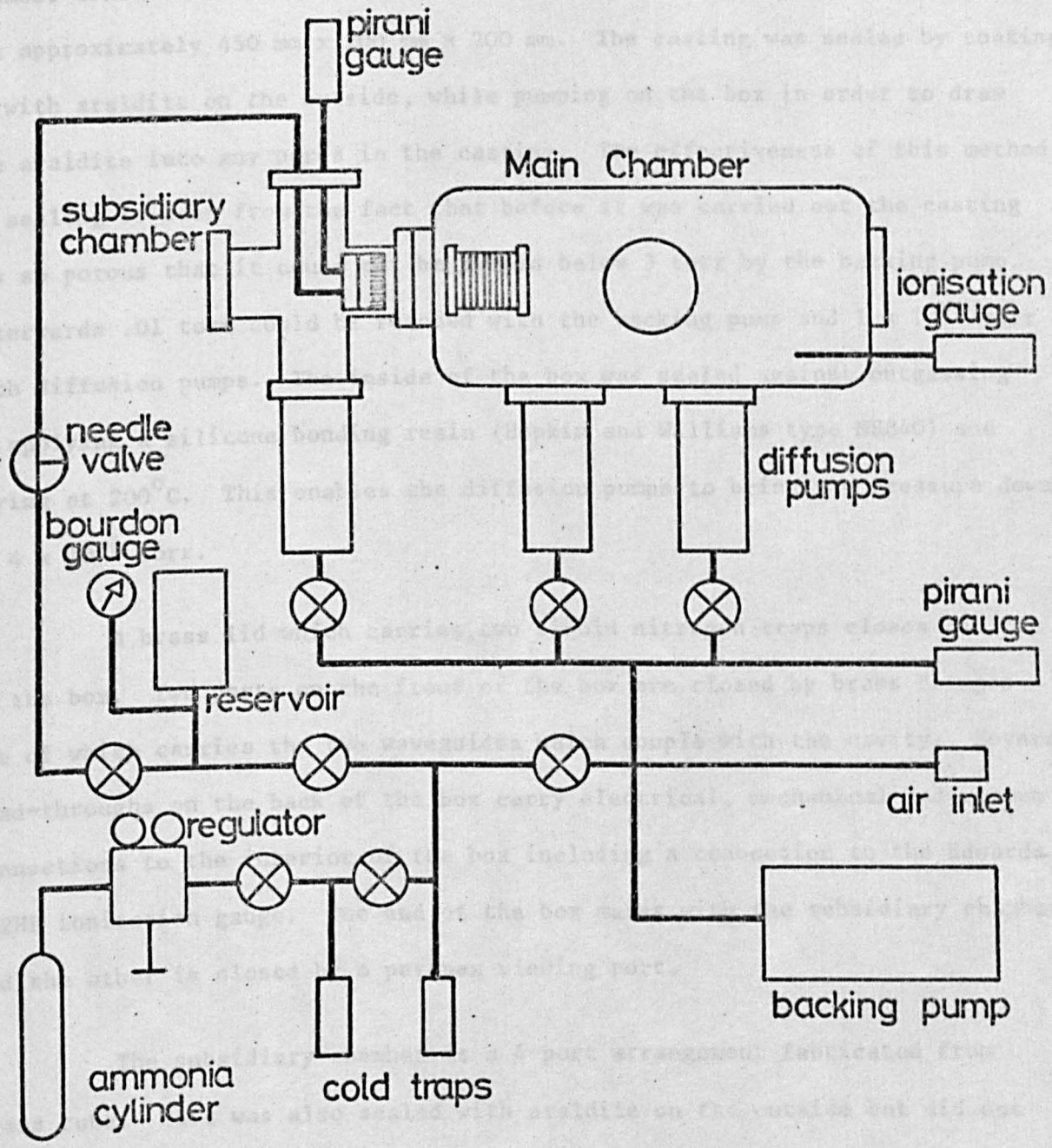

Fig 3.2 Diagram showing the arrangement of the two vacuum chambers, the pumping system and the ammonia purification plant.

3.2.2 The Vacuum Chambers

Fig. 3.3 shows a general view of the maser. The two vacuum chambers are mounted horizontally on a wooden bench and cushioned with rubber. The main chamber consists of an aluminium bronze casting in the shape of a rectangular box approximately 450 mm x 200 mm x 200 mm. The casting was sealed by coating it with araldite on the outside, while pumping on the box in order to draw the araldite into any pores in the casting. The effectiveness of this method of sealing is seen from the fact that before it was carried out the casting was so porous that it could not be pumped below 3 torr by the backing pump. Afterwards .01 torr could be reached with the backing pump and 1×10^{-5} torr with diffusion pumps. The inside of the box was sealed against outgassing by applying a silicone bonding resin (Hopkin and Williams type MS840) and curing at $200^{\circ}C$. This enables the diffusion pumps to bring the pressure down to 4×10^{-6} torr.

A brass lid which carries two liquid nitrogen traps closes the top of the box. Two ports on the front of the box are closed by brass flanges one of which carries the two waveguides which couple with the cavity. Several lead-throughs on the back of the box carry electrical, mechanical and vacuum connections to the interior of the box including a connection to the Edwards IG2HB ionization gauge. One end of the box mates with the subsidiary chamber and the other is closed by a perspex viewing port.

The subsidiary chamber is a 4-port arrangement fabricated from brass tube. This was also sealed with araldite on the outside but did not require an interior coating. One port mates with the main chamber. Opposite is a smaller port closed by a flange carrying a mechanical leadthrough which enables longitudinal movement of the nozzle from outside the vacuum chamber. The top of the subsidiary chamber is closed by a flange carrying a liquid nitrogen trap and ammonia gas lead-throughs.

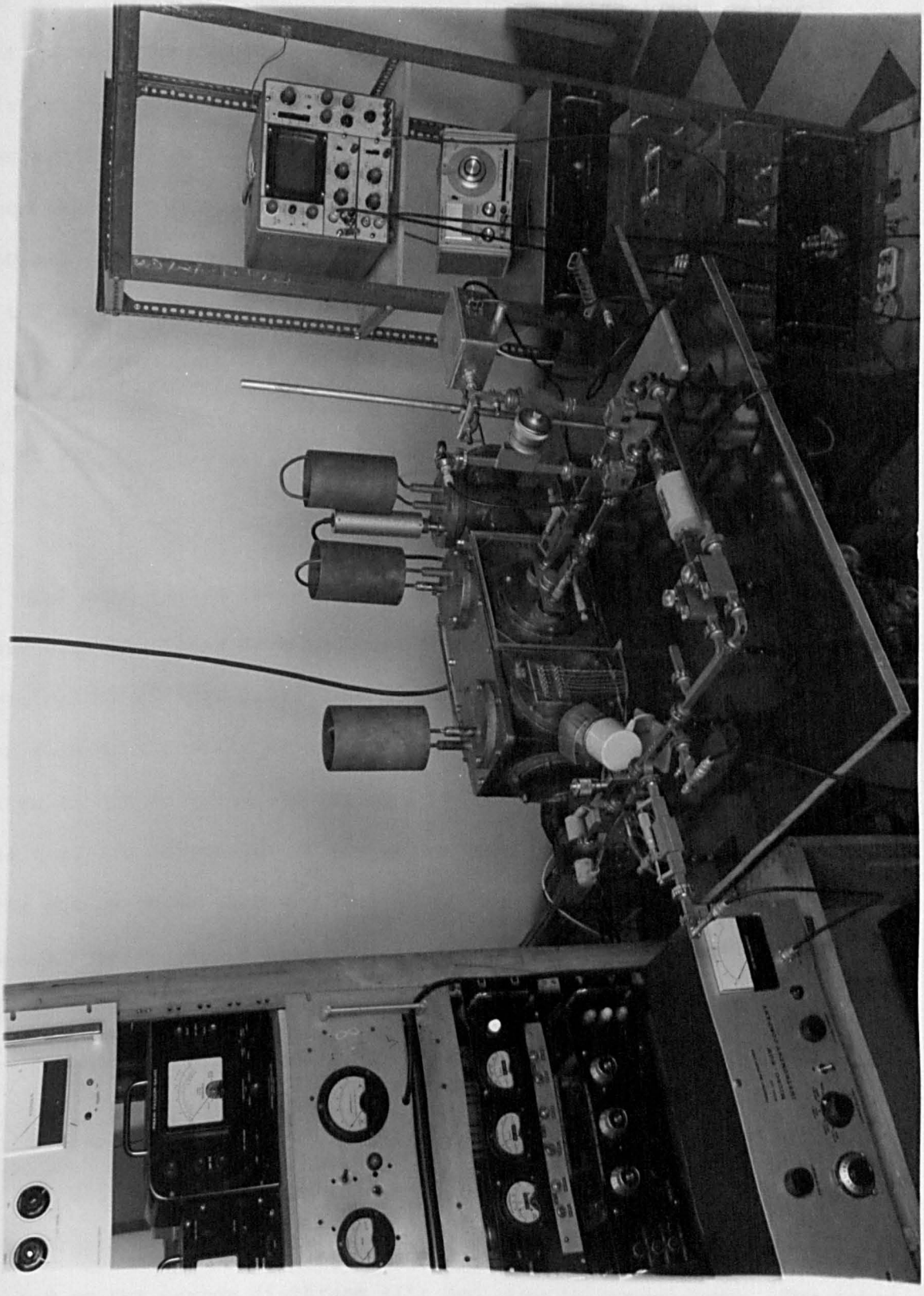

Fig. 3.3 General view of the maser.

3.2.3 The Liquid Nitrogen Traps

Each liquid nitrogen trap consists of a lagged liquid nitrogen reservoir outside the vacuum chamber, and a copper tube which runs from the reservoir into the vacuum chamber and back to the reservoir, thus passing twice through a vacuum flange. The tube is fitted with copper fins inside the vacuum chamber to provide a large pumping surface area. A short length (about 60 mm) of thin-walled cupronickel tube is employed as the connection between the copper tube and the vacuum flange. This provides a low conductivity thermal path between the liquid nitrogen trap and its surroundings, which minimises cooling of the vacuum chamber and boil-off of the liquid nitrogen. Silver solder is used for all joints which are subject to thermal cycling.

The main vacuum chamber is fitted with two such traps (for clarity the liquid nitrogen traps have not been shown in Fig. 3.2 but may be seen in the photograph of Fig. 3.3). The first has two cooled plates which lie on either side of the state separator, and whose edges are carefully smoothed so as not to encourage arcing from the electrodes of the separator. Molecules that are thrown out of the molecular beam by the state separator are frozen out on these plates. The second has a coil of tube to which are soldered several copper fins giving it a total surface area of 0.04 m^2. This trap is placed at the other end of the chamber so that it intercepts molecules emerging from the cavity.

The subsidiary chamber is designed to pump a much larger volume of gas than its 2 inch diffusion pump is capable of handling alone. This is because a large proportion of the ammonia gas emerging from the nozzle is not directed at the narrow diaphragm slit and must be pumped away. The tubes carrying liquid nitrogen from the reservoir run down to the lower part of

the chamber, and support some copper fins immediately over the diffusion pump orifice. This cooled baffle has a total surface area of 0.02 m^2, and freezes out most of the excess ammonia before it can enter the pump.

3.2.4 The Ammonia Supply

The arrangement of the valves and pipes which constitute the ammonia supply system is shown in Fig. 3.2. The source of the ammonia is a lecture size cylinder of anhydrous liquid ammonia. From this cylinder the gas passes through a pressure regulator, which is adjusted so that the gas enters the purification system at a little above atmospheric pressure.

Purification of the ammonia is carried out by freezing it in traps cooled with liquid nitrogen. Impurity gases which have not condensed are then pumped away using the same Metrovac GRD1 pump as is used to back the diffusion pumps. The trap is warmed and the ammonia is allowed to expand into the reservoir. Before the temperature of the cold trap rises to $0^{o}C$, it is closed off from the reservoir so that water vapour is not transferred with the ammonia. A second stage of purification may be carried out by re-freezing the ammonia from the reservoir in the second cold trap. The pure ammonia is passed to the nozzle assembly through a hand valve which closes off the supply, and a fine needle valve which controls the gas flow.

The removal of non-condensing impurities by this method of purification is essential if the liquid nitrogen traps of the maser are to work efficiently as pumps in the vacuum chambers. If the purification described above is not carried out, then the pressure of non-condensable impurities in the main chamber is sufficient to prevent the maser from oscillating. The removal of water vapour is desirable, because it may become adsorbed by the components of the maser.

3.2.5 The Nozzle and State Separator.

The diaphragm plate which closes off the subsidiary vacuum chamber from the main chamber, and which carries the diaphragm slit, also supports the state separator and the nozzle unit. Two parallel rods on the subsidiary chamber side of the plate carry the nozzle unit, and allow it to slide to and from the diaphragm slit; the state separator plugs into a pair of lugs on the main chamber side. No method for mutually aligning these components is necessary since the plate is constructed with sufficient accuracy to fix their geometry correctly. The assembly is shown in Fig. 3.4.

Plastic tubes connect the nozzle chamber with two gas lead-throughs in the upper flange plate of the subsidiary chamber. One lead-through is supplied with ammonia from the needle valve through a nylon tube. Above the other is mounted an Edwards pirani gauge head (type M5C) which therefore monitors the pressure in the nozzle chamber, immediately behind the multiple nozzle tubes. The high tension supply for the state separator is led into the main vacuum chamber via a vacuum seal constructed from a long-reach sparking plug.

Slotted holes are provided in the diaphragm plate for the bolts which secure it to the vacuum chamber port. This provides for horizontal adjustment of the whole nozzle and state separator assembly, in order to align it with the centre of the cavity. Sufficient movement is possible to allow the assembly to be aligned with the second axial maximum of electric field in the cavity if the cavity is operated in axial mode orders higher than 1. The relative position of the assembly with respect to the cavity is shown in Fig. 3.5.

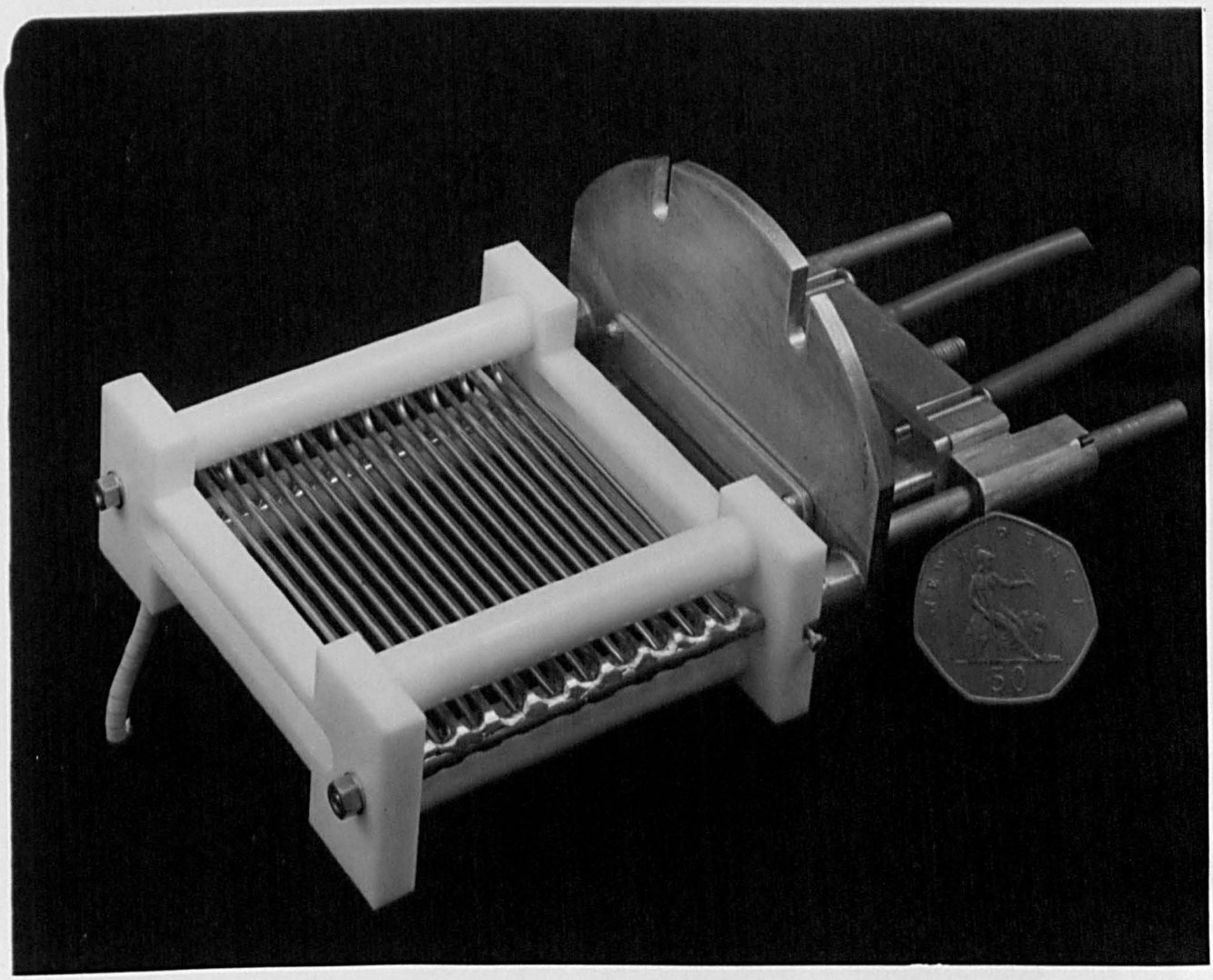

Fig. 3.4 State separator and nozzle unit mounted on the diaphragm plate.

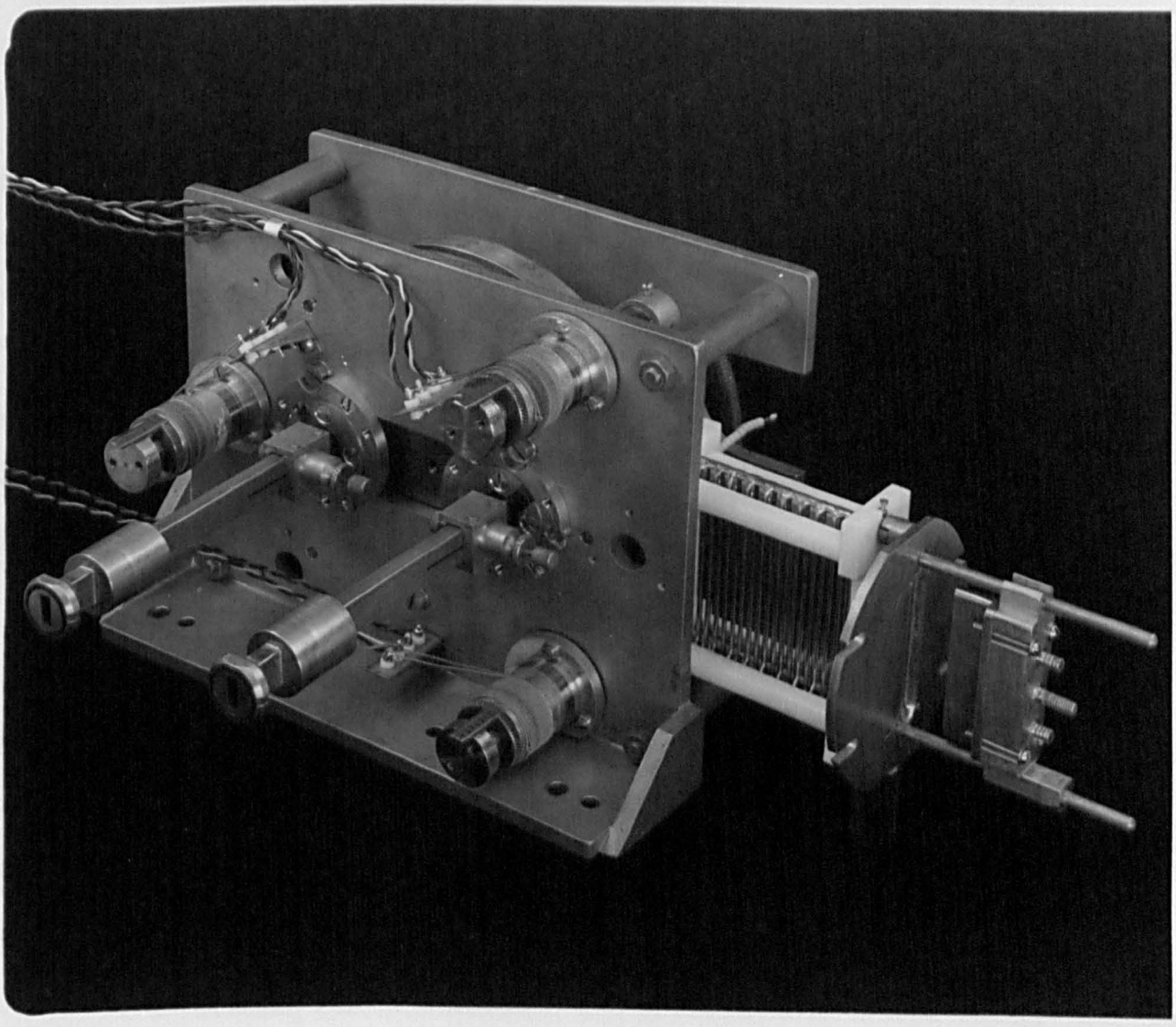

Fig. 3.5 Cavity, state separator, diaphragm plate and nozzle unit in their correct relative positions.

3.2.6 The Cavity and its Coupling Waveguides

The design and construction of the Fabry-Perot cavity has been discussed in Sec. 3.4. Here its method of mounting in the main vacuum chamber is described.

The cavity is supported on and bolted to a rectangular frame, which in turn is bolted to the floor of the main vacuum chamber. This frame can be seen below the cavity in the overhead view of the apparatus in Fig. 3.6. This figure also shows the two waveguides which couple with the cavity and which pass through a flange on the front of the main vacuum chamber. The waveguides are fitted with cylindrical barrels where they pass through the flange. These barrels (clearly visible in Fig. 3.5) enable vacuum tight joints to be made with the flange by means of O-ring seals, and also allow the waveguide assemblies to be rotated while the maser is under vacuum.

It was early found that the forces, which press the waveguides inwards as a result of atmospheric pressure, can bow the coupling mirror of the cavity, and adversely affect the Q-factor of the cavity. An adjustable spring mounting, shown in Fig. 3.7, enables the two waveguides to be pulled outwards until the effect of atmospheric pressure is just neutralised and no forces are transmitted to the Fabry-Pérot mirror.

A rotating shaft passing through a vacuum seal in the rear wall of the main chamber provides mechanical tuning of the cavity in the manner described in Sec. 1.4.4. The electrical connections for thermal tuning of the cavity are provided by electrical lead-throughs, also in the rear wall of the chamber. These, together with the high tension lead-in for the state separator supply, may be seen in Fig. 3.6.

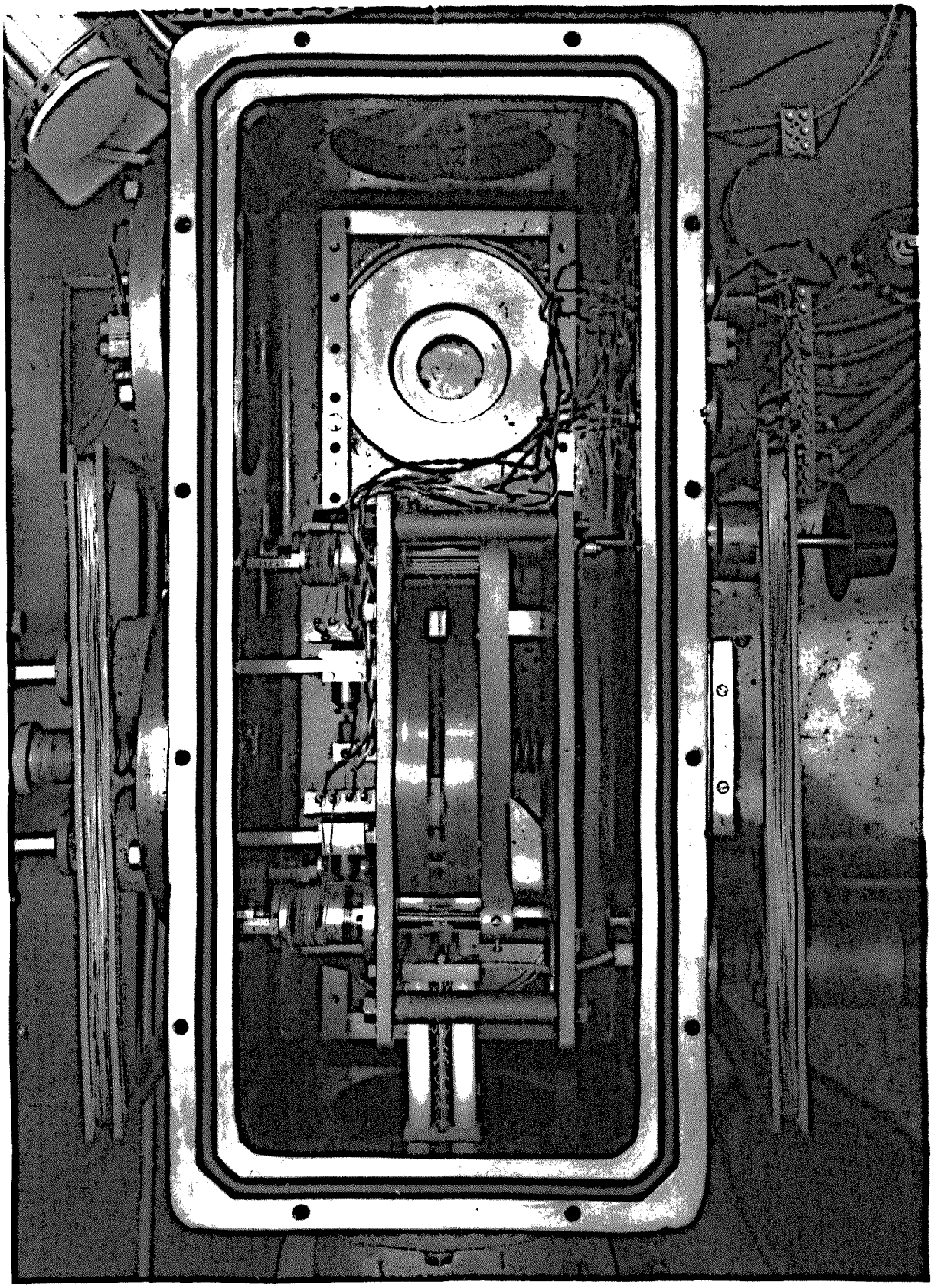

Fig. 3.6 View of main vacuum chamber from above showing cavity and state separator in position.

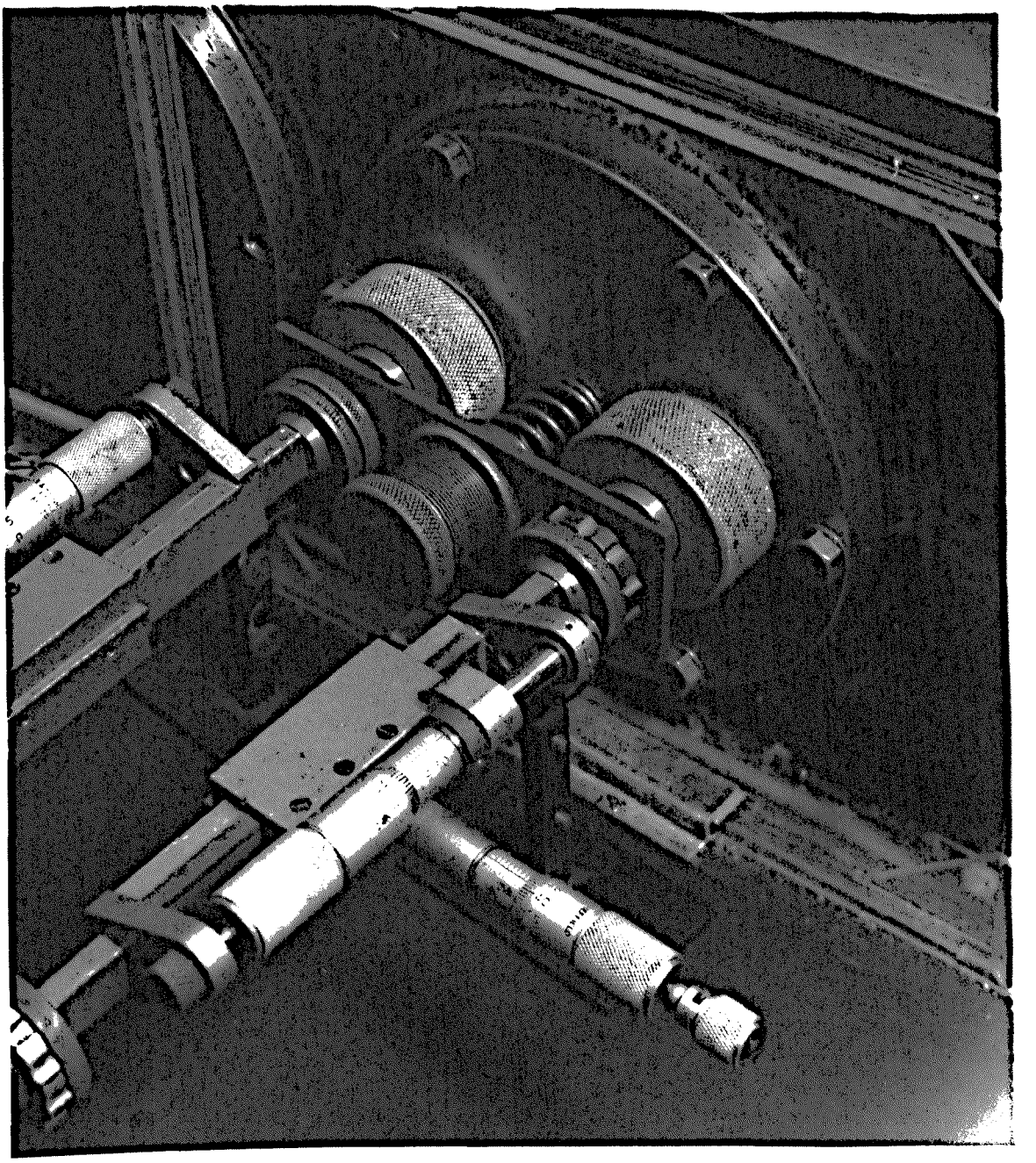

Fig. 3.7 View of the waveguide vacuum seals showing the pressure relief plate and spring.

3.3 MICROWAVE DETECTION SCHEMES

3.3.1 Superheterodyne Detection

The choice of a superheterodyne scheme for detection of small microwave signals is a natural one. A microwave crystal detector has a 1/f dependence of flicker noise on frequency, f, and the noise figure of the detector is not comparable with electronic noise figures unless the frequency of detection is above about 10 MHz. In the present work an intermediate frequency (I.F.) of 30 MHz was chosen.

Pound, 1948 describes how a crystal rectifier may be used both as a mixer and as a modulator. A mixer crystal requires a relatively large microwave signal of constant amplitude at the local oscillator (L.O.) frequency incident on it, in order to bias the crystal into the steeply sloping region of its D.C. characteristic. A small microwave signal at the signal frequency (S.F.) then produces a proportional output from the mixer at a frequency equal to the difference between the signal and L.O. frequencies. This is the intermediate frequency. The conversion gain of the mixer is the ratio of the output power at the I.F. to the input power at the S.F. Since the crystal mixer is a passive device, its conversion gain is usually less than unity.

The conversion gain, G, of a mixer is proportional to the slope of the D.C. characteristic of the crystal. Fig. 3.8 shows the behaviour of the conversion gain of a typical mixer crystal, with variation in L.O. power. It rises to a maximum value and then generally falls slowly with further increase in power. The noise power developed by the crystal at the I.F., P, is also shown in Fig. 3.8. This is approximately proportional to the incident L.O. power. The overall noise figure, F,

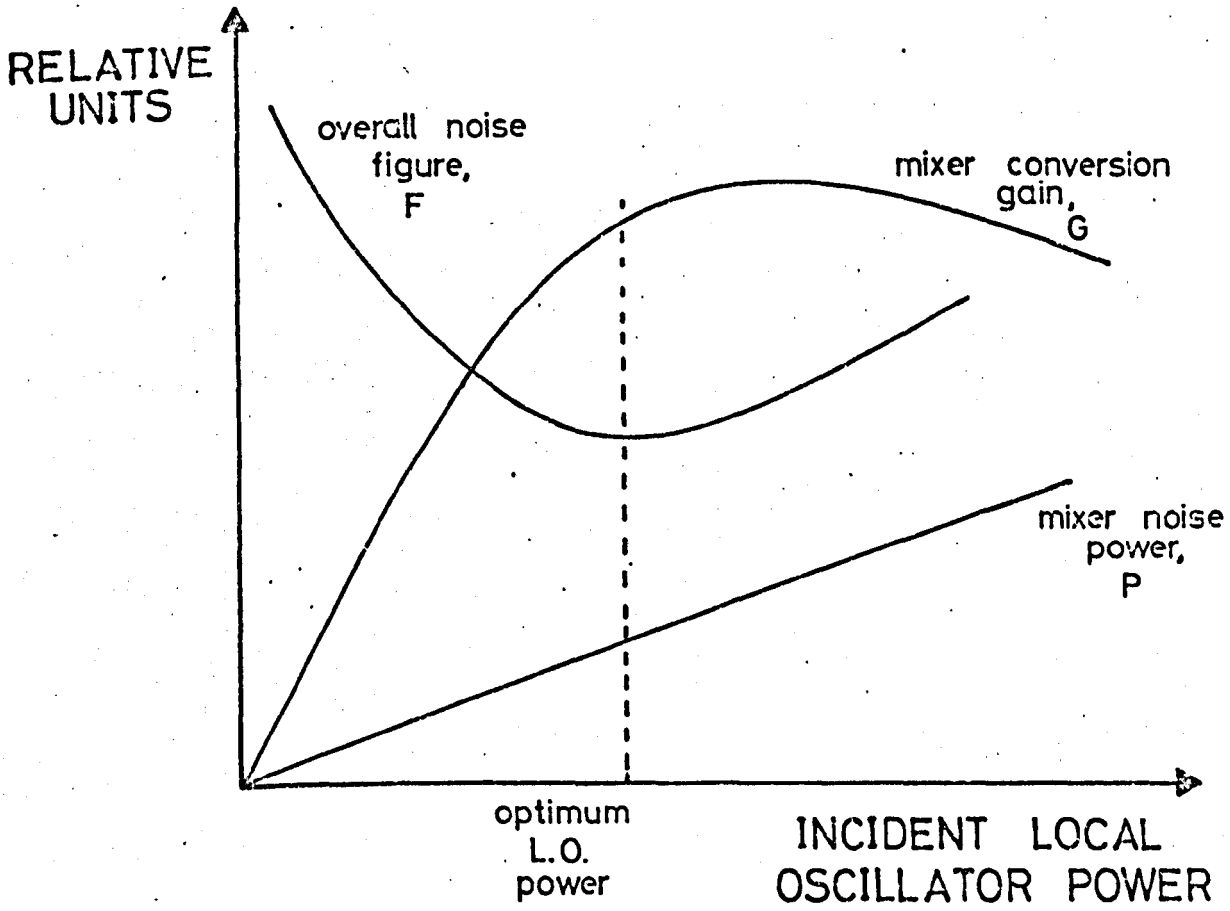

Fig. 3.8 General behaviour of a microwave mixer crystal

of the mixer would be obtained in a practical example by combining these two experimentally determined curves.

F. is shown sketched against L.O. power in Fig. 3.8, and it can be seen to pass through a minimum value. This minimum occurs somewhat below the maximum in the conversion gain characteristic. For the 1N26A and 1N26C crystals used in the present work, the conversion gain maximum occurs at approximately 1mW L.O. power. The signal to noise ratio of the I.F. detection systems used here was observed to pass through a minimum at about 0.5mW L.O. power.

A 1N26A crystal is also used as a modulator in the detection schemes described in the following sections. Pound, 1948 describes how an applied voltage shifts a crystal diode's operating point so that it presents a different impedance at microwave frequencies. If the applied voltage is varied sinusoidally, the microwave power reflected from the crystal is amplitude modulated at the frequency of the applied voltage. Thus two sidebands appear at frequencies $f + \Delta f$ and $f - \Delta f$ where f is the frequency of the incident microwaves, and Δf the modulation frequency. One of these sidebands is used in the present work as a signal to stimulate the maser.

3.3.2 The Transmission Detection Scheme

This was the detection scheme most often employed with the Fabry-Pérot maser. It made use of the transmission properties of the two port cavity. It is shown in Fig. 3.9 and the description of its operation which follows refers to this figure.

Microwave power from the klystron passes via a 6dB directional coupler an attenuator and an isolator to the circulator A and thence to the modulator crystal B. The impedance of this crystal is modulated at

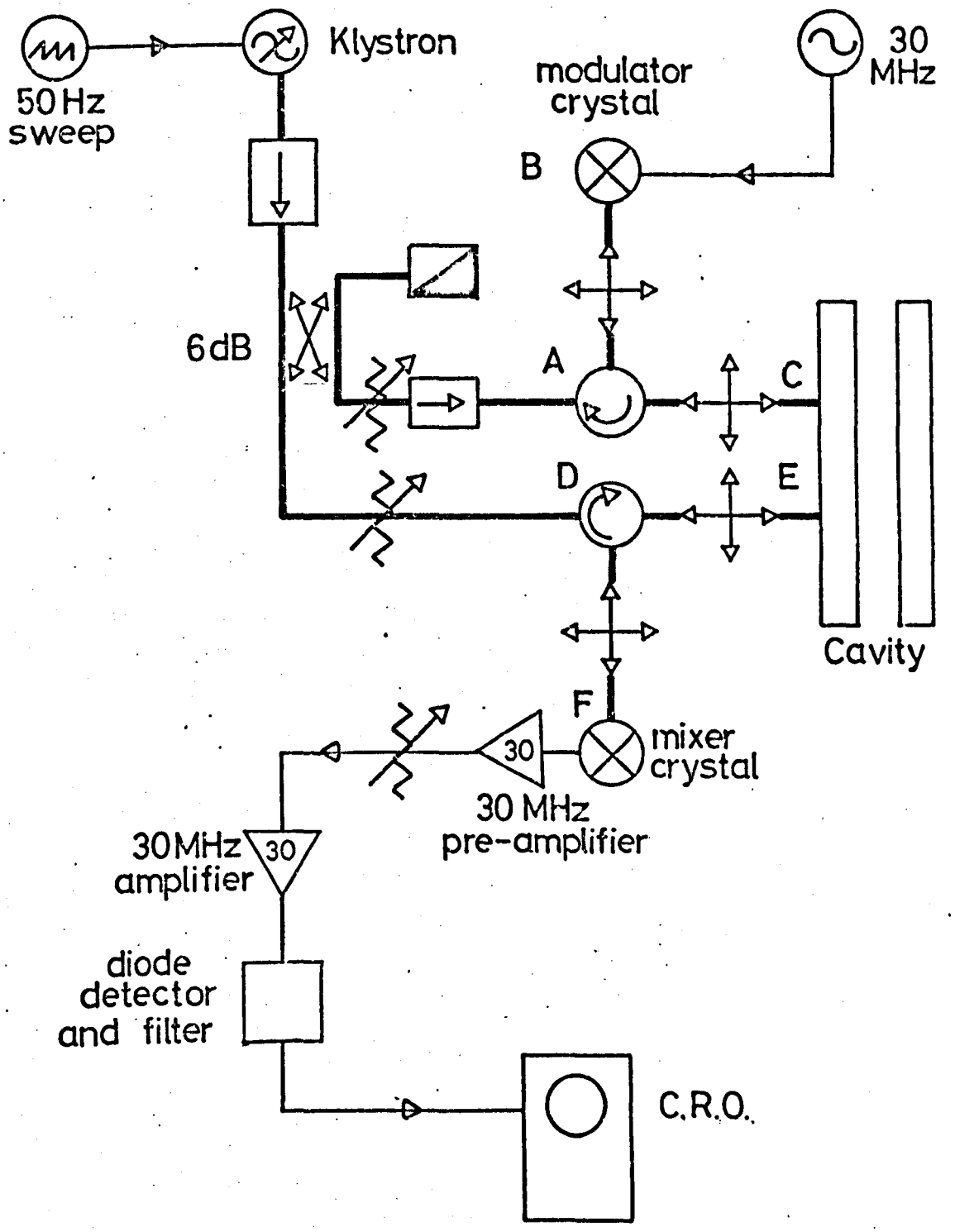

Fig. 3.9 The transmission detection circuit

30 MHz by a R.F. generator so that 30 MHz sidebands are impressed on the power reflected from it. The frequency of the klystron is such that one of these sidebands occurs at the frequency of the maser transition. The reflected and sideband signals pass via the circulator to the cavity input port C. Since the cavity is tuned to the maser transition frequency, only the sideband at this frequency enters the cavity and provides the stimulation signal for the maser.

Power from the klystron also passes via an attenuator and circulator D to the cavity output port E. Since the cavity is not tuned to the klystron frequency, all this power is reflected by the cavity coupling iris and arrives via the circulator D at the mixer crystal F. It provides the L.O. power for the mixer. At the same time, a signal from the maser is coupled out of the cavity at port E and also appears at the mixer crystal F. The output from the mixer is a signal at 30 MHz whose amplitude is proportional to the amplitude of the maser signal.

The 30 MHz signal is amplified by the two I.F. amplifiers. It is detected by the diode detector and filtered by an R-C filter before being displayed on the oscilloscope. If the diode detector has a linear characteristic, this display is proportional to the maser signal amplitude. With a 50 Hz sawtooth sweep applied to the klystron reflector the stimulating signal is frequency swept through the maser transition, enabling all four modes of display described in Sec. 3.3.5 to be employed.

3.3.3 The Microwave Bridge Detection Scheme

The microwave bridge circuit shown in Fig. 3.10 is due to Herrmann and Bonanomi, 1956 and is widely used as a maser detection system. Its operation is similar in principle to the circuit just described but the sideband modulation and mixer detection both occur in the same part of

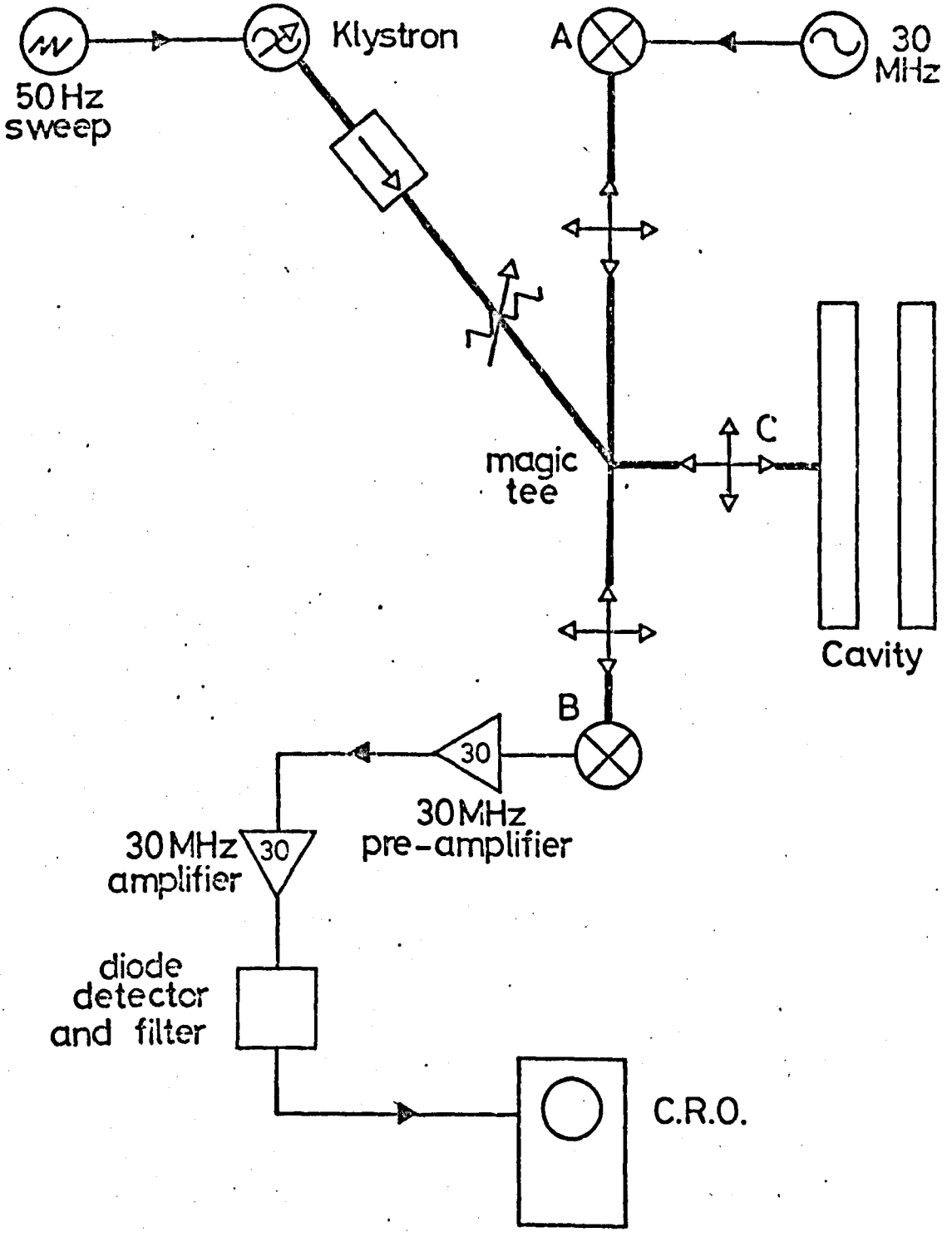

Fig. 3.10. The microwave bridge detection circuit

the microwave circuit and the maser signal is observed in reflection from the cavity port. The operation of this circuit is described with reference to Fig. 3.10.

Power from the klystron at the L.O. frequency is split by the magic tee between arms A and B of the bridge. Sidebands are formed by reflection at the modulator crystal in arm A. The reflected power from A splits between the klystron arm of the bridge and arm C where it falls on the cavity coupling hole. Power in the sideband at the maser frequency is coupled into the cavity and provides the stimulating signal. The signal from the maser is coupled out of the cavity at the same hole and splits between arms A and B. In arm B it falls, with the local oscillator signal from the klystron, on the mixer crystal. The 30 MHz signal from the mixer is amplified and detected as before.

With this circuit the second sideband signal is also present in the bridge and provides a steady 30 MHz signal from the mixer crystal. This biases the diode detector into the linear part of its characteristic so that correction for the non-linear region is unnecessary. However it has two disadvantages: the maser signal splits between two arms of the bridge so that approximately 3 dB of it is lost; and noise carried in the second sideband is also present at the I.F.

The microwave bridge was employed in this work when the signals from the two cavity ports had to be monitored separately and simultaneously (see Chap. 6). Two identical detection systems were used in the circuit shown in Fig. 3.11 and the two output signals were displayed on a double beam oscilloscope.

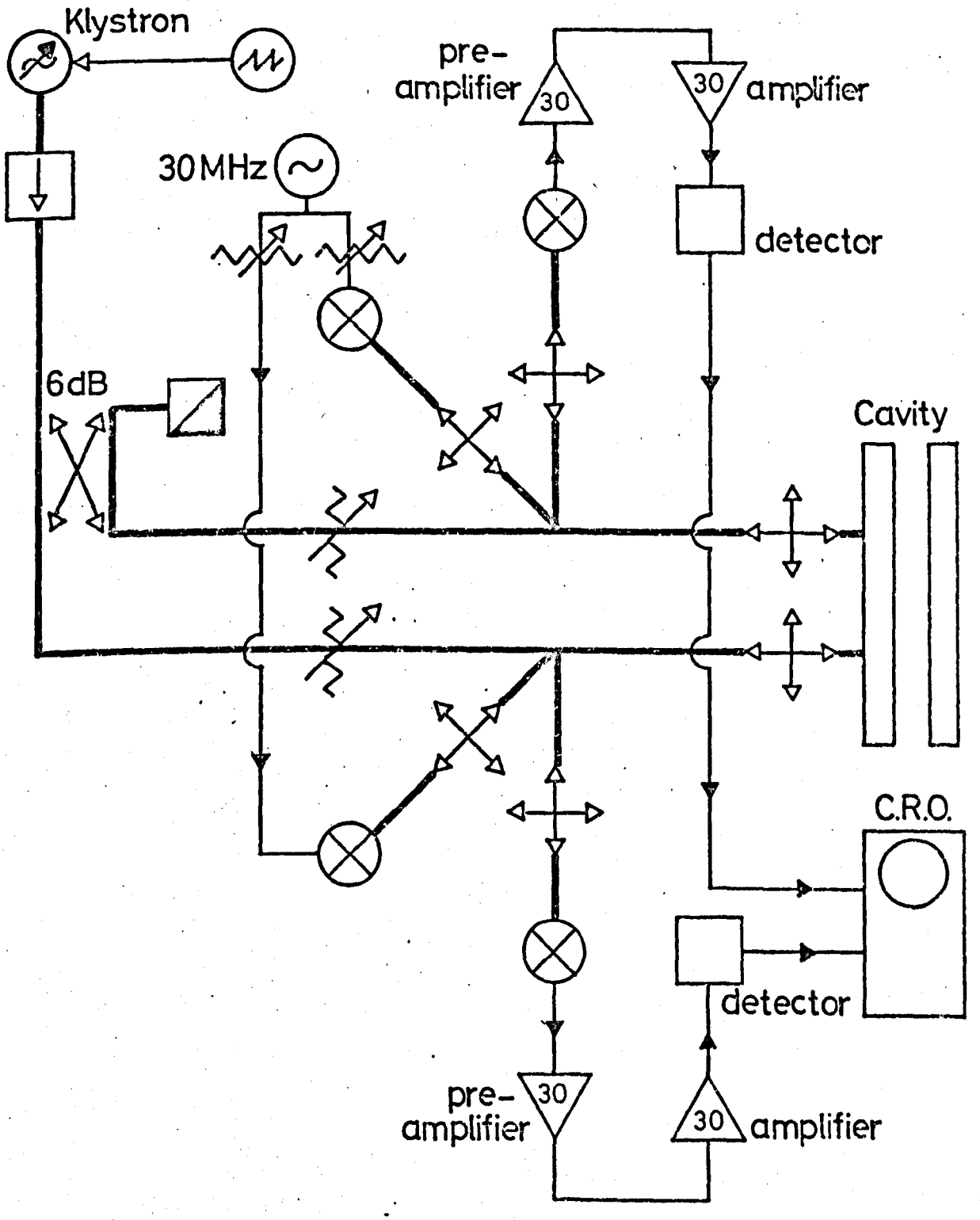

Fig. 3.11. Double microwave bridge detection circuit.

3.3.4 A Novel Phase Sensitive Detection Scheme.

A detection scheme, involving a phase sensitive detector (P.S.D.) at the I.F. instead of a diode detector, was designed for use where linear detection at very small signal levels was required, but no stray sideband signal could be tolerated. It was employed throughout the measurements of maser gain described in Chap. 4. Fig. 3.12 shows the circuit of the P.S.D. scheme and it will be described with reference to this figure.

The klystron is stabilised at the L.O. frequency by means of a phase-lock loop. A 5 MHz variable crystal oscillator is multiplied to 450 MHz in a multiplier chain (Micro Now model 101C) and then applied to a step recovery diode (Hewlett-Packard 33004A). The 53rd harmonic generated by the diode at approximately 24000 MHz is mixed with the klystron signal at the L.O. frequency in a 1N26A crystal mixer, to produce a signal at 60 MHz. This signal is amplified and phase compared with a local 60 MHz crystal oscillator in the frequency stabiliser (Micro Now model 202) and the difference signal is applied to the klystron reflector. This system is capable of stabilising the klystron frequency to within the maser linewidth for periods of the order of 10 minutes.

The rest of the microwave circuit is similar to that used in the transmission detection scheme of Sec. 3.3.2 except for the microwave phase shifter, A. Clearly this alters the phase both of the power incident on the modulator crystal, B and of the power reflected from the crystal. Its net effect is to shift the phase of the stimulating sideband entering the cavity port, C, and therefore of the signal arriving at the mixer crystal, D, with respect to the Klystron L.O. signal and the 30 MHz generator, E. It may be shown that the 30 MHz I.F. signal arriving at F is thereby shifted in phase with respect to the reference signal at G, which is derived from the

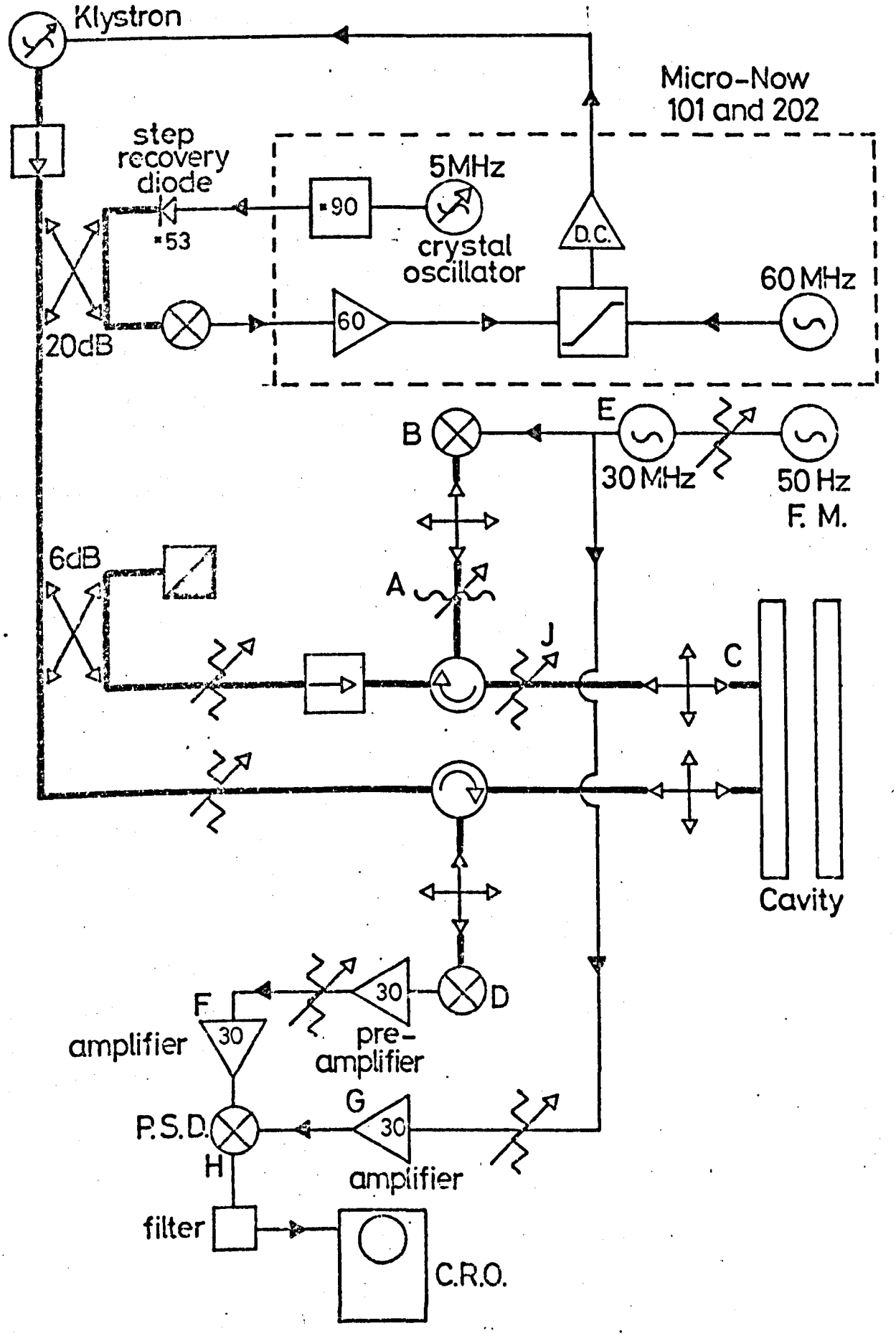

Fig 3.12 The phase sensitive detection circuit.

generator E. The P.S.D., H, provides linear detection of the signal when the phase shifter A is set so that the 30 MHz signals at F and G are in phase. This setting is generally quite simple since it merely involves setting A for maximum signal from the P.S.D. It is convenient to apply a small frequency modulation at 50 Hz to the 30 MHz generator E in order to sweep the maser line for display purposes.

The P.S.D. used in this scheme was a Hatfield MD4 diode bridge. The linearity of the detector was carefully checked by changing the level of the signal at the I.F. using a calibrated attenuator. The linearity of the mixer and detector together were also checked by comparing the output from the P.S.D. with the level of the sideband microwave signal entering port C. This signal level was altered by means of the calibrated attenuator, J. No departure from linearity could be detected in either set of measurements. The calibrated attenuator, J was also used throughout the amplification measurements described in Chap. 4, to alter the level of the input stimulating signal.

3.3.5 Modes of Display of the Maser Signal

There are four modes of display which are commonly used to observe the maser signal. These may be classified according to the level of excitation of the maser and whether or not a stimulating signal is present. They are described in turn in this section with reference to the three detection schemes of Secs. 3.3.2 - 3.3.4.

3.3.5.1 Spectroscopic Mode

Here the maser is operated below its oscillation threshold, and a stimulating signal is swept slowly through the spectral lines of the maser transition. If the input signal is sufficiently small, then the

output from the maser is proportional to the available gain and represents the spectrum of the maser transition. In order to observe weak transitions in the spectrum with a satisfactory signal to noise ratio, the input signal is often increased so that the most intense spectral lines are saturated. The observed intensities of the spectral components are not proportional to their natural intensities but are modified by the process of state separation (Gordon, 1955).

This mode of display may be used with all three of the detection schemes described here. The stimulating signal is the appropriate klystron sideband which is swept in frequency through the maser transitions either by modulating the klystron reflector or by frequency modulating the 30 MHz sideband generator. The sweep repetition rate is usually 50 Hz. The intensity of the stimulating signal is adjusted to give the required display on the oscilloscope screen. Fig. 3.13(a) is a spectroscopic display of the J = 3, K = 3 transition of ammonia showing the main line and the quadrupole satellites.

3.3.5.2 Molecular Ringing

If the main line of the maser transition is observed in the spectroscopic mode under conditions close to the oscillation threshold and/or at a high rate of scan through the line, then molecular ringing may be observed. Molecular ringing occurs when an assembly of molecules has been subjected to a driving electromagnetic field. When the field is removed, the assembly continues to radiate for a finite time (Bloom, 1956). Under the highly regenerative conditions of a maser close to oscillation threshold, this effect is particularly prominent and the maser may continue to radiate for many milliseconds after the removal of the field.

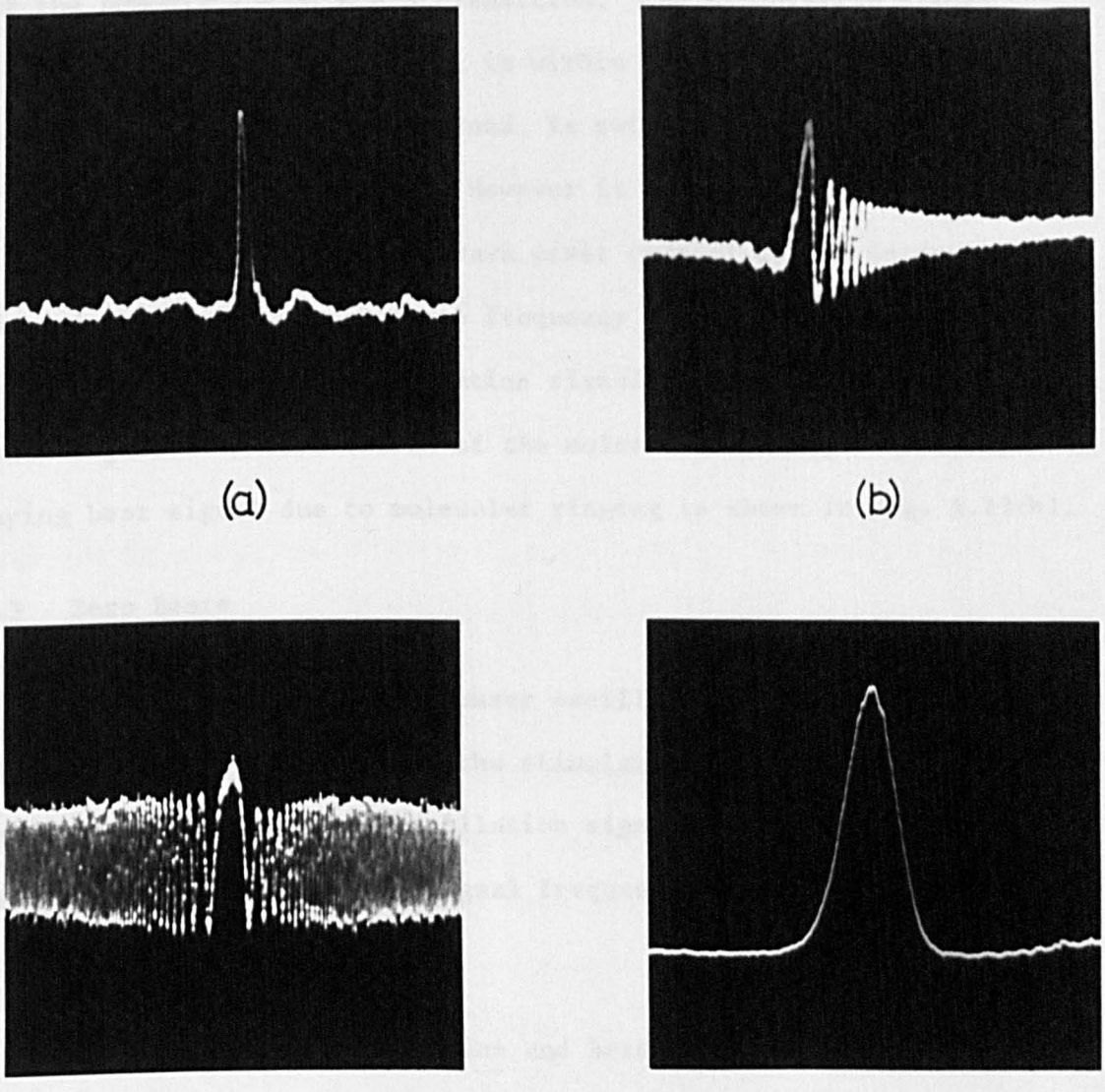

Fig. 3.13 Photographs to illustrate the four display modes.
(a) spectroscopic mode (b) molecular ringing
(c) zero beats (d) bandpass display

Molecular ringing may be observed with all three methods of detection if the stimulating signal is swept rapidly through the main line of the ammonia J = 3, K = 3 transition. The stimulating signal behaves as a driving field while it is within the linewidth, but as far as the molecular assembly is concerned, is switched off when it no longer lies within the linewidth. However it beats with the decaying signal from the maser in the microwave mixer crystal of the detection system, and provides a signal whose frequency is proportional to the frequency separation of the stimulation signal and the maser transition. This beat signal aids observation of the molecular ringing. An example of a decaying beat signal due to molecular ringing is shown in Fig. 3.13(b).

3.3.5.3 Zero Beats

A useful way to observe maser oscillations consists in providing a swept signal, such as the stimulating signal described in (a) and (b) above, with which the oscillation signal beats. As the swept signal passes through the maser signal frequency the condition known as zero beats is obtained.

When using the transmission and bridge detection schemes of Secs. 3.3.2 and 3.3.3 the swept signal is the stimulating signal. The maser oscillation as observed in this detection mode is not completely independent of this signal; indeed if the amplitude of the stimulating signal is large, complete quenching of the oscillation may occur as the signal passes through the zero beat condition (Lainé, 1967). If the P.S.D. detection scheme of Sec. 3.3.3 is employed, however, no stimulating signal need be present. Beats occur between the P.S.D. reference signal and the I.F. signal from the maser oscillation. In order to sweep through the zero beat condition the reference may be swept by frequency modulating

the 30 MHz signal generator. An example of the zero beats method of display is shown in Fig. 3.13(c).

3.3.5.4 I.F. Bandpass Display

The amplitude of oscillation of the maser is often measured by a method of display which involves tracing out the I.F. amplifier bandpass with the I.F. signal derived from the maser oscillator. If the local oscillator is swept through a frequency range greater than the amplifier bandpass, then the output signal from the mixer passes through the range of frequencies accepted by the amplifier. The output from the detector is a display of the frequency response of the I.F. system, and the height of the response curve is proportional to the maser oscillation amplitude.

An example of such a display is shown in Fig. 3.13(d). It may only be obtained with the transmission and bridge detection schemes of Secs. 3.3.2 and 3.3.3 which employ diode detectors. The phase shifts associated with a bandpass amplifier prevent it from being used with the phase sensitive detection scheme of Sec. 3.3.4.

3.4 CHARACTERISTICS OF THE MASER

3.4.1 The Oscillation Amplitude Characteristics

The way in which the amplitude of oscillation of a maser varies with the two parameters, pressure behind the nozzle and voltage applied to the state separator, is well known (Barnes, 1959). It may usefully be represented by a 3-dimensional surface, whose height above

the plane containing the axes of pressure and voltage represents the oscillation amplitude (Bardo, 1969). The curve in which the surface intersects the plane is then the locus of values of pressure and voltage for which the maser just starts to oscillate, i.e. the oscillation threshold curve.

The characteristics measured for the 33 hole nozzle array and the parallel ladder state separator are shown in Figs. 3.14 and 3.15. In Fig. 3.14 the oscillation amplitude is plotted against state separator voltage for various values of nozzle pressure, and in Fig. 3.15 against nozzle pressure for values of separator voltage. These two families of curves give a complete picture of the oscillation behaviour of the maser when the geometrical parameters of the maser components are fixed. The oscillation amplitude was measured using the transmission detection scheme and the I.F. bandpass display mode. The non-linear region in the detector characteristic (See Sec. 3.3.2) has not been corrected for in these graphs, but this does not invalidate the conclusions drawn from them.

The saturation behaviour of the oscillation amplitude with nozzle pressure is demonstrated in Fig. 3.15. On this graph is also plotted the background pressure in the vacuum chamber. It is clear that saturation occurs for background pressures of the order of 5×10^{-6} torr which corresponds to a mean free path for ammonia molecules of about 15 metres. It is inconceivable that the saturation can be due to collisions of the molecular beam with background molecules, so that it must indicate collision within the separator itself. A separator of more open design is therefore indicated. The tapered separator described in Sec. 2.5.2 is evaluated in Sec. 3.4.3. An interesting feature of the amplitude/pressure

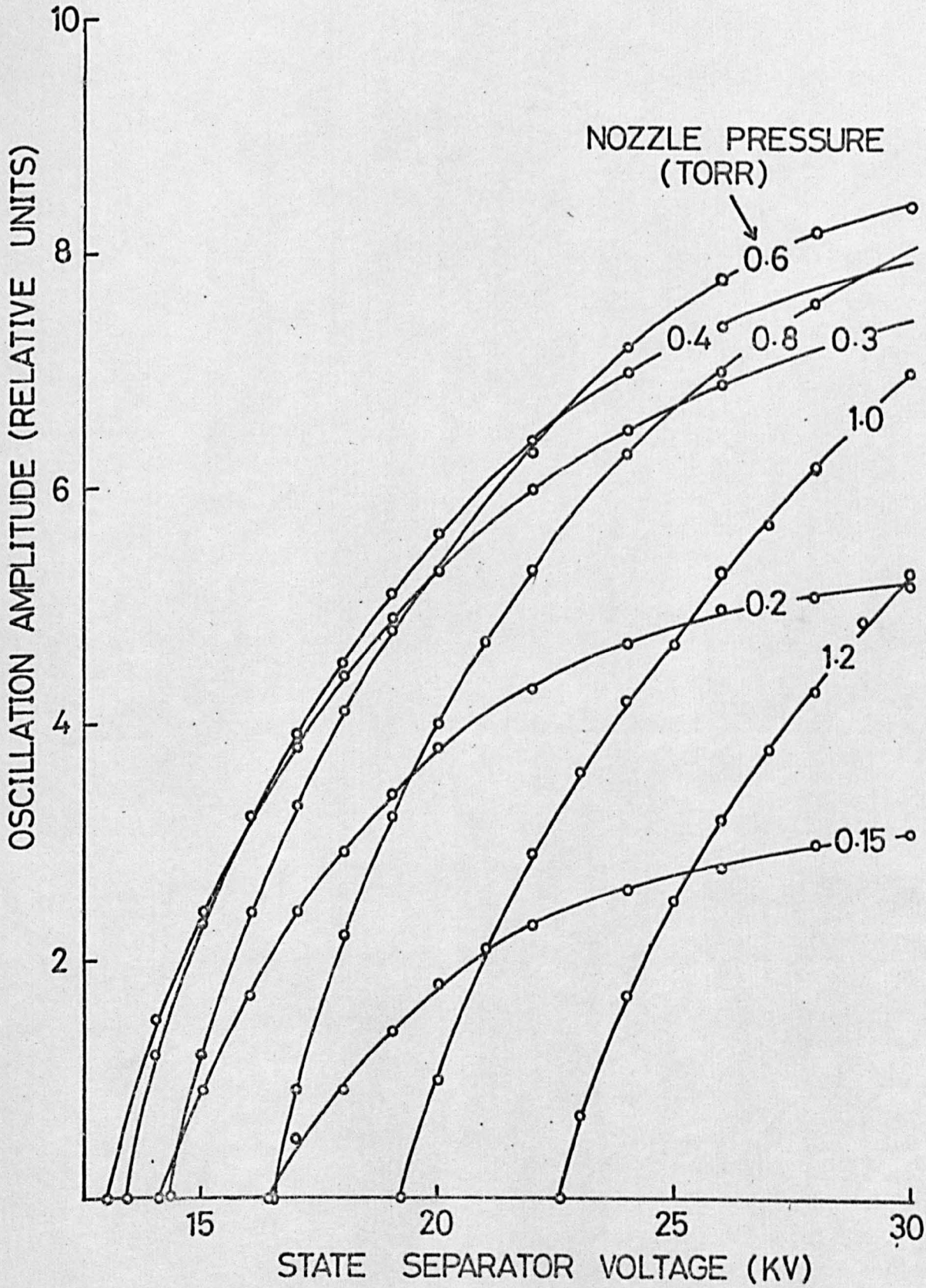

Fig. 3.14 Oscillation amplitude characteristics

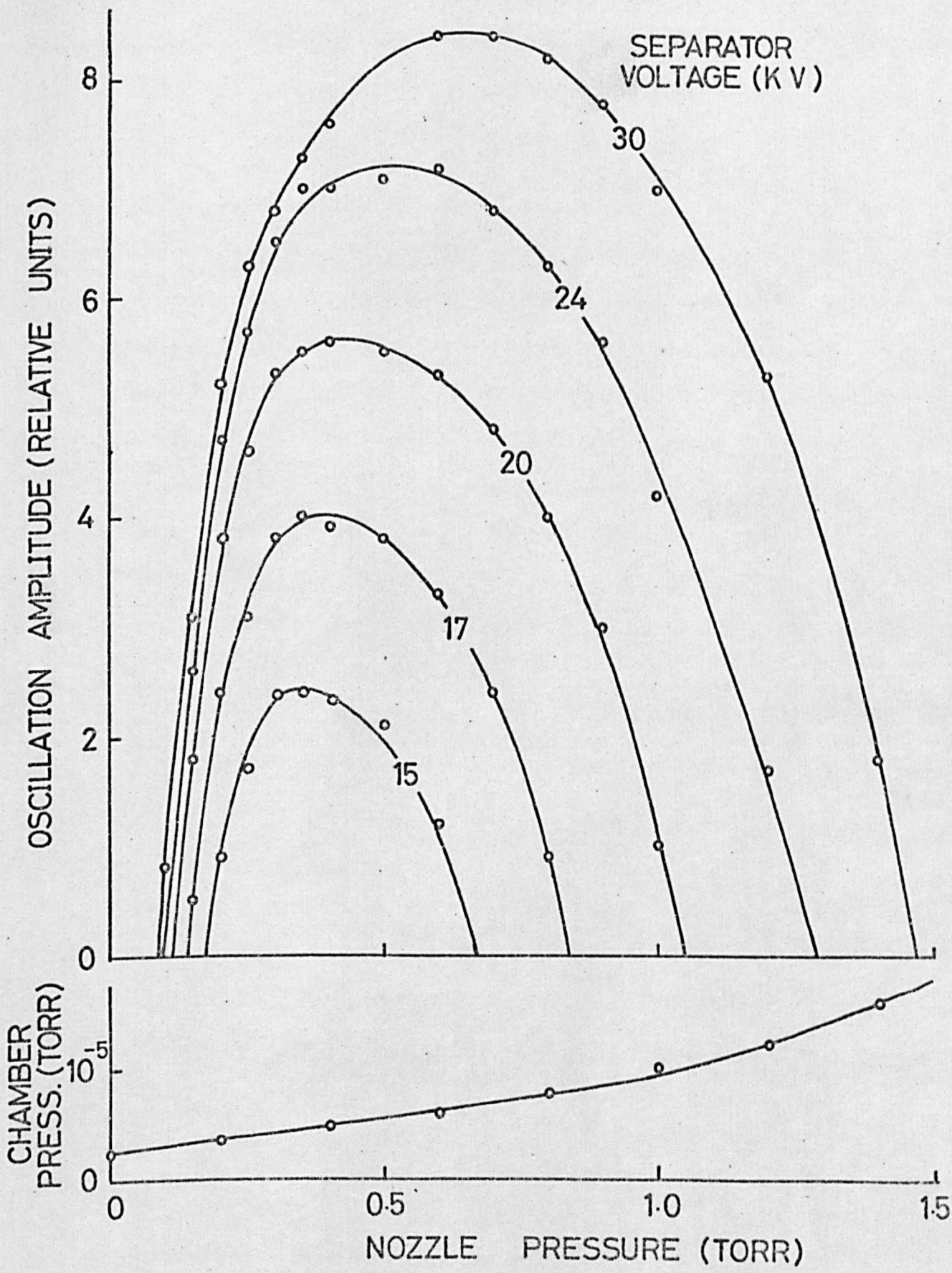

Fig 3.15 Oscillation amplitude characteristics and vacuum chamber background pressure.

characteristic is the shift of the saturation pressure to higher values as the separator voltage increases. The state separator is able to clear a larger input flux of molecules without being choked by molecular collisions, as the separator voltage increases.

The two most useful indicators of the efficiency of a state separator are the oscillation threshold voltage and the amplitude of oscillation of the maser. If comparisons between state separators are required over a period of time the former is generally used because it does not require the properties of the detection system to remain the same for the duration of the comparisons. With the Fabry-Pérot maser it is important that the cavity be carefully tuned when such comparisons are to be made. Variation in the Q-value of the cavity will affect the values of threshold voltage measured. For this reason the best threshold obtained for a state separator is not always reproducible with the Fabry-Pérot maser. For the parallel ladder separator the best threshold obtained was 12.8 KV at a nozzle pressure of 0.35 torr. Maximum amplitude of oscillation at 30 KV was obtained with 0.65 torr behind the nozzle.

3.4.2 Nozzle Position

The only aspect of the maser geometry which it was convenient to make variable was the position of the nozzle unit in relation to the diaphragm between the vacuum chambers. This controls the angular spread of the beam emerging into the main chamber, but at the same time alters the input flux of molecules to the state separator. The nozzle position and the pressure behind the nozzle are therefore not independent of one another.

Families of curves were plotted to establish the optimum combination of pressure and nozzle position. Two such families are

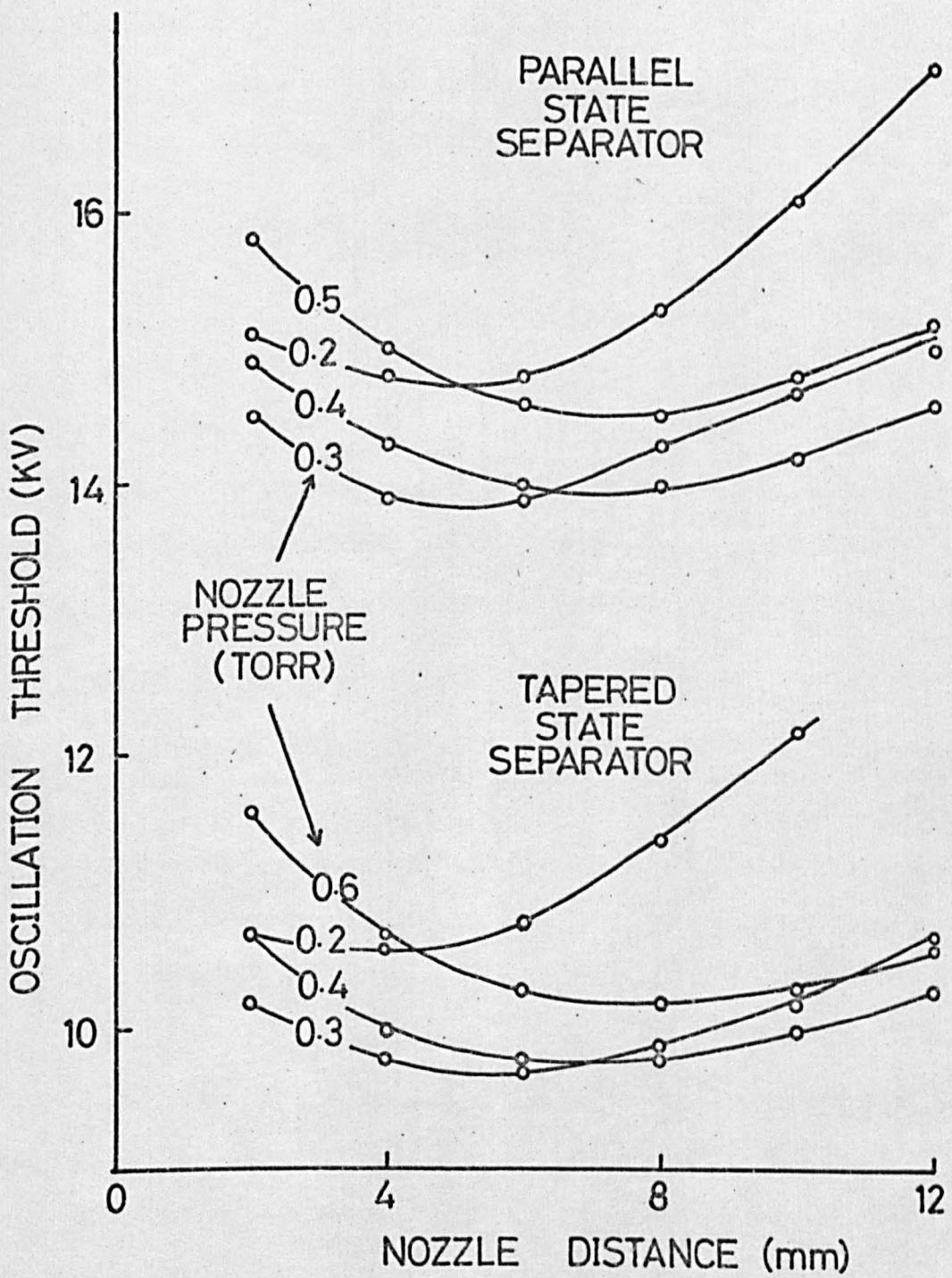

Fig. 3.16 Oscillation threshold voltage plotted against the distance of the nozzle behind the diaphragm for two state separators.

shown in Fig. 3.16 where the lowest oscillation threshold is used as the criterion for establishing the optimum operating conditions. The two families correspond to the parallel and tapered state separators. The optimum nozzle position for both separators was found to be 6 mm behind the diaphragm. This position was also observed to be optimum at high levels of oscillation.

3.4.3 Comparison of Two State Separators

The tapered state separator was constructed towards the end of the project in an effort to achieve higher beam fluxes so that the maser would oscillate in the TEM_{10} mode of the cavity. This mode had a Q of only 1700. In this respect it was unsuccessful but it nevertheless showed that considerable improvements are possible in the performance of the maser by careful design of the state separator.

The separator has been described in Secs. 2.3.2 and 2.3.3, but a few aspects of its design will be highlighted here. The electrode separation of the ladder arrays was smaller than that of the parallel separator (3.2 mm. instead of 4.0 mm.) and since the electrode thickness was the same - (1.6 mm.) the transparency of the tapered separator was poorer than that of the parallel type. The distance between the electrode banks at the entry to the separator was 1.6 mm. - only half that of the parallel separator so that the number of molecules entering it at a given nozzle pressure was also halved. In view of this, it is surprising that the oscillation amplitude obtained with the tapered separator was much higher than that obtained with the parallel separator.

Their oscillation amplitude characteristics, corrected for detector non-linearity, are shown plotted on the same relative amplitude

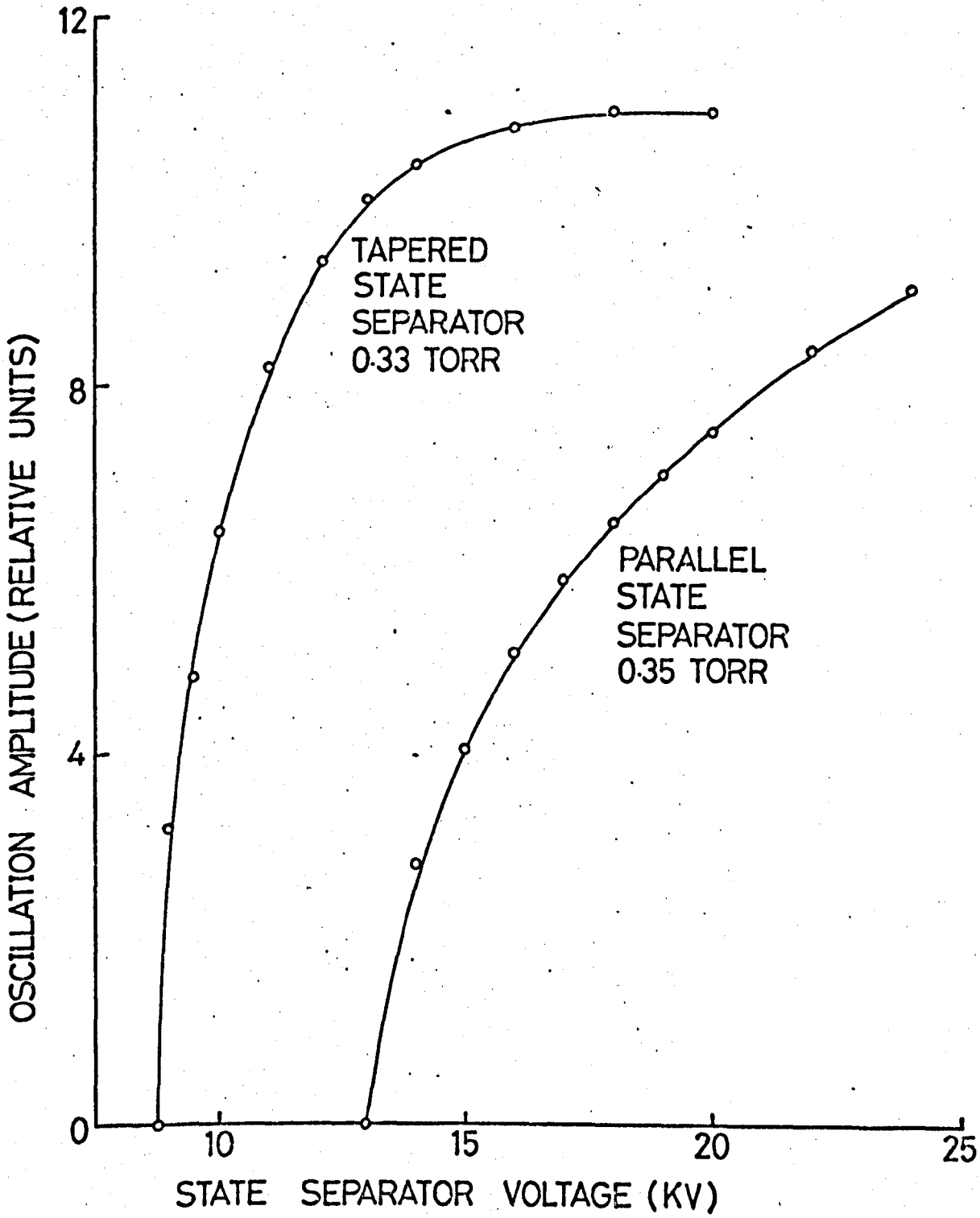

Fig. 3.17 Comparison of oscillation amplitude for two state separators.

scale in Fig. 3.17. The curve corresponding to the tapered separator shows a saturation behaviour for voltages above about 18 KV. This is probably a further consequence of its small angle of capture, in that when the critical velocity of Eqn. 2.9 is greater than the transverse velocity v_y of the majority of molecules entering the separator, no more molecules are available to be focussed as the voltage is increased. Becker, 1963B has also noticed a saturation behaviour with ladder separators, and particularly with tapered ladder separators.

Fig. 3.18 shows a comparison between the threshold curves of the two state separators. These measurements do not represent the best threshold values achieved, which were 8.2 KV for the tapered separator and 12.8 KV for the parallel separator.

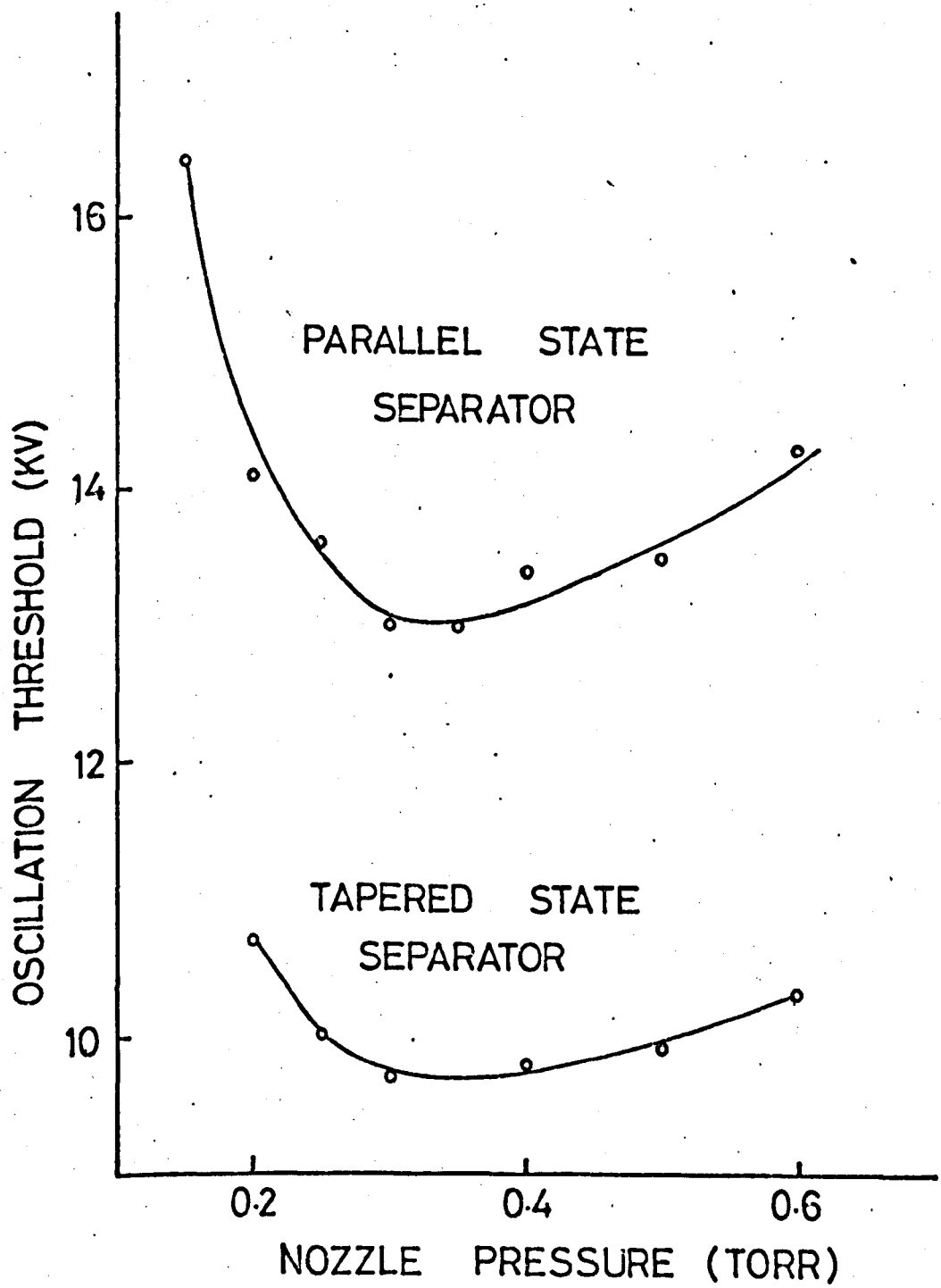

Fig 3.18 Comparison of oscillation threshold voltage for two state separators.

CHAPTER 4

THE MASER AS AN AMPLIFIER

4.1 INTRODUCTION

A molecular beam maser acts as a sensitive high gain amplifier if it is operated under regenerative conditions close to its threshold of oscillation (Gordon et al, 1955). Stable gains in excess of 50 dB can be achieved with an ammonia beam maser (Collier and Wilmshurst, 1966) and noise figures close to unity have been measured (Alsop et al, 1957; Gordon and White, 1958). The frequency of a beam maser is dictated by the molecular transition on which it is operated. Its bandwidth is primarily determined by the average time of flight of a molecule through the cavity and for a typical ammonia beam maser is 5 KHz. However under regenerative conditions it may be narrowed to as little as 100 Hz (Helmer, 1957; Zuev and Cheremiskin, 1962). An ammonia beam maser saturates at an output power of about 10^{-9} W (Collier and Wilmshurst, 1966) and linear amplification is only possible well below saturation. For these reasons its usefulness as a practical amplifier is somewhat limited.

However, the beam maser has been employed as an amplifier in a few specific instances. In the noise measurements performed by Gordon and White, 1958 on an ammonia maser, a second maser was used to amplify the noise output from the first. In experiments which employ a second

cavity to examine the molecular beam emerging from the first, the second cavity may be regarded as a maser amplifier for the polarisation signal impressed on the beam (Lainé and Bardo, 1971). A particularly interesting application of the ammonia maser amplifier, in which the input signal was not derived from the same or another maser, was its employment as a pre-amplifier to improve the signal-to-noise ratio of an electron spin resonance spectrometer (Gambling and Wilmshurst, 1964; Collier and Wilmshurst, 1966).

The most widespread use of molecular beam masers is for spectroscopy on the maser material. In a maser spectrometer the amplifying properties of the maser are employed to examine the structure of a spectral line. An input signal is swept past the molecular resonance frequency so that the output signal traces the molecular amplifier response. Historically, the first such application for a maser was by Gordon, 1955 to examine the hyperfine structure of the ammonia inversion spectrum. Since that time the maser has been used as a spectrometer to investigate a number of different materials. A comprehensive list of spectral lines examined is given by Lainé, 1970.

In the present work the behaviour of the Fabry-Pérot maser as an amplifier was investigated as a preliminary to examination of its behaviour as an oscillator. The possibility of operation of this type of maser in more than one mode can be explored in a controlled manner when it is run as an amplifier. The purpose of this chapter is to present and interpret the experimental work which was performed on the Fabry-Pérot maser under conditions of amplification.

In Sec. 4.2 a simple theory of the maser amplifier is presented and used to derive the amplification factor and the excitation parameter of

the maser. The measurement of the amplification factor is described and some of the experimental results obtained with the maser are given. In Sec. 4.3 the possibility of making measurements of the amplification factor in more than one direction in the cavity is discussed. It is seen how such measurements can yield information about the molecular beam. Finally some deductions which concern the transition from amplification to oscillation are made.

4.2 EXCITATION IN A SINGLE MODE

4.2.1 Simple Theory of the Maser Amplifier.

Although the J = 3, K = 3 transition of ammonia is complicated by the presence of the quadrupole interaction of the nitrogen nucleus and the magnetic interactions of the hydrogen nuclei, for most purposes the ammonia beam maser may be regarded as a two level system. Some departures from this simple description are considered in Chapter 5 where the behaviour of the maser in the presence of magnetic fields is discussed. In this section, however, only two levels, upper and lower denoted by the subscripts 1 and 2 respectively are assumed.

In the presence of a radiation field $E\cos(2\pi\nu t)$ the probability that a molecule in one of the two states will make a transition to the other is given by Wittke, 1957 as

$$S = \frac{(pE/h)^2}{(\nu-\nu_o)^2+ (pE/h)^2} \sin^2\{\pi[(\nu-\nu_o)^2+ (pE/h)^2]^{\frac{1}{2}}t\} \qquad 4.1$$

where p is the electric dipole matrix element connecting the two states

and $\nu_o = (W_1-W_2)/h$ is the transition frequency between the two energy levels.

In the simple theory of the molecular beam maser, a beam of molecules in state 1 and all having velocity v, are considered to pass through a region of uniform radiation field amplitude E having length L in the direction of travel of the molecules. The microwave power emitted by the molecules is then given by

$$P = Nh\nu_o \frac{(pE/h)^2}{(\nu-\nu_o)^2+ (pE/h)^2} \sin^2\{\pi[(\nu-\nu_o)^2 + (pE/h)^2]^{\frac{1}{2}}L/v\} \qquad 4.2$$

where N is the number of upper state molecules passing through the region in unit time, or more correctly the difference $N_1 - N_2$ of the populations in the upper and lower states.

In order to describe a real maser, a suitable average of the electric field distribution weighted by the volume distribution of the molecules in the cavity must be used in place of E. Moreover, in order to take the non-uniform velocity distribution of the molecules into account, Eqn. 4.2 must be integrated over this distribution (Shimoda, Wang and Townes, 1956). For many purposes, however, it is sufficient to use the simple description given by Eqn. 4.2 and it will be used here without further justification.

Eqn. 4.2 describes the magnitude and spectral line shape of the power emitted by the molecular system, in terms of the amplitude E and frequency ν of the radiation field. At the centre of the spectral line, $\nu = \nu_o$ and Eqn 4.2 becomes

$$P = Nh\nu_o \sin^2(\pi LpE/hv) \qquad 4.3$$

The power P is emitted in phase with the radiation field E and therefore itself contributes an amount E_o to the radiation field where

$$P = \nu_o V E_o^2 / 4Q \qquad 4.4$$

In this equation V represents the cavity volume and Q the cavity Q factor. Thus E is made up of two contributions, E_i due to the power input to the cavity and E_o due to the molecules:

$$E = E_i + E_o \qquad 4.5$$

In an oscillating maser, E_i is absent and the power output from the molecules provides all of the radiation field. The case considered here, however, is that of the maser amplifier where E_i is finite. Combining Eqns. 4.3 - 4.5 to eliminate P and E gives

$$E_i = (h\nu/\pi Lp) \sin^{-1}\{(V/4QNh)^{\frac{1}{2}} E_o\} - E_o \qquad 4.6$$

For sufficiently small E_o ($E_o \ll \{V/4QNh\}^{\frac{1}{2}}$) the approximation $\sin^{-1} x \simeq x$ may be used to write

$$E_i \simeq \left[\frac{\nu}{\pi Lp}\left(\frac{Vh}{4QN}\right)^{\frac{1}{2}} - 1\right] E_o \qquad 4.7$$

Eqn. 4.7 shows that for small input signals the maser behaves as a linear amplifier, whose internal electric field gain K defined by

$$K = (E_o + E_i)/E_i \qquad 4.8$$

is given by

$$K = \frac{1}{1 - 2\pi Lp(QN/Vh)^{\frac{1}{2}}/\nu} \qquad 4.9$$

The internal gain is a useful parameter, because it is independent of the behaviour of the external microwave detection system and of the coupling to the maser cavity. It will be seen in Sec. 4.2.2. that it is possible to measure K directly.

Krupnov and Skvortsov, 1965D employ another parameter, η, which they call the excitation parameter of the maser:

$$\eta = 1 - 1/K \qquad 4.10$$

Substituting for K from Eqn. 4.9 gives

$$\eta = \frac{2\pi Lp}{v}\left(\frac{QN}{Vh}\right)^{\frac{1}{2}} \qquad 4.11$$

so that η shows a particularly simple dependence on N. Also, η lies between zero and unity in the amplification region and equals unity at the oscillation threshold of the maser. From Eqn. 4.11 it is seen that the excitation parameter is also meaningful in the oscillation region although it is not so readily measured. In the Russian literature, η is usually related to the simple univelocity theory of Basov and Prokhorov, 1955A, 1955B.

4.2.2 The Maser Amplifier Characteristics

The useful amplification of the maser depends not only on the internal gain K derived in the previous section, but also on the coupling into and out of the maser. For example, the power gain of a maser with a reflection coupled cavity, coupling coefficient β, is given by

$$G = 4\beta^2K^2/(1 + 2\beta)^2 \qquad 4.12$$

With a transmission cavity having coupling coefficients β_1 and β_2 at the two ports,

$$G = 4\beta_1\beta_2 K^2/(1 + \beta_1 + \beta_2)^2 \qquad 4.13$$

However, with a transmission cavity it is possible to measure K directly, because the output coupling port samples the electric field in the cavity without the complicating presence of the input signal. This means that the microwave amplitude falling on a detector placed in the output waveguide is directly proportional to the amplitude of the electric field in the cavity.

Practical measurement of the midband (i.e. at the spectral line centre) internal amplification factor is straightforward. The upper trace in Fig. 4.1 shows an oscilloscope display of the output signal from the maser when the input signal is swept in frequency through 20 KHz about the maser transition frequency. The signal amplitude off-resonance is a sample of E_i, the cavity field amplitude due to the input signal. This is compared with the signal amplitude observed at line centre which is a sample of $E_i + E_o$, the cavity field amplitude resulting from midband molecular amplification of E_i. The zero signal level for both samples is the level observed on the display when the input microwaves are switched off. In Fig. 4.1 the two measurements which are made are the heights X and Y. If the display is proportional to the microwave electric field amplitude incident on the detector, then the internal amplification factor is given by

$$K = Y/X \qquad 4.14$$

The phase-sensitive detection circuit which was used to make these measurements is described in Sec. 3.3.4 and Fig. 3.12. The

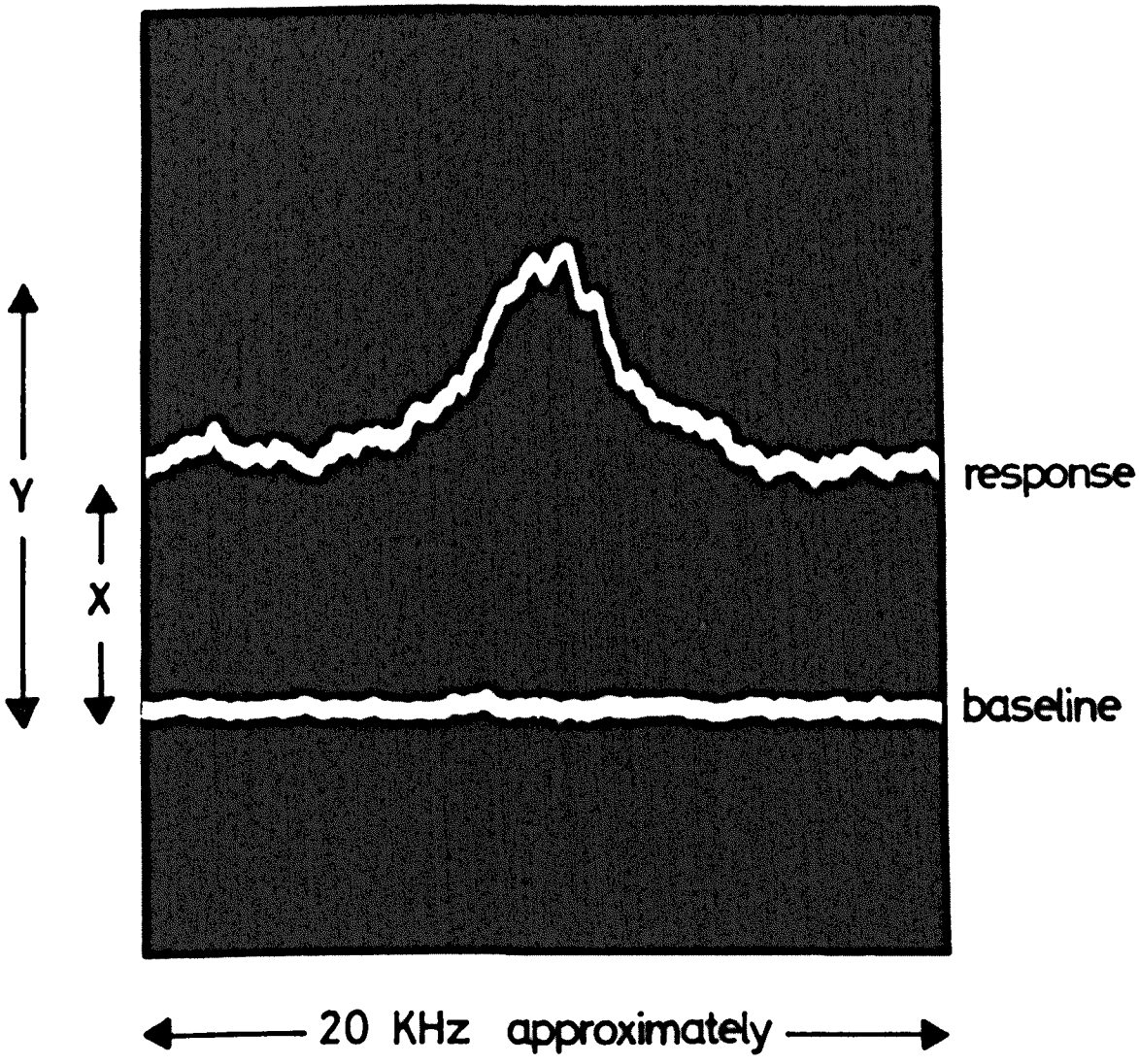

Fig 4.1 Double exposure photograph showing the amplifier response of the maser and the baseline display observed when the input microwave signal is switched off.

calibrated attenuator J shown in this figure was used to change the level of the input signal (one 30 MHz sideband of the stabilized klystron). The signal was swept through the maser transition frequency by frequency modulating the 30 MHz oscillator used to generate the sidebands. A calibrated R.F. attenuator was placed between the I.F. pre-amplifier and amplifier in order to keep the I.F. signal in the dynamic range of the I.F. amplifier and P.S.D.

Fig. 4.2 shows a set of maser amplifier characteristics (plots of Y against X) which were measured in this way. The decibel scales shown on the axes in this graph are referred to an arbitrary voltage (510 mV) at the output of the P.S.D. Absolute measurements in terms of maser output power were not possible because the equipment necessary to calibrate the detection system was not available.

The theoretical curves shown for comparison with the experimental results require some explanation. These have been calculated using the simple theory of Sec. 4.2.1. Eqn 4.6 has the form

$$E_i = A \sin^{-1}(B E_o) - E_o \qquad 4.15$$

where A and B are constants for a given molecular beam flux. B determines the saturation value E_s of the molecular contribution E_o to the electric field amplitude, according to

$$E_s = 1/B \qquad 4.16$$

The function $1/(1-1/AB)$ is the small signal gain of a given characteristic; curves for 10, 20 and 30 dB gain are shown in Fig. 4.2. The measured saturation values of E_o have been used to obtain B in order to plot the theoretical characteristics. This method of normalisation was employed by Collier and Wilmshurst, 1967 in order to make a similar comparison between theory and experiment.

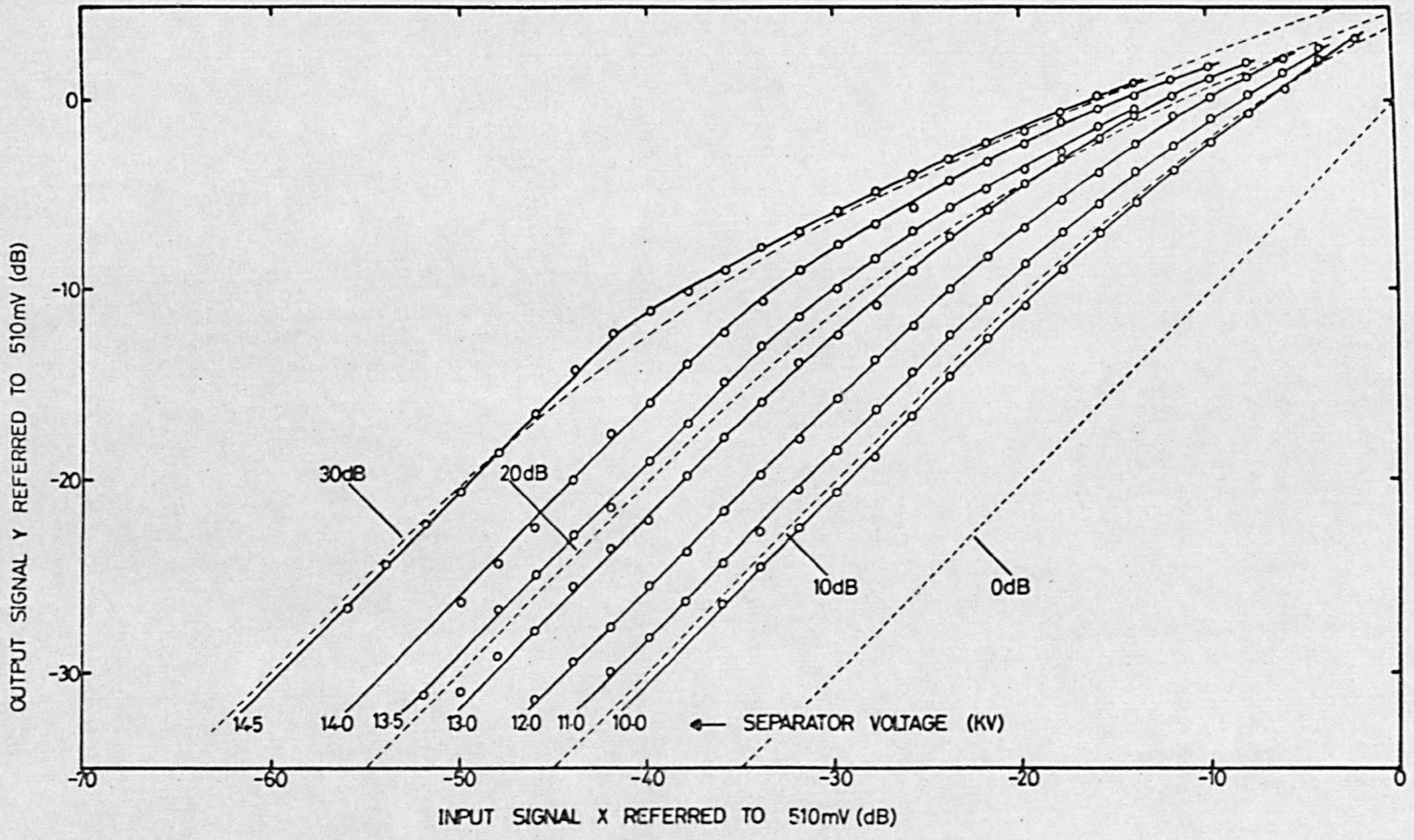

Fig. 4.2 Maser Amplifier Characteristic for the mode direction 0°.

Fig. 4.2 indicates reasonably good agreement between theory and experiment throughout the range of excitation of the maser used in this work (gains between 10 and 30 dB).

4.3 EXCITATION IN OTHER MODES

4.3.1 Linear Modes of the Fabry-Pérot Cavity

Consideration of the circular symmetry of the Fabry-Pérot cavity shows that it must support a given TEM mode with its electric field vector in any direction parallel to the mirrors. Any one such mode can be regarded as derived from an orthogonal pair of linearly polarised, frequency degenerate modes having their electric field vectors perpendicular to one another. In general, any mode which can be derived by combination of this pair of modes with arbitrary amplitude and phase is supported by the cavity. Thus the general case is a TEM mode with elliptical polarisation of its electromagnetic field. This chapter is concerned with those modes whose electromagnetic field is linearly polarised but may have any direction of polarisation in the cavity. Such a mode will be called a linear mode, and the angle which its electric field vector makes with the molecular beam axis will be referred to as the mode direction.

In the maser amplifier the mode direction θ is determined by the direction of polarisation of the stimulating field E_i. This in turn coincides with the direction of the electric field vector in the input waveguide, which for TE_{10} mode propogation is perpendicular to the broad face of the waveguide. In Sec. 1.4.5 it was mentioned

that the construction of the Fabry-Pérot cavity allowed the coupling waveguides to be rotated, so that they could couple with different components of the electric field in the cavity. The diagram in Fig. 4.3 shows the input waveguide A oriented so that it excites the mode direction θ, and the output waveguide B similarly oriented so that it couples most strongly with the same mode. During investigations of the behaviour of the maser as an amplifier, both waveguides always had a common orientation. Some experiments in which the two waveguides were placed in separate orientations are described in Chapter 5.

In Sec. 2.4.2 the orientation of the molecules in the molecular beam was discussed. It was concluded that, on leaving the electric field of the state separator, the molecules are preferentially oriented along the beam axis. This means that the net contribution of all the molecules to the cavity field is greatest when the field is a linear mode whose mode direction is 0°. However, in Sec. 2.4.3 it was pointed out that the preferential orientation of the molecules can be modified by the presence of stray electric or magnetic fields in the region between the state separator and the cavity. The linear modes of the Fabry-Pérot cavity provide a useful means for investigating the preferential orientation of the molecules in the beam. This was recognised by Krupnov and Skvortsov, 1965C who measured the amplification of a formaldehyde maser operating at 72.8 GHz for the mode directions 0° and 90°.

In the present work the maser amplifier characteristics were measured for the mode directions 0°, 45° and 90°. The experimental curves of Fig. 4.2 represent the characteristics for 0°. The small signal internal amplification factor K obtained from each of these characteristics has been plotted against state separator voltage in Fig. 4.4, together

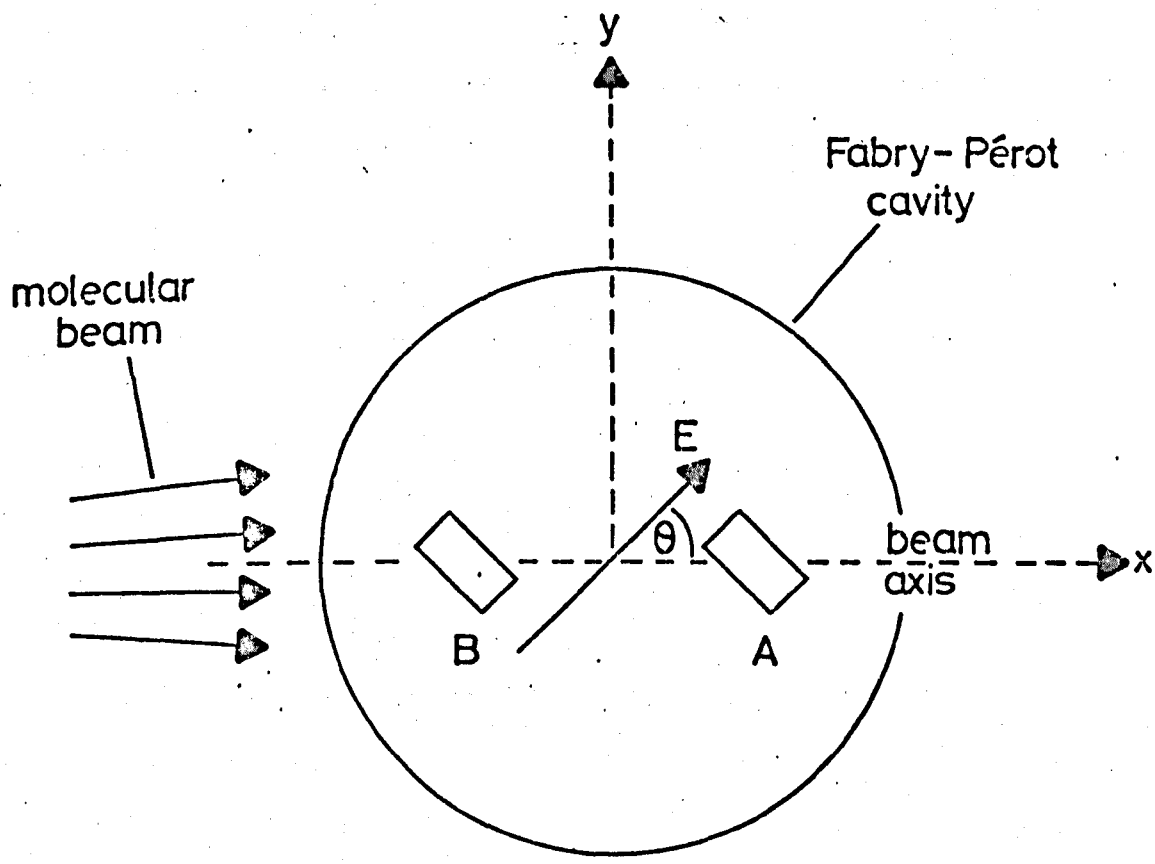

Fig. 4.3 Diagram showing the waveguides A and B oriented to couple most strongly with a linear mode whose electric field vector E makes an angle θ with the molecular beam axis.

with the results from similar characteristics measured for mode directions 45^{o} and 90^{o}. The three curves of Fig. 4.4. show that the amplification factor of the maser is very different for the three orientations. However the results are complicated by the fact that the Q of the cavity is also different (the values measured with the three waveguide orientations are appended to the curves in Fig. 4.4). Since the amplification of the maser depends not only on the effective number of molecules but also on the cavity Q (see Eqn 4.9), these curves cannot be related directly to the preferential orientation of the molecules in the beam. In Sec. 4.3.2 the excitation parameter is normalised to remove the effect of the cavity Q anisotropy.

Another point in relation to Fig. 4.4 is that it is not possible to make meaningful measurements of the amplification of the maser for state separator voltages higher than the voltage at which the maser starts to oscillate. This is because the presence of the oscillation field in the cavity affects the difference in the populations of the two maser levels. This is true even if the oscillation establishes itself in the linear mode orthogonal to that in which the measurements are being made, because many of the molecules radiate into both modes. In fact with the detection scheme used here, it was not possible to make measurements at all unless the two linear modes were orthogonal, because the oscillation field produced a strong beat signal on the oscilloscope display. Thus the curves of Fig. 4.4 do not extend to separator voltages above those at which oscillations were established in the maser, i.e. above 14.8, 13.5 and 12.8 KV respectively for the measurements made with mode directions 0^{o}, 45^{o} and 90^{o}.

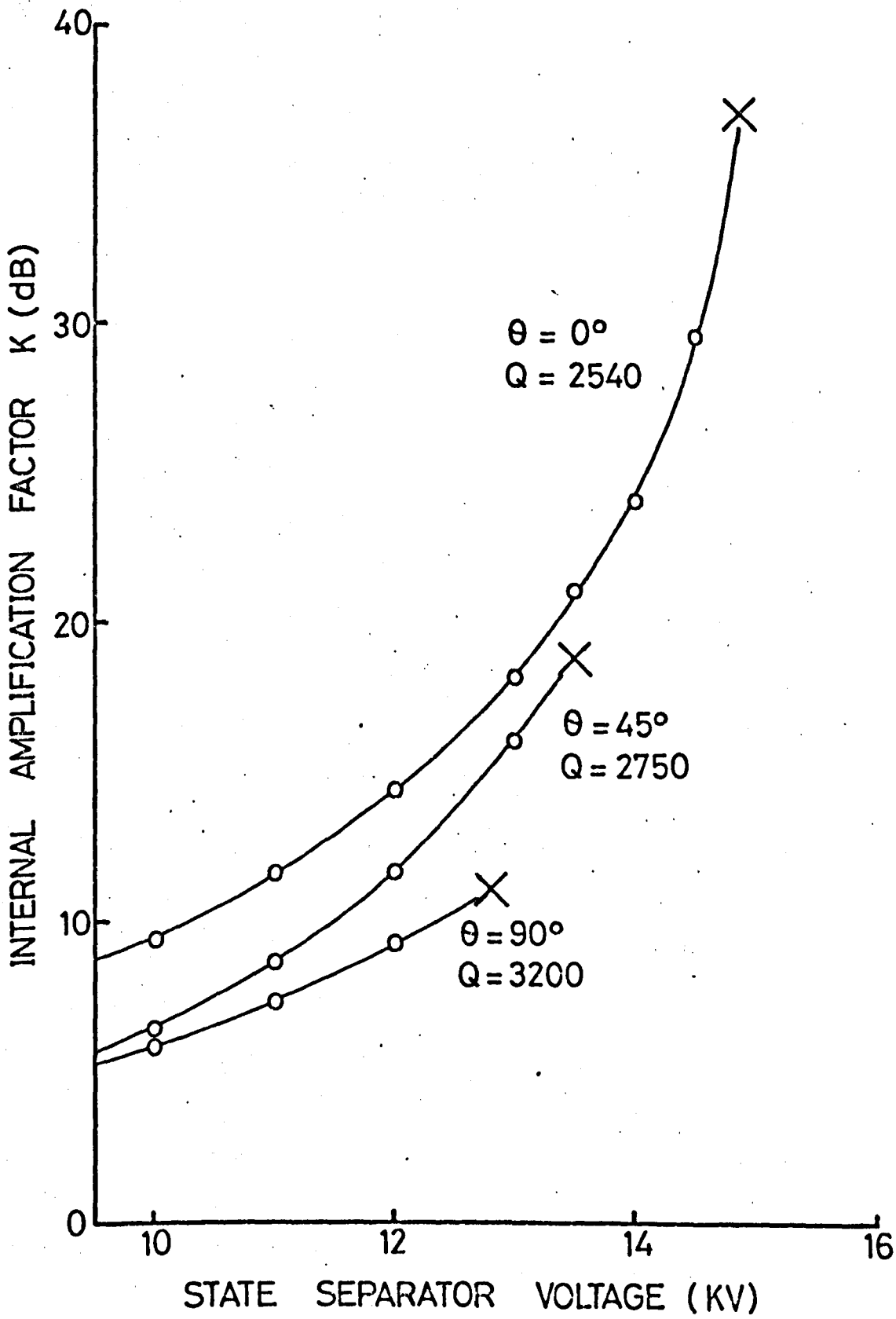

Fig 4.4 Amplification of the maser in three directions θ plotted against separator voltage. The crosses indicate thresholds of oscillation.

4.3.2 Normalisation of η and Preferential Orientation

The excitation parameter η is more simply related to the maser variables N and Q than is the amplification K. For this reason it has been used as a design criterion in some of the Russian work (Krupnov and Skvortsov, 1965B,C,D; Zuev and Cheremiskin, 1962). Krupnov and Skvortsov, 1965B obtained values of η for formaldehyde using a Fabry-Pérot maser in the mode direction 0^o and 90^o. They obtained $\eta(0) = 0.55$ and $\eta(90) = 0.20$, giving a quantitative value to the preferential orientation by using the ratio $\eta(0)/\eta(90) = 2.75$.

In order to measure the amplification factor in the two orientations required, they placed the nozzle and state separator unit in two positions relative to the cavity so that the molecular beam axis made angles of 0^o or 90^o with the electric field vector of the cavity mode. Since the cavity mode remained the same, the cavity Q was unchanged for the two measurements.

In the present work the position of the state separator and cavity were not changed, but the waveguide orientations were altered in order to excite different linear modes. In this case Eqn. 4.11 must be written

$$\eta(\theta) = \frac{2\pi Lp}{v} \left(\frac{Q(\theta)N(\theta)}{Vh}\right)^{\frac{1}{2}} \qquad 4.17$$

where $N(\theta)$ reflects the preferential orientation of the molecules in the beam and $Q(\theta)$ measures the anisotropy of the cavity's Q-factor.

In principle it is possible to obtain the dependence of η on θ experimentally, by coupling to the cavity in different directions θ and measuring the amplification in each direction. In practice $Q(\theta)$ is not uniquely defined during such a series of measurements, because

the nature of the loading presented to the cavity by the coupling holes depends on the waveguide orientations. However, if both the excitation parameter and the loaded Q, Q_ℓ, are measured for each orientation θ, the excitation parameter may be normalised with the help of Eqn. 4.17 to an arbitrary value of Q, Q_o, such that η_o reflects only the variation of N with θ:

$$\eta_o(\theta) = \eta(\theta)\left(\frac{Q_o}{Q_\ell(\theta)}\right)^{\frac{1}{2}} = \frac{2\pi Lp}{v}\left(\frac{Q_o N(\theta)}{Vh}\right)^{\frac{1}{2}} \qquad 4.18$$

In Fig. 4.5 the un-normalised excitation parameter $\eta(\theta)$ has been plotted against the state separator voltage for the three cases $\theta = 0^o$, 45^o and 90^o. The experimental points represent the same measurements as those in Fig. 4.4. The ratios $\eta_o(0)/\eta_o(90)$ and $\eta_o(0)/\eta_o(45)$ obtained from these measurements by normalising η in accordance with Eqn. 4.18 are shown in Table 4.1. The values of $\eta_o(o)/\eta_o(90)$ are found to be very much lower for the ammonia maser operating on the J = 3, K = 3 inversion line than for Krupnov and Skvortsov's formaldehyde maser.

Table 4.1 Normalised excitation parameter ratios for different values of separator voltage, V.

V	$\eta_o(0)/\eta_o(90)$	$\eta_o(0)/\eta_o(45)$
10KV	1.52	1.32
11KV	1.46	1.22
12KV	1.39	1.14
13KV		1.08

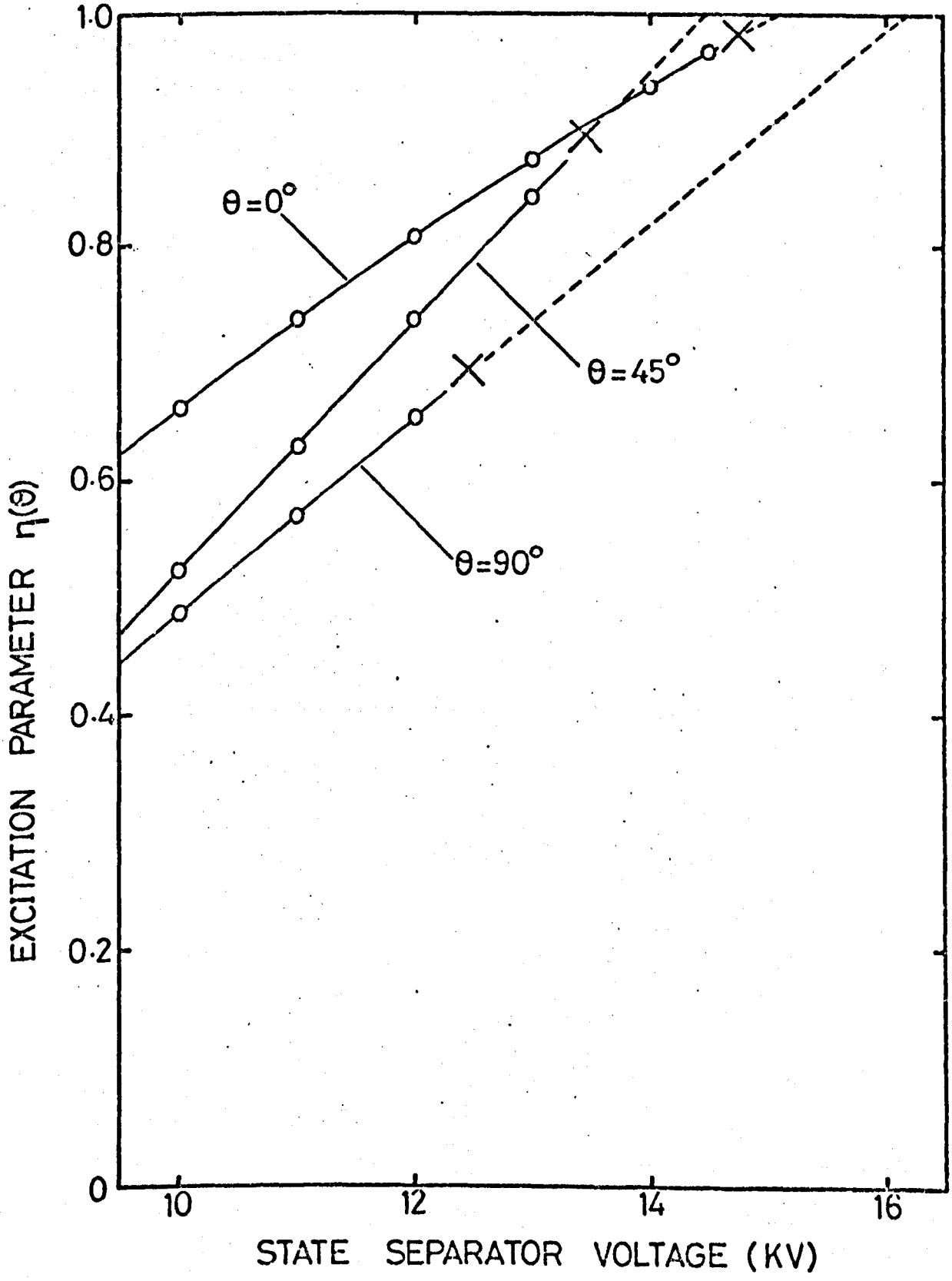

Fig 4.5 Experimental values of excitation parameter plotted against state separator voltage. The crosses indicate thresholds of oscillation.

This is to be expected from the different behaviours of the two types of molecules in the electric field of the state separator. The formaldehyde maser of Krupnov and Skvortsov, 1965C worked on the $1_{01} \rightarrow 0_{00}$ transition of formaldehyde. They show that if the state separation of the molecules is perfect, the only molecules of the 1_{01} level which enter the cavity are those with magnetic quantum number M = 0. If these molecules are adiabatically reoriented by a state separator fringe field whose direction coincides with the beam axis, then their transition probability is maximum for the mode direction $\theta = 0^{\circ}$ and is zero for $\theta = 90^{\circ}$. Ideally, the ratio $\eta(0)/\eta(90)$ is expected to be infinite.

Gordon, 1955 describes the state separation of ammonia molecules in the J = 3, K = 3 rotational level for a state separator with cylindrical symmetry. The pairs of levels $M = \pm 3, \pm 2, \pm 1$ are all state separated but not to the same extent. The relative numbers of molecules in these levels which are focused by such a separator are proportional to M^2. Mednikov and Parygin, 1963 calculate that the ratio $\eta_o(0)/\eta_o(90)$ is approximately 2 in this case. If the arguments of Gordon are applied to a state separator with planar symmetry such as the ladder type which was used in the present work, the numbers of focused molecules are found to be proportional to $|M|$. Repeating the calculations of Mednikov and Parygin for this case, a value of 1.56 is found for the ratio $\eta_o(0)/\eta_o(90)$. This compares well with the value of 1.52 obtained at the lowest measured separator voltage of 10 KV but cannot account for the variation of $\eta_o(0)/\eta_o(90)$ with separator voltage which was observed (see Table 4.1).

However, the simple treatment of Gordon, 1955 which is used here does not take into account the departure from the quadratic Stark effect which is noticed in ammonia for high values of electric field. There is a gradual transition to linear Stark effect which starts at around 3 KV mm^{-1}. This is indicated by Eqn. 2.8 and shown in the potential energy diagram of Fig. 2.2(see Sec. 2.2.2). The departure from the quadratic Stark effect depends on the magnetic quantum number in that it occurs at a lower value of electric field for large values of $|M|$ than for small values. Eqn. 2.9 shows that the effectiveness of the state separation process is reduced by departure from the quadratic Stark effect. Hence the effectiveness of state separation for molecules which have large $|M|$ is diminished by comparison with those having small $|M|$ as the state separator voltage is increased. The preferential orientation depends on the superior focussing which is experienced by molecules with large $|M|$, and is therefore expected to diminish as the state separator voltage is increased.

The preferential orientation of the molecules may be pictured in terms of a polar diagram which describes the ratio $\eta_o(\theta)/\eta_o(0)$ with respect to the direction θ. The measured values of the ratio $\eta_o(0)/\eta_o(45)$ show a greater rate of decrease with increase in state separator voltage, than do the measured values of the ratio $\eta_o(0)/\eta_o(90)$ (see Table 4.1). This effect can also be seen from the relative slope of the lines in Fig. 4.5. A possible explanation for this anomalous behaviour is that the polar diagram not only changes shape but also rotates as the state separator voltage is changed. The direction of maximum η must be moving from $\theta = 0^o$ towards $\theta = 45^o$ as the voltage is increased. A possible mechanism for such a rotation is the spatial reorientation which results from the presence of stray magnetic or non-uniform electric fields in the region between the state separator and the cavity (see Sec. 2.4.3).

If this explanation is correct then the fringe field of the state separator must be an important component of the field or fields responsible. Clearly the behaviour of the preferential orientation in the maser is quite complicated, and requires a detailed investigation which is outside the scope of this work to resolve its exact behaviour.

4.3.3 Extrapolation of η and the Onset of Oscillation

According to the principle of maximum emission (Tang and Statz, 1967) oscillation must establish itself in the maser in that mode which provides the largest radiation field in the cavity. From the considerations presented in Sec. 4.3.1 it is clear that in general this is an elliptically polarised mode. If a preferentially oriented molecular beam is present in a Fabry-Pérot maser whose cavity has zero anisotropy, the mode of maximum emission might be expected to be the linear mode whose mode direction coincides with the axis of preferential orientation. In a real cavity it will probably be a mode with low cavity loss, in general an elliptically polarised one, which is close to the linear mode. The experimental data presented in Fig. 4.5 can be used to test this hypothesis.

It is convenient that η shows an approximately linear dependence on the state separator voltage over the measured range. This fact has been used in extrapolating η for $\theta = 45^{\circ}$ and $\theta = 90^{\circ}$ to the points where $\eta = 1$. A value of $\eta = 1$ indicates the threshold of oscillation of the maser. In this case the extrapolated lines yield the thresholds for oscillation to occur in the two linear modes with mode directions 45° and 90°. These are seen to be 14.5 KV and 16.2 KV respectively. Oscillation is actually observed to start, when measurements are being made in these mode directions, at 13.5 KV

and 12.8 KV respectively, thus indicating that oscillation establishes itself in modes quite distinct from those in which measurement is taking place.

When the waveguides have orientations of 90° the mode in which oscillation establishes itself is known to be close to the linear mode with mode direction 0°, by the fact that the onset of oscillation is very difficult to observe. Thus the oscillation mode is almost orthogonal to the mode direction 90°. When the waveguides have orientation 0° the extrapolated oscillation threshold is 15.1 KV. Oscillation is actually observed at 14.9 KV. This suggests that although oscillation is not established in exactly the mode direction 0° it is close to it.

The loading imposed by the waveguides on the cavity is very different in the three orientations, as is evidenced by the fact that the three oscillation thresholds are so different. Nevertheless, the mode in which oscillation establishes itself appears to be nearly the same in the three cases. This indicates that the nature of the mode is governed by the preferential orientation rather than by the cavity anisotropy. There is a difficulty of interpretation here, once again associated with the measurements in the mode direction 45°. In Fig. 4.5 the extrapolated threshold for 45° is lower than that for 0°. This seems to indicate that oscillation should be established close to 45° rather than close to 0°.

CHAPTER 5

THE MASER AS AN OSCILLATOR

5.1 INTRODUCTION

The intention in this work was to investigate the modes of oscillation of the maser by changing the orientations of the waveguides and monitoring the signals coupled from the cavity. Two factors which militate against such a technique because they make it difficult to interpret the signals clearly, have been discussed in the previous chapter. Firstly the coupling parameter of a coupling hole is not independent of waveguide orientation. Secondly the waveguide loading provides one of the anisotropy mechanisms of the cavity, and the oscillation behaviour is sensitive to its being changed. A magnetic field applied to the maser in the region of the cavity, however, proved to be a useful tool for investigation of the oscillation mode, and at the same time permitted the observation of some interesting Zeeman effects.

The high field Zeeman behaviour of the ammonia $J = 3$, $K = 3$ inversion line is uncomplicated (Jen, 1948). Each energy level splits into seven $(2J + 1)$ levels, each corresponding to a different value of the magnetic quantum number M. Because the upper and lower levels of the transition have the same rotational quantum number J, the Zeeman sublevels associated with these levels are all equally spaced (Townes and Schawlow, 1955). If the magnetic field and microwave field

are parallel, only transitions with $\Delta M = 0$ are excited and the level splitting cannot be detected. If the magnetic and microwave fields are at right angles, only transitions with $\Delta M = \pm 1$ are observed. In this case 4J transitions are allowed, but because the levels are equally spaced only two transition frequencies are observed. For most purposes the molecule behaves as though it were a simple $J = \frac{1}{2}$ system (Logachev et al, 1968).

The behaviour of the ammonia 3,3 line in fields below 10^{-3} T is complicated by level crossing and anti-crossing of its hyperfine components (Lefrère, 1973). However, the transitions which may occur still fall into the two categories $\Delta M = +1$ and $\Delta M = -1$, and two effective spectral line centres can be defined in this low field region. In the present work the exact behaviour of these two lines is unimportant so long as their frequency separation is monotonically increasing with magnetic field. It will be seen in Sec. 5.4.3 that this is the case.

In order to observe the effects of the Zeeman splitting the $\Delta M = \pm 1$ transitions must be excited. Thus a magnetic field at right angles to the plane of the maser oscillation field vector, i.e. along the axis of the cylindrical Fabry-Pérot maser cavity, was required. In what follows this axis is referred to as the z-axis. The axes x, y and z form the right-handed cartesian set shown in Fig. 5.1, in which the x-axis coincides with the molecular beam direction. The x- and y-axes are the same as those used in Chapter 4 (see Fig. 4.3).

The maser was sensitive to magnetic fields an order of magnitude smaller than the Earth's magnetic field. Two pairs of

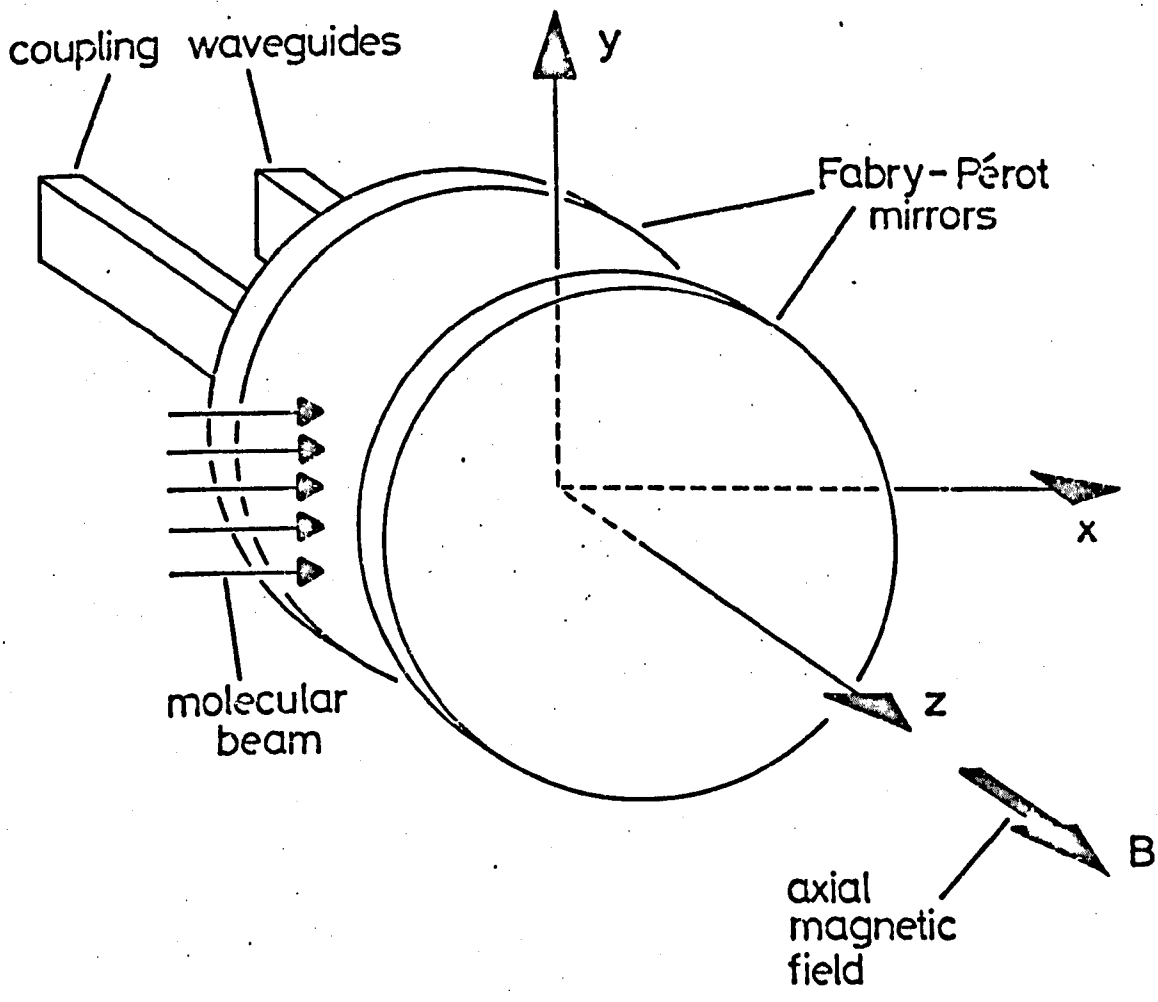

Fig. 5.1 The system of axes used to describe the magnetic characteristics of the maser.

rectangular coils were built, to cancel the local magnetic fields in the vicinity of the maser, and to enable a known field to be applied along the z-axis. The production and measurement of this magnetic field is described in Appendix A.

The three main effects observed in the presence of the axial magnetic field are described in Sec. 5.2. The measurements establish that the mode of oscillation of the maser has an elliptical polarisation, and the behaviour of this polarisation in the magnetic field is examined empirically. In Sec. 5.3 the theory of the Zeeman laser is presented. The behaviour of the Fabry-Pérot maser is in many respects similar to a laser and the theory presented here gives an insight into this behaviour. It is seen that in both cases the additional degree of freedom, permitted by the Fabry-Pérot cavity compared with conventional cavities, allows some interesting effects to occur. In Sec. 5.4 the observations of Sec. 5.2 are related to the theory of Sec. 5.3. It will be seen that a clear picture of the oscillation behaviour of the maser emerges, although some difficulties of interpretation remain. Additional results which help to clarify the interpretation are also presented in Sec. 5.4.

5.2 EXPERIMENTS WITH THE ZEEMAN MASER

5.2.1 The Static Magnetic Characteristics

The purpose of the measurements described in this section was to examine the mode of oscillation of the maser by comparing the signals coupled from the two cavity ports. The maser was operated in an axial

magnetic field with the two coupling waveguides, A and B, at right angles to one another. Two waveguide configurations were employed, with A and B coupling respectively to the directions 0° and 90°, and 45° and -45°. The amplitudes of oscillation observed are shown plotted against applied magnetic field in Figs. 5.2 and 5.3.

The detection system employed was the double microwave bridge described in Sec. 3.3.3 and shown in Fig. 3.11. The 30 MHz oscillator was switched off, and the method of I.F. bandpass display, described in Sec. 3.3.5, was employed to measure the oscillation signal amplitudes detected by the two bridges.

The coupling parameters of the two coupling holes and the sensitivity of the two detection systems were not necessarily equal. However it is possible to normalise the output signals from the two detection systems, and it is the normalised relative oscillation amplitudes which are plotted in Figs. 5.2 and 5.3. The method of normalisation is discussed below.

The following behaviour is noticed on examination of the two graphs. When the magnetic field is zero, a maximum is observed in the signal coupled out in the direction 0°, and a minimum is found in the direction 90°. For a positive field of 4×10^{-5} T (approximately twice the horizontal component of the Earth's magnetic field) a maximum is observed at -45° and a minimum at $+45^{\circ}$. For a negative field of similar magnitude, the maximum is observed at $+45^{\circ}$ and the minimum at -45°. The minima correspond to a signal amplitude approximately half that of the maxima.

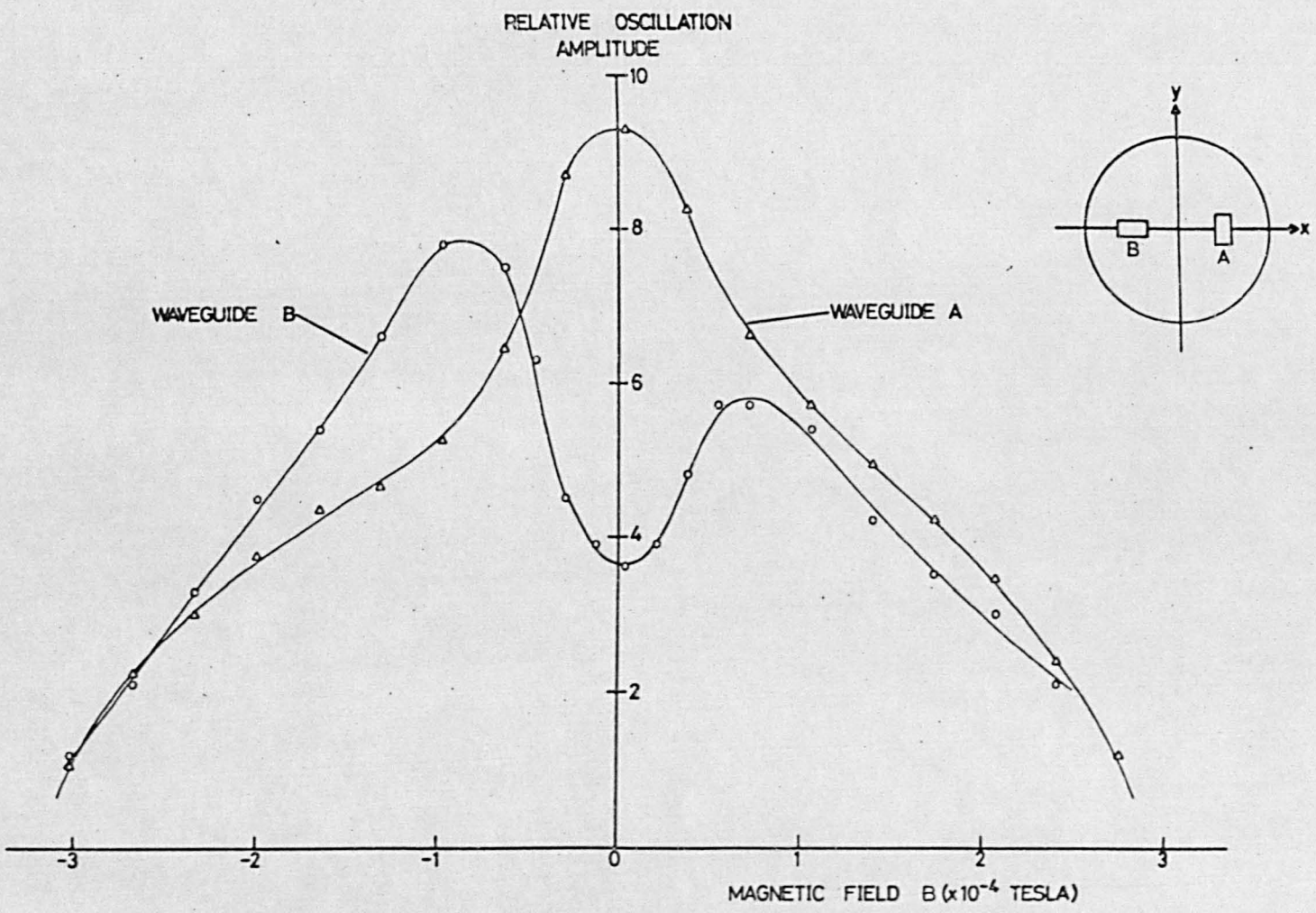

Fig. 5.2 Oscillation amplitudes observed in the directions 0°(waveguide A) and 90°(waveguide B) in the presence of an axial magnetic field.

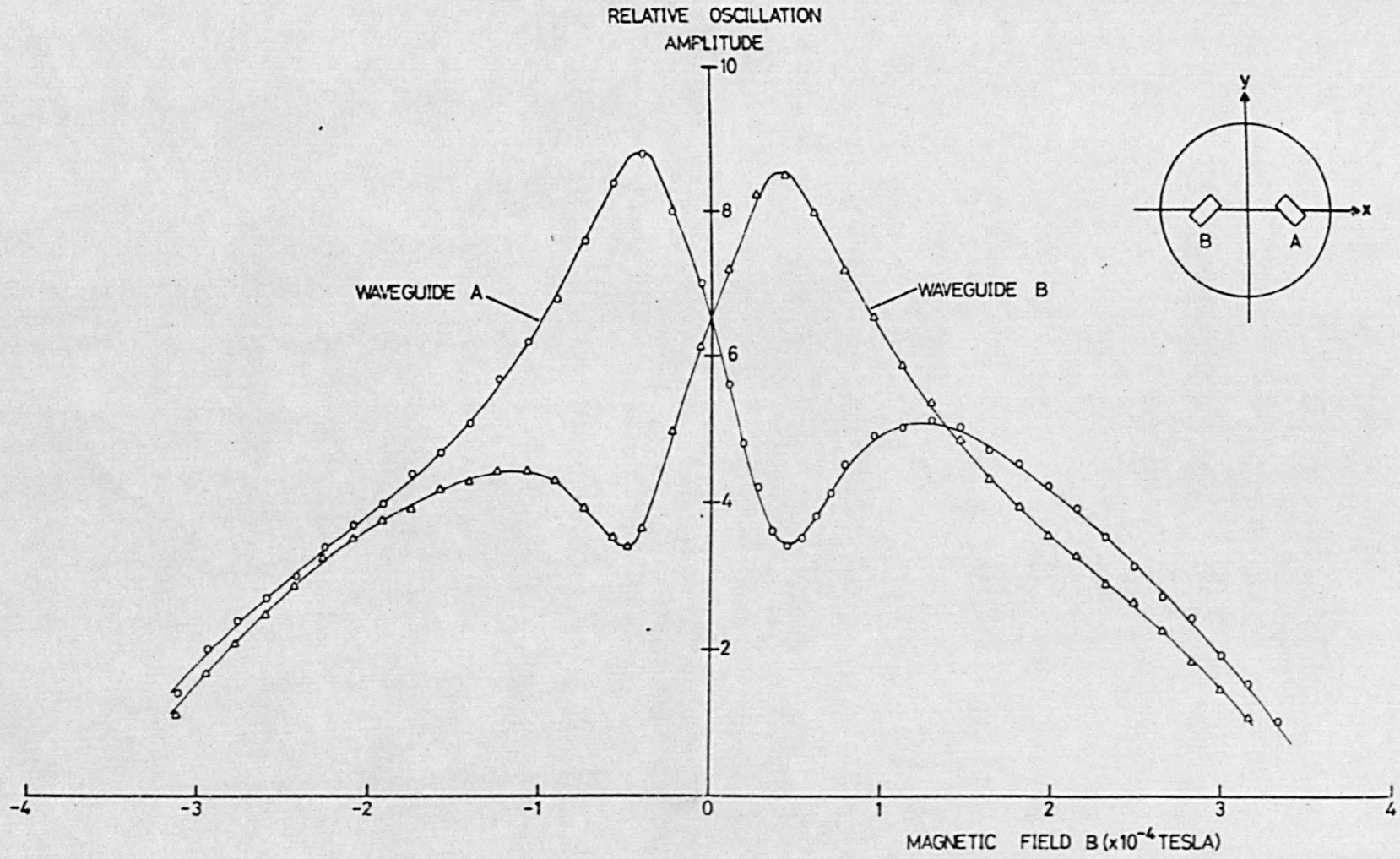

Fig. 5.3 Oscillation amplitudes observed in the directions $+45^{\circ}$ (waveguide A) and -45° (waveguide B) in the presence of an axial magnetic field.

These results are interpreted as being due to an elliptical mode of oscillation, whose axis ratio is approximately 2, and the direction of whose major axis in the x - y plane is sensitive to the magnetic field applied along the z axis. The major axis rotates from making an angle of $+45^{\circ}$ with the x-axis to an angle of -45° as the magnetic field is changed by only 8×10^{-5} T. The maximum and minimum angles reached are difficult to determine because the mode appears to become circular before $+90^{\circ}$ or -90° are attained. The overall oscillation amplitude is reduced by application of the magnetic field, because of spectral line broadening, and is quenched in a field of approximately $\pm 3.5 \times 10^{-4}$ T.

This interpretation of the results has been used in order to normalise the outputs A and B in Fig. 5.3. In zero applied magnetic field the major axis of the ellipse lies at 0° and the oscillation amplitudes observed in the directions -45° and $+45^{\circ}$ should be equal. The measurements made at -45° have been scaled by a constant factor in order to obtain this. The mode of oscillation appears to be circular in fields above about 2×10^{-4} T, so the measurements made at 90° have been scaled in an attempt to make the curves of Fig. 5.2 register in this region.

The ellipticity of the mode is defined by

$$e = (c^2 - d^2)/c^2 \qquad 5.1$$

where c and d are the maximum and minimum oscillation amplitudes observed (i.e. the major and minor semi-axes of the oscillation ellipse). The graphs indicate that e is probably constant below 4×10^{-5} T, and is

found from Fig. 5.3 to be 0.85. However the ellipticity is actually very dependent on the tuning of the cavity. By careful tuning it could be made equal to unity, as observed by disappearance of the signal detected at 90^{o} in zero magnetic field, or at -45^{o} and 45^{o} respectively in the appropriate positive and negative magnetic field strengths.

The measurements presented in Figs. 5.2 and 5.3 are complicated by a hysteresis phenomenon which has not been shown in these graphs. It will be discussed in Sec. 5.4.2.

5.2.2 The Transient Magnetic Characteristics

In this section a transient behaviour of the maser, observed in the presence of a magnetic field, is described. If a strong stimulating signal at the transition frequency is injected into the maser cavity through one coupling port, a linear mode of high intensity is established in the cavity. Molecules which enter the cavity are polarised by the microwave field of this mode. When the stimulating signal is switched off, the microwave field decays until it reaches its steady state value. If the maser is being operated below oscillation threshold, this value is zero. If the maser is above oscillation threshold, the field decays to the appropriate elliptical mode, which has been described in the previous section. The transient magnetic characteristics reflect the way in which the decay takes place in the presence of a magnetic field.

Typical examples of the magnetic transients observed in the presence of an axial magnetic field, are shown in Fig. 5.4. Following stimulation of the molecular assembly, a periodic modulation of the maser signal was noticed. The frequency of the modulation showed an

approximately linear dependence on applied magnetic field strength, and frequencies from a few hundred Hz to several KHz were measured. The upper limit was only dictated by the maximum field which could be applied to the maser using the coils described in appendix A.

Figs 5.4(a) and 5.4(b) show transients observed with the maser operated below oscillation threshold. Fig. 5.4(a) is an early photograph taken using a bar magnet, placed outside the maser vacuum chamber, to provide a magnetic field in the vicinity of the Fabry-Pérot cavity. The arrow shows the point in time at which the stimulating signal was applied to one of the waveguides. The signal shown in the photograph was observed in the second waveguide, which was placed in the orthogonal direction to which the stimulating field could not normally couple. This signal was only seen when a molecular beam was present in the maser, and when a magnetic field was applied.

Fig. 5.4(b) is a photograph taken at a later date, using the rectangular coils to produce a magnetic field of approximately 2×10^{-4} T. The improved homogeneity of the field enabled the signal to be observed more clearly. Here the signal was observed in the same waveguide orientation as that in which the stimulating signal was applied. The latter was a frequency-modulated microwave signal which was swept through the maser transition frequency.

The use of such a frequency modulated signal, which stimulates the molecular assembly while it is momentarily within the linewidth of the transition, is well-known (Lainé, 1966; Lainé and Kakati, 1969). Subsequent to stimulating the assembly it is used to aid detection of the maser signal. The two signals beat together in the I.F. detector to

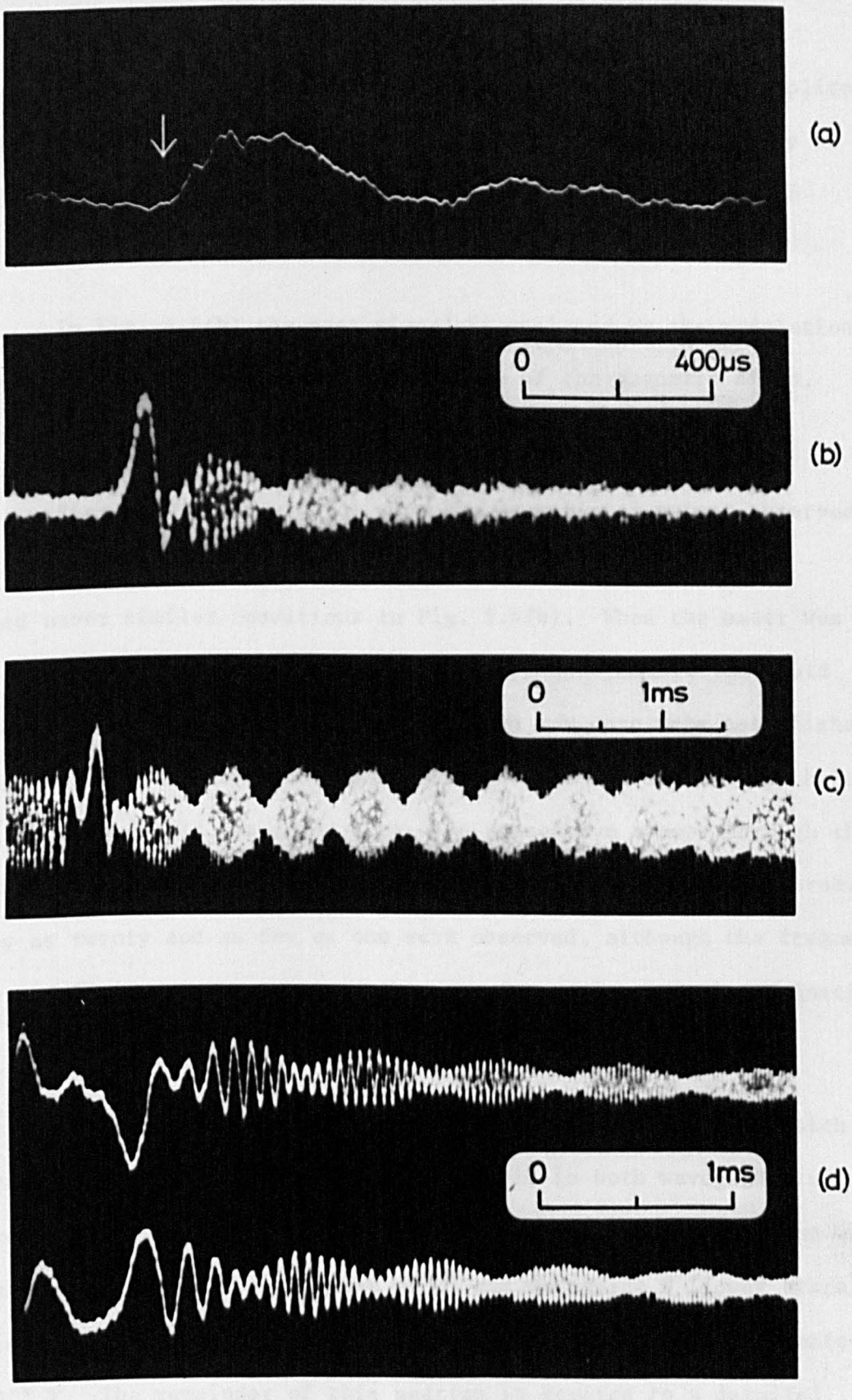

Fig. 5.4 Magnetic Transients. Applied field strengths are:
(a) unknown (b) $2{\cdot}2 \times 10^{-4}$ T
(c) $1{\cdot}4 \times 10^{-4}$ T (d) $0{\cdot}74 \times 10^{-4}$ T

produce a low frequency signal (typically several KHz), whose amplitude is proportional to that of the maser signal. This beat signal may be clearly displayed on an oscilloscope. This is the method by which molecular ringing is commonly displayed (see Sec. 3.3.5).

In Fig. 4.5(b) the beat signal is enclosed by the modulation envelope, which results from the application of the magnetic field, and which is characteristic of the magnetic transient.

Figs. 5.4(c) and 5.4(d) show the magnetic transient observed above oscillation threshold. The signal shown in Fig. 5.4(c) was obtained under similar conditions to Fig. 5.4(b). When the maser was above oscillation threshold many cycles of this transient modulation could be executed before a steady state oscillation was once more established. Some instability in the transient behaviour which was not evident below oscillation threshold was found here. On successive sweeps through the line the number of modulation cycles executed could differ considerably. As many as twenty and as few as one were observed, although the frequency of the modulation always remained the same for a given applied magnetic field.

Fig. 5.4(d) is typical of a series of measurements in which the transient was investigated by observing it in both waveguides using different mutual waveguide orientations. This photograph was taken with waveguide A (upper trace) oriented at 0^{o} and waveguide B (lower trace) oriented at 90^{o}. The applied magnetic field strength was approximately 1×10^{-4} T. The remainder of this section is devoted to a detailed description of this series of measurements.

The microwave arrangement which was used was essentially the double microwave bridge described in Sec. 3.3.3. However, the 30 MHz oscillator which was used to generate sidebands of the klystron signal, was only fed to the modulator crystal on one of the microwave bridges. This ensured that only one linear mode was set up in the cavity by the stimulating sideband, even when the cavity waveguides were placed at different orientations. The klystron was phase locked to a crystal oscillator (using Micro Now 101C and 202 equipment) and the stimulating sideband was swept in frequency by modulating the 30 MHz oscillator. This arrangement was the same as that used in the P.S.D. form of detection described in Sec. 3.3.4, and enabled a more stable display of the transient signal to be obtained.

Detection of the maser signal following stimulation was by observing the beat signal between the stimulating sideband and the maser oscillation, as described above. However, this relied on the presence at the crystal mixer of a microwave signal derived from the stimulating sideband. In the case where the two waveguides are at right-angles, this signal cannot be obtained in the second microwave bridge by transmission through the cavity. In this case it had to be simulated at the intermediate frequency, by injecting part of the output from the 30 MHz oscillator into the I.F. chain between pre-amplifier and amplifier.

During the series of measurements, waveguide A was always oriented to couple with the mode direction 0^{o}. Waveguide B was placed in several different orientations. The signals observed from waveguides A and B were displayed on a double beam oscilloscope, thus enabling the relative phases of the two modulation envelopes to be compared.

Table 5.1 gives a summary of the waveguide orientations used together with the corresponding measured phase differences between the two signals. A close correspondence between the angular difference in waveguide orientation and the phase difference is noticed. This indicates that the oscillation polarisation in the cavity rotates or tumbles in the x-y plane. The signal observed in each waveguide represents the projection of the tumbling oscillation on the fixed direction to which that waveguide couples. The direction of the tumbling is seen to depend on the sign of the applied magnetic field, being negative in fields applied in the positive z-direction, and positive in opposite fields. The closeness of the correlation between the waveguide orientation and the phase difference indicates that the angular velocity of the tumbling is nearly uniform.

Table 5.1 Phase differences between the transient modulation signals observed in the two cavity waveguides. Waveguide orientations are relative to the x-axis. Positive magnetic field is along the positive z-axis. Positive phase difference indicates a time lag of the signal in waveguide B over that in waveguide A.

Mag. field direction	Waveguide orientation		Phase difference
	A	B	
+	0^{o}	-45^{o}	52^{o}
+	0^{o}	0^{o}	5^{o}
+	0^{o}	45^{o}	46^{o}
+	0^{o}	90^{o}	-90^{o}
-	0^{o}	-45^{o}	-66^{o}
-	0^{o}	0^{o}	-1^{o}
-	0^{o}	45^{o}	50^{o}
-	0^{o}	90^{o}	92^{o}

Finally, it can be seen from Figs. 5.4(c) and (d) that the tumbling polarisation is probably elliptical. In general the modulated signals have a finite minimum amplitude. This minimum amplitude represents the momentary coincidence of the minor axis of the oscillation ellipse and the waveguide direction; the maximum amplitude is caused by coincidence of the major axis with the waveguide direction

5.2.3 The Dynamic Magnetic Characteristics

If the maser was operated as an oscillator in a very small magnetic field, a steady modulation signal could sometimes be observed even in the absence of a stimulating signal. This effect was only observed for magnetic fields below about 5×10^{-5} T and was still evident close to zero magnetic field. It only occurred for a narrow region of cavity tuning, and the mechanical tuning range had to be searched carefully in order to observe it. The signal was also sensitive to matching in the input and output waveguides (i.e. adjustment of the matching units of the microwave bridges), to state separator voltage and nozzle pressure. For each of these variables a narrow range of settings could be found within which the effect was observed. The shape of the modulation envelope varied widely as can be seen from the examples of the observed signals shown in Figs. 5.5 - 5.7.

The oscillations were detected with the double microwave bridge arrangement using a phase locked klystron as the common local oscillator, and feeding both modulation crystals from the 30 MHz generator. However the generator was operated without F.M. sweep and at such a frequency that it provided a sideband of the klystron signal only a few KHz to one side of the maser transition frequency. In this way

a beat signal, amplitude modulated by the dynamic characteristic, was displayed from both detection systems.

No satisfactory approach to the investigation of the dynamic characteristic was found. Because the effect was extremely sensitive to changes in cavity loading, it was not possible to make a change in the waveguide orientations and still remain within the range for which the effect was observed. If the observation of the signal with a second waveguide configuration was required, adjustments to other parameters such as the cavity tuning or cavity matching were also needed in order to restore the effect. In general the shape of the modulation envelope was changed by such adjustments, so that the signals observed in the two configurations could not be directly compared. Some dependence of the modulation frequency on magnetic field strength was observed, but the effect was lost if significant changes in magnetic field were made. In the paragraphs which follow some general discussions of the photographs shown in Figs. 5.5 - 5.7 are presented.

The pairs of traces shown in Fig. 5.5 were obtained with orthogonal waveguides in orientations 0^{o} and 90^{o}. These photographs have been selected as being representative of a series of measurements in which the nozzle pressure was changed progressively from 0.16 torr to 0.30 torr. Outside this range of pressures no modulation of the oscillation envelope was observed. The nozzle pressure was chosen as the variable in these measurements, because the dynamic characteristics were found to be less sensitive to changes in this parameter than to changes in other parameters of the maser.

At the low end of the pressure range the signals observed can

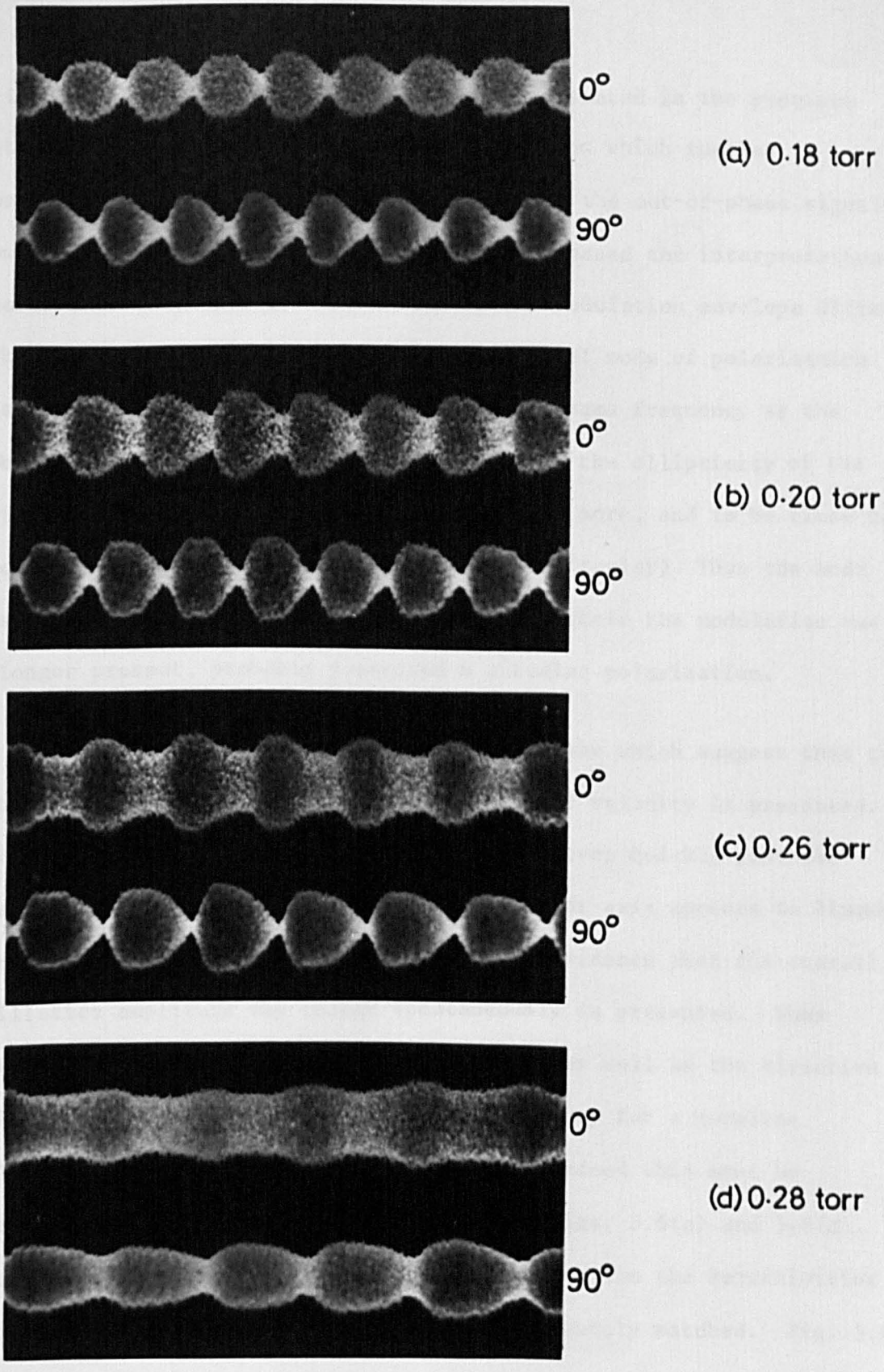

Fig. 5.5 Dynamic magnetic characteristics for separator voltage 30 KV and a magnetic field of approximately 1×10^{-5} T. Nozzle pressures and waveguide orientations are indicated.

be interpreted in the light of the results presented in the previous section. An elliptical oscillation polarisation which tumbles spontaneously in the x - y plane would produce the out-of-phase signals shown in Fig. 5.5(a). As the pressure is increased the interpretation becomes more interesting. The minima of the modulation envelope differ markedly in Figs. 5.5(b) and (c). An elliptical mode of polarisation whose ellipticity changes periodically at the same frequency as the tumbling has to be postulated. In Fig. 5.5(d) the ellipticity of the oscillation appears to be nearly constant once more, and to be close to zero (the oscillation polarisation is almost circular) Thus the mode present for nozzle pressures above 0.30 torr, where the modulation was no longer present, probably possessed a circular polarisation.

In Fig. 5.6 a collection of photographs which suggest that the tumbling does not take place at uniform angular velocity is presented. In Fig. 5.6(a) the minor axis of the ellipse moves quickly past the waveguide directions (0^{o} and 45^{o}), but the major axis appears to linger near these directions. In Fig. 5.6(b) clear evidence that the overall oscillation amplitude may change spontaneously is presented. Thus periodic changes to the oscillation amplitude as well as the direction and ellipticity of the ellipse are probably necessary for a complete explanation of the dynamic characteristics. Indeed this must be invoked in order to explain the waveforms of Figs. 5.6(c) and 5.6(d). In most of the photographs presented in this section the sensitivities of the two detection systems have been approximately matched. Fig. 5.6(d) is an exception in this respect.

The signals shown in Fig. 5.7 are derived from a single

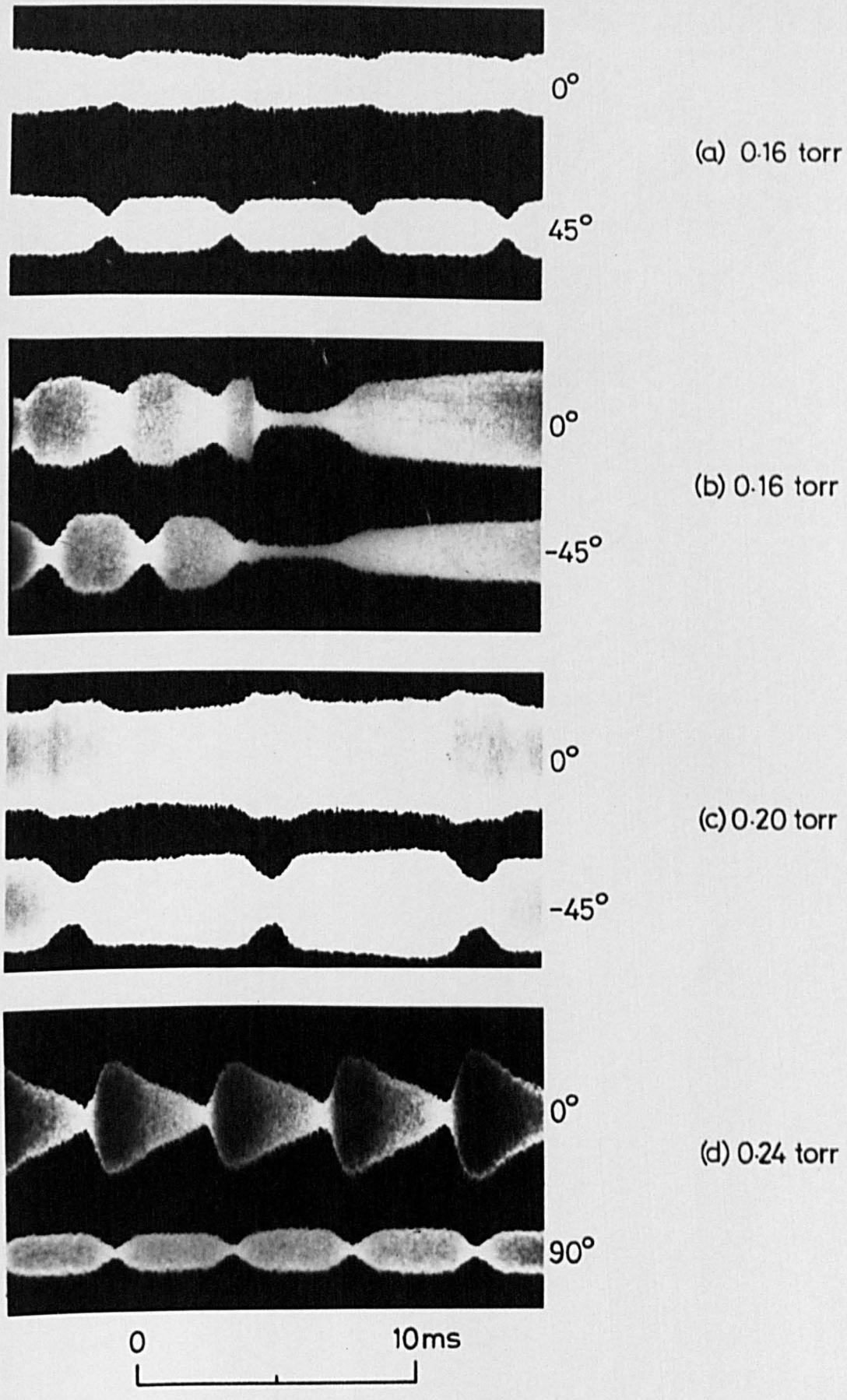

Fig. 5.6 Dynamic magnetic characteristics for separator voltage 30KV and a magnetic field of approximately 1×10^{-5} T. Nozzle pressures and waveguide orientations are indicated.

waveguide oriented at 0^{o}. They have been selected from a series of photographs representing the effect of progressive change in the voltage applied to the separator. The range over which the dynamic characteristic was observed was from 17.5 KV to 20.5 KV. Like the nozzle pressure, the state separator voltage was a parameter to which the dynamic characteristic was relatively insensitive.

Figs. 5.7(a) and (b) show the emergence of the curious waveform shown in Fig. 5.7(c). Fig. 5.7(d) is typical of the signals observed from 19 KV to 20.5 KV, over which range the modulation became progressively more uneven and sporadic in its appearance until steady oscillation set in once more at separator voltages above 20.5 KV. These photographs show that if the rotating ellipse interpretation is adhered to, complicated changes in direction and shape of the ellipse must be postulated.

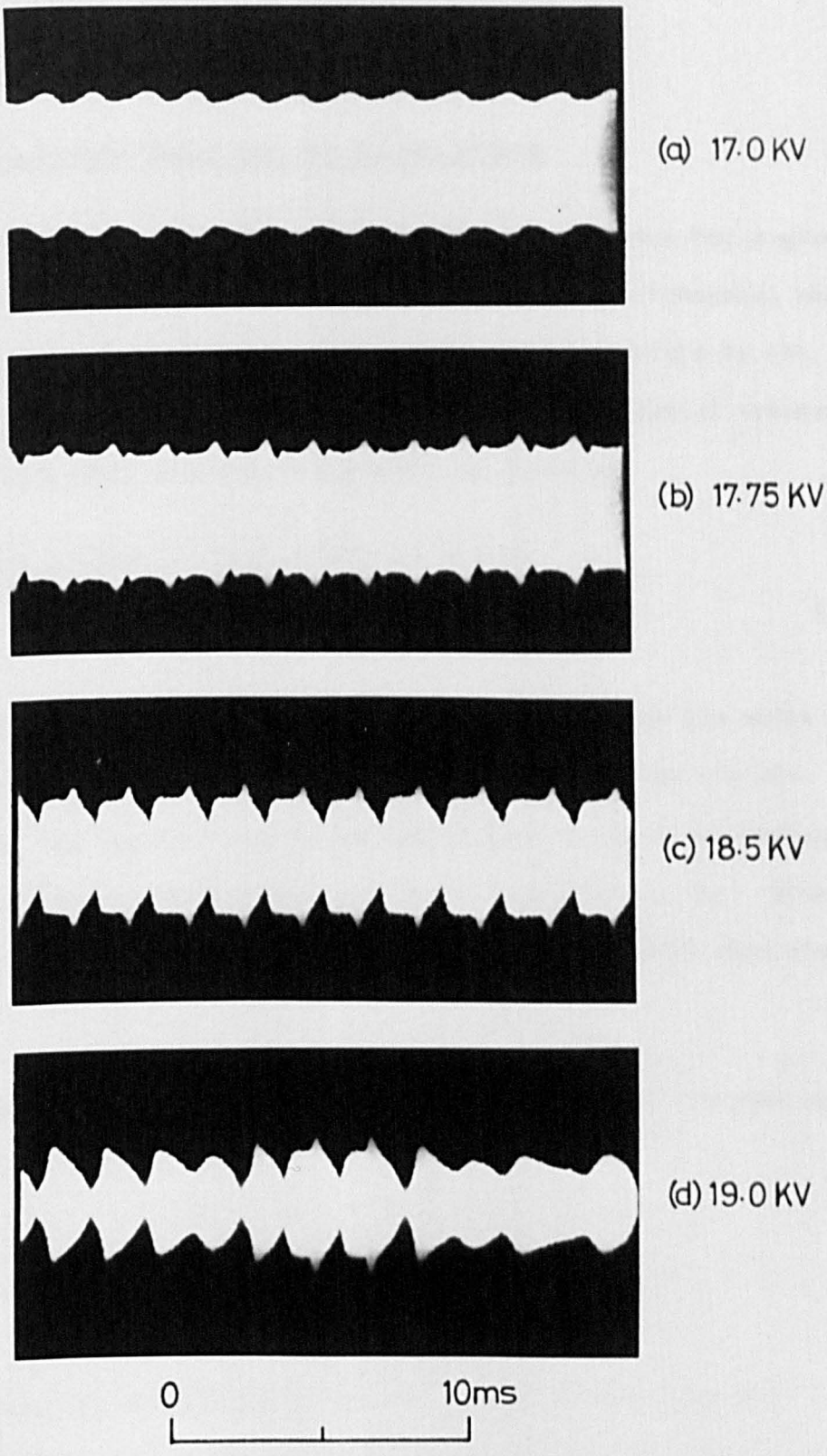

Fig. 5.7 Dynamic magnetic characteristics for waveguide orientation 0°, nozzle pressure 0·33 torr and a magnetic field of approximately 1×10^{-5} T. Separator voltages are indicated.

5.3 THEORY OF THE ZEEMAN LASER

5.3.1 Degenerate Modes and the Zeeman Effect

The Fabry-Pérot cavity has two degenerate modes for a given spatial resonance. These may be any pair of mutually orthogonal modes having their distribution of electromagnetic field governed by the function $U_{mnq}(x,y,z)$, which is associated with that spatial resonance. Thus the oscillating electric field might be given by

$$\underline{E}(x,y,z,t) = \{E_x \underline{i} \exp[-i(\nu_x t + \phi_x)] + E_y \underline{k} \exp[-i(\nu_y t + \phi_y)]\} U(x,y,z) \qquad 5.2$$

where E_x and E_y are the electric field amplitudes of the two modes linearly polarised in the x and y directions, the ν's and ϕ's are respectively the angular frequencies and phases of these two modes, and $\underline{i}$ and $\underline{k}$ are the basis vectors in the x- and y-directions. Here the system of coordinates is intended to be identical with that shown in Fig. 5.1.

Of particular interest are the two orthogonal circular modes described by the basis vectors

$$\begin{aligned} \underline{e}_+ &= (\underline{j} - i\underline{k})/\sqrt{2} \\ \underline{e}_- &= (\underline{j} + i\underline{k})/\sqrt{2} \end{aligned} \qquad 5.3$$

The (+) subscript refers to the mode whose polarisation has its angular momentum vector in the z-direction, and the (-) subscript to the opposite mode. By analogy with Eqn. 5.2, the oscillating electric field of these two polarisations can be written

$$\underline{E}(x,y,z,t) = \{E_+\underline{e}_+ \exp[-i(\nu_+ t + \phi_+)] + E_-\underline{e}_- \exp[-i(\nu_- t + \phi_-)]\}U(x,y,z) \qquad 5.4$$

This representation is particularly useful when treating the Zeeman laser, because the (+), (-) modes may be excited individually by the $\Delta M = \pm 1$ circularly polarised σ-components of a Zeeman split line. Under conditions of pumping close to the threshold for maser action only one spatial resonance is excited, but two opposite circular polarisations are observed in the presence of a magnetic field along the axis of the laser cavity (i.e. the z-axis). Statz et al, 1962 obtained a beat frequency of 1050 Hz from a Helium-Neon laser when its output was observed through a linear polariser. They attributed the beats to the effect of the component of the Earth's magnetic field along the axis of the laser, and showed that when an axial magnetic field was deliberately applied, the observed frequency increased linearly with field. With higher levels of pumping, the Zeeman behaviour is complicated by the emergence of other oscillating spatial modes, but may still be interpreted in terms of degenerate pairs of modes (Paananen et al, 1963; Culshaw and Kannelaud, 1964).

The frequency difference between the two polarisations is not the natural frequency separation of the Zeeman components but is modified by the well-known cavity pulling effect (Garrett, 1967). In the laser, where the frequency width $\Delta\nu_c$ of the cavity resonance is much smaller than the width $\Delta\nu_\ell$ of the spectral line, the pulling effect is approximately proportional to the ratio of the two widths:

$$\nu \simeq \nu_c + (\nu_\ell - \nu_c)\Delta\nu_c/\Delta\nu_\ell \qquad 5.5$$

where ν is the oscillation frequency and ν_c and ν_ℓ are the centre frequencies of the cavity and spectral line respectively. Eqn. 5.5 holds to a good approximation so long as $|\nu_\ell - \nu_c|$ is small compared with $\Delta\nu_\ell$. The effect of pulling on the beat frequency between the two Zeeman components is to reduce that frequency by the factor $\Delta\nu_c/\Delta\nu_\ell$. Thus the beat frequency is given by

$$\Delta\nu = \frac{2g\mu_m B}{h} \cdot \frac{\Delta\nu_c}{\Delta\nu_\ell} \qquad 5.6$$

where the natural frequency splitting between the two components is $2g\mu_m B/h$.

Sargent et al, 1967A, 1967B have provided a theory of the Zeeman laser which is based on the well-known theory of the laser by Lamb, 1964. They show that, ideally, beats between the Zeeman components should be observed right down to zero splitting, but that in practice mode competition and mode frequency locking prevent this. Tomlinson and Fork, 1967 have interpreted the theory for the case of axial magnetic fields and have compared it with experiment. In particular they have analysed the approach to the frequency locked condition, and their results in this area are of considerable interest in the present work. These four papers form the basis from which the results obtained with the Fabry-Pérot maser will be interpreted. Selected parts of the theory they contain and some of the computer solutions they present are described in the following sections.

5.3.2 The Coupled Oscillator Equations

The basic equations for a pair of coupled laser oscillators, written in the (+), (-) notation are (Sargent et al, 1967B)

$$\dot{E}_+ = E_+(\alpha_+ - \beta_+ E_+^2 - \theta_{+-} E_-^2) \qquad 5.7$$

$$\dot{E}_- = E_-(\alpha_- - \beta_- E_-^2 - \theta_{-+} E_+^2) \qquad 5.8$$

$$\nu_+ + \dot{\phi}_+ = \Omega + \sigma_+ + \rho_+ E_+^2 + \tau_{+-} E_-^2 \qquad 5.9$$

$$\nu_- + \dot{\phi}_- = \Omega + \sigma_- + \rho_- E_-^2 + \tau_{-+} E_+^2 \qquad 5.10$$

Their derivation will not be considered here although it will be touched on in Sec. 5.4.1.

Eqns. 5.7 and 5.8 describe the relationship between the amplitudes E_+ and E_- of the two coupled oscillators, in this case the two circular modes. Eqns. 5.9 and 5.10 are the frequency determining equations and involve the angular frequencies ν_+ and ν_- and the phases ϕ_+ and ϕ_- of the oscillators. The (+) subscript refers to the polarisation which has its angular momentum in the same direction as a positive axial magnetic field, and the (-) subscript to the opposite polarisation. Ω, which appears in Eqns. 5.9 and 5.10 represents the degenerate frequency of the unperturbed cavity modes.

The α's, β's, θ's, σ's, ρ's and τ's in Eqns. 5.7 - 5.10 are complicated functions of the atomic level parameters, magnetic field, excitation conditions and cavity tuning. Their physical significance is explained by Fork and Sargent, 1966, whose explanations are paraphrased here.

α_+ is the unsaturated gain of the laser for the (+) mode.

$\beta_+ E_+^2$ gives the decrease in the gain of the (+) mode due to saturation (level depletion) by the (+) mode (i.e. self-saturation).

$\theta_{+-} E_-^2$ gives the decrease in the gain of the (+) mode due to saturation by the (-) mode (i.e. cross-saturation).

σ_+ represents the frequency shift of the (+) mode from its unperturbed value caused by the dispersion of the unsaturated medium. In the Zeeman case this is the displacement of the Zeeman line from the natural molecular transition frequency.

$\rho_+ E_+^2$ is a change in this frequency shift as a result of self-saturation of the (+) mode.

$\tau_{+-} E_-^2$ is a similar change in the frequency shift due to cross-saturation of the (+) mode.

Throughout these explanations the transposition (+) $\leftrightarrow$ (-) may be made.

Following Lamb, 1964, the amplitude equations may be transformed by introducing

$$X = I_+ = E_+^2 \qquad 5.11$$

$$Y = I_- = E_-^2$$

where I_+ and I_- are the intensities of the two oscillations. Eqns. 5.7 and 5.8 become

$$\dot{X} = 2X(\alpha_+ - \beta_+ X - \theta_{+-} Y) \qquad 5.12$$

$$\dot{Y} = 2Y(\alpha_- - \beta_- Y - \theta_{-+} X) \qquad 5.13$$

where $\underline{\dot{X}}$ and $\underline{\dot{Y}}$ are shown as vectors to indicate that they will be plotted in the phase plane X, Y.

The condition for a steady state oscillation is

$$\underline{\dot{X}} = 0 \, , \quad \underline{\dot{Y}} = 0 \qquad 5.14$$

and is represented in the X, Y phase plane by the point of intersection of the two lines

$$\begin{aligned} L_1 &: \beta_+ X + \theta_{+-} Y = \alpha_+ \\ L_2 &: \theta_{-+} X + \beta_- Y = \alpha_- \end{aligned} \qquad 5.15$$

together with the single frequency solutions

$$X = \alpha_+/\beta_+ \, , \quad Y = 0 \qquad 5.16$$

$$X = 0, \quad Y = 0 \qquad 5.17$$

$$X = 0, \quad Y = \alpha_-/\beta_- \qquad 5.18$$

5.3.3 Phase Diagrams

Phase diagrams in the X, Y plane may be drawn from Eqns. 5.12 and 5.13 in order to determine the stabilities of the solutions 5.15 - 5.18. A solution which is stable for one set of the α's, β's and θ's may be unstable for another set. In general a separate phase diagram is required for each set of these coefficients under consideration.

Briefly, a phase diagram is a set of curves drawn in the X, Y plane which indicate, for any value of X and Y, the direction $\underline{V} = \underline{\dot{X}} + \underline{\dot{Y}}$ in which the phase point (X, Y) will move towards a stable solution

of Eqns. 5.12 and 5.13. A stable solution is indicated by the convergence of the phase curves towards the phase point representing that solution. An unstable solution is represented by a stationary point through which no phase curves pass.

A phase diagram may be obtained graphically by plotting the direction of the vector $\underline{V}$ for a large number of points (X, Y) and joining up the resulting vectors into a series of curves, known as trajectories. It may also be obtained by programming the problem on an anologue computer, setting up different initial conditions (X_o, Y_o) and recording the behaviour of the phase point (X, Y) as it moves towards a stable equilibrium point. Lamb, 1964 obtained phase diagrams for Eqns. 5.12 and 5.13 with the aid of an analogue computer. They are reproduced for three important coefficient combinations in Figs. 5.8 - 5.10.

Fig. 5.8 shows the situation when both modes are above threshold for oscillation ($\alpha_+ > 0$, $\alpha_- > 0$) but one is favoured by virtue of its higher gain ($\alpha_+ = 1$, $\alpha_- = 0.4$). The phase diagram shows that there is a stable equilibrium phase point on the X-axis at (α_+/β_+, 0) while an unstable equilibrium exists on the Y-axis at (0, α_-/β_-). Referring to the explanation of the coefficients given in Sec. 5.3.2 it is seen that oscillation in the favoured (+) mode with intensity α_+/β_+ inhibits oscillation in the unfavoured mode by depressing its effective gain from α_- to a negative value α_-' where, from Eqn. 5.13,

$$\alpha_-' = \alpha_- - \theta_{-+}\alpha_+/\beta_+ \qquad 5.19$$

The new threshold for oscillations in the (-) mode is $\alpha_- = \theta_-\alpha_+/\beta_+$

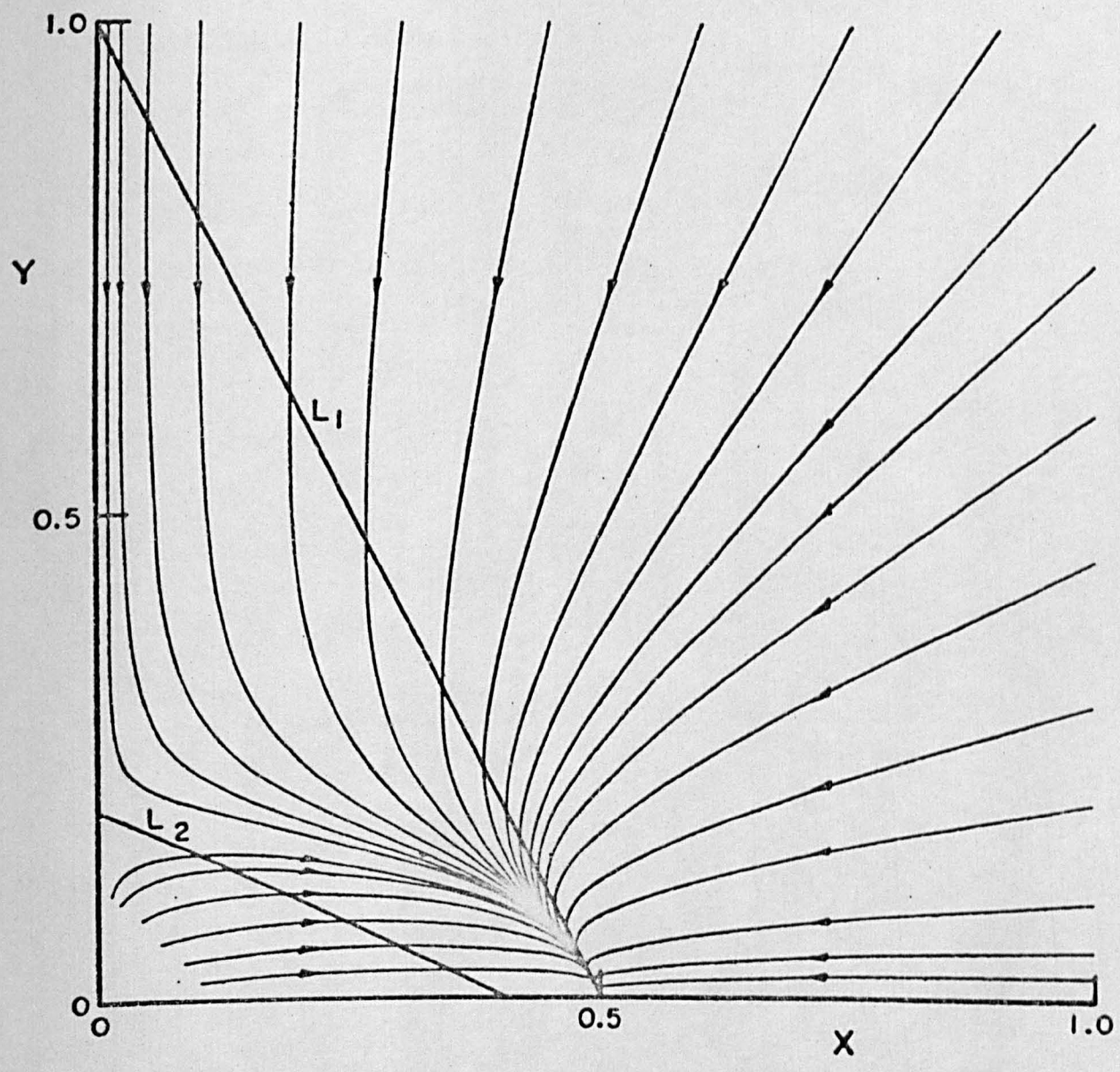

Fig. 5.8 Phase diagram showing mode inhibition: $\alpha_+ = 1$, $\alpha_- = 0.4$, $\beta_+ = \beta_- = 2$, $\theta_{+-} = \theta_{-+} = 1$ (after Lamb, 1964).

instead of $\alpha_- = 0$, and this new threshold has not been reached.

The two other important cases, for which both modes are above threshold, occur when $\alpha'_+ > 0$, $\alpha'_- > 0$ and when $\alpha'_+ < 0$, $\alpha'_- < 0$. These cases may be described in terms of a coupling coefficient

$$C = (\theta_{+-}\ \theta_{-+})/(\beta_+\ \beta_-) \qquad 5.20$$

and are given by $0 < C < 1$ and $C > 1$ respectively. The first is the case of weak coupling in which both polarisations oscillate simultaneously, and the second is the case of strong coupling for which either may oscillate but in doing so inhibits the other. There is a third, relatively unimportant case, neutral coupling, for which $C = 1$.

Fig. 5.9 illustrates the weak coupling case. The two single frequency operating points given by the solutions 5.16 and 5.18 are unstable, whereas the double frequency operating point given by the solution of Eqns. 5.15 is stable. The strong coupling case is shown in Fig. 5.10 where the single frequency operating points are seen to be stable and the double frequency point is unstable. Which of the single frequency points is chosen by the system for steady state oscillation depends on its starting conditions, because it is the starting conditions which determine which trajectory of Fig. 5.10 the system is on initially. If the system starts from zero oscillation intensity (0,0), the starting trajectory, and hence the mode which finally establishes itself, will be determined by noise. A strongly coupled system exhibits hysteresis when parameters which decide the shape of the phase diagram (e.g. cavity tuning) are altered.

Sargent et al, 1967B show that some laser transitions exhibit weak coupling, while some are strongly coupled in small applied magnetic field. The coupling parameter decreases with field so that a strongly

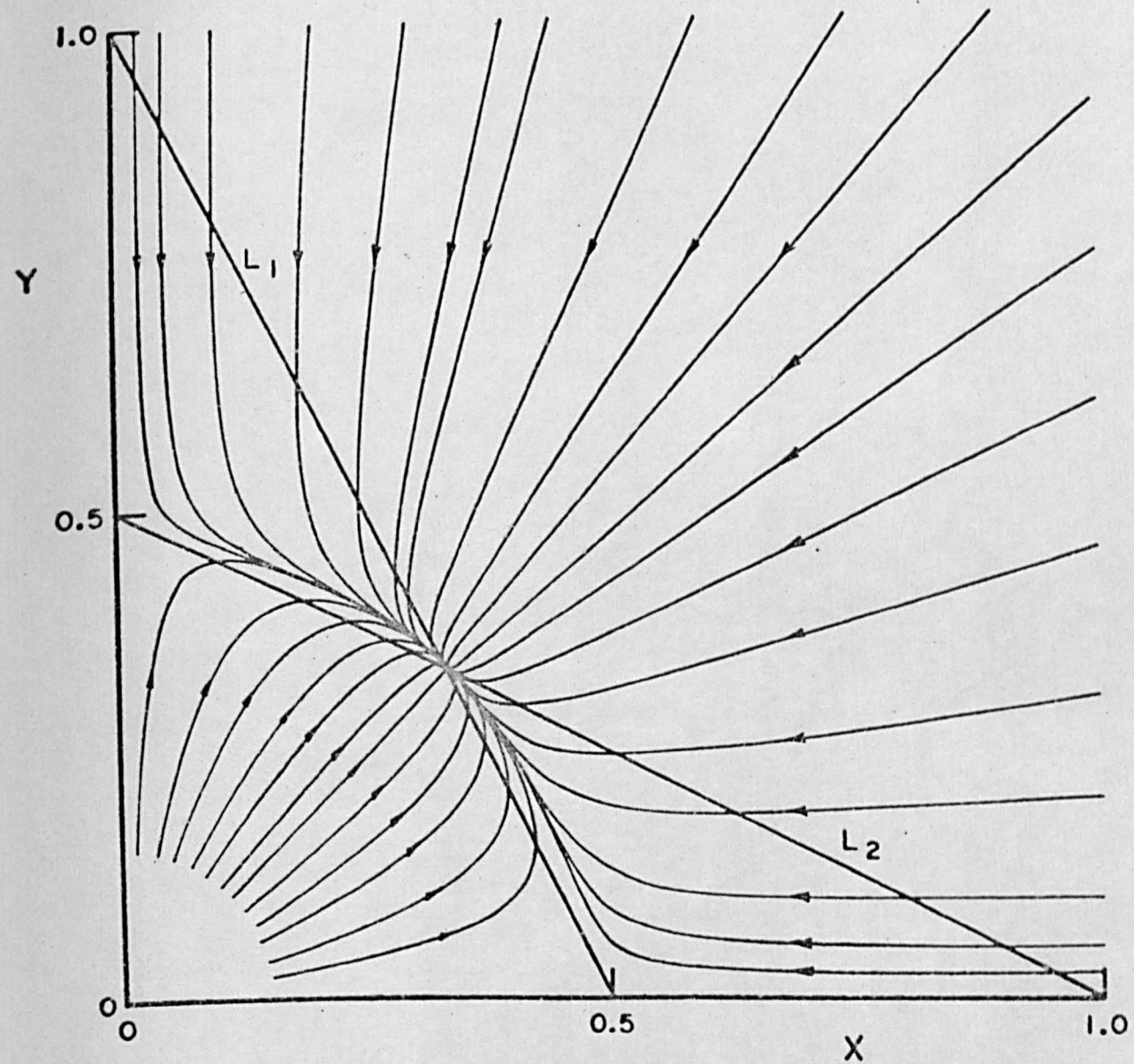

Fig. 5.9 Phase diagram showing weak coupling: $\alpha_+ = \alpha_- = 1$, $\beta_+ = \beta_- = 2$, $\theta_{+-} = \theta_{-+} = 1$ (after Lamb, 1964).

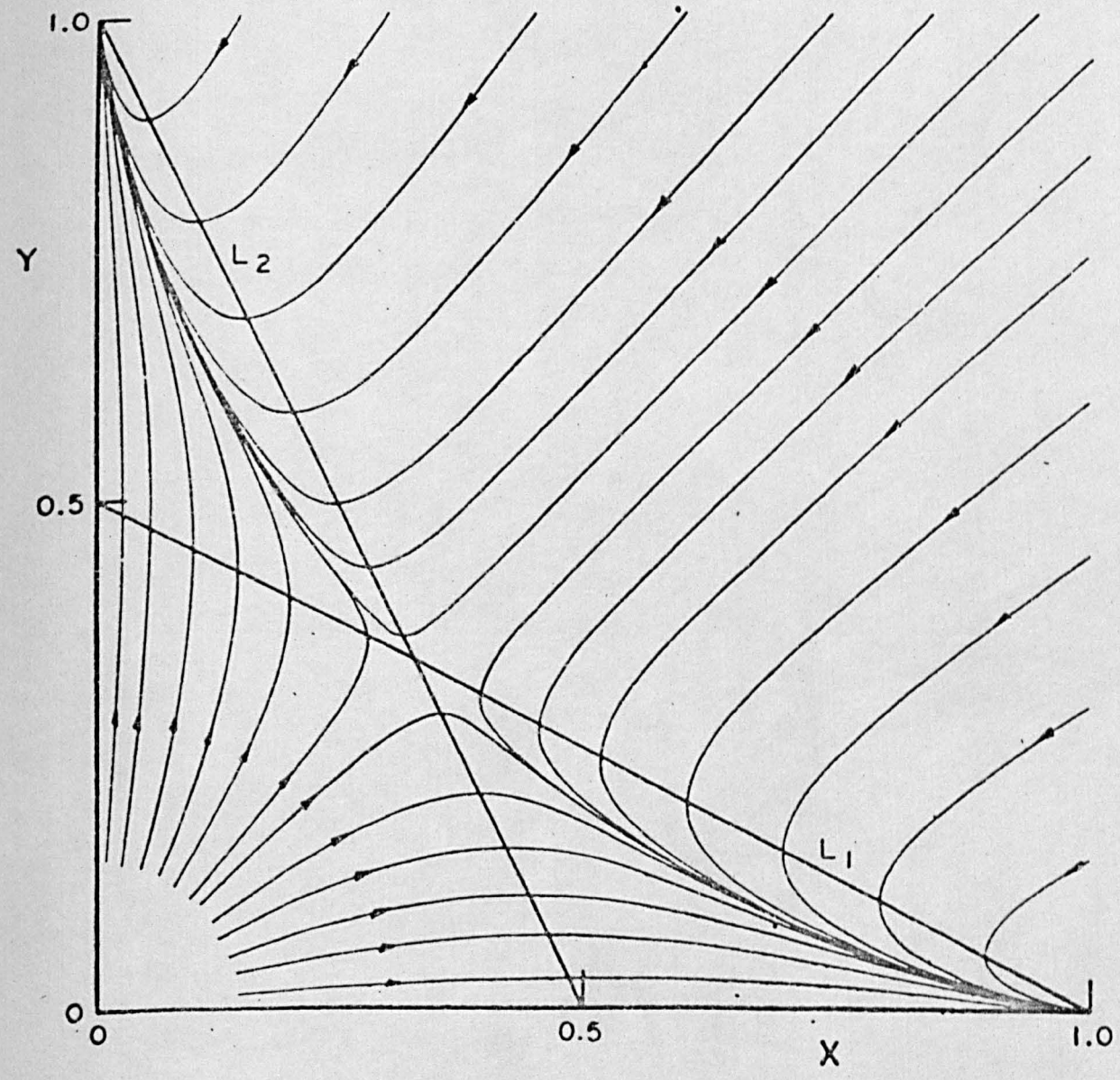

Fig. 5.10 Phase diagram showing strong coupling:
$\alpha_+ = \alpha_- = 1$, $\beta_+ = \beta_- = 1$, $\theta_{+-} = \theta_{-+} = 2$
(after Lamb, 1964)

coupled system always becomes weakly coupled when the field is sufficiently large. Strong coupling is observed between the two oscillations of a beam maser operated in high order cavity modes (Becker, 1967). Later in this chapter it is shown that the ammonia inversion transition for J = 3, K = 3 exhibits weak coupling between its Zeeman components. Evidence is also presented which suggests that the case of inhibition of the weaker mode (phase diagram, Fig. 5.8) is applicable to the ammonia maser when the applied magnetic field is large enough to nearly quench the oscillation in the maser.

5.3.4 The Tumbling Ellipse

The behaviour of a Zeeman laser exhibiting double frequency operation under weak coupling conditions will now be considered in further detail. If the two oscillations are due to the circularly polarised $\Delta M = \pm 1$ σ-components coupling with the two orthogonal circular modes of the cavity, then the oscillating electric field in the cavity is given by Eqn. 5.4 where E_+, E_-, ν_+, ν_-, ϕ_+, ϕ_- are defined by Eqns. 5.7 - 5.10. Using Eqns. 5.2 to write $\underline{e}_+$ and $\underline{e}_-$ in terms of the rectangular coordinate basis vectors $\underline{j}$ and $\underline{k}$, the real part of Eqn. 5.4 becomes

$$\underline{E} = (1/\sqrt{2})\left[E_+\{\underline{j}\cos(\nu_+ t + \phi_+) - \underline{k}\sin(\nu_+ t + \phi_+)\}\right.$$
$$\left. + E_-\{\underline{j}\cos(\nu_- t + \phi_-) + \underline{k}\sin(\nu_- t + \phi_-)\}\right] U(x,y,z) \qquad 5.21$$

This may be rearranged to give

$$\underline{E} = \sqrt{2}\left[(E_+ + E_-)\cos(\nu_+ t + \phi_+ - \tfrac{1}{2}\psi)\{\underline{j}\cos(\tfrac{1}{2}\psi)\right.$$
$$- \underline{k}\sin(\tfrac{1}{2}\psi)\} + (E_+ - E_-)\sin(\nu_+ t + \phi_+ - \tfrac{1}{2}\psi)$$
$$\left.\{-\underline{j}\sin(\tfrac{1}{2}\psi) - \underline{k}\cos(\tfrac{1}{2}\psi)\}\right] U(x,y,z) \qquad 5.22$$

where

$$\psi = (\nu_+ - \nu_-)t + (\phi_+ - \phi_-) \qquad 5.23$$

Eqn. 5.22 represents a vector which at any point (x, y, z) in the cavity is rotating in such a way that it describes an ellipse with major axis $2\sqrt{2}(E_+ + E_-)U(x,y,z)$ and minor axis $2\sqrt{2}|E_+ - E_-|U(x,y,z)$. The directions of the major and minor axes are given by the unit vectors $\{\underline{j}\cos(\frac{1}{2}\psi) - \underline{k}\sin(\frac{1}{2}\psi)\}$ and $\{-\underline{j}\sin(\frac{1}{2}\psi) - \underline{k}\cos(\frac{1}{2}\psi)\}$ respectively. Thus the ellipse, which represents the envelope of the vector $\underline{E}$, itself rotates with angular velocity $\frac{1}{2}\dot{\psi}$ where from Eqn. 5.23

$$\dot{\psi} = (\nu_+ - \nu_-) + (\dot{\phi}_+ - \dot{\phi}_-) \qquad 5.24$$

The signal coupled from the laser through a linear polariser is an amplitude modulated signal of modulation depth $(E_+ + E_-)/|E_+ - E_-|$. The modulation is due to rotation of the ellipse and has frequency

$$\Delta\nu = \left[\int_0^{2\pi} \dot{\psi}^{-1}\, d\psi\right]^{-1} \qquad 5.25$$

If the rotation has constant angular velocity $\dot{\psi}$, then $\Delta\nu = (\dot{\psi}/2\pi)$.

5.3.5 The Effect of Anisotropy in the System

Sargent et al, 1967B consider anisotropy in the cavity to be described in terms of the different Q-factors, Q_x and Q_y, of the cavity for two orthogonal linear modes. The Q-factors of the two circular modes remain equal in the presence of this anisotropy since they are given by

$$Q_{\pm} = 2(Q_x^{-1} + Q_y^{-1})^{-1} \qquad 5.26$$

However, the anisotropy can lead to frequency locking of the two circular oscillation modes, and can give rise to some interesting associated effects.

Sargent et al write Eqns. 5.7 - 5.10 in the following form to include the effect of cavity anisotropy:

$$\dot{E}_+ = E_+(\alpha_+ - \beta_+E_+^2 - \theta_{+-}E_-^2) - \tfrac{1}{4}\{(\nu/Q_x) - (\nu/Q_y)\}E_- \cos\psi \qquad 5.27$$

$$\dot{E}_- = E_-(\alpha_- - \beta_-E_-^2 - \theta_{-+}E_+^2) - \tfrac{1}{4}\{(\nu/Q_x) - (\nu/Q_y)\}E_+ \cos\psi \qquad 5.28$$

$$\nu_+ + \dot{\phi}_+ = \Omega + \sigma_+ + \rho_+E_+^2 + \tau_{+-}E_-^2 + \tfrac{1}{4}\{(\nu/Q_x) - (\nu/Q_y)\}(E_+/E_-)\sin\psi \qquad 5.29$$

$$\nu_- + \dot{\phi}_- = \Omega + \sigma_- + \rho_-E_-^2 + \tau_{-+}E_-^2 - \tfrac{1}{4}\{(\nu/Q_x) - (\nu/Q_y)\}(E_-/E_+)\sin\psi \qquad 5.30$$

where $\nu = (\nu_+ + \nu_-)/2$ and ψ is given by Eqn. 5.23. Substituting Eqns. 5.29 and 5.30 into Eqn. 5.24 gives

$$\dot{\psi} = \sigma_+ - \sigma_- + \rho_+E_+^2 - \rho_-E_-^2 + \tau_{+-}E_-^2 - \tau_{-+}E_+^2 + \tfrac{1}{4}\{(\nu/Q_x) - (\nu/Q_y)\}(E_+/E_- + E_-/E_+)\sin\psi \qquad 5.31$$

Eqns. 5.27 - 5.30 can be solved analytically by taking the steady state solution of Eqns. 5.7 and 5.8, which was described above with the aid of phase diagrams, as an approximate solution of Eqns 5.27 and 5.28. In this way Eqns. 5.29 and 5.30 can be solved independently of Eqns. 5.27 and 5.28, treating E_+ and E_- as constant coefficients.

Eqn. 5.31 then has the form

$$\dot{\psi} = a + b \sin \psi \qquad 5.32$$

where $a/2\pi$ is the beat frequency in the absence of anisotropy, and b is proportional to the anisotropy term. For $|a/b| > 1$ there is a solution of Eqn. 5.3.2 which represents a beat frequency

$$\Delta\nu = \pm (1/2\pi)(a^2 - b^2)^{\frac{1}{2}} \qquad 5.33$$

Fig. 5.11 shows the general behaviour of Eqn. 5.33 for the case where the function a represents simple Zeeman splitting, proportional to the applied magnetic field B. It is seen that the beat frequency is no longer proportional to B in the region near $B = 0$, but reduces to zero for finite B when $a = \pm b$.

Although the beat frequency $\Delta\nu$ of Eqn. 5.33 is constant for a given value of B, the phase angle ψ does not change uniformly with time. Eqn. 5.32 shows that $\dot{\psi}$ varies between $a + b$ and $a - b$ during one cycle ($0 < \psi < 2\pi$). Remembering that the ellipse of Sec. 5.3.4 has an angle $\frac{1}{2}\psi$ between its major axis and the x-axis, it is seen that Eqn. 5.32 leads to non-uniform rotation of the oscillation ellipse and consequently to distortion of the modulation envelope observed from the linear polariser.

In the region $|a/b| < 1$ Eqn. 5.32 can only be solved for $\dot{\psi} = 0$. Thus the behaviour of ψ is assymptotic in time, and converges to one of the two solutions

$$\psi_1 = -\sin^{-1} (a/b) \qquad 5.34$$

$$\psi_2 = \pi + \sin^{-1} (a/b) \qquad 5.35$$

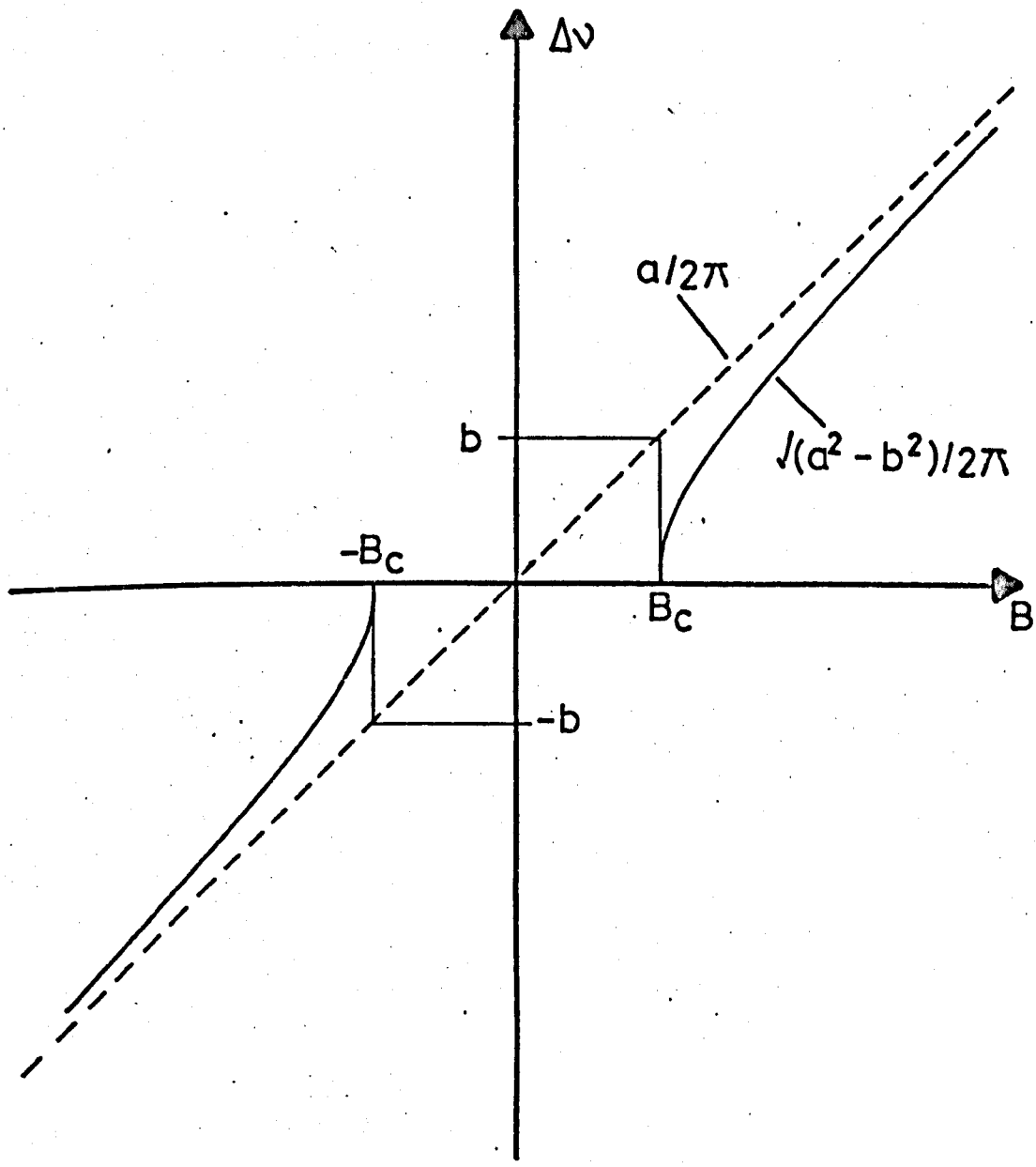

Fig. 5.11 Behaviour of the beat frequency $\Delta\nu$ in the presence of anisotropy b as a function of magnetic field B - see Eqn. 5.33.

A small vibrations analysis shows that only one of these two solutions is stable. If the anisotropy term b is positive it is ψ_2, while if b is negative ψ_1 is the stable value. Clearly in this solution the oscillation ellipse does not rotate dynamically in the magnetic field but has a fixed inclination $\frac{1}{2}\psi$ to the x-axis for a given B. This corresponds to frequency locking of the two oscillators. The inclination of the ellipse depends on the value of B. In Eqn. 5.34, as H is increased between the critical values $-B_c$ and $+B_c$ (see Fig. 5.11), $\frac{1}{2}\psi$ moves from $\pi/4$ to $-\pi/4$.

The approximate solution of Eqns. 5.27 - 5.30 described above is only useful for very small values of the anisotropy. If the mode amplitudes E_+ and E_- are allowed to fluctuate, the behaviour becomes very complex. Tomlinson and Fork, 1967 have computed solutions which show that the periodic solution (Eqn. 5.33) can be accompanied by large periodic changes in the relative amplitudes of the two oscillation modes. In terms of the oscillation ellipse, not only its direction but also its shape is a periodic function of time. In addition they find other solutions in which the ellipse swings between two directions in the cavity without performing a complete rotation. Such solutions correspond to the two circular oscillations alternately locking and unlocking. Thus the ellipse does not have time to complete a full rotation in the cavity, before locking sets in and its starts assymptotically to approach the locked position (Eqn. 5.34). Before this position is reached the oscillations unlock and tumbling begins again. The nature of the behaviour is found to be very sensitive to cavity tuning. All of these solutions can be obtained for a single value of B close to the point of frequency locking, by changing the cavity tuning.

5.4 EXPLANATION OF THE ZEEMAN MASER EXPERIMENTS

5.4.1 Application of the Zeeman Laser Theory to the Maser.

The theory of Logachev et al, 1968 deals with the behaviour of a molecular beam maser with a magnetic field applied. Their equations describe a pair of oscillators which contribute to, and are coupled by, a single electromagnetic field (the cavity field). This treatment is relevant to a maser having a cylindrical or rectangular cavity, where there is no degeneracy of the cavity mode. It cannot be used to describe the Zeeman effect in the Fabry-Pérot maser, although there are some similarities in behaviour.

Despite this inability of the Logachev theory to describe the Fabry-Pérot maser, it is interesting to compare its results with those of the coupled oscillator theory. The dependence of beat frequency on magnetic field which is suggested by the Logachev theory is similar in shape to Fig. 5.11. However the critical value of field B_c is fixed by the dimensions of the cavity and the molecular beam velocity, and corresponds to a splitting between the two Zeeman components equal to the molecular linewidth. In short, biharmonic oscillation of the maser is predicted when the Zeeman components are resolved. It is tempting to think of this as a special case of the coupled oscillator theory, for which the anisotropy in the cavity is due to its ability to support only one linear mode. However, inspection of Eqn. 5.31 shows that the anisotropy term is infinite under these conditions, and the equations cannot be solved.

In the Fabry-Pérot maser, two oscillation fields can exist more or less independently of one another. In a perfect cavity there is no coupling via the electromagnetic field, only coupling through depletion of molecular levels common to the transitions which contribute to the

oscillations. This means that there is no mutual constraint on the frequencies of the two oscillations, and in the Zeeman case gives rise to an oscillation ellipse which has complete freedom to move in the x - y plane of the cavity. It has been seen how this behaviour is predicted by the equations of the Zeeman laser theory (Eqns. 5.7 - 5.10). Some coupling via the electromagnetic field is introduced when the cavity anisotropy is included in the theory (Eqns. 5.27 - 5.30).

The coupled oscillator Eqns. 5.7 - 5.10 represent the simplest form which such a system can take. In order to understand their relevance to the maser, consider the instantaneous power emitted by an assembly of N_1 upper state molecules in the presence of a mean radiation field E_1

$$P_1 = \frac{dW_1}{dt} = \left(\frac{\pi^2 \, p\nu_o}{3h\Delta\nu_o} \right) N_1 \, E_1^2 \qquad 5.36$$

(Heavens, 1964), where p is the dipole moment matrix element for the transition, frequency ν_o, and $\Delta\nu_o$ is the effective molecular linewidth. N_1 consists of the number of molecules NL/v which are found instantaneously in the cavity, depleted by the action of the radiation fields acting within the molecular linewidth. Here, following the symbology of Sec. 4.2, N is the number of molecules entering the cavity in unit time, L is the effective length of the cavity, and v is the mean molecular velocity. Thus if only one radiation field E_1 is present in the cavity, N_1 can be written

$$N_1 = \alpha N - \beta N E_1^2 \qquad 5.37$$

where α and β are constants ($\alpha = L/v$).

Considering for a moment N_1 described by the single oscillator equation 5.37, it will be seen that Eqn. 5.36 takes the form

$$P_1 = \alpha^* NE_1^2 - \beta^* NE_1^4 \qquad 5.38$$

Thus there is a close parallel between the oscillator theory and the simple maser theory of Sec. 4.2.1, since expansion of the sine term in Eqn. 4.3 yields

$$P = h\nu_o \left(\frac{\pi Lp}{h\nu}\right)^2 NE^2 - \frac{h\nu_o}{36}\left(\frac{\pi Lp}{h\nu}\right)^4 NE^4 + \ldots \qquad 5.39$$

If two radiation fields E_1 and E_2 are present in the cavity, Eqn. 5.37 is written

$$N_1 = \alpha N - \beta NE_1^2 - \theta NE_2^2 \qquad 5.40$$

The instantaneous stored energy W_1 in the cavity as a result of the radiation field E_1 is given by

$$W_1 = \frac{\epsilon_o V E_1^2}{8\pi} \qquad 5.41$$

where V is the cavity volume. Substituting Eqns. 5.40 and 5.41 in Eqn. 5.36 gives

$$\frac{dE_1}{dt} = \left(\frac{4\pi^3 p\nu_o}{3Vh\Delta\nu_o}\right) E_1 (\alpha N - \beta NE_1^2 - \theta NE_2^2) \qquad 5.42$$

which may be written in the familiar form (c.f. Eqns 5.7 and 5.8)

$$\dot{E}_1 = E_1 (\alpha_1 - \beta_1 E_1^2 - \theta_{12} E_2^2) \qquad 5.42$$

The derivation of the coupled oscillator equations will not be pursued further here, and in what follows they will be assumed to be applicable

to the molecular beam maser. It will be seen that there is strong experimental evidence that this is so.

An interesting point emerges in connection with the application of these equations to the maser. The time constant for re-establishment of a population difference in the maser is related to the average time of flight of a molecule through the cavity. In consequence recovery of the maser after level depletion must take of the order of 300 μs. Hence the non-linear effects which result from the β and θ terms of the equations cannot occur at frequencies much above 3 KHz. This restriction should apply to amplitude fluctuations of the maser oscillations, but not to the beat phenomena which result from their different frequencies.

Consider now the frequency behaviour of the Zeeman maser in connection with the Zeeman laser theory. Although the independent oscillations of the maser and of the laser exist because of the mode degeneracy of the cavity, the effect of the cavity on their frequencies is rather different. It has been seen in Sec. 5.3.1 that the Zeeman laser beat frequency is considerably affected by the cavity pulling. In the maser the frequency width $\Delta\nu_c$ of the cavity resonance is much larger than the natural width $\Delta\nu_\ell$ of the spectral line so that Eqn. 5.5 must be rewritten

$$\nu \simeq \nu_\ell + (\nu_c - \nu_\ell)\, \Delta\nu_\ell/\Delta\nu_c \qquad 5.44$$

(Gordon et al, 1955). In the laser the oscillation frequency is controlled largely by the cavity resonance and is merely perturbed by the spectral line. Eqn. 5.44 shows that in the maser the converse is true; the

oscillation frequency is controlled by the spectral line and is perturbed by the cavity resonance.

The beat frequency which would be observed between the two Zeeman components of a maser transition can be represented, analagously to Eqn. 5.6.

$$\Delta\nu = \frac{2g\mu_m B}{h}\left(1 - \frac{\Delta\nu_\ell}{\Delta\nu_c}\right) \qquad 5.45$$

In the ammonia maser $\Delta\nu_\ell$ is typically 5×10^3 Hz while $\Delta\nu_c$ is about 1×10^7 Hz. The Zeeman beat frequency $\Delta\nu$ is therefore reduced by a negligible factor of about 0.9995, due to cavity pulling.

In chapter 4 the anisotropy of the cavity and the preferential orientation of the molecular beam were treated separately. However both were seen to affect the polar diagram of excitation parameter, represented by Eqn. 4.17, in a similar way. Thus the anisotropy terms in the coupled oscillator equations represent the effects of both mechanisms, although for convenience they have been written in terms of the linear Q-values Q_x and Q_y. In chapter 4 it was seen that the preferential orientation had the greater effect on the polar diagram of excitation parameter. Since the preferential orientation of the molecular beam is along the x-axis, it is assumed in what follows that $Q_x > Q_y$. It will be seen that the anisotropy locking of the oscillations represents the preference of the oscillation ellipse major axis to lie in the x-direction.

5.4.2 The Static Characteristics and the Hysteresis Phenomena

In Fig. 5.12 one half of the experimental curves presented in Fig. 5.3 (the half for negative values of magnetic field H) is

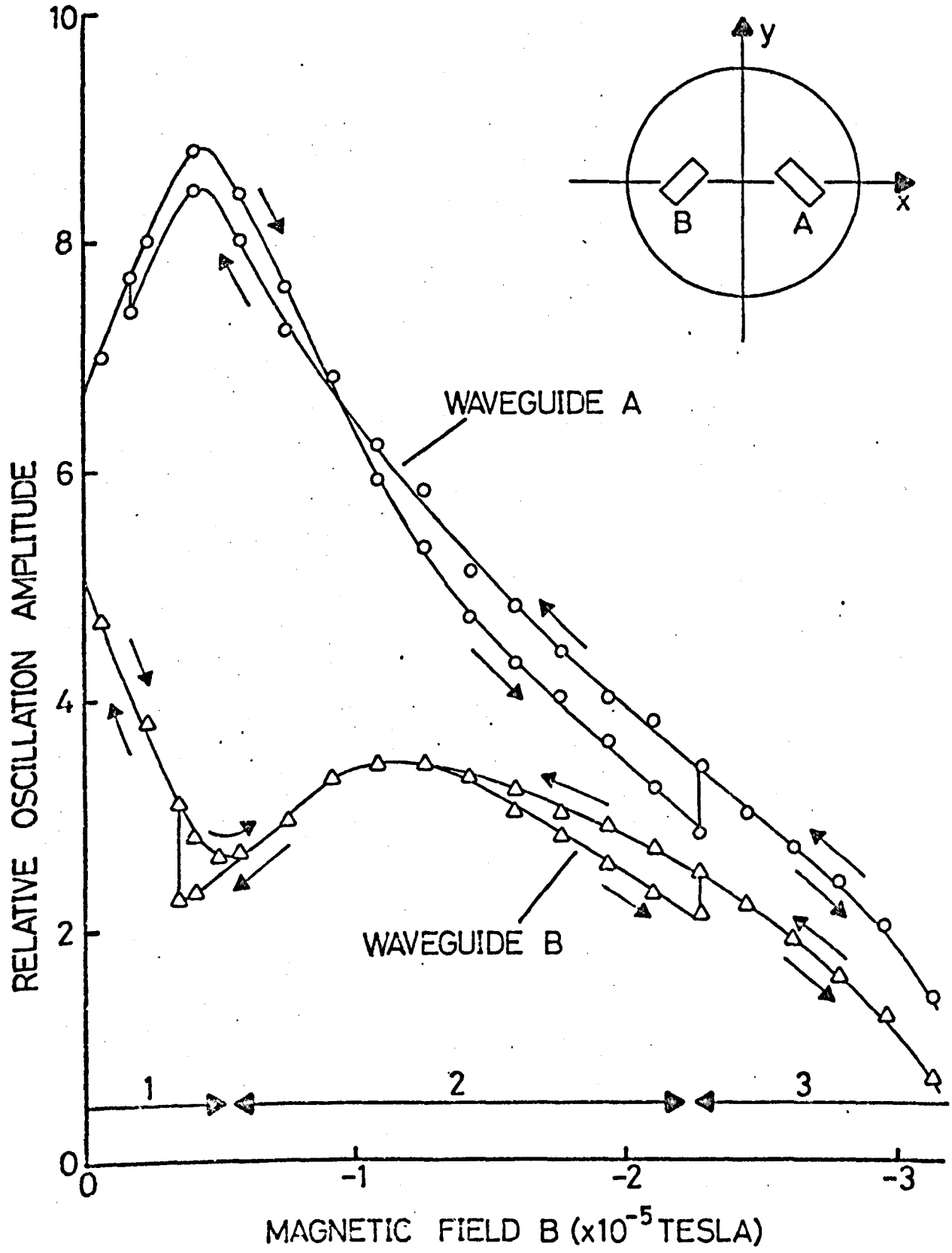

Fig. 5.12 Static magnetic characteristics drawn for negative values of magnetic field B showing the hysteresis jumps and indicating the regions 1, 2 and 3.

redrawn in order to include hysteresis phenomena which were noticed during the measurements. For convenience the two curves have not been normalised. From this graph it can be seen how Fig. 5.3 was drawn using only the maximum values of the signal amplitudes recorded for any given value of magnetic field.

The measurements show two distinct hysteresis jumps, each recorded in both waveguide orientations, -45° and 45°. The fact that the corresponding jumps do not appear at exactly the same value of magnetic field on the two curves is due to experimental error. At the time of measurement only one I.F. system (preamplifier and amplifier) was available so that the two sets of measurements representing the two curves could not be recorded simultaneously. Normal apparatus drifts account for the discrepancy. The hysteresis jumps were difficult to observe consistently, although sufficient evidence was gathered to confirm that Fig. 5.12 shows a complete set of all those jumps which it was possible to observe. Associated with each of the jumps was a transient beat signal similar to the magnetic transient.

The static characteristics will be discussed in terms of the three regions 1, 2 and 3 which are shown in Fig. 5.12. The discussion is intended to be as relevant to positive field values as it is to the negative values shown in this figure.

The region 1 is explained by the coupled oscillator theory as a region of anisotropy locking. Assuming that the ellipticity of the oscillating polarisation remains at the value of 0.85 measured from Fig. 5.3 (see Sec. 5.2.1) the inclination of its major axis to the

x-axis may be obtained from the same graph. This measured inclination is shown plotted against magnetic field in Fig. 5.13, where the result is compared with the expected behaviour given by Eqn. 5.34. The expected behaviour has been calculated using measured values for the function a in the equation. These measurements of the low field Zeeman splitting of the ammonia 3,3 line are described in the next section. The value of the critical field B_c, which was chosen in order to perform the calculations, is 4.65×10^{-5} T. This is the mean of the positive and negative values of field at which the oscillation ellipse is observed to reach inclinations of -45° and 45° respectively. The discrepancy between the observed behaviour and the expected behaviour in Fig. 5.13 can be attributed to changes in the ellipticity of the oscillating polarisation, but is probably also associated with the transition to the second locking region 2, which is described below.

It is instructive to consider the direction in which the ellipse is expected to rotate in the x - y plane. In the presence of a magnetic field and for transitions associated with emission of energy, such as those which occur in a maser, a $\Delta M = -1$ transition has a higher frequency than a $\Delta M = +1$ transition. The term a of Eqn. 5.32 is essentially given by

$$a = \sigma_+ - \sigma_- \qquad 5.46$$

where σ_+ and σ_- represent respectively the frequency separations of the modes with positive and negative angular momentum with respect to the z-axis. In a positive axial magnetic field (i.e. directed along the z-axis) these correspond to the $\Delta M = +1$ and $\Delta M = -1$ transitions, while in a negative field they correspond to the $\Delta M = -1$ and $\Delta M = +1$ transitions, respectively. It

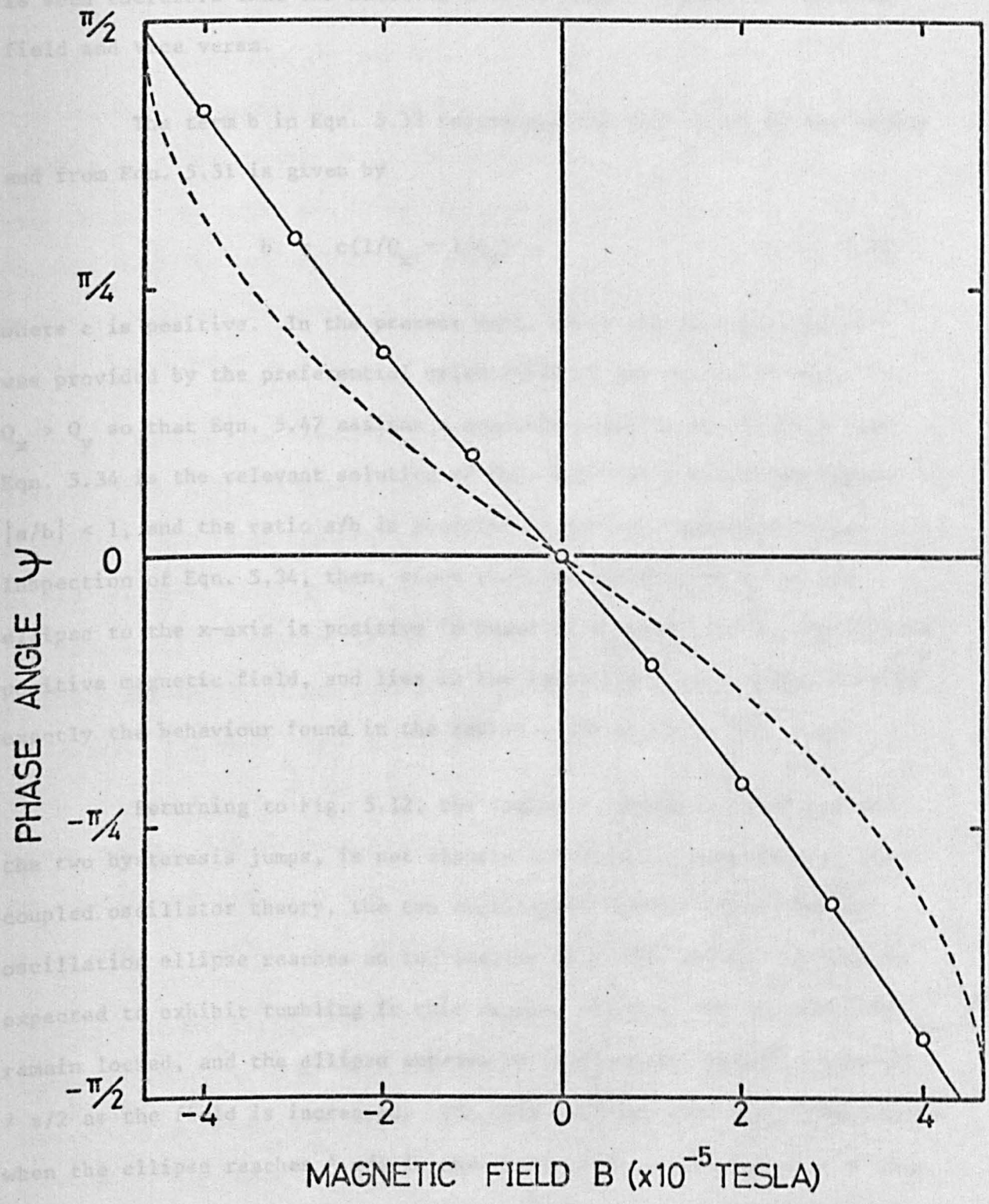

Fig. 5.13 The angle Ψ obtained by measurement of the inclination $1/2\,\Psi$ of the oscillation ellipse (solid line), together with a curve calculated from Eqn. 5.34 (broken line).

is seen therefore that the function a has a negative value in positive field and vice versa.

The term b in Eqn. 5.32 represents the anisotropy of the cavity and from Eqn. 5.31 is given by

$$b = c(1/Q_x - 1/Q_y) \qquad 5.47$$

where c is positive. In the present work, where the main anisotropy was provided by the preferential orientation of the molecular beam, $Q_x > Q_y$ so that Eqn. 5.47 assigns a negative value to b. In this case Eqn. 5.34 is the relevant solution of Eqn. 5.32 for the locking region $|a/b| < 1$, and the ratio a/b is positive in positive magnetic field. Inspection of Eqn. 5.34, then, shows that the inclination $\frac{1}{2}\psi$ of the ellipse to the x-axis is positive in negative magnetic field, negative in positive magnetic field, and lies in the range $\pi/4 > \frac{1}{2}\psi > -\pi/4$. This is exactly the behaviour found in the region 1 and shown in Fig. 5.13.

Returning to Fig. 5.12, the region 2, which is found between the two hysteresis jumps, is not clearly understood. According to the coupled oscillator theory, the two oscillators should unlock when the oscillation ellipse reaches an inclination of $\pm \pi/4$, and the ellipse is expected to exhibit tumbling in this region. Instead the oscillations remain locked, and the ellipse appears to continue its rotation towards $\pm \pi/2$ as the field is increased. The only evidence that something happens when the ellipse reaches $\pm \pi/4$ is the observation of the hysteresis jump. That both circular oscillations continue to be supported by the maser in the region 2, is evidenced by the oscillation polarisation remaining elliptical.

In order to explain this phenomenon a second locking mechanism may be postulated. As the magnetic field is increased, the transition from one locking mechanism to the other appears to be smooth. When the field is returned towards zero, the second mechanism continues to hold the ellipse until the anisotropy locking has gained strength. Then the ellipse flips into anisotropy lock. The nature of the second locking mechanism will not be considered further here, but it will be discussed in Sec. 5.4.4 and Sec. 6.3.

Region 3 is easily explained on the basis of the first phase diagram (Fig. 5.8) which describes inhibition, or capture, of the oscillation which has the smaller amplitude. The two circular oscillations were known to have different amplitudes during these measurements because otherwise a linear oscillation polarisation would have been observed. This was probably due to slight mis-tuning of the cavity. At the higher values of field used, the oscillation amplitudes were reduced by broadening of the spectral line due to the magnetic field inhomogeneity (measurements of the inhomogeneity will be found in Appendix A). According to the discussion of Sec. 5.3.3, inhibition of the oscillation with the smaller amplitude should occur when its oscillation amplitude becomes sufficiently small.

In the region 3 the oscillation polarisation is observed to be circular, which is to be expected if only one of the two oscillations is present. The second hysteresis is interpreted as the onset of mode inhibition, i.e. mode capture. When the magnetic field is changed in the reverse direction (towards smaller field strengths) the second oscillation builds up from noise without the appearance of a jump in amplitude.

5.4.3 The Magnetic Transients and the Low Field Zeeman Effect

From the discussions of the previous section it is clear that the magnetic transients recorded under oscillation conditions represent the return of the coupled oscillator system to a locked condition after displacement from this equilibrium. If the anisotropy terms of Eqns. 5.27 and 5.28 can be ignored, then the phase diagram for the weakly coupled system (Fig. 5.9) describes the amplitude behaviour. In terms of this phase diagram, the stimulation of the maser by a strong linearly polarised signal corresponds to displacement of the oscillator system to a phase point (X_o, Y_o) which lies on the trajectory $X = Y$. The approach of the system to equilibrium, following the displacement, occurs along the trajectory $X = Y$ at a rate governed by the α's β's and θ's of the equations. In the maser this approach to the steady state is expected to occur in a time of the order of that taken by an average molecule to traverse the cavity.

The transient frequency behaviour of the maser is more interesting. The approach to the frequency locked condition takes many times longer than the approach to amplitude equilibrium. Indeed transient beats have been observed continuing right through one cycle of a 50 Hz repetitive sweep with no sign of diminishing. The fact that the number of cycles of the beat observed on successive stimulations of the line varied widely, seems to indicate that the effect is sensitive to the phase of the stimulating signal relative to the phases of the oscillations which already exist in the cavity. In this respect it is noteworthy that no such instability of the transient was observed below oscillation threshold. The transient solution of the frequency determining equations 5.29 and 5.30 appears to be a problem of considerable interest. The present work however is confined to discussion of the

observed transient signals.

The frequency of the transient modulation appeared to be a function of the magnetic field strength only. No dependence on other parameters, in particular the tuning of the cavity, was detected in the range of frequencies measured (300 Hz to 5400 Hz). Since tuning the cavity is expected to affect its anisotropy (see Sec. 5.4.4), this provides experimental evidence that the transient beat frequency does not depend appreciably on the anisotropy term in Eqn. 5.31. Some further evidence in support of this premise is the observation of the magnetic transient effect in an ammonia beam maser having a cylindrical cavity (Lefrère, 1973). In such a maser the coupling between the two oscillators is much greater than in the Fabry-Pérot maser, and it is expected that any effect due to the coupling will be accentuated, The frequencies observed in the present work and in Lefrère's have not been precisely compared, but they are known to exhibit the same general behaviour.

In the absence of any effect due to anisotropy, the frequency of the magnetic transient should be equal to the beat frequency between the two oscillations in an isotropic cavity. This frequency is $a/2\pi$, where from Eqns. 5.31 and 5.32

$$a = \sigma_+ - \sigma_- + \rho_+ E_+^2 - \rho_- E_-^2 + \tau_{+-} E_- - \tau_{-+} E_+^2 \qquad 5.48$$

Thus the magnetic transient provides a means of determining the function a.

If the coefficient ρ_+, ρ_-, τ_{+-}, τ_{-+} in Equation 5.48 are negligible, or if the amplitudes E_+ and E_- of the oscillations are sufficiently small, this function is the natural Zeeman splitting $\sigma_+ - \sigma_-$.

Thus it should be possible to examine the low field Zeeman behaviour of ammonia using the magnetic transient.

Unfortunately the only example of a complete set of frequency measurements, which are available at the time of writing, were made with magnetic material probably present in the maser. They have however been checked against some isolated measurements made with the magnetic material removed, and no serious discrepancy has been found. The measurements are shown for positive values of magnetic field in Fig. 5.14. A mirror image of these results (to within 5% accuracy) were obtained for negative values.

The frequencies plotted in Fig. 5.14 are those of the beat envelopes observed. The beat frequency derives from tumbling of the oscillation ellipse at angular frequency $\frac{1}{2}\psi$ (see Sec. 5.3.4) and represents the projection of the tumbling ellipse on the waveguide direction. In one rotation of the ellipse, two cycles of the beat envelope are traced out, giving the angular frequency of the beat as $\dot{\psi}$. Thus the frequency of the modulation envelope corresponds to the frequency difference $a/2\pi$ between the two Zeeman components. The curve shown in Fig. 5.14 has been used to calculate the expected behaviour of the static oscillation ellipse as was described in Sec. 5.4.2.

In Eqn. 5.32 the direction of the tumbling is determined by the sign of the function a. The argument of the previous section showed that this sign is negative for positive field values and vice versa. Experimentally (see Sec. 5.2.2) the sign of the rotation vector with respect to the positive z-direction was found to exhibit the same behaviour.

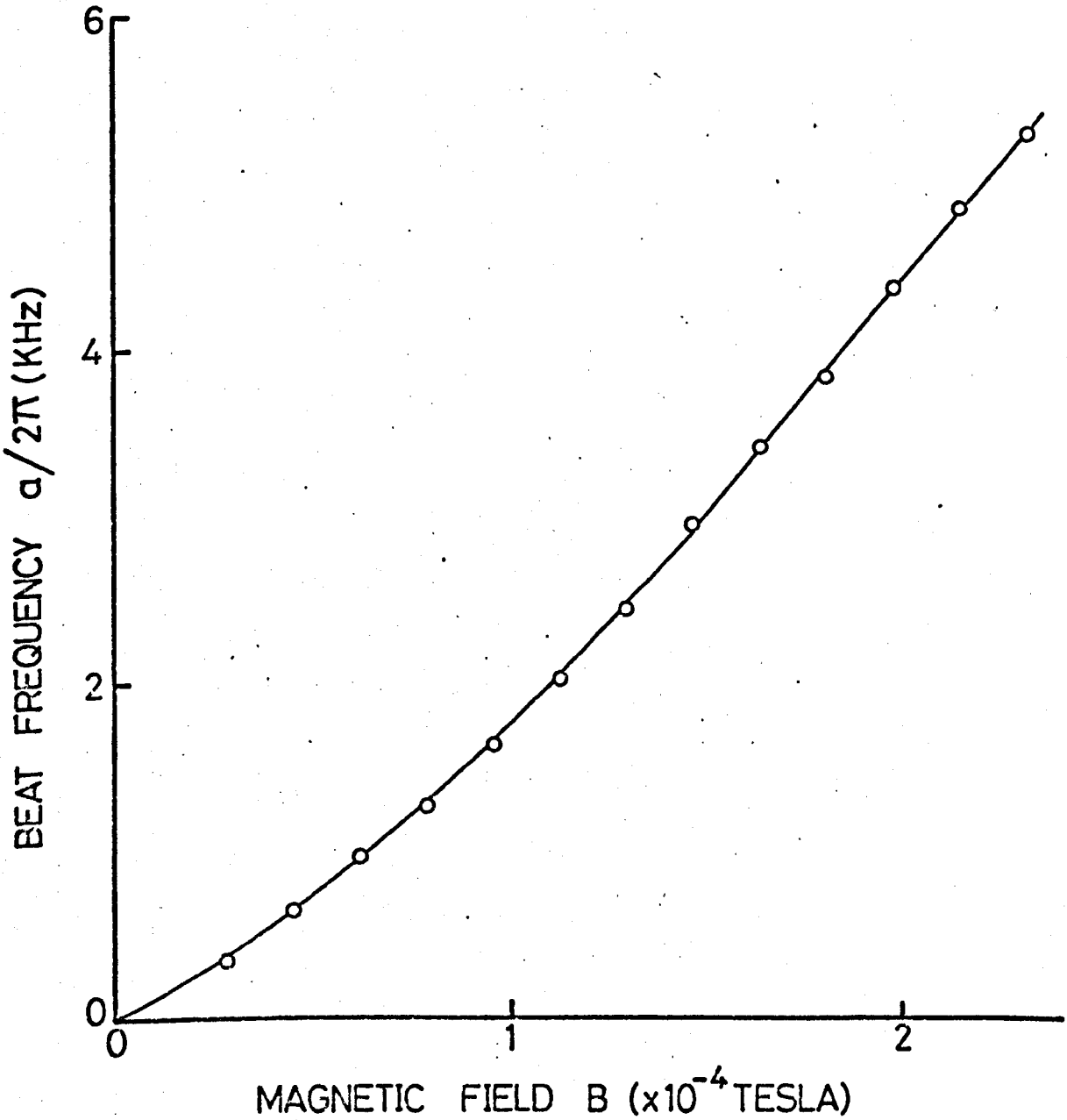

Fig. 5.14 Observed beat frequency of the magnetic transients plotted against axial magnetic field strength.

5.4.4 The Dynamic Characteristics and Control of the Anisotropy

The coupled oscillator theory predicts that tumbling of the oscillation ellipse will take place when the magnetic field strength is greater than the critical value B_c (i.e. when the Zeeman splitting term a in Eqn. 5.32 is larger than the anisotropy coefficient b). However it has been seen that in the maser the two oscillations do not unlock, and the existence of a second locking mechanism acting in the region 2 of Fig. 5.12 has been postulated to explain this discrepancy. The dynamic characteristics described in Sec. 5.2.3 are only observed for small values of the magnetic field strength (below about 5×10^{-5} T), in which the oscillations should be locked by the cavity anisotropy.

However a means by which the cavity anisotropy may be changed exists in the Fabry-Pérot maser. In Sec. 1.4.4 the three-armed frame which is an important component of the mechanical fine tuning mechanism was described. This frame, which transmits the tuning movement to the tuning mirror, was not constructed symmetrically because its shape was constrained by the size of the vacuum chamber. When the pressure on the frame is changed, not only is the mirror spacing altered thereby, but also a slight tilting of the tuning mirror about the vertical axis (the y-axis) takes place. The effect of such a relative tilting of the two mirrors must be to degrade the Q-value of the cavity Q_x for a mode linearly polarised along the x-axis, while leaving Q_y unchanged. By this preferential degrading of the cavity Q, it should be possible to cancel (or nearly so) the effect of the preferential orientation of the molecular beam, so that near isotropy of the cavity results. In such an isotropic cavity the oscillation ellipse should be free to tumble.

It is significant, then, that the dynamic characteristics were only observed for small ranges of parameters. Parameters such as coupling hole matching and waveguide orientation affect the Q-anisotropy of the cavity. It has been seen in chapter 4 that the preferential orientation of the molecular beam depends on the state separator voltage. It is particularly significant that the effect was found to be extremely sensitive to tuning of the cavity carried out using the fine tuning mechanism. Clearly, all of these parameters affect to a greater or lesser extent the balance of anisotropy mechanisms in the maser.

This explanation may also hold an important clue to the nature of the second locking mechanism. In order that tumbling of the oscillation ellipse shall occur for the magnetic field values mentioned above (-5×10^{-5} T to 5×10^{-5} T), the mechanism must be effectively inactive for this narrow range of magnetic field strength close to zero. The inference is that the locking mechanism is associated with the magnetic field itself.

If the explanation of anisotropy balance is correct, the maser can be brought close to the point at which locking occurs throughout the range of magnetic field mentioned, simply by manipulation of the maser parameters. The computer simulation of the coupled oscillators carried out by Tomlinson and Fork, 1967, reveals that some interesting effects occur near this point. Some of these effects have been briefly described in Sec. 5.3.5. Non-uniform tumbling of the oscillation ellipse is found to produce waveforms similar to those shown in Figs. 5.5(b), (c) and 5.6(d). Also alternate locking and unlocking of the oscillators occurs. This can explain the curious waveforms observed in Fig. 5.7 since the spike, clearly observed in Figs. 5.7(b) and 5.7(c), can be associated with a sudden change in the condition of the oscillators.

CHAPTER 6

DISCUSSION AND SUGGESTIONS FOR FURTHER WORK

6.1 THE CAVITY

A molecular beam maser employing a Fabry-Pérot cavity is normally operated with a mirror separation of $\lambda/2$ or λ. This is in contrast to the use of the cavity in a laser where the longitudinal mode order is very high. The masers of Barchukov et al, 1963 and Krupnov and Skvortsov, 1964 for example, were operated with mirror separations of λ and $\lambda/2$ respectively. In the present work a separation of $\lambda/2$ was used exclusively because no improvement in cavity Q could be obtained by using a separation of λ.

These small separations are used because of the difficulty of engineering a high filling factor using molecular beams passing through the active region of a large cavity. Also the use of a longitudinal mode order of 1 or 2 avoids the effect of nodal plane crossing by the molecules of the beam. Since there is a phase reversal of the radiation field seen by a molecule, as it crosses one of the nodal planes which lie parallel to the mirror surfaces, a molecule which is emitting radiation to the field before it crosses will absorb radiation from the field afterwards. Its net contribution to the radiation field may be close to zero. It is permissible to operate a maser with a cavity separation of λ, so long as the plane of symmetry of the state separator

is aligned with the nodal plane in the centre of the cavity. Mirror spacings of $3\lambda/2$ and above, however, will not usually be advantageous without a system of baffles to collimate the state separated molecular beam and remove those molecules which would otherwise cross nodal planes.

The theoretical work and much of the experimental work in the literature dealing with open resonators is oriented towards cavities for lasers. Some experimental studies have been performed in the region of interest to the present work, but no comparisons with the theory have hitherto been made. The work which has been presented in chapter 1 represents an attempt to fill this gap, and also to establish techniques for further studies of open resonators in the microwave region.

As a result of this work, it is possible to predict with some confidence the Q-factors of plane parallel Fabry-Pérot cavities built for the microwave region. Suppose, for example, a cavity with copper mirrors is to be designed for use at a wavelength of 12.5 mm, so that the theoretical diffraction loss at a mirror separation of $\lambda/2$ is only 10% of the total loss. The conduction loss Q, Q_c is given by Eqns. 1.12 and 1.15. Using the values, $\sigma = 5.99 \times 10^7$ ohm^{-1} m^{-1}, $\mu = 1$, $\nu = 2.4 \times 10^{10}$ Hz, $q = 1$, Q_c is found to be 7500. It was found in Sec. 1.5.3 that the theoretical diffraction Q had to be reduced by a factor of 0.7 to fit the measured values. By applying the same factor to the example considered here, Q_d is reduced from 67500 to 47200, and the expected unloaded Q becomes 6530. If two coupling holes each with a coupling coefficient of 0.05 are to be constructed, then the expected loaded Q is 5940. The Vainshtein theory predicts that a mirror diameter of 240 mm is necessary

in order to obtain a diffraction loss Q of 67500.

In Sec. 1.2.6 it was seen that the surface accuracy required for the mirrors can be estimated with the help of an empirically determined flatness criterion, K. A value of 0.3 was determined for this criterion. Using this value in the above example indicates that the mirror surfaces need to be flat to $\pm$ 3 x 10^{-4} mm approximately. The experience gained in the present work indicates that so long as such a restriction applies to any overall convexity of the mirror, departures from flatness of greater vertical deviation can be tolerated over small areas.

The construction of a Fabry-Pérot cavity with large mirrors, such as that described in the example above, will enable the operation of an ammonia beam maser at higher levels of oscillation. This, together with equipment to provide a more uniform magnetic field in the maser, will enable the work with the Zeeman maser to be pursued to higher field strengths. It should also enable work in the TEM_{10} mode, and perhaps in higher modes, to be carried out under oscillation conditions. In this respect, it will be interesting to make further comparisons of cavity Q with the theory in these higher modes.

One particular aspect of the construction of the present cavity which requires some attention is the tuning mechanisms. It will be important, if more precise work with the cavity is to be carried out in the future, to provide improved mechanisms which enable accurate and reproduceable setting of the cavity.

Some interesting studies of open cavities with other than plane parallel mirrors should be possible using the techniques described in chapter 1. One cavity which should prove ideal for use in molecular beam

masers is the flat-roof resonator of Toraldo di Francia, 1965. This combines the low loss associated with closed cavities with the open structure of the Fabry-Pérot cavity. However the mode degeneracy effects described in this work could not be studied using such a resonator. Some preliminary work has already been performed by the Author to investigate a semi-conical type of resonator using the equipment described in this thesis (Lainé and Smart, 1971).

6.2 THE MASER AMPLIFIER

The work described in chapter 4 has successfully established an experimental technique for examining the preferential orientation (anisotropy) of the molecular beam. Two points about the technique which should be emphasised are the following. First, the method of normalisation described in Sec. 4.3.2 (see in particular Eqn. 4.18) relies on the correctness of the dependence of η on Q given by Eqn. 4.11. It is important to perform this normalisation, in order to study the anisotropy of the beam alone, rather than the combined anisotropy of beam and cavity. Second, in order to carry out the normalisation, an accurate method for measuring the loaded Q of the cavity must be available.

Eqn. 4.11 is derived from the simple univelocity theory, but the dependence of η on Q which it shows is fundamental to any theory of the maser amplifier. This dependence does not appear to have been checked experimentally, presumably because emphasis in the past has been on the maser as an oscillator rather than as an amplifier. The Fabry-Pérot maser is the ideal equipment with which to measure it, because significant changes in the Q of the cavity can be caused, without off-tuning the

cavity, by only slightly tilting the mirrors relative to one another. If their relative tilt can be controlled from outside the maser vacuum chamber, while keeping other parameters of the maser constant, then the measurement of the $\eta|Q$ relationship can be accomplished. Unfortunately this is not possible with the present cavity, because the three tuning micrometers cannot be controlled from outside the chamber, and the thermal tuning units do not provide sufficient tuning range. It may be practicable to perform the experiment using a conventional maser, by off-tuning its cavity. A transmission cavity operating in the E_{010} mode would be required for such a maser.

Two anomalous behaviours have been observed during the experimental work described in this thesis. The first concerns the behaviour of the ratio $\eta_o(0)/\eta_o(\theta)$ for $\theta = 45^o$ when the state separator voltage is changed (see Sec. 4.3.2). This was tentatively ascribed to electric field, or electric and magnetic field, spatial reorientation effects in the region of the fringe field of the state separator. The second is the persistence of phase locking of the coupled oscillations, in magnetic field strengths for which the coupled oscillator theory predicts that spontaneous tumbling of the oscillation ellipse should occur (see Sec. 5.4.2). A second locking mechanism, caused in some way by the presence of the magnetic field, was tentatively postulated to explain this anomaly.

Therefore, an important priority in planning further work with the Fabry-Pérot maser, must be to examine the phenomenon of spatial reorientation and its effect on the anisotropy of the molecular beam. Measurement of the normalised excitation parameter with many different waveguide orientations (e.g. every 15^o from -90^o to $+90^o$) would allow a complete polar diagram of the molecular beam anisotropy to be constructed.

A set of such polar diagrams, measured for different magnetic field strengths and/or separator voltages, would amount to a precise study of the effects of spatial reorientation due to these variables.

Examination of spatial reorientation caused by the separator fringe field is not limited to separator voltages below the normal threshold of oscillation (as were the measurements described in chapter 4). Krupnov and Skvortsov, 1965D measured excitation parameters at higher separator voltages by using reduced beam intensity. Spatial reorientation effects due to electric fields other than the separator fringe field, applied in the path of the molecular beam in the manner of Basov et al, 1964, could also be studied precisely using this technique.

Thus it can be seen that determination of the normalised excitation parameter constitutes a powerful technique for the elucidation of some of the mechanisms present in the molecular beam maser. In particular it provides a means for making quantitative measurements of the effects of electric and magnetic fields on a molecular beam. Previously these effects have only been studied qualitatively.

6.3 THE MASER OSCILLATOR

The work described in Chapter 5 has made a useful contribution towards a complete understanding of the behaviour of the oscillating Fabry-Pérot maser. It has been seen that some of the effects observed can be caused by magnetic fields of smaller magnitude than the Earth's field. This is relevant to an explanation of the low frequency (∿600Hz) biharmonic behaviour reported by Barchukov et al, 1964, which in the light of the present work appears to have been due to the dynamic characteristic discussed in Secs. 5.2.3 and 5.4.4.

The high frequency (∿3.8KHz) beat which they noticed is not explained by the magnetic behaviour, however, because a field strength of approximately 1.7×10^{-4}T would be needed in order to produce it. A possible explanation is operation of the maser in a high order mode of the cavity (i.e. TEM_{10} or higher), when a doppler split line is observed in stimulated emission (Krupnov and Skvortsov, 1965A). Becker, 1965 observed a hysteresis jump between two single frequency modes of oscillation when using the E_{013} mode of a cylindrical cavity, but it is by no means certain that biharmonic oscillation cannot establish itself in a high order mode. The maser of Barchukov et al actually oscillated in the TEM_{00} mode, but they indicate that another mode, presumably the TEM_{10}, which had a Q of 1000 and a frequency separation of 20MHz from the first, was also present in the cavity. This mode, then, overlapped the oscillation frequency of the maser so that some of the oscillation field must have coupled to it. The microwave field which established itself in the cavity was presumably

a sum of the radiation fields in both the modes, in which case the spectral line shape should have some of the characteristics of a doppler split line. With the present maser, no effect due to the TEM_{10} mode was observed, but the Q of this mode was somewhat higher than in the cavity of Barchukov et al.

An alternative, but similar explanation is doppler splitting of the line due to the effect of nodal plane crossing by some of the molecules. In Sec. 6.1 it was remarked that nodal plane crossing can occur in a maser which uses a mirror separation of λ, if the state separator axis is not aligned with the central nodal plane of the cavity. It should be possible to investigate the effect of nodal plane crossing in the present maser, but at the time of writing it is not known whether the maser will oscillate in the TEM_{002} mode using the present cavity.

One important mechanism, which was not discussed in Chapter 5 and which is known to be present in the maser, is the spatial reorientation which occurs in a magnetic field (see Sec. 2.4.3). Calculation shows that the inhomogenity of the magnetic field applied using the rectangular Zeeman coils (see Appendix A), is such that the main Fourier component seen by a molecule, travelling through the field region with a velocity of 5×10^5 mm.s^{-1}, is 20Hz. This frequency is an order of magnitude smaller than the precession frequency calculated in Sec. 2.4.3 for an ammonia molecule with J=3, K=3 in a uniform magnetic field of 1×10^{-4}T. Thus precession of the molecules in the field is an accurate description of the spatial reorientation effects which occur for fields greater than 1×10^{-4}T and is probably a good approximation for fields above 1×10^{-5}T.

The state separator fringe field is expected to extend almost to the edge of the cavity in the present apparatus, so that precession only starts when the molecule enters the cavity. In a magnetic field of 1×10^{-4}T the precession rate is 770 rad.s^{-1}, so that an average molecule precesses through an angle of 0.23 rad., during its transit across the diameter (150mm) of the cavity. The effect of this precession on any processes occurring in the cavity, is probably similar to that of a precession through one half of this angle, but which occurs outside the cavity. However, two "smearing" effects may have to be taken into account, one due to the velocity distribution in the molecular beam and the other due to the precession's occurring within the cavity. For example, the polar diagram of preferential orientation will not only be rotated in the x,y plane of the apparatus, as a result of magnetic spatial reorientation, but will also have its anisotropy reduced, and possibly destroyed if the applied magnetic field is large. It should be possible to measure this effect accurately in the experiments described in Sec. 6.2.

The magnetic moment of ammonia is negative so that its direction of precession is positive in a negative magnetic field and vice versa. The angle between the axis of preferential orientation and the x-axis, therefore, has the same sign as that between the oscillation ellipse and its axis of anisotropy locking. Since the preferential orientation probably provides the main anisotropy locking mechanism, it is seen that spatial reorientation can increase the angle between the oscillation ellipse and the x-axis. However, the magnitude of the effect is rather small. In a field of 4.65×10^{-5}T, at which value the oscillation ellipse was observed to reach an angle of $\pm\pi/4$, it only contributes 0.06 rad or 3.1° to the

inclination of the ellipse. In addition it cannot explain the presence of the first hysteresis jump shown in Fig. 5.12, and therefore does not contribute to an understanding of the locking region 2 shown in this diagram.

Consider the magnitude of the Zeeman splitting in comparison with the spectroscopic linewidth of the maser. The full linewidth is given by $\Delta\nu_\ell \simeq 1.2\bar{v}/L$ (Shimoda et al, 1956), where the mean molecular velocity $\bar{v} \simeq 5 \times 10^5 mm.s^{-1}$ and the length of the cavity in the direction of the beam $L \simeq 150mm$. These values give $\Delta\nu_\ell \simeq 4KHz$. The two spectral components due to the Zeeman splitting are expected to be clearly resolved when their frequency separation is equal to $\Delta\nu_\ell$. From Fig. 5.14 the value of magnetic field for which the splitting is 4KHz is found to be $1.9 \times 10^{-4}T$. Experimentally the splitting was just observed with a field of $1.53 \times 10^{-4}T$.

The theory of Logachev et al, 1968, which describes the Zeeman effect in a maser with a cylindrical cavity, suggests that two oscillations should be observed when the Zeeman components are resolved. In the Fabry-Pérot maser the two circular oscillations are present up to a field of $2.2 \times 10^{-4}T$, where mode inhibition of one of them occurs. Thus the second locking mechanism, acting in the region 2 of Fig. 5.12, has a strength at least comparable with that which locks the oscillations in a cylindrical cavity maser. Clearly the mechanism of molecular beam anisotropy does not have a strength of this magnitude, particularly since it is liable to be weakened somewhat at the higher values of magnetic field by the "smearing" effect of the preferential orientation.

Further work remains to be done, then, to elucidate the nature of the second locking mechanism. The exact behaviour of the oscillation ellipse as the magnetic field is changed may be the clue

to this nature. An experiment to observe this behaviour can be devised in the following way.

The microwave signals in the two coupling waveguides are related in phase and amplitude to the projection of the oscillation ellipse on the waveguide direction. If the phase relationship is maintained through two stages of mixing, firstly to an I.F. of 30MHz, and secondly to a frequency of a few KHz, the two signals derived from the waveguides can be applied to the x- and y- amplifiers of an oscilloscope. Lissajou figures which follow faithfully the polarisation of the microwaves in the cavity will be drawn by this arrangement.

Such a technique might also be used to study the shape of the ellipse during the observation of the dynamic characteristics. Since the ellipse tumbles at a frequency of a few hundred Hz, high speed photography would be needed in order to make recordings of its behaviour. The shape and angular velocity of the ellipse is expected to vary considerably as parameters which alter the anisotropy of the maser are changed. Some means of controlling the anisotropy in a known way must be found in order to make this study fruitful. Mechanisms for controlling the relative tilt of the cavity mirrors accurately in conjunction with measurements of Q in different directions might be used. Alternatively the anisotropy of the beam might be controlled in a measured way by spatial reorientation outside the cavity.

In the work described in this thesis, the Zeeman laser theory has been used to interpret the results of the maser. It should be possible to obtain useful information with the maser, which can be extrapolated to the equivalent laser systems. In particular, electronic

techniques such as the one described above, which cannot be used at laser frequencies, may contribute to an understanding of the behaviour of laser modes for which there are analogous modes in the maser.

APPENDIX A

PRODUCTION OF A MAGNETIC FIELD IN THE MASER

The purpose of the field coil assembly was to provide a known, uniform field within the maser cavity, at right-angles to the plane of the cavity mirrors (i.e. in the z-direction). Unfortunately the requirement of uniformity of the field could not be met because the shape of the coils was dictated by the geometry of the maser vacuum chamber and associated equipment. This in turn made it difficult to determine the effective value of the magnetic field strength provided by the coils, because the nature of the field averaging in the maser was not accurately known. However, the measurements described in this appendix show that the field strength probably varies by no more than 10% in the region in which its effect was important, and that its effective strength could be established to better than 5%.

The arrangement used consisted of a pair of rectangular coils to produce the field in the z-direction (coils A in Fig. A.1). In addition a second pair of rectangular coils were used to neutralise the vertical component of the Earth's magnetic field (coils B in Fig. A.1). The local Earth's magnetic field was found to lie almost exactly in the y - z plane. A very small x - component was deemed negligible, and indeed was later found to be of smaller magnitude than certain field inhomogeneities which could not be removed from the apparatus.

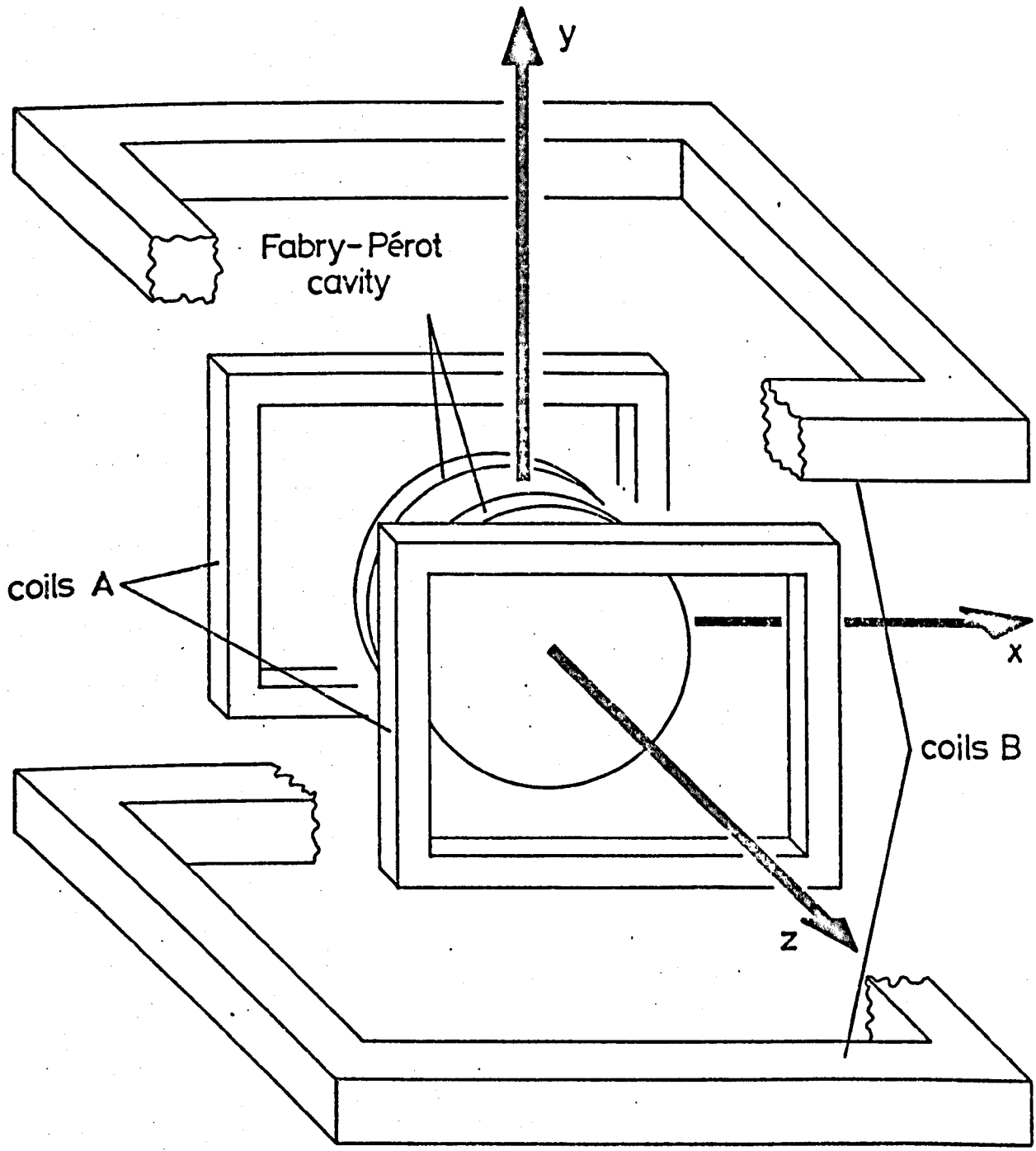

Fig. A.1 Arrangement of the rectangular coil pairs.

A pair of square coils may be used in a "Helmholtz" configuration for which both the first and second order differentials with respect to each of the x, y and z co-ordinates disappear at the centre of the coil pair (Rudd and Craig, 1968). The separation of the coils in such a configuration is 0.5445 x L, where L is the length of a side of the coils. Unfortunately the use of such a coil pair, or a conventional Helmholtz pair, was impossible without major structural changes to the maser. Both the coil pairs used were rectangular, although it was possible to approximate the geometry of the coils B fairly closely to the ideal.

Considerable local inhomogeneities in the field within and near the maser were largely removed by de-gaussing magnetic material comprising the apparatus (e.g. the diffusion pumps). When this had been done it was possible to neutralise the y-component of the Earth's field, leaving only small residual variations from zero of the field which were less than 5×10^{-6} T (the vertical component of the Earth's field is 2.9×10^{-5} T). The magnitude of these residual variations were checked from time to time during the experimental work with magnetic fields, and were never found to have significantly changed.

The inhomogeneity of the field produced by coils A was important, since this was the field used to investigate the Zeeman behaviour of the maser. A small computer program was written to calculate the expected field variation in the region between the cavity plates (i.e. in the x - y plane). This expected field variation is plotted in Fig. A.2, as a fraction of the value at the centre, along three different radii of the cavity - x = 0, x = y and y = 0.

In order to confirm that the expected field was not seriously

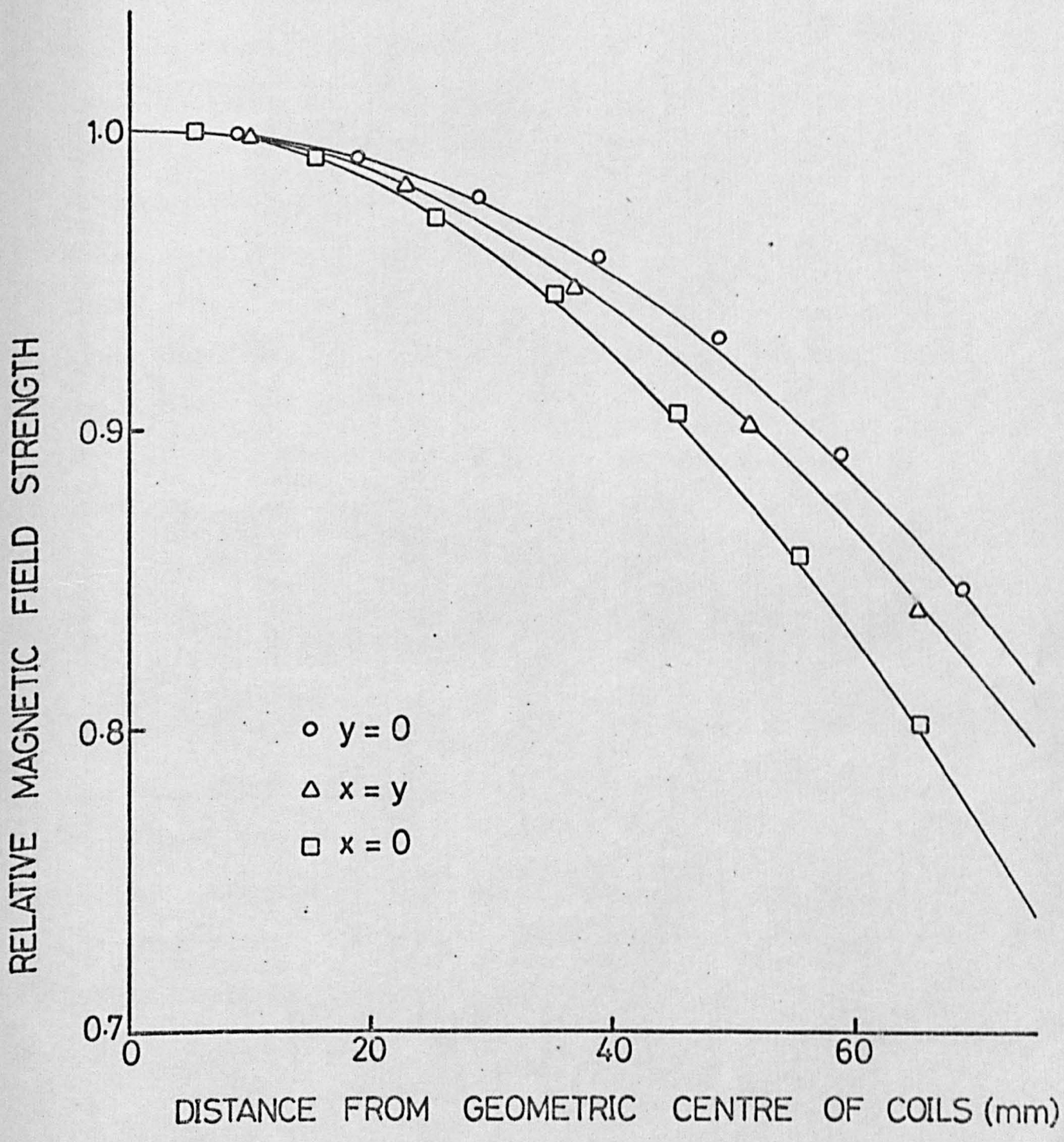

Fig. A.2 Measured (points) and computed (lines) relative magnetic field strengths along three radii $y=0$, $x=y$ and $x=0$ from the geometric centre of the rectangular coils A.

modified by the proximity of any magnetic material in the maser apparatus, an experimental check was made of the field produced by the coils. For this the signal from a small search coil of many turns with a mean area of 100 mm^2 was fed to a phase sensitive detector (Brookdeal PP313A/LA350). The reference for the P.S.D. and the current passing through the coil pair were both derived from an audio oscillator by suitable amplification. The frequency of the oscillator was set to 20 Hz, at which frequency the magnetic screening of the alternating field due to the conducting material of the maser vacuum chamber had previously been shown to be negligible. A frequency of 20 Hz was not satisfactory if the copper cavity mirrors were in place. Their screening effect was noticeable down to 2 Hz. The mirrors had to be removed, therefore, for the purpose of measurement. The magnetic properties of the copper mirrors, however, were negligible compared with some of the other materials, e.g. stainless steel and aluminium bronze, used in the construction of the maser.

This method of measuring the homogeneity of an alternating field produced by the coils was approximately 100 times more sensitive than could have been achieved using a conventional search coil and galvanometer with a direct current through the coils. It therefore enabled a search coil of small dimensions to be used, so that the field could be sampled with only a small spatial averaging. The results obtained are shown as the points in Fig. A.2 while the lines represent the computed field. The results confirm that there was little or no modification of the field by magnetic material in the maser. However they also indicate that the field near the edge of the cavity was as low as 75% of the field at its centre (along the radius $x = 0$).

The effective average magnetic field is difficult to determine. It must be a function of the following:

(i) The magnetic field distribution.

(ii) The microwave field distribution.

(iii) The distribution of the molecules in the cavity.

(iv) The effective contribution of the molecules at different positions in the cavity, which itself is a function of the beam intensity and the microwave field strength in the cavity.

However it is certainly true that the magnetic field in the central region of the cavity, where the microwave field is strongest makes the greatest contribution to the magnetic effects observed. It is probably also true that there are few, if any, contributing molecules present in the upper and lower regions of the cavity (i.e. for large $|y|$) owing to the shape of the molecular beam.

Measurements of the average field were made using a large search coil having many turns placed centrally between the mirrors of the Fabry-Pérot cavity. This coil had an effective diameter of approximately two-thirds of the cavity diameter, on the assumption that molecules outside the region defined by this diameter had little or no effect on the maser signal. Thus although the field strength could be as much as 25% low at the circumference of the cavity, compared with at its centre, the variation over the effective region was probably only 10%.

The average field strength, defined in this way, was determined as a function of the current through the coils by measuring the charge passing through a ballistic galvanometer connected to the coil, when the coil was quickly reversed between the cavity mirrors. The ballistic

galvanometer was calibrated in the usual way using a known change of current in the primary winding of a standard mutual inductance, whose secondary winding was in series with the coil and galvanometer. The method of reversing the search coil in the field enabled the Earth's horizontal component of magnetic field to be determined during the calibration of the rectangular coils.

It is interesting to note that the calibration of the field experimentally yielded a figure of $1.69 \pm .02 \times 10^{4}$ TA^{-1}, while the expected value obtained by computation was 1.708×10^{-4} TA^{-1}. A figure of 1.70×10^{-4} TA^{-1} was used during the experimental work described in this thesis. The measured value of the horizontal component of the Earth's and stray magnetic fields in the maser was $9 \pm 1 \times 10^{-6}$ T.

APPENDIX B

MEASUREMENT OF THE CAVITY COUPLING COEFFICIENTS

Two methods which have been used to measure the cavity coupling coefficients are described in this appendix.

The coupling coefficient for a cavity microwave port is generally determined by making voltage standing wave ratio (VSWR) measurements in the waveguide associated with the port. If a wave of voltage amplitude V_i, incident on a load, gives rise to a reflected wave of amplitude V_r, then the VSWR is given by

$$S = \frac{V_i + V_r}{V_i - V_r} = \frac{1 + V_r/V_i}{1 - V_r/V_i} \qquad \text{B.1}$$

Measurements of VSWR are of practical importance because they can be related directly to Z_o and Z_L where Z_o is the characteristic impedance of the waveguide transmission line and Z_L is the impedance of the load:-

$$S = Z_L/Z_o \qquad (Z_L > Z_o) \qquad \text{B.2}$$

$$S = Z_o/Z_L \qquad (Z_L < Z_o) \qquad \text{B.3}$$

If the load is a cavity resonator then its coupling coefficient is defined at the resonant frequency by

$$\beta = Z_o/Z_L \qquad \text{B.4}$$

Thus for an undercoupled cavity $(0 < \beta < 1)$, $\beta = 1/S$; for an overcoupled cavity, $(\beta > 1)$, $\beta = S$; while for a critically coupled cavity, $\beta = S = 1$. The cavity used in a molecular beam maser is normally undercoupled in order to provide a high value of loaded Q. For this case, Eqn. B.1. gives

$$\beta = \frac{1}{S} = \frac{1 - V_r/V_i}{1 + V_r/V_i} = \frac{1 - \rho^{\frac{1}{2}}}{1 + \rho^{\frac{1}{2}}} \qquad \text{B.5}$$

where $\rho = (V_r/V_i)^2$ is the power reflection factor of the cavity port at resonance. Thus, in the absence of equipment to make VSWR measurements, the power reflection factor may be used to calculate β.

Away from the resonant condition, the load presented by the cavity is infinite and all the power incident on the cavity is reflected - the reflection coefficient is unity. With a cavity such as the Fabry-Pérot which is easily tuned to a new resonant frequency, a comparison of the power reflected on resonance with that reflected off resonance can readily be made. The ratio of the two powers is just ρ.

The simple microwave arrangement which was used to compare the reflected powers is shown in Fig. B.1(a). The crystal B monitored the power reflected from the cavity; the value of the crystal current when the cavity was exactly on-tune was noted. The cavity was off-tuned far enough that it no longer absorbed power from the microwave circuit. The additional attentuation required at A to bring the crystal current reading back to its original value then gave the ratio of the two reflected powers. An attenuator calibrated accurately over a small range was needed at A since the reflection coefficient ρ was invariably close to unity.

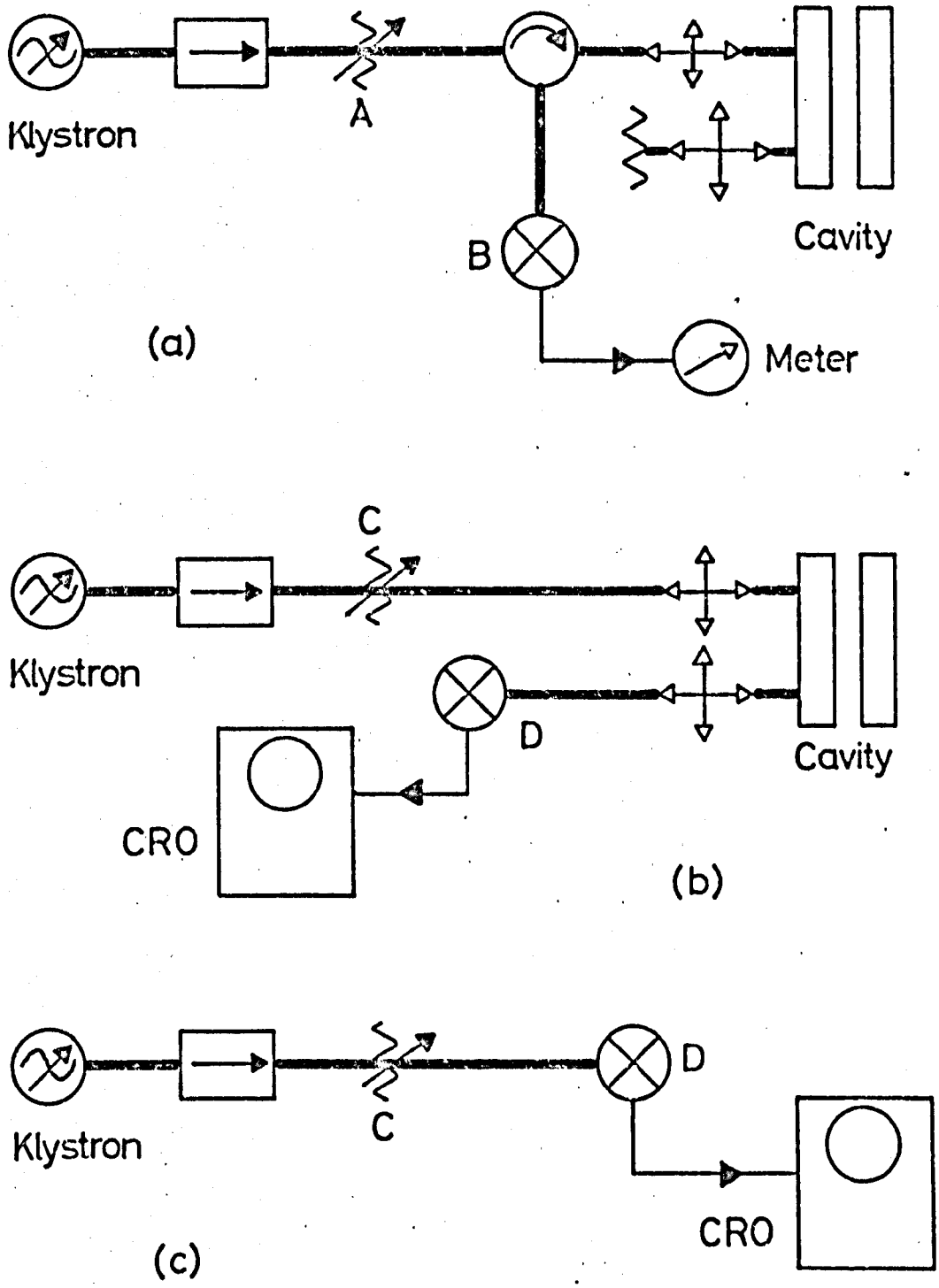

Fig B.1 (a) Microwave arrangement for measuring reflection coefficient.
(b) and (c) Microwave arrangements for measuring insertion loss.

The coupling coefficient β was obtained by substituting the experimental value of ρ in Eqn. B.5.

An alternative method which is useful when the cavity has two identical coupling holes is to make measurements of the insertion loss of the cavity at resonance. The power transmitted through a cavity P_t is given at resonance in terms of the incident power P_i by (Harvey, 1963B),

$$P_t = \frac{4\beta_1\beta_2 P_i}{(1+\beta_1+\beta_2)^2} \qquad \text{B.6}$$

where β_1 and β_2 are the two coupling coefficients. For identical coupling holes ($\beta_1 = \beta_2 = \beta$). Eqn. B.6 gives

$$L = \frac{(1+2\beta)^2}{4\beta^2} \qquad \text{B.7}$$

where $L = P_i/P_t$ is the insertion loss factor for the cavity at resonance. The common coupling coefficient β is given by the positive root of the quadratic equation B.7:

$$\beta = \frac{1 + \sqrt{L}}{2(L-1)} \qquad \text{B.8}$$

For very weak coupling ($\beta << 1$) the approximation

$$\beta = 1/\sqrt{L} \qquad \text{B.9}$$

is valid.

Measurement of the insertion loss of the cavity using the microwave arrangements shown in Figs. B.1(b) and (c) was straightforward. With the cavity in circuit - Fig. B.1(b) - and the klystron tuned to its resonant frequency, the voltage developed at the crystal D was observed.

The microwave arrangement was then changed to that shown in Fig. B.1(c) where the same crystal and crystal holder were used to monitor the power which had been incident on the cavity input port. The increase in attenuation at C, which was needed to bring the voltage now developed at the crystal to the same value as that observed previously, equalled the insertion loss, L, of the cavity. The common coupling coefficient, β, was then obtained by substituting L into Eqn. B.8 or B.9. For this method of measurement, the voltage developed at the crystal was monitored on an oscilloscope having a sensitive Y-trace amplifier. A 50 Hz sawtooth sweep was applied to the klystron to display its mode on the oscilloscope and the measurements were conveniently made at mode centre.

In order to use this second method it was necessary to be sure that the two coupling coefficients β_1 and β_2 were equal. Although the coupling holes of the Fabry-Pérot cavity were identical, the coupling waveguides were fitted with variable matching stubs which enabled the coupling at the two ports to be varied. Thus the method could only be used when either the matching stubs were completely withdrawn from the waveguides (minimum coupling), or they were both tuned for maximum transmission through the cavity (maximum coupling at both ports). In practice the latter was used.

APPENDIX C

MEASUREMENT OF THE CAVITY QUALITY FACTOR

The loaded Q-factor for a cavity may be determined with considerable accuracy by plotting the cavity response curve in reflection. Such a method, devised in collaboration with W.S. Bardo, is described by Bardo, 1969. It used a Klystron which was phase locked to a harmonic of a tuneable crystal oscillator whose frequency was measured with a digital frequency meter. The response curve was plotted in terms of calibrated attenuator settings by keeping the crystal current reading due to the reflected microwaves constant. The accuracy of this method depended on the calibration accuracy of the attenuator and on the depth of the cavity response. When used to measure the Q of the TEM_{00} mode of the Fabry-Pérot cavity, having a coupling coefficient of 0.115, and a loaded Q of 2400, its accuracy was estimated to be ±2%.

This method is too tedious to be useful where many Q measurements are required. It was therefore only used to confirm that there were no systematic errors in a second and quicker method. The latter, which involved the location of the half-power points of the cavity response on an oscilloscope display, is described here. It was found to be accurate to within ±5% for the range of Q values measured (1000 to 3000).

The loaded Q factor, Q_ℓ, is usually determined by measuring the frequency separation Δf between the half-power points on the cavity response curve and using the relation

$$Q_\ell = f_o/\Delta f \qquad \text{C.1.}$$

where f_o is the centre frequency of the response. Determinations of Δf may be made by tuning a source of constant microwave power across the response (observed in either transmission or reflection) and making frequency determinations at the half-power points. The difficulty invariably encountered when using a klystron as the power source, is that its power output is not constant with frequency across the reflector mode.

However, since the power delivered by a klystron at its mode centre generally varies only slowly with mechanical tuning of the klystron resonator, a source of microwave power, nearly constant with respect to frequency, may be achieved by using the mechanical tuning and always making measurements at the centre of the klystron mode. This method was employed here, using the microwave arrangement shown in Fig. C.1. The klystron reflector voltage was swept with a 50 Hz sawtooth waveform so that the cavity response, observed by transmission of microwave power through the cavity, could be displayed on the oscilloscope. The peak of the cavity response was placed at mode centre and its height noted. The attenuation at B was reduced by 3dB so that, when the two wings of the response curve were each brought to mode centre in turn by tuning the klystron, the half-power points could be readily located by finding the points on each wing which had the same height on the display as noted previously.

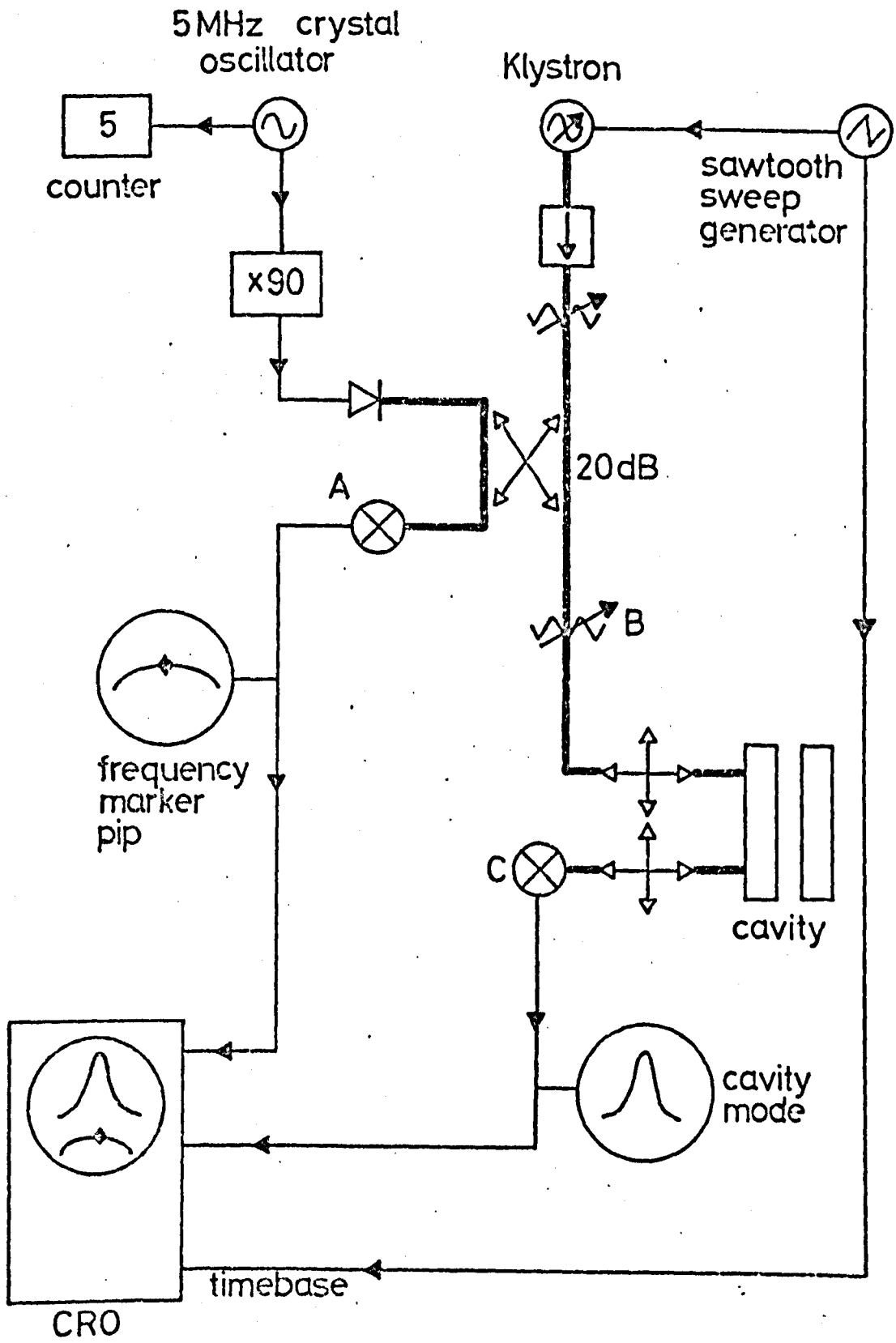

Fig C.1 Apparatus used to measure cavity Q.

The frequency determinations were made by displaying a marker pip, whose position could be adjusted to coincide with a half-power point, on the second trace of the twin-beam oscilloscope. The pip was the beat signal between the swept klystron and a harmonic of a tuneable crystal oscillator. The crystal frequency was multiplied 90 times to 450 MHz in a frequency multiplier chain (Micro-Now model 101C), and then applied to a step-recovery diode (Hewlett-Packard 33004A) mounted in K-band waveguide. The 53rd harmonic of the 450 MHz signal at approximately 24000 MHz was mixed with the klystron signal at the crystal mixer (A), and displayed as a zero beat pip on the oscilloscope trace. The frequency of the 5 MHz crystal oscillator was measured with a digital frequency meter. If the frequencies of the oscillator at the two half-power points were F_1 and F_2, then

$$\Delta f = 90 \times 53 \, (F_2 - F_1) \qquad \text{C.2}$$

and

$$f_o = 90 \times 53 \, (F_1 + F_2)/2 \qquad \text{C.3}$$

Substituting in Eqn. C.1 :-

$$Q_\ell = \frac{(F_1 + F_2)}{2(F_2 - F_1)} \qquad \text{C.4}$$

Thus only the two determinations of the crystal oscillator frequency F_1 and F_2 were required for each Q_ℓ determination.

The unloaded Q-factor, Q_u, of the Fabry-Pérot cavity is used in Chapter 1 for comparison with theory. This may be obtained from Q_ℓ, if the coupling coefficients at the two coupling holes β_1 and β_2 are known, by using the relation (Harvey, 1963B)

$$Q_u = Q_\ell \, (1 + \beta_1 + \beta_2) \qquad \text{C.5}$$

The determination of β_1 and β_2 is described in Appendix B.

APPENDIX D

KEY TO SYMBOLS USED IN THE CIRCUIT DIAGRAMS

Amplifier (30 MHz)

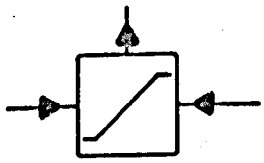

Phase discriminator

Sawtooth waveform generator

Oscillator

Variable frequency oscillator (including klystron)

Detector or mixer (in particular, microwave crystal)

Diode (in particular, step recovery diode)

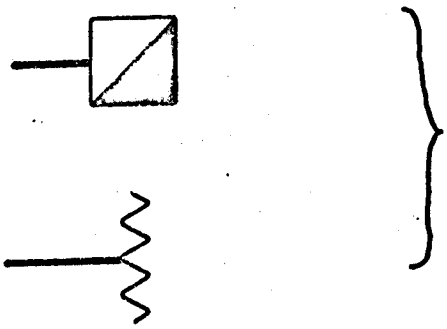

Matched loads

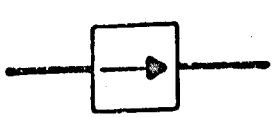

Isolator (forward direction indicated by arrow)

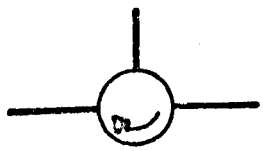

3 port circulator

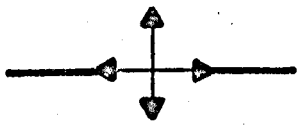

Matching unit

Variable attenuator

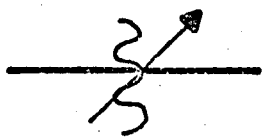

Variable phase shifter

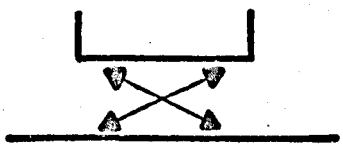

Directional coupler

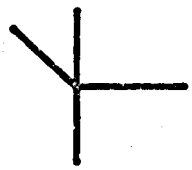

Magic tee

REFERENCES

Alsop, L.E., Giordmaine, J.A., Townes, C.H. and Wang, T.C., 1957: Phys. Rev., 107, 1450.

Barchukov, A.I. and Prokhorov, A.M., 1959: Radio Engng. Electron. Phys., 4, 216.

Barchukov, A.I. and Prokhorov, A.M., 1961: Trans. 10th. Ampère Soc. Colloq., 14, 494.

Barchukov, A.I. and Petrov Yu. N., 1962: Radio Engng. Electron. Phys., 7, 387.

Barchukov, A.I., Prokhorov, A.M. and Savranskii, V.V., 1963: Radio Engng. Electron. Phys., 8, 385.

Barchukov, A.I., Prokhorov, A.M. and Savranskii, V.V., 1964: Quantum Electronics III, ed. P. Grivet and N. Bloembergen (N.Y. Columbia Univ.) 419.

Bardo, W.S., 1969: Ph.D. Thesis, University of Keele.

Bardo, W.S. and Lainé, D.C., 1971: J. Phys. E: Sci. Instr. 4, 595.

Barnes, F.S., 1959: Proc. IRE, 47, 2085.

Basov, N.G. and Prokhorov, A.M., 1955A: Disc. Faraday Soc., 19, 96.

Basov, N.G. and Prokhorov, A.M., 1955B: Usp. Fiz. Nauk., 57, 485.

Basov, N.G. and Zuev, V.S., 1961: Instrum. Exptl. Tech., 1, 122.

Basov, N.G., Oraevskii, A.N., Strakhovskii, G.M. and Tatarenkov, V.M., 1964: Sov. Phys. JETP, 18, 1211.

Becker, G., 1963A: Z. angew. Phys., 15, 218.

Becker, G., 1963B: Z. angew. Phys., 15, 13.

Becker, G., 1965: Z. angew. Phys., 20, 398.

Bleaney, B.I. and Bleaney, B., 1962: Electricity and Magnetism (Oxford Clarendon Press) 258.

Bloom, S., 1956: J. Appl. Phys., 27, 785.

Bogomolov, G.D., 1963: High-power Electronics, Collection of Articles No. 3, (Moskva Izd-vo Nauka) 148.

Checcacci, P.F., Scheggi, A.M. and Toraldo di Francia G., 1964: Alta Frequenza, 33, 720.

Checcacci, P.F. and Scheggi, A.M., 1965: Appl. Optics, 4, 1529.

Checcacci, P.F., Consortini, A. and Scheggi, A.M., 1966A: Proc. IEEE, 54, 1329.

Checcacci, P.F., Scheggi, A.M. and Toraldo di Francia, G., 1966B: Electron. Lett., 2, 64.

Collier, R.J. and Wilmshurst, T.H., 1966: Phys. Lett., 23, 333.

Collier, R.J. and Wilmshurst, T.H., 1967: Brit. J. Appl. Phys., 18, 1053.

Culshaw, W., 1962: Trans. IRE, MTT-10, 331.

Culshaw, W. and Kannelaud, J., 1964: Phys. Rev., 133, A691.

Dicke, R.H., 1958: Off. Gaz. U.S. Pat. Off., 734, 526.

Dyke, T.R., Tomasevich, G.R., Klemperer, W. and Falconer, W.E., 1972: J. Chem. Phys., 57, 2277.

Einstein, A., 1917: Phys. Z., 18, 121.

English, T.C. and Zorn, J.C., 1973: Methods of Experimental Physics, 3, (Academic Press, N.Y., to be published).

Feynmann, R.P., 1965: The Feynmann Lectures on Physics, Vol. III, (Addison-Wesley, Reading, Mass.) Chap. 9.

Fork, R.L. and Sargent, M. III, 1966: Proceedings of the International Conference on Physics of Quantum Electronics, ed. P.L. Kelley, B. Lax and P.E. Tannenwald; (McGraw-Hill, N.Y.) 611.

Fox, A.G. and Li, T., 1961: Bell Syst. Tech. J., 40, 453.

Gambling, W.A. and Wilmshurst, T.H., 1964: Quantum Electronics III, ed. P. Grivet and N. Bloembergen (N.Y. Columbia Univ.) 401.

Garrett, C.G.B., 1967: Gas Lasers (McGraw-Hill, N.Y.) 25.

Giordmaine, J.A. and Wang, T.C., 1960: J. Appl. Phys., 31, 463.

Gordon, J.P., 1955: Phys. Rev., 99, 1253.

Gordon, J.P., Zeiger, H.J. and Townes, C.H., 1955: Phys. Rev., 99, 1264.

Gordon, J.P. and White, L.D., 1958: Proc. Inst. Radio Engrs., 46, 1588.

Grigor'yants, V.V. and Zhabotinskii, M.E., 1961: Radio Engng. Electron. Phys., 6, 260.

Hara, K., Kobayashi, T., Matsui, T., Nakase, T. and Yonezaki, G., 1971: Jap. J. Appl. Phys., 10, 1066.

Harvey, A.F., 1963A: Microwave Engineering (Academic Press, London) 65.

Harvey, A.F., 1963B: ibid, 201.

Heavens, O.S., 1964: Optical Masers (Methuen, London) 25.

Helmer, J.C., 1957: Phys. Rev., 107, 902.

Helmer, J.C., Jacobus, F.B. and Sturrock, P.A., 1960: J. Appl. Phys., 31, 458.

Herrmann, J. and Bonanomi, J., 1956: Hel. Phys. Acta, 29, 448.

Hibben, S.G., 1969: Microwave J. (Nov. 1969), 59.

Hirono, M., 1959: J. Radio Res. Lab., 6, 515.

Jen, C.K., 1948: Phys. Rev., 74, 1396.

Krupnov, A.F., 1959: Izv. Vyssh. Uch. Zav. Radiofiz., 2, 658.

Krupnov, A.F. and Skvortsov, V.A., 1964: Sov. Phys. JETP, 18, 1426.

Krupnov, A.F. and Skvortsov, V.A., 1965A: Sov. Phys. JETP, 20, 1079.

Krupnov, A.F. and Skvortsov, V.A., 1965B: Instrum. Exper. Tech., 1, 126.

Krupnov, A.F. and Skvortsov, V.A., 1965C: Radio Engng. Electron. Phys., 10, 320.

Krupnov, A.F. and Skvortsov, V.A., 1965D: Sov. Radiophys., 8, 148.

Lainé, D.C., 1966: Phys. Lett., 23, 557.

Lainé, D.C., 1967: Electron. Lett., 3, 454.

Lainé, D.C. and Kakati, D., 1969: J. Phys. B: Atom. Molec. Phys., 2, 152.

Lainé, D.C., 1970: Rep. Prog. Phys., 33, 1001.

Lainé, D.C. and Bardo, W.S., 1971: J. Phys. B: Atom. Molec. Phys., 4, 1738.

Lainé, D.C. and Smart, G.D.S., 1971: J. Phys. D: Appl. Phys., 4, L23.

Lamb, W.E. Jr., 1964: Phys. Rev., 134, A1429.

Lefrère, P.R., 1973: Ph.D. Thesis, University of Keele (to be submitted).

Logachev, V.A., Murozov, V.N., Savva, V.A. and Strakhovskii, G.M., 1968: Radio Engng. Electron. Phys., 13, 1764.

Marcuse, D., 1961A: J. Appl. Phys., 32, 743.

Marcuse, D., 1961B: Proc. Inst. Radio Engrs., 49, 1706.

Marcuse, D., 1962: IRE Trans. Instrum., I-11, 187.

Mednikov, O.I. and Parygin, V.H., 1963: Radio Engng. Electron. Phys., 8, 685.

Miller, R.C. and Kusch, P., 1955: Phys. Rev., 99, 1314.

Murina, T.M. and Prokhorov, A.M., 1963: Optics and Spectrosc. 15, 119.

Naumov, A.I., 1963: Sov. Phys., Tech. Phys., 8, 88.

Ogura, H. and Yoshida, Y., 1964: Jap. J. Appl. Phys., 3, 546.

Olander, D.R., Jones, R.H. and Siekhaus, W.J., 1970: J. Appl. Phys., 41, 4388.

Ooms, G., 1968: Appl. Sci. Res., 19, 198.

Paananen, R., Tang, C.L. and Statz, H., 1963: Proc. IEEE, 51, 63.

Pound, R.V., 1948: Microwave Mixers (M.I.T. Radiation Lab. Series Vol. 16, McGraw-Hill, N.Y.) 56.

Prokhorov, A.M., 1958: Sov. Phys. JETP, 34, 1140.

Rudd, M.E. and Craig, J.R., 1968: Rev. Sci. Instr., 39, 1372.

Sargent, M.III, Lamb, W.E. Jr. and Fork, R.L., 1967A: Phys. Rev., 164, 436.

Sargent, M.III, Lamb, W.E. Jr. and Fork, R.L., 1967B: Phys. Rev., 164, 450.

Schawlow, A.L. and Townes, C.H., 1958: Phys. Rev., 112, 1940.

Schulten, G., 1966: Frequenz, 20, 10.

Shimizu, T. and Shimoda, K., 1961: J. Phys. Soc. Japan, 16, 777.

Shimoda, K., Wang, T.C. and Townes, C.H., 1956: Phys. Rev., 102, 1308.

Shimoda, K., 1957: J. Phys. Soc. Japan, 12, 1006.

Siekhaus, W.J., Jones, R.H. and Olander, D.R., 1970: J. Appl. Phys., 41, 4392.

Statz, H., Paananen, R. and Koster, G.F., 1962: J. Appl. Phys., 33, 2319.

Strakhovskii, G.M., Tatarenkov, V.M. and Shumyatskii, P.S., 1966: Radio Engng. Electron. Phys., 11, 438.

Takami, M. and Shimizu, T., 1966: J. Phys. Soc. Japan, 21, 973.

Takeuchi, N., Shimoda, K. and Ogawara, Y., 1966: Jap. J. Appl. Phys, 5, 608.

Tang, C.L. and Statz, H., 1967: J. Appl. Phys., 38, 2963.

Tomlinson, W.J. and Fork, R.L., 1967: Phys. Rev., 164, 466.

Toraldo di Francia, G., 1965: Applied Optics, 4, 1267.

Townes, C.H., 1951: The maser was first proposed by Nethercot of the University of Columbia on behalf of Townes at a symposium on submillimetre waves at the University of Illinois in May 1951 (Alsop et al, 1957).

Townes, C.H. and Schawlow, A.L., 1955: Microwave Spectroscopy (McGraw-Hill, N.Y.) 287.

Vainshtein, L.A., 1963: Sov. Phys. JETP, 17, 709.

Vonbun, F.O., 1958: J. Appl. Phys., 29, 632.

Welling and Andreson, 1964: IEEE Trans. MTT-12, 249.

Wittke, J.P., 1957: Proc. IRE, 47, 291.

Zimmerer, R.W., 1962: Rev. Sci. Instr., 33, 858.

Zimmerer, R., 1963: IEEE Trans., MTT-11, 371.

Zimmerer, R.W., Anderson, M.V., Strine, G.L. and Beers, Y., 1963: IEEE Trans., MTT-11, 142.

Zuev, V.S. and Cheremiskin, I.V., 1962: Radio Engng. Electron. Phys., 7, 869.